

DOCTORAL THESIS

Contribution of Nano- and Microgrids to Topological Power Plants Regarding Voltage and Frequency Control

Jorge Luis Helguero Cruz

TALLINN UNIVERSITY OF TECHNOLOGY
DOCTORAL THESIS
60/2023

Contribution of Nano- and Microgrids to Topological Power Plants Regarding Voltage and Frequency Control

JORGE LUIS HELGUERO CRUZ



TALLINN UNIVERSITY OF TECHNOLOGY

School of Engineering

Department of Electrical Power Engineering and Mechatronics

This dissertation was accepted for the defence of the degree 26/10/2023

Supervisor: Prof. Dr. Argo Rosin
Department of Electrical Power Engineering and Mechatronics
School of Engineering
Tallinn University of Technology
Tallinn, Estonia

Co-supervisor: Prof. Dr.-Ing. Dr. h.c. Helmuth Biechl
Institute of Electrical Power Systems (IEES)
Kempten University of Applied Sciences
Kempten, Germany

Opponents: Mehdi Savaghebi, Professor in Power Electronic-Enabled Power Systems
Department of Engineering Technology
Technical University of Denmark (DTU)
Lyngby, Denmark

Sami Repo, Professor of Smart Grids, Electrical Engineering
Faculty of Information Technology and Communication Sciences
Tampere University
Tampere, Finland

Defence of the thesis: 01/12/2023, Tallinn

Declaration:

Hereby I declare that this doctoral thesis, my original investigation and achievement, submitted for the doctoral degree at Tallinn University of Technology has not been submitted for doctoral or equivalent academic degree.

Jorge Luis Helguero Cruz

.....
signature



European Union
European Regional
Development Fund



Investing
in your future

Copyright: Jorge Luis Helguero Cruz, 2023

ISSN 2585-6898 (publication)

ISBN 978-9916-80-063-8 (publication)

ISSN 2585-6901 (PDF)

ISBN 978-9916-80-064-5 (PDF)

Printed by EVG Print

TALLINNA TEHNIKAÜLIKOOL
DOKTORITÖÖ
60/2023

Nano- ja mikrovõrkude mõju topoloogilistele elektrijaamadele pinge ja sageduse juhtimise kontekstis

JORGE LUIS HELGUERO CRUZ



Contents

List of Publications	7
Author's Contribution to the Publications	8
Abbreviations	9
Symbols	10
1 Introduction	15
1.1 Thesis Objectives	16
1.2 Hypotheses	16
1.3 Research Tasks	16
1.4 Contribution and Dissemination	17
2 State of the Art	18
2.1 Transition from Traditional to Modern Power Systems	18
2.1.1 Generation	19
2.1.2 Transmission	23
2.1.3 Distribution	27
2.2 Ancillary Services	29
2.2.1 Congestion Management	30
2.2.2 Network Recovery	30
2.2.3 Voltage Stability	30
2.2.4 Frequency Stability	33
2.3 Voltage-Sourced Inverters	39
2.4 Clustering Generation and Load	40
2.4.1 Nanogrid	40
2.4.2 Microgrid	42
2.4.3 Virtual and Topological Power Plant	42
2.5 Conclusions	44
3 Development and Validation of Mathematical Models of the Nanogrid for Frequency and Voltage Control	46
3.1 Demonstrator	46
3.1.1 Nanogrid	47
3.1.2 Microgrid	55
3.2 Subsystems	56
3.2.1 Home Battery Energy Storage System I	59
3.2.2 Home Battery Energy Storage System II	62
3.2.3 Photovoltaic System	65
3.3 Complete System Including Control Centre	72
3.3.1 Dynamic Model of the Grid-Connected Nanogrid	72
3.3.2 Power Distribution Control (PDC)	79
3.3.3 Stability Analysis Considering Communication Delays	82
3.4 Conclusions	91
4 Development of a Method for the Optimal Provision of Ancillary Services by a TPP ..	93
4.1 Modelling and Simulation of Active and Reactive Power Flow and Node Voltages ..	93
4.1.1 Load Flow Calculation Methodology	93
4.1.2 Optimization Methodologies	98
4.1.3 Simulation Results with Respect to Distribution Grid Restrictions	102

4.2 Cost-Benefit Analysis of the Provision of Ancillary Services by Topological Power Plants.....	113
4.3 Planning Criteria for a Distribution Grid with Ancillary Service Capability	114
4.4 Conclusions	116
5 Conclusions and Future Work	118
5.1 Conclusions	118
5.2 Future Work	118
List of Figures	120
References	124
Acknowledgements.....	134
Abstract.....	135
Lühikokkuvõte.....	136
Appendix	137
Curriculum vitae	181
Elulookirjeldus.....	182

List of Publications

The list of author's publications, on the basis of which the thesis has been prepared:

- I J. Helguero, A. Rosin, H. Biechl. Stability Analysis of a Nanogrid Considering Communication Delay Time. 10th International Conference On Electrical and Electronics Engineering (ICEEE 2023).
- II J. Helguero, S. Galeano, A. Rosin, H. Biechl. Provision of Reactive Power by Nanogrids as part of a Topological Power Plant in a Low Voltage Network. 2020 International Conference on Smart Energy Systems and Technologies (SEST).
- III T. Häring, A. Rosin, T. M. Kull, J. Helguero, H. Biechl. Thermal Modelling of a Control Center for Flexibility Analysis in nZEB Nanogrids. 2020 IEEE 61st International Scientific Conference on Power and Electrical Engineering of Riga Technical University (RTU CON).
- IV J. Helguero, A. Rosin, H. Biechl. Provision of Ancillary Services of a Nanogrid in Grid Connected Mode. 2019 Electric Power Quality and Supply Reliability Conference (PQ) & 2019 Symposium on Electrical Engineering and Mechatronics (SEEM).
- V S. Uebermasser, C. Groiss, A. Einfalt, N. Thie, M. Vasconcelos, J. Helguero, H. Laaksonen, P. Hovila. Requirements for coordinated ancillary services covering different voltage levels. 24th International Conference & Exhibition on Electricity Distribution (CIRED) and IET Journals, Volume 2017, Issue 1, October 2017, p. 1421-1424.
- VI A. Rahmoun, A. Armstorfer, J. Helguero, H. Biechl, A. Rosin. Mathematical modeling and dynamic behavior of a Lithium-Ion battery system for microgrid application. 2016 IEEE International Energy Conference (ENERGYCON).

Author's Contribution to the Publications

The author's contributions to the papers are:

- I Jorge Helguero, as the main author, examined the stability of a nanogrid considering communication delay time by analyzing the pole-zero plot of the system. Furthermore, Jorge Helguero developed and validated the small-signal model of the nanogrid.
- II Jorge Helguero, as the main author, developed an optimization algorithm for the provision of reactive power at the PCC of a topological power plant as well as for the minimization of active power losses within it.
- III Jorge Helguero, as co-author of the paper, performed and evaluated temperature measurements for the thermal model of a container with control centre purposes.
- IV Jorge Helguero, as the main author, developed a concept of a nanogrid that can provide ancillary services to the distribution grid. The concept was implemented in a real demonstrator as well as in a simulation environment.
- V Jorge Helguero, as co-author of the paper, contributed to the technical requirements for the expansion of the demonstrator in the Innovation Cell Germany.
- VI Jorge Helguero, as co-author of the paper, developed in PSCAD™ the modelling of the Energy Storage System (ESS) with focus on power electronics and control loops.

Abbreviations

AC	Alternating Current
CSI	Current-sourced Inverter
DC	Direct Current
DG	Distributed Generation
DS	Distributed Storage
EHV	Extra High Voltage
ENTSO-E	European Network of Transmission System Operators for Electricity
HBESS I	Home Battery Energy Storage System I
HBESS II	Home Battery Energy Storage System II
HV	High Voltage
HVDC	High Voltage Direct Current
IGBT	Insulated Gate Bipolar Transistor
LV	Low Voltage
MIMO	Multiple Input Multiple Output
MPP	Maximum Power Point
MPPT	Maximum Power Point Tracker
MV	Medium Voltage
PCC	Point of Common Coupling
PDC	Power Distribution Control
PI	Proportional Integral
PLL	Phase-locked Loop
PV	Photovoltaic
RES	Renewable Energy Source
RGA	Relative-gain Array
RMS	Root Mean Square
SISO	Single Input Single Output
SOC	State of Charge
SOH	State of Health
SPWM	Sine Pulse Width Modulation
TPP	Topological Power Plant
TSO	Transmission System Operator
VPP	Virtual Power Plant
VSI	Voltage-sourced Inverter

Symbols

A	Matrix
ACE	Area Control Error
c_i	Contribution to the primary power/frequency control in a control block or area i
$c(x)$	Function representing constraints
$C_{DC1,2}$	Capacitors 1 and 2 at the output of the bidirectional DC/DC converters of HBESS II
$C_{DCLink}^{PV1,2}$	DC link capacitor of the PV systems 1 and 2
E_i	Annual energy production within a control block or control area i
E_u	Annual energy production of the synchronous area
F_i	Cost rates of the generation unit i
\hat{f}	Amplitude
$\vec{f}(t)$	Space phasor
f_n	Nominal frequency
f_{set}	Frequency set point
$f_x(t)$	Sinusoidal function of the phase x
f_α	Real component of the space phasor
f_β	Imaginary component of the space phasor
$\vec{G}(s)$	Transfer function matrix
$G_{xy}(s)$	Transfer functions part of the transfer function matrix $\vec{G}(s)$
i_{abc}^x	Current in abc-Frame at the output of the DG/DS x in the demonstrator
$i_{bat}^{HBESS_I}$	DC current at the output of the battery model of HBESS I
$i_{bat1,2}$	Current 1 und 2 at the output of the battery modules 1 and 2 in HBESS III
\underline{I}	Current phasor
I_b	Load of the branch b
I_i	Current at the bus i
$\underline{I}_{1,2}$	Current phasor flowing through the impedance $Z_{K,Net}$
i_{dq}	Current in dq-Frame at the output of a VSI
$i_{d,q}^{load}$	Current of the load in dq-Frame
$i_{HBESS_I,d,q}^g$	Current at the output of HBESS I in global dq-Frame
i_{dq}^{Grid}	Current at the grid side in dq-Frame
$i_{d,q}^{HBESS_I}$	Current in dq-Frame at the output of HBESS I
$i_{i,d,qHBESS_I}$	Current after the integrator in the inner control loop of HBESS I (dq-Frame)
$i_{ref,d,q}^{HBESS_I}$	Reference current in dq-Frame for the inner loop controller of HBESS I (dq-Frame)
$I_{dq,ref}^x$	Reference current in dq-Frame for the inner loop controller of the DG/DS x in the demonstrator
\vec{i}	Space phasor equivalent of $i_x(t)$

I_K^n	Subtransient fault current (RMS)
I_{max}	Maximum loading of a branch
I_{MPP}	Current at MPP (data sheet)
$i_{pv1,2}$	DC current at the output of the strings 1 and 2
$i_x(t)$	Current of the phase x flowing at the AC side of a VSI
K	Factor analogous to the network power frequency characteristic
k	Sum of the number of elements of the interval of reactive power for the nanogrid p
$K_P^{HBESS_I}(s)$	Transfer function of the power controller of HBESS I
$K_P^{HBESS_{II}}(s)$	Transfer function of the power controller of HBESS II
$K_P^{PV_{1,2}}(s)$	Transfer function of the power controller of the PV systems I and II
$K_V^{HBESS_{II}}(s)$	Transfer function of the voltage controller of HBESS II
$K_V^{PV_{1,2}}(s)$	Transfer function of the voltage controller of the PV systems I and II
$K_I^{HBESS_I}(s)$	Transfer function of the current controller of HBESS I
$K_I^{HBESS_{II}}(s)$	Transfer function of the current controller of HBESS II
$K_I^{PV_{1,2}}(s)$	Transfer function of the current controller of the PV systems I and II
$k_{i_{PLL}}$	Integral gain of the PLL controller
$k_{p_{PLL}}$	Proportional gain of the PLL controller
$k_{s_{PLL}}$	Smoothing gain of the PLL controller
L	Inductance representing the output impedance of a VSI
$L_{1,2}$	Inductances in the bidirectional DC/DC converter of HBESS II or cable connecting HBESS I with PCC
L_5	Equivalent inductance of the load and cable in the nanogrid
L_{Grid}	Inductance representing the cable connection between the nanogrid and the external grid
$L_{DC}^{HBESS_I}$	Inductance of the bidirectional DC/DC converter of HBESS I
$L_{DC}^{PV_{1,2}}$	Inductance of the DC/DC converter of the PV system 1 and 2
L_{eq}^x	Equivalent output inductance of the DG/DS x in the demonstrator
\vec{n}_p	Number of elements of the interval for a nanogrid p
$O(x)$	Objective function
P_0	Active power programmed schedule values at the tie-lines
P_2	Active power at the load
$P_{batset_{1,2}}$	Set points 1 and 2 for the controllers of the bidirectional DC/DC converters of HBESS II
P_{BP}	Active power break point of the PV inverter in the demonstrator
PF_{max}	Maximum power factor of the PV inverter in the demonstrator
P_{HBESS_I}	Actual active power of HBESS I
$P_{HBESS_{act}}$	Actual active power of the home battery storage system
P_i	Active power at the bus i
P_i^{sch}	Scheduled active power at the bus i
$P_{DC}^{PV_{1,2}}$	Transfer function of the power controller of the DC/DC converter in the PV systems I and II

P_{load}	Active power of the load
P_{losses}	Active power losses
P_{MPP}	Active power at MPP (data sheet)
$P_{MPP_{1,2}}$	Active power at MPP of the PV system I and II (modelling)
P_n	Nominal active power
$P_{PV_{act}}$	Actual AC active power of the PV inverter in the demonstrator
P_{PV}	Active power of the PV system
$P_{pv_{1,2}}$	Actual DC active power of the PV systems 1 and 2
$P_{red_{1,2}}$	Active power reduction of the PV systems 1 and 2
$P_{red_{1,2}}^Q$	Active power reduction of the PV systems 1 and 2 (for reactive power provision)
P_{ref}^x	Active power set point of the DG/DS x in the demonstrator
$P_{surplus}$	Active power surplus
$P_{\dot{u}}$	Addition of all active power measurements at the tie-lines
Q_2	Reactive power at the load
$Q_{Farm_y}^i$	Reactive power of the farm y in the time step i
Q_{HBESS_I}	Actual reactive power of HBESS I
$Q_{HBESS_{max}}$	Maximum reactive power of the home battery storage system
Q_i	Reactive power at the bus i
Q_i^{sch}	Scheduled reactive power at the bus i
Q_{losses}^i	Reactive power losses at the time step i
Q_{max}	Maximum reactive power of the PV inverter in the demonstrator
\vec{Q}_{nano}	Vector representing the reactive power of all nanogrids
$Q_{Nanogrid_x}^i$	Reactive power of the nanogrid x in the time step i
$Q_{PV_{max_blue}}$	Maximum reactive power of the PV inverter in the demonstrator (blue zone)
$Q_{PV_{max_green}}$	Maximum reactive power of the PV inverter in the demonstrator (green zone)
Q_{ref}^x	Reactive power set point of the DG/DS x in the demonstrator
$Q_{set,TPP}^i$	Reactive power set pint at the PC of the TPP at the time step i
R	Resistance representing the output impedance of a VSI
R_1	Resistance of the cable connecting HBESS I and PCC
R_5	Equivalent resistance of the load and cable in the nanogrid
R_{grid}	Resistance representing the cable connection between the nanogrid and the external grid
R_{eq}^x	Equivalent output resistance of the DG/DS x in the demonstrator
s	Droop of a generator
$S_{HBESS_{rated}}$	Rated apparent power of the home battery storage system
S_x	Duty cycle of the switch x
S_K''	Subtransient short circuit power
\vec{S}_{nanop}	Intervals of reactive power for a nanogrid p

$S_{PV_{rated}}$	Rated apparent power of the PV inverter in the demonstrator
T_a^x	Delay due to the switching frequency of the inverter in the DG/DS x of the demonstrator
U	Voltage magnitude (slack)
U_n	Rated line-to-line voltage
v_{abc}^x	Voltage in abc-Frame at the output of the DG/DS x in the demonstrator
$v_{dq}^{g,Grid}$	Voltage at the grid side in global dq-Frame
$v_{dq}^{g,HBESS_I}$	Voltage in global dq-Frame at the output of HBESS I
v_{dq}^{PCC}	Voltage at PCC in dq-Frame
$v_{d,q}^{HBESS_I}$	Voltage in dq-Frame at the output HBESS I
v'_{abc_x}	Input signal for the voltage source in the simplified model of the DG/DS x in the demonstrator
$v'_{d,q,HBESS_I}$	Input signal for the voltage source in the simplified model of HBESS I (dq-Frame)
$v_{i,d,q,HBESS_I}$	Voltage after the integrator in the inner control loop of HBESS I (dq-Frame)
v_d^x	Direct component of the voltage at PCC of the DG/DS x in the demonstrator
$V_{DCLink}^{HBESS_I}$	DC link voltage of HBESS I
$V_{DCLink_{ref}}^{HBESS_I}$	Set point of the DC link voltage controller of HBESS I
$V_{DCLink_{ref}}^{HBESS_{II}}$	Set point of the DC link voltage controller of HBESS II
$V_{DCLink_{ref}}^{PV_{1,2}}$	Set point of the DC link voltage controller of the PV systems I and II
V_{DC}	DC link voltage of HBESS II
$V_{DC_{ref}}^{PV_{1,2}}$	Set point of the DC link voltage controller of the PV system I and II
$V_{DC_{ref}}$	Set point of the DC link voltage controller of HBESS II
$V_{DC}^{PV_{1,2}}$	DC link voltage of the PV systems I and II
$v_{pv_{1,2}}$	Voltage at the output of the strings 1 and 2
\underline{V}_2	Voltage phasor at the load
V_d	Voltage of the bus bar d
v_{max}	Maximum voltage of bus bar d
v_{min}	Minimum voltage of bus bar d
$V_{i,j}$	Voltage at the bus i or j
$\vec{V}_s(t)$	Space phasor equivalent of $V_{sx}(t)$
$\vec{V}_t(t)$	Space phasor equivalent of $V_{tx}(t)$
V_{MPP}	Voltage at MPP (data sheet)
\hat{V}_s	Amplitude of the function $V_{sx}(t)$
$V_{sx}(t)$	AC voltage of the phase x at the PCC of the VSI
V_{tdq}	Voltage in dq-Frame at the terminals of the DC/AC converter
$V_{tx}(t)$	Voltage of the phase x at the terminals of the DC/AC converter
y_{ij}	Admittance between the bus i and j

Z	Magnitude of the impedance representing transmission lines
$Z_{K,Net}$	Magnitude of the internal impedance of the network
Z_L	Magnitude of the load impedance
Δf	Quasi-steady-state frequency deviation
ΔP	Power deviation due to a disturbance in a power system
ΔP_i	Power deviation due to a disturbance in a control block or area i
ΔQ	Reactive power step
$\Delta U_{1,2}$	Voltage at the impedance $Z_{K,Net}$
$\delta_{i,j}$	Angle related to the voltage at the bus i or j
ε	Phase shift
θ	Angle of the impedance representing transmission lines
ϑ	Angle of the load impedance
θ_0	Initial phase angle of the function $f_x(t)$
θ_{ij}	Angle related to the admittance y_{ij}
$\theta_{ref,HBESS_I}$	Set point of the PLL (HBESS I)
θ_{HBESS_I}	Feedback signal of the PLL (HBESS I)
λ_i	Network power frequency characteristic in a control block or area i
τ	Time delay
ρ	Phase shift
φ	Angle of the slack in a transmission system
ω	Angular frequency of the function $f_x(t)$
ω_{rHBESS_I}	Angular frequency of the PLL (HBESS I)
ω_s	Angular frequency of the global frame

1 Introduction

Power systems have changed tremendously not only in the generation, but also from the legal perspective (Schwab, 2020). Moreover, two main processes have caused in-depth changes in the energy supply, especially in Europe. These are:

- Liberalization of the electricity market
- Climate change

Before 1998, the energy supply market in Europe was completely different from the energy supply market today. Each energy supply company had its own defined supply area (monopole); this means that the customers could be supplied only by one provider. The liberalization of the electricity market in 1998 meant that customers were able to choose the electricity supplier independent of the local connection to the grid.

On the other hand, the rise of the temperature on Earth due to the climate change is being produced mainly by the high emission of greenhouse gases, especially CO₂ or carbon dioxide. The decarbonization (substitution of primary energy sources such as hard coal through solar radiation, wind, water or biomass) and the decommissioning of conventional power plants (e.g., lignite and hard coal) are a measure to reduce the CO₂ emissions and thus fight against the climate change. The European Union has five aims related to its energy policy, two of them regarding energy efficiency and reduction of CO₂. The five main objectives are (Parliament, 2021):

- To ensure energy security through solidarity and cooperation between European countries
- To ensure the functioning of a fully integrated internal energy market
- To improve energy efficiency and reduce dependence on energy imports
- To decarbonize the economy and move towards a low-carbon economy in line with the Paris Agreement
- To promote research in low-carbon and clean energy technologies

Due to the European Union's energy policy, the presence of the renewable energy sources (RESs) in electric power systems in the continent has been increasing tremendously in the last years. This and the shutdown of conventional power plants are modifying the traditional electric power systems to a more decentralized structure. Moreover, a reorganization of the conventional voltage and frequency control must be considered by the application of new methods dealing with this issue. In addition, tasks performed by conventional power plants must be taken over more and more by RESs when big power plants are being decommissioned step by step in the future. Otherwise, the change will lead to an instability of the transmission grid.

With the installation of RES and the decommissioning of conventional power plants taking place, current power systems will be modified to a system of systems that should operate as one (ENTSO-E, Vision on Market Design and System Operation towards 2030). These systems should have a special characteristic, which is interoperability. Microgrids and nanogrids are important contributors to that, since they facilitate interoperability by clustering controllable loads as well as RES. Indeed, this clustering offers not only interoperability with other systems within the system, but also can provide a proper coordination between TSOs (Transmission System Operators) and DSOs (Distribution System Operators).

This scientific work presents a new approach for providing voltage and frequency control from distribution grids. This thesis comprises the provision of active and reactive power for voltage and frequency control by topological power plants (TPPs),

which include nano- and microgrids. Regarding frequency control this work is focusing on delivering active power for secondary and tertiary power/frequency control. Firstly, this research work focuses on the modelling of the dynamic behaviour of a nanogrid in grid-connected mode as well as on the distributed generation (DG) and distributed storages (DS) part of it. The models are validated by specific measurements at a demonstrator in Wildpoldsried, which is a small village located in the south of Germany. Finally, this scientific work concentrates on the development of a method to minimize power losses when providing reactive power by a TPP. In this part of the research, load flow calculations and optimization methods are applied.

1.1 Thesis Objectives

The main goal of this scientific work is to research and develop a new approach for the contribution to voltage control and frequency control in power systems based on the provision of active and reactive power by nano- and microgrids as well as TPP. Additional objectives of this scientific work are:

- To develop detailed and simplified models of DG and DS for dynamic analysis of a nanogrid in grid-connected mode
- To analyze the stability of a nanogrid in grid-connected mode considering time delays
- To develop an optimization method for the provision of reactive power at the PCC with the goal to minimize power losses within TPP

1.2 Hypotheses

The main hypotheses of this thesis are:

- For control and stability analysis, the switching of the IGBT of the inverters in DS and DG can be neglected.
- The stability of a nanogrid in grid-connected mode can be influenced by time delays present in communication infrastructures.
- New method based on local optima enables a TPP in a LV network to provide reactive power to the MV level with a maximum relative error of 5%.
- New method based on local optima will make it possible to reduce power losses significantly when providing reactive power to the MV level by a TPP.

1.3 Research Tasks

The main research tasks of this thesis are:

- Analysis of the integration of RES and provision of ancillary services by them in modern power systems
- Definition and categorization of ancillary services
- Definition of a nanogrid, a microgrid and a TPP
- Detailed mathematical explanation of the development of simplified models for subsystems in a nanogrid when neglecting IGBT
- Development and validation of detailed and simplified mathematical models of subsystems in a nanogrid
- Development and validation of a complete system (including subsystems of a nanogrid as well as control centre)
- Stability analysis of a nanogrid considering communication delays

- Development of a method for the optimal provision of ancillary services by a TPP
- Development of a method for the optimal provision of ancillary services by a TPP as well as for the minimization of active power losses within the TPP

1.4 Contribution and Dissemination

This thesis presents an extensive view into the provision of ancillary services by nano- and microgrids as well as topological power plants. Contributions were made in the modelling of distributed generation, distributed storages as well as in combining them for time domain simulations. Moreover, contributions include operation strategies for the provision of ancillary services by interlinked nanogrids. This work is recommended for network studies (transient and steady state) in the distribution and transmission systems.

Scientific Novelties:

- Detailed and simplified mathematical models of home battery storage systems as well as photovoltaics part of a nanogrid in grid-connected mode were developed to be used in power system analysis.
- A novel systematic approach was developed for analyzing the impact of time delays on the stability of nanogrids in grid-connected mode.
- A novel method based on local optima for the provision of ancillary services by a TPP was developed.
- A novel method was introduced to minimize active power losses within the TPP when delivering ancillary services at the PCC.

Practical Novelties:

- Concepts for the provision of ancillary services were developed to be used in distribution systems as a measure to compensate the decommissioning of conventional power plants and thus guarantee the stability of power systems.
- A method of supplying scheduled values of reactive power by a TPP was developed to contribute to a stable power system operation when conventional power plants are decommissioned.

The scientific work presented in this thesis was published and presented orally in 6 international publications. In addition, the research was introduced in 1 doctoral school.

The outcomes of this thesis are part of the investigations carried out in the projects “IREN2” and “DeCAS”, which were funded by the German Federal Ministry for Economic Affairs and Climate Action. Also, the research of “ZEBE Center of Excellence for zero energy and resource efficient smart buildings and districts” (TAR16012) and “FinEst Centre for Smart Cities (VFP19031 / 856602)” is provided.

2 State of the Art

Due to political decisions and climate change, conventional power plants are being decommissioned. At the same time, the integration of RES is experiencing a tremendous increase, especially in LV networks. Additionally, the decommissioning of conventional power plants means the reduction of the provision of ancillary services, which need to be taken over by RES.

Since the focus of this thesis is on the contribution of nano- and microgrids to a TPP regarding the ancillary services frequency and voltage control, the state the art of this scientific work is structured according to the following topics:

- Transition from traditional to modern power systems
- Ancillary services
- Voltage-sourced inverters
- Clustering generation and load

2.1 Transition from Traditional to Modern Power Systems

Power systems followed a centralized structure, which is basically composed of generation, transmission and distribution systems. However, this centralized structure is being modified due to the integration of RES and the decommissioning of conventional power plants, as seen in Figure 2-1 (mainly in the distribution systems). This generates a bidirectional load flow (Henninger, 2019), (Birkelbach, Woiton, Thiele, & Westermann, 2018). On those bases, the main characteristics of modern power systems are described in the following sections (in sections 2.1.2 and 2.1.3, the focus is on Germany).

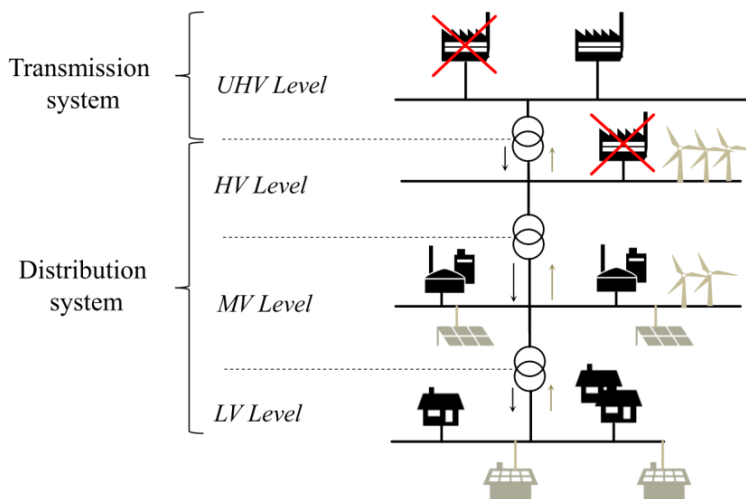


Figure 2-1. Overview of the current situation of a power system: Decommissioning of conventional power plants, integration of RES as well as change in the direction of the power flow (Henninger, 2019).

2.1.1 Generation

In Europe, power is generated by conventional power plants and RES. Conventional power plants are categorized as nuclear power plants, lignite power plants, hard coal power plants, and gas power plants. On the other hand, RESs are basically classified as hydropower plants, wind power systems, PV power plants, electrical energy storages, biomass/biogas power plants, geothermal power generation, and fuel cells. In particular, conventional power plants are being decommissioned due to climate change policies. For example, in Germany, 132 of these power plants were shut down from 2012 until 2020 (Bundesnetzagentur, Krafwerkliste, 2021). Next, a brief explanation of each conventional power plant as well as RES is presented:

Nuclear power plants: Electricity is generated by the process of nuclear fission (splitting apart nuclei) in a reactor. The heat generated by the reactor boils the water circulating in the system into steam, which rotates a turbine and a generator. Nuclear power plants have generally cooling towers (heat exchanger), where steam or water vapor is released (Schwab, 2020). The number of operable reactors in Europe is 106; the reactors under construction, planned as well as proposed are 4, 7 and 15, respectively. This data corresponds to the European member states as of February 2021 (Association, 2021). In Germany, in order to increase nuclear safety, the last three power plants (Isar 2, Emsland and Neckarwetheim 2) were shut down in April 2023.

Lignite and hard coal power plants: The principle is the same for these two kinds of power plants. They produce electrical energy based on lignite or hard coal, which is crushed, dried, and reduced to dust. The dust is burnt, which is a combustion process that emits carbon dioxide (CO₂). Then, it heats water to produce steam. The steam is guided to the turbines. The rotary movement of the turbines in combination with a generator produces electrical energy, which is sent to the electric power system (LEAG, 2021). Most of these power plants employ cooling towers, where water taken from a river circulates for cooling purposes. One part of this water is reutilized after the cooling process; the other part is lost due to evaporation and thus steam is released from the cooling towers. There are around 707 coal power plants in the European member states. These plants are either already closed or pledged to shut down (Analytics, 2021), (Europe, 2021).

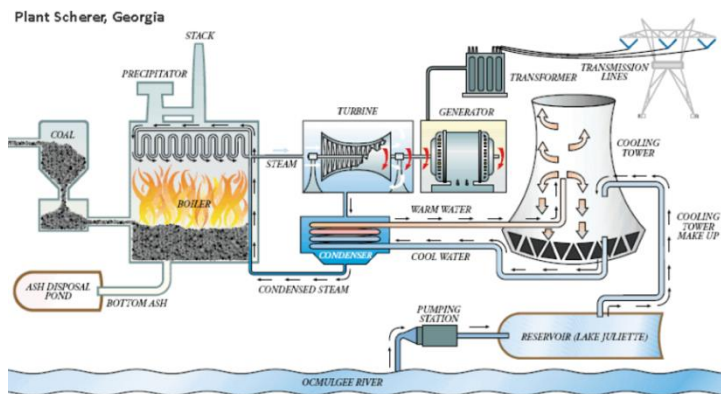


Figure 2-2. Example of a hard coal power plant in Georgia (USA) (Survey, 2021).

Gas power plants: These power plants burn natural gas to produce electrical energy. The principle of functionality is the same as in lignite and hard coal power plants, the difference is that air is compressed to spin the turbine. CO₂ is emitted when burning natural gas, but according to (Quaschnig, 2021), specific CO₂-emissions in relation to one kWh electricity by natural gas are around 60% and 57% lower than the CO₂-emissions of lignite and hard coal, respectively. In Europe, there are around 760 of these power plants (Ltd., 2021).

Hydropower plants: They work in a way similar to lignite and hard coal power plants. In the case of hydropower plants, water is used to produce the rotary movement of the turbines, which in combination with a generator produces electrical energy. According to (Nature, 2021), by the end of 2019, there were 21,387 hydropower plants in Europe and 8,785 were planned or under construction.

Wind power plants: Wind power plants convert wind into electricity. Additionally, they consist of a mechanical, electrical subsystem. The mechanical subsystem has usually a hub, main bearing, shafts, brakes, and a gear box, as seen in Figure 2-3. On the other hand, the electrical system has one generator and power electronics. Three types of generators can be distinguished here: DC, asynchronous as well as synchronous generators.

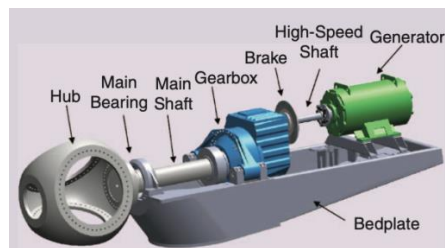


Figure 2-3. Typical configuration of a mechanical subsystem in a wind power plant (Novakovic, Duan, Solveson, Nasiri, & Ionel, 2016).

Regarding the installed capacity in Europe in 2020 (see Figure 2-4), The Netherlands led the installation of wind power plants with 1.979 GW, followed by Germany and Norway with 1.650 GW and 1.532 GW, respectively. Figure 2-5 shows the installed capacity in Europe from 2011 until 2020. Europe installed 14.7 GW of new wind power plants in 2020. This is reduction of around 5.7% compared to the previous year.

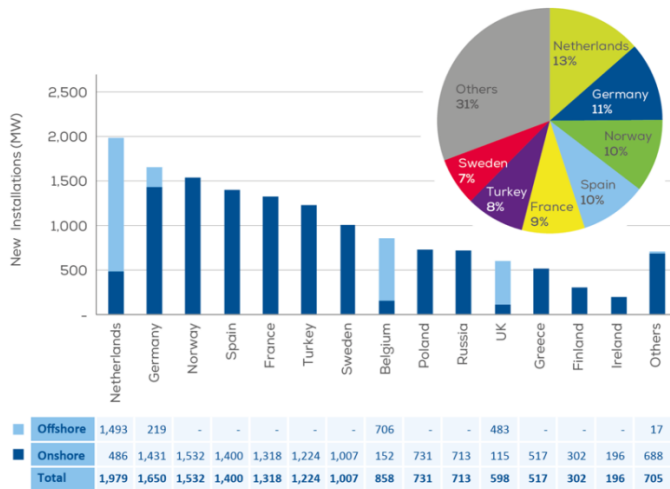


Figure 2-4. New installations of wind power plants in European countries in 2020 (WindEurope, 2021).

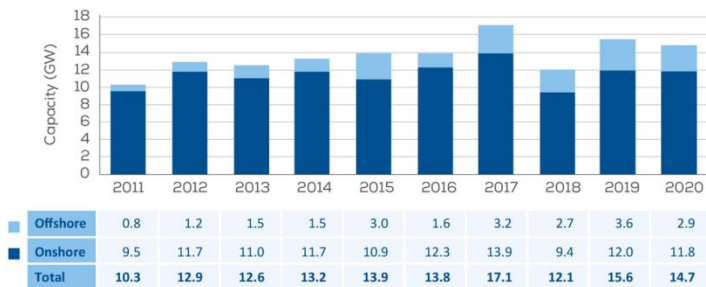


Figure 2-5. Installed capacity of wind power plants in Europe from 2011 until 2020 (WindEurope, 2021).

PV power plants: In these power plants, the solar radiation is transformed to electricity by using PV cells (arranged in a module, a string of series-connected modules, or an array of parallel-connected strings). These cells generate DC current and DC voltage, which, in turn, are transformed by a DC/AC inverter and then passed through a filter. Sometimes DC/DC converters are applied so that the minimum DC voltage at the input of the DC/AC inverter is achieved, otherwise the power cannot be supplied at the AC side.

The stacked bar graph of Figure 2-6 shows the annual installed capacity of PV in the 27 member states of the European Union (2000-2020). It shows the increase of the installed capacity by 110% in 2020 compared to 2019. Moreover, by the end of 2020, European countries installed 18.2 GW; the second-best year after 2011, whose annual installed capacity was 21.4 GW.

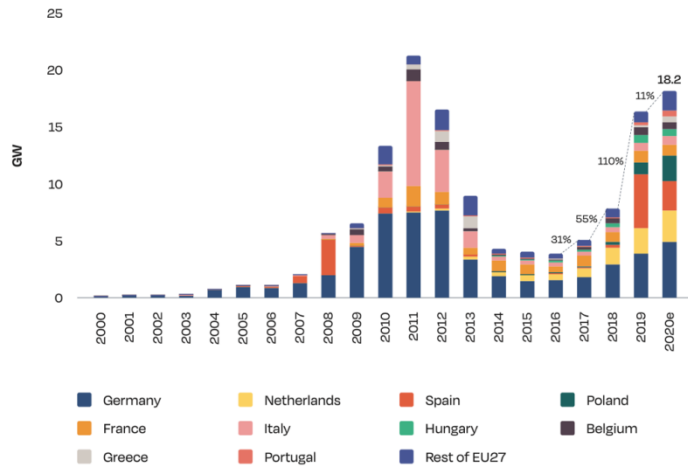


Figure 2-6. EU27 Annual solar PV installed capacity 2000-2020 (Schmela, 2020).

Electrical energy storages: These are systems that storage electrical energy depending on the energy used, as seen in Figure 2-7. For example, electrochemical energy storage systems store chemical energy that will be later converted to electrical energy. Electrical energy storages can be applied to provide the following services (Zhang, et al., 2017):

- Electricity energy time-shift
- Peak load management
- Reduced curtailment of RES
- Primary frequency response, fast frequency response and synthetic inertia-like response
- Reactive power and voltage support
- Critical load support during islanding and black-start capability

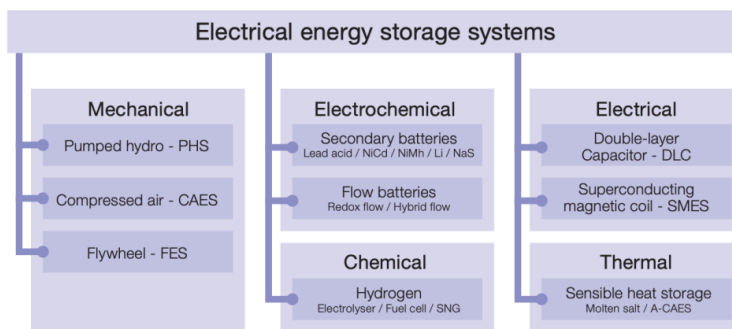


Figure 2-7. Classification of electrical energy storage systems (Commission I. E., 2021).

The market of electrical energy storage systems is growing. For instance, from 2013 until 2019, home storage systems (battery capacity lower than 30 kWh) in Germany showed an exponential behaviour in their cumulative installed storage capacity and inverter power, as depicted in Figure 2-8.

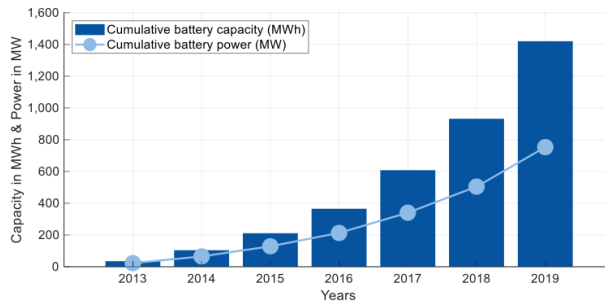


Figure 2-8. Cumulative battery capacity and battery inverter power of home storage systems in Germany (Figgener, et al., 2020).

Biomass/Biogas power plants: In this kind of power plants, electrical and thermal energy are generated by applying biogas or biomass as energy source. Such a process is called cogeneration or also named combined heat and power (CHP) (Valov, 2020). According to (Commission E., 2021), the total CHP electrical capacity in the 27 European Union countries was around 133.60 GW.

Geothermal power generation: These power plants use the heat within the Earth to produce electrical energy. The principle of functionality is the same as in lignite and hard coal power plants, with the difference of the source. In 2020, the installed power capacity in Europe was 3000 MW_{el} (Sanner, 2019).

Fuel cells: These are devices that convert chemical energy into electrical energy, without the emission of polluting gases. When applying hydrogen as fuel, heat, water, and electricity are generated (Melo, Yahyaoui, Farias, Frizera, & Tadeo, 2018). Fuel cells are applied in transportation (buses, trains, personal vehicles) and power generation. For example, surplus energy from wind and solar parks can be used to produce hydrogen by applying electrolysis of water (decomposition into oxygen and hydrogen gas). The produced hydrogen can be used later as fuel.

2.1.2 Transmission

There are three possible types of transmission in power systems: single-phase and three-phase systems as well as the HVDC power links (Heuck, Dettmann, & Schulz, 2013).

Single-phase systems are applied in electric railways. In Germany, for example, the nominal voltages for these single-phase systems are 110 kV, 60 kV, and 15 kV.

HVDC power links are currently required in Germany since more and more decentralized generation units are being installed far away from the consumers. In Germany, the distance between the offshore wind power plants located in the north and the consumers situated in the south of the country (high presence of industry) could reach 1,000 km. HVDC power links are a very good solution in these situations (Valov, 2020). In order to transport power through long distances, DC technology is fundamental, since AC transmission lines are technically and economically disadvantageous (Pisani, Bruno, Saad, Rault, & Clerc, 2019). Technically, as stated in (Heuck, Dettmann, & Schulz, 2013), the voltage drop in steady state depends on the ohmic resistances; the capacitive and inductive reactances are not decisive. Undoubtedly, there is no reactive power and no eddy currents. This means that conductors with smaller cross-sections can be applied. As a consequence, economical advantages are obvious

compared to AC technology. Figure 2-9 shows a single-line diagram of a HVDC power link. The AC power is transformed to DC through a rectifier and then turned again into AC by applying an inverter.

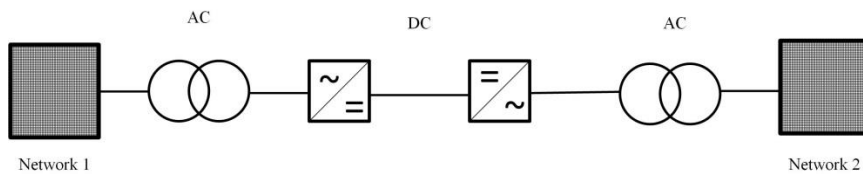


Figure 2-9. HVDC power link (Heuck, Dettmann, & Schulz, 2013).

The public transmission system is a three-phase system. There are grids with meshed topology that are required for the transportation of electrical energy to the distribution system. This means that each node is supplied from at least two sides. If one line fails, the other can take over the full power transmission. This is the so-called n-1 criterion (Schwab, 2020). Conventional power plants, offshore wind power plants, and hydroelectric power plants are directly connected to the transmission systems. Moreover, transmission systems are control areas, which are spatially defined grids under the responsibility of the transmission system operators (Bundesnetzagentur, Control area, 2021). These control areas are interconnected with tie-lines. In the case of Germany, there are four control areas located in the EHV level. These are the 380 kV and 220 kV grids. The latter are older grids and the 380 kV voltage level has gained acceptance through the years (Heuck, Dettmann, & Schulz, 2013). The German transmission system operators are 50Herzt, Amprion, Tennet, and TransnetBW; they have the following tasks:

- Provision of ancillary services such as power/frequency control (for keeping the balance between generation and demand), voltage control and loss compensation. These ancillary services should be also provided by RES connected in the transmission systems.
- Transport of electrical energy over long distances not only with conventional AC systems but also with HVDC power links.



Figure 2-10. German 380 kV and 220 kV EHV level including HVDC networks (Schäfer K. , 2022).

The presence of RES has caused modifications in the transmission systems. Before their integration, the load flow was unidirectional. The compensation of voltage drops at the MV level are/were carried out by applying transformers with voltage control (Valov, 2020). Furthermore, the cross-sections of overhead lines are increased and the Flexible AC Transmission Systems (FACTS) are being deployed so that the transmission capacity can be improved. Additionally, tie-lines, which are the physical connection between control areas (see section 2.2.4) were not designed for transporting electricity surplus from RES. This issue produces congestions in the network, such as node voltages out of the allowed limits. Congestion management methods, such as power curtailment or redispatch (see section 2.2.1), are applied to eliminate these problems.

The integration of RES and the decommissioning of conventional power plants have brought new questions regarding the reactive power provision in EHV levels (transmission systems). The active power produced by RES in all voltage levels is transported through long distances, which, in turn, can originate in an inductive behaviour of the transmission lines. This inductive behaviour is produced when the transported active power is greater than the natural load or surge impedance load (SIL) of the transmission line (Kundur, 1993). Usually transmission lines have a capacitive behaviour, since the natural load is high compared to the transported active power

(Biechl, 1992), (Nayak, Sehgal, & Sen, 2006). When the inductive behaviour of the transmission lines is imminent at EHV levels, the lack of capacitive reactive power could occur. Thus, this must be provided nowadays by the RES (e.g., hydropower plants as well as by wind power plants connected at EHV levels), as conventional power plants are being decommissioned. On the other hand, on HV and MV levels, RESs have an inductive behaviour for voltage support (reduction of the voltage at PCC) due to the active power supply into the network (active power supply increases the voltage at PCC). From the EHV voltage level, this will cause a voltage drop at this voltage level (Valov, 2020), which, in turn, increases the risk of voltage collapse. Voltage collapse occurs when the system voltage decreases slowly as the active power demand rises, until a critical point is reached (Crow & Lesieutre, 1994), (Dobson, Glavitsch, Liu, Tamura, & Vu, 1992), (Liang, Chai, & Ravishankar, 2022). Figure 2-11 shows the equivalent circuit of a transmission system (source, impedance due to the transmission line and load) with its respective power-voltage curve in per units (also called P-V curve). This curve is used for stability analysis, and it is created with a set of load flow results by varying the active and reactive power of the load. There is a point where the load flow cannot converge anymore; this is the so-called $V_{critical}$. Furthermore, at this point, the derivative of the P-V curve is infinite. Only above this point, a stable operation of the transmission system is possible and if the load is inductive, then the system can reach the critical point faster than in the capacitive case (Schwab, 2020). To counteract these issues, reactive power compensation devices are being installed in transmission systems. For example, the transmission system operator TransnetBW (located in the south of Germany) applies the following technologies (TransnetBW, 2023):

- Shunt reactors for voltage reduction
- Mechanically Switched Capacitor with Damping Network or MSCDN for voltage increase
- Static Synchronous Compensator or STATCOM for voltage increase and reduction

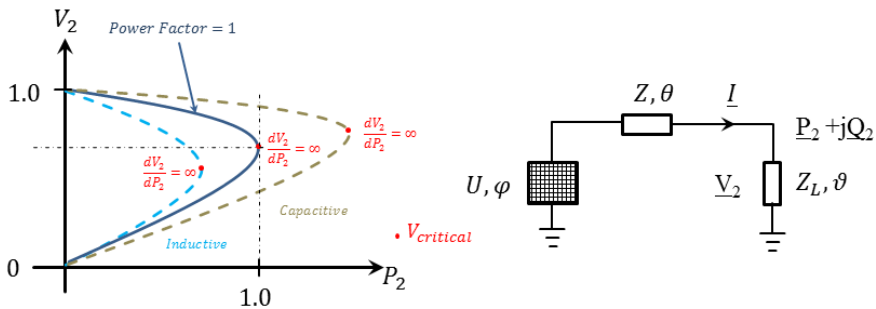


Figure 2-11. Power-voltage curve and equivalent circuit of a transmission system.

Another important characteristic of modern power systems with high presence of RES and less conventional power plants (less synchronous machines) is the reduction of inertia, which resists to changes in the speed of electrical machines. This inertia is provided by the stored kinetic energy in these machines (Mehigan, et al., 2020). In power systems with a high number of RES (inverter-based) and low synchronous machines, the frequency dynamics is faster, which can lead to large transient frequency

and oscillations; on the other hand, the presence of mainly synchronous machines makes the dynamics of the system slower (Ulbig, Borsche, & Andersson, 2015). Furthermore, the complexity grows due to the volatile and random behaviour of RES based on the solar and wind energy, which makes the inertia a function of the time. However, in the literature, possible solutions to this issue are mentioned. For example, in (Li, et al., 2022), wind turbines can contribute to the inertia due to the very high kinetic energy stored in their rotating masses. In addition, it is also mentioned that DC-link capacitors installed in PV systems as well as in battery storage systems can contribute to the inertia; here a virtual inertia constant of a capacitor is defined.

2.1.3 Distribution

A distribution system is a grid part of a power system that delivers the electrical energy generated in the transmission system to the end consumers (reason for using the word distribution). Distribution systems are implemented in the voltage levels between 1 and 35 kV in Europe according to the standard EN 50160 (DIN) and have usually a radial topology. Additionally, in Germany, there are around 900 DSOs and the length of the network (LV, MV and HV) reaches about 1.8 MM km (Schäfer K. , 2022).

In Germany, the 110 kV grid in the HV level of this country is considered as part of the distribution system. This is due to the increasing load densities in big cities, which pushes structures to appear in the voltage level that can be also found in the MV level (Heuck, Dettmann, & Schulz, 2013). The length of this HS network in Germany is around 95,000 km (Bundesnetzagentur, Netzentwicklungsplan 2030 (2019)). Big cities, big industries as well as wind and PV parks are connected here.

In the case of the MV level in Germany, the usual voltage levels are 20 kV and 10 kV for the MV (sometimes also 30 kV), frequently with a ring structure (Schäfer K. , 2022). Industry and RES are also connected here. Moreover, the length of that network in Germany is around 520,000 km (Bundesministerium für Wirtschaft und Energie).

The LV level in Germany is mainly operated for households. Besides, the nominal voltage is 400 V, and most of the RES are connected in this voltage level. The length of that network in Germany is around 1,193,000 km (Bundesministerium für Wirtschaft und Energie).

Nowadays there are important changes due to the integration of RES as well as the connection of more and more electronic devices. Distribution systems were designed for a unidirectional load flow, but the integration of RES has caused new challenges in the planning of distribution grids in the middle and low voltage level. For example, the inductive reactive power is provided by the RES so that the voltages at the point of connection are within the permitted limits. However, this provision of inductive power has a disadvantage, which is the increase of the losses within the distribution system. On the other hand, most of the electronic devices are connected in the low voltage level. For the conversion from the AC to the DC current, these electronic devices usually have capacitors, which change the power factor of the distribution grid in the low voltage level from inductive to capacitive. This capacitive behaviour of the distribution grid in the low voltage level should be compensated by installing inductive compensators within the distribution grid, so that the exchange of reactive power with the upstream grid is avoided; thus, the increase of losses is within the power system.

For unidirectional load flows, the voltage support is performed by the installation of capacitor banks. The connection of RES in the distribution system has carried to a local voltage support by RES and not only to the reinforcement of the network by installing

cables and overhead lines with new cross-sections, but also to the adaptation of protection systems to bidirectional load flows. Additionally, the voltage limits are exceeded due to the power injection from RES. For this reason, different voltage control techniques are being applied in distribution systems to keep the voltage within the allowed limits (Xu & Taylor, 2008), (Turiman, et al., 2022), (Zeraati, Hamedani Golshan, & Guerrero, 2018):

- On-load Tap Changers (OLTCs)
- Reactive power supply by inverters
- Power curtailment or reduction of the power production
- Energy storage
- Network reconfiguration or closing/opening of switches
- Static synchronous compensator (STATCOM)
- Demand side management or reduction of the power consumption

Moreover, one important parameter that has been reduced due the integration of RES and the decommissioning of conventional power plants is the RMS subtransient fault current I_K'' . The reason is that RESs are based on inverters with $I_K'' \approx I_n$, where I_n is the nominal current (Grumm, et al., 2018), (Keller, Kroposki, Bravo, & Robles, 2011). On the other hand, conventional power plants with synchronous generators can deliver an RMS subtransient fault current that is eight times greater than the nominal current. The reduction of the RMS subtransient fault current leads to the reduction of the subtransient short circuit power S_K'' , as seen in equation (2-1), where U_n is the rated voltage, c is the voltage factor according to DIN EN 60909 (VDE, DIN EN 60909-0, 2016), and $Z_{K,Net}$ is the internal impedance of the network. The latter is important for the quantification of harmonics as well as flicker and computation of the voltage variation in network planning and integration of RES (Plenz, et al., 2021).

$$S_K'' = \sqrt{3} \cdot U_n \cdot I_K'' = \frac{c \cdot U_n^2}{Z_{K,Net}} \quad (2-1)$$

Network operators usually provide the short circuit power of the network (external grid), and thus the internal impedance where the installation of the RES is planned. According to (2-2), which is based on Figure 2-12, the reduction of the short circuit power (increase of the internal impedance of the network) causes an increase in the voltage variation $\Delta U_{1,2}$.

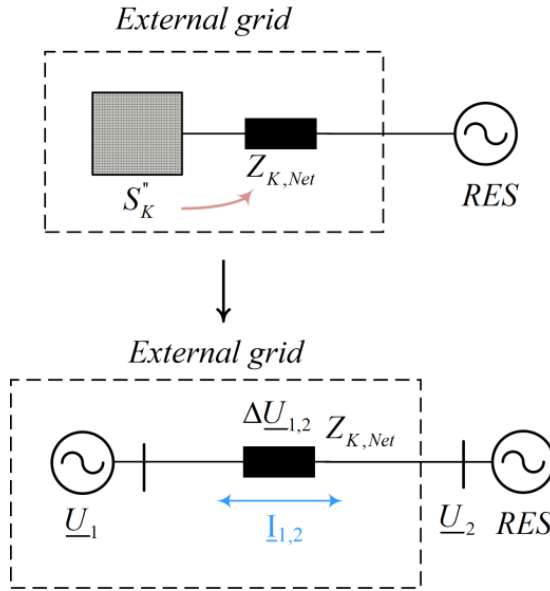


Figure 2-12. Connection of a RES unit to an external grid.

$$\Delta \underline{U}_{1,2} = \sqrt{3} \cdot I_{1,2} \cdot Z_{K,Net} \quad (2-2)$$

2.2 Ancillary Services

This section presents the state of the art regarding ancillary services and their classification. Due to the importance of the ancillary services for frequency stability (secondary and tertiary power/frequency control) well as for voltage stability (reactive power) in this scientific work, these are described in more detail.

Ancillary services can be defined as the resources required for reliable and secure transmission or distribution system operation (Kaushal & Van Hertem, 2019). A definition from ENTSO-E states that ancillary services are a range of functions provided by the TSO itself or acquired by the TSO from other users, so that they can guarantee the security of the power system (ENTSO-E, Market Committee, 2020).

In the literature, the classification of ancillary services is not homogeneous. For example, ancillary services are classified according to (Braun, 2008) and (Kaushal & Van Hertem, 2019) depending on whether an island operation or grid-connected mode is required. According to (Schäfer K. , 2022), ancillary services are classified to four categories, as seen in Figure 2-13; this categorization is reasonable and is presented in this scientific work. The descriptions of the following categories correspond mainly to (Schäfer K. , 2022); other sources were also reviewed:

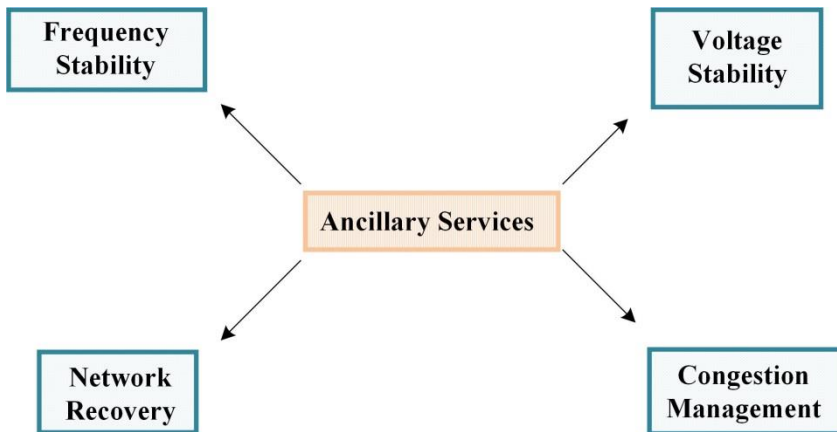


Figure 2-13. Ancillary services (Schäfer K. , 2022).

2.2.1 Congestion Management

The goal of the congestion management is to ensure that all the sources and resources are protected against overloading. Such tasks as redispatch/congestion management belong to that category. Operators of power plants submit schedules to the transmission system operators (schedule means how the power plant will operate during a specific period). Then, with this information, the transmission system operators perform load flow calculations, which help to get an overview of the state of the power system (voltages and overloading of branches within the allowed range). If the results of the load flow calculations are permissible, then the submitted schedules can be implemented by the operator of the power plant. If the results of the load flow computations are impermissible, the submitted schedules are intervened and corrected by the transmission system operator. In Germany, this modification of the schedule for prevention of network congestion is called redispatch, which is nowadays applied due to the high presence of RES.

2.2.2 Network Recovery

The main task here is to restore the supply as soon as possible after faults within the power system. Important topics here are black start capability and island mode. A blackout is an uncontrollable and unpredictable fault in a power system that leads to a breakdown of supply to consumers in large areas of the power system (Bundesnetzagentur, Stromnetz, 2023). Within the network recovery, there are important topics such as blackout capability and island mode. The black start capability is the faculty of a power plant to start functioning without energy coming from the external network. There are power plants that require starting energy from the network in order to begin the operation. For such power plants, this is impossible after a blackout.

2.2.3 Voltage Stability

Voltage stability means keeping the voltage constant within a defined range. To guarantee voltage stability, capacitive or inductive reactive power is required. In addition, it is important to identify sources of reactive power so that the voltage

stability can be ensured. Reactive power provision from other voltage levels, operation of STATCOM (Static Synchronous Compensators), application of tap changers or synchronous condensers (generators without active power production) are examples of approaches for reactive power provision for voltage stability.

The tasks of the voltage stability ancillary service are (Biechl, 1992):

- To compensate reactive power close to a required place by trying to avoid the transport over long distances
- To achieve balanced voltage profiles within the network
- To optimize the generation and consumption of reactive power so that active power losses are minimized.

The voltage stability ancillary service can be categorized in three types of control approaches (Rebours, Kirschen, Trotignon, & Rossignol, 2007):

Primary voltage control: This is an instantaneous local control similar to the primary power/frequency control. This control stabilizes the voltage at the terminals of, for example, generation units based on droop control (Braun, 2008) or load tap changers in the case of transformers. The response time of this control is in the order of few seconds due to local measurements and relative small time constants (Al-Majed, 2008), (Biechl, 1992).

Secondary voltage control: It controls the reactive power provision of multiple generation units, inductor or capacitor banks, synchronous condensers or load tap changers based on the measurements of one or multiple bus bars, also called pilot buses (Al-Majed, 2008), (Taranto, Martins, Falcao, Martins, & dos Santos, 2000) (Biechl, 1992). For this reason, this control is centralized. Furthermore, the coordination is performed by the network operator, which manages the provision of reactive power by accessing local generation units or load tap changers for some transformers within a regional voltage region and by calling them up to participate in the voltage control (Rebours, Kirschen, Trotignon, & Rossignol, 2007). Additionally, the response time of this type of control is in the range of 30 and 100 seconds (Al-Majed, 2008).

Tertiary voltage control: It performs the provision of the reactive power set points for the secondary voltage control to optimize the voltage profiles of the power system and to minimize the active power losses. These set points are generated based on optimal power flows. The response time of the tertiary voltage control ranges from 15 minutes to several hours (Al-Majed, 2008), (Braun, 2008), (Rebours, Kirschen, Trotignon, & Rossignol, 2007).

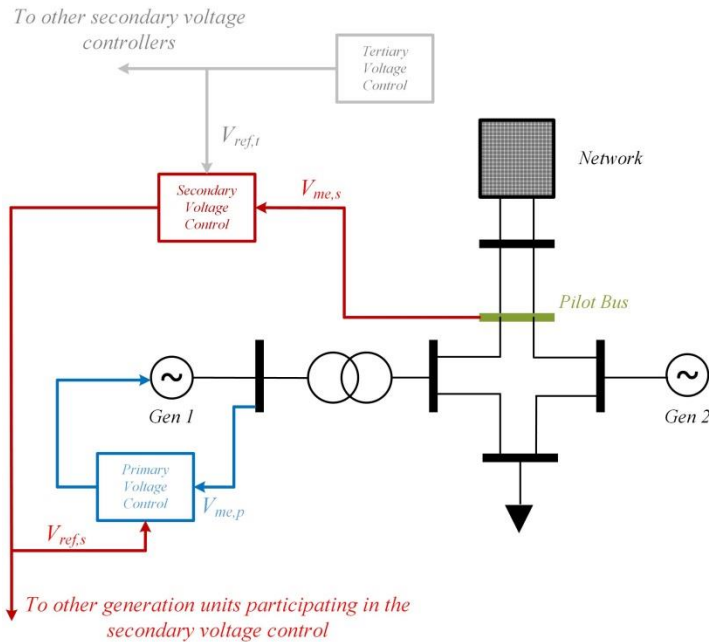


Figure 2-14. Overview of the primary, secondary and tertiary voltage controller in a specific region (Al-Majed, 2008), (Taranto, Martins, Falcao, Martins, & dos Santos, 2000).

Voltage controllers (primary, secondary, and tertiary) are outlined in Figure 2-14, where a very good example of a primary voltage control is an AVR (Automatic Voltage Regulator), which is applied for maintaining the output voltage of a synchronous generator at a defined value. Figure 2-14 also shows the pilot bus, which is essential for the measurements of the secondary voltage control. Regarding this pilot bus, it should be selected such that its voltage characteristic represents its region. This is achieved when the electrical distance between the pilot bus and the other bus bars within the region is small. At the same time, the electrical distance between the pilot bus and the adjacent regions should be large enough (Biechl, 1992). An example of pilot busses and regions is represented in Figure 2-15. Apart from that, the tertiary control generates the set points for the secondary control based on an optimization (optimal power flow (Lopera-Mazo & Espinosa, 2018)) process, and as mentioned before, its objective is to enhance the voltage profiles and to minimize the active power losses.

As shown above, the voltage controllers for voltage stability have a hierarchical structure.

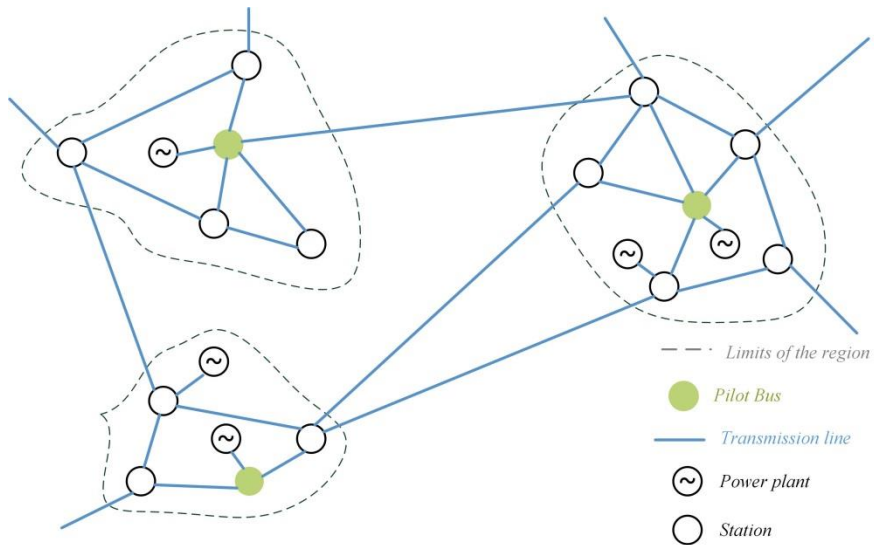


Figure 2-15. Example of an electrical network with pilot busses and three different regions (Biechl, 1992).

2.2.4 Frequency Stability

Before describing this ancillary service, it is necessary to present the definitions of synchronous areas, control blocks as well as control areas.

The European continent is a combination of synchronous areas. A synchronous area is defined as “areas covered by synchronously interconnected TSOs, such as the synchronous areas of Continental Europe, Great Britain, Ireland-Northern Ireland and Nordic and the power systems of Lithuania, Latvia and Estonia, together referred to as ‘Baltic’ which are part of a wider synchronous area” (Schittekatte, Reif, & Meeus, 2019). An example of a synchronous area in Europe is the UCTE (Union for the Co-ordination of Transmission of Electricity), which is in the continental part of Europe, depicted in Figure 2-16. The main task of the UCTE is to define technical and organizational rules for the unrestricted interoperability of the members regarding power exchange and support in case of faults. Currently there are 23 UCTE members; the geographical limits are also shown in Figure 2-16. The UCTE members together with other synchronous areas are part of the ENTSO-E (European Network of Transmission System Operators for Electricity) (Schwab, 2020), (Gerasimov, Gerasimov, & Nikolaev, 2014). The ENTSO-E members are also shown in Figure 2-16: UCTE, Nordel (Nordic Electric System Operators), UKTSOA (United Kingdom Transmission System Operators Association), ATSOI (Association of Transmission System Operators in Ireland), and BALTSO (Baltic Transmission System Operators). Furthermore, Figure 2-16 indicates correspondingly the type of connections between the different synchronous areas.

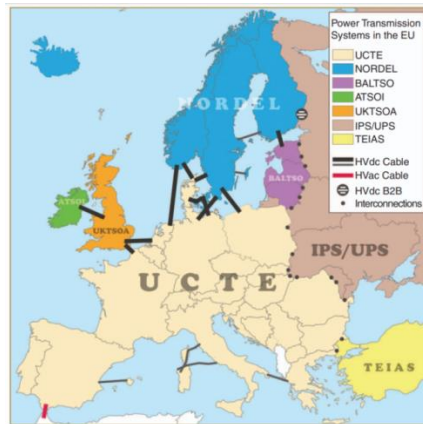


Figure 2-16. Synchronous areas in Europe (Bompard, Fulli, Ardelean, & Masera, 2014).

The synchronous area of the continental part of Europe (UCTE) is divided into control blocks (see Figure 2-17), where each of them is responsible for the frequency control (Ippolito, Musca, & Zizzo, 2021). At the same time, a control block can contain one or several control areas. A control area is defined as: “a coherent part of the interconnected system operated by a single system operator.” (Schittekatte, Reif, & Meeus, 2019). In other words, a control area is a TSO. In Germany, there are four control areas or TSOs. These are represented by 50Herzt, Amprion, Tennet, and TransnetBW. The control block is formed by the four TSOs plus Energinet, which is the TSO and control area in Denmark West. Another example is France. Here there is just one control area or TSO, which is operated by RTE (Réseau de Transport d’Electricité). In this example, the control block is also managed by RTE.

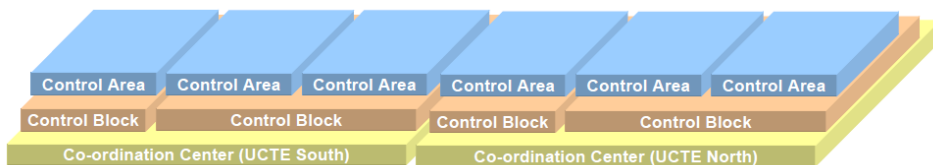


Figure 2-17. Structure of the UCTE (Fussi, 2011).

After analyzing the structure of a synchronous area, it is necessary to understand which types of power plants are part of a synchronous area. A description of the transmission and distribution systems in Germany is presented. These topics are covered in the last chapter.

For every moment in time, the load and generation must be balanced. The frequency stability ancillary service is required when an imbalance between the electrical load and the power generation occurs. Additionally, depending on the frequency deviation, different control loops may be necessary for maintaining the frequency stability of the power system (Beaty, 2013), which is shown in Figure 2-18. In Europe, there are four types of frequency control (Kaushal & Van Hertem, 2019):

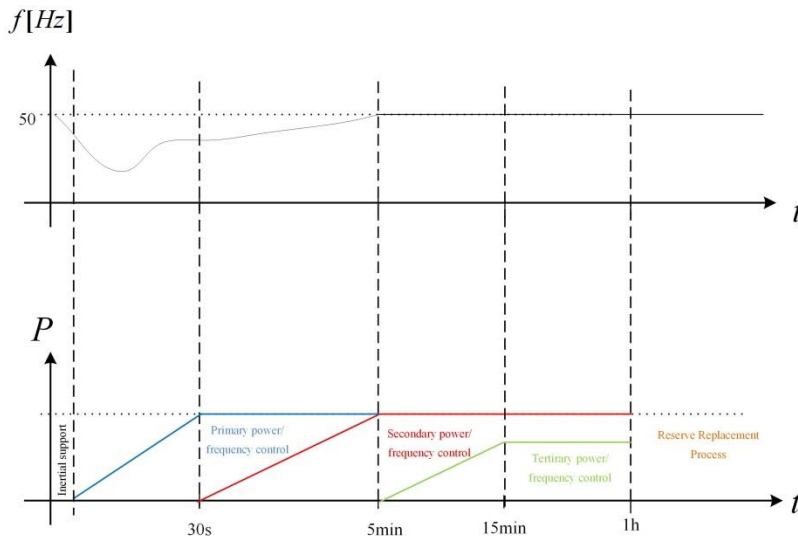


Figure 2-18. Overview of frequency control as a function of time.

Inertia support or instantaneous reserve: As described in (Schäfer K. F., 2020), when an active power imbalance occurs, a share of the electrical power takes place immediately, which means a distribution of power among the electrical machines depending on the impedances of the grid as well as on the generators. This process occurs in a short time. Afterwards, a mechanical load sharing among the synchronous machines follows in the network depending on the moment of inertia. That type of frequency control is the so-called inertia support or instantaneous reserve, which in other words is produced by the kinetic energy of the rotating parts of the generators when an imbalance between electrical load and power generation occurs. It occurs in the frequency range of ± 10 mHz (also called dead band) around the nominal frequency. It is necessary to point out that there is no other control within this dead band. In (dena, 2014), it is mentioned that RES, such as wind power systems or PV, do not contribute to the inertial support unless technical modifications are carried out.

Primary power/frequency control: It is also called FCR (Frequency Containment Reserve). This control, as presented in (Bevrani, 2014) and (Schäfer K. F., 2020), is activated when the frequency deviates by more than ± 10 mHz (dead band) in the power system. Furthermore, its full activation takes place automatically within 30 s after the frequency deviation and the period to be covered is $0 < t < 15$ min per fault event. Its aim is to stabilize the frequency in case of power fluctuations. Moreover, this type of control is local and occurs at the generation units. In other words, it is a decentralized control. Additionally, the primary power/frequency control is a droop-based control, and its response is within a few seconds. Also, this droop-based mechanism behaves as a proportional control, which means that the primary power/frequency control brings the frequency of the power system to a fix value (stabilization), but not to the nominal (50 Hz in Europe). Generators participating in this ancillary service follow the curve shown in Figure 2-19. The figure shows that for frequencies lower than 49.8 Hz, the generator supplies 100% of the maximum offered active power for the primary power/frequency control. At frequencies higher than 50.2 Hz, the generator consumes 100% of the maximum offered active power.

Within the dead band, neither supply nor consumption of active power by the generator occurs. For other cases, the control of active power is performed linearly and behaves according to the droop of a generator (with nominal active power P_n) according to

$$s = \frac{\Delta f / f_n}{\Delta P / P_n} \quad (2-3)$$

Moreover, there is an important parameter called the network power frequency characteristic, which is the quotient of the power deviation ΔP due to the disturbance in the power system and the quasi-steady-state frequency deviation Δf (ENTSO-E, 2009, Policy1, 2009), (Fussi, 2011). The network power frequency characteristic in a control block or control area i is given by

$$\lambda_i = -\frac{\Delta P_i}{\Delta f} \text{ in MW/Hz} \quad (2-4)$$

The greater this parameter, the lower is the frequency deviation after a disturbance. For example, if the network power frequency characteristic in continental Europe is around 18,000 MW/Hz and if a power plant of 1,000 MW is disconnected, then this disconnection will produce a frequency deviation of -0,056 Hz.

Each control block and control area contributes to the primary power/frequency control. The requested contribution c_i is given by

$$c_i = \frac{E_i}{E_u} \quad (2-5)$$

where E_i is the annual energy production (including energy production for export) within a control block or control area and E_u is the annual energy production of the synchronous area (e.g., UCTE) (Ippolito, Musca, & Zizzo, 2021), (Fussi, 2011). The addition of all contributions c_i within the synchronous area must be 1.

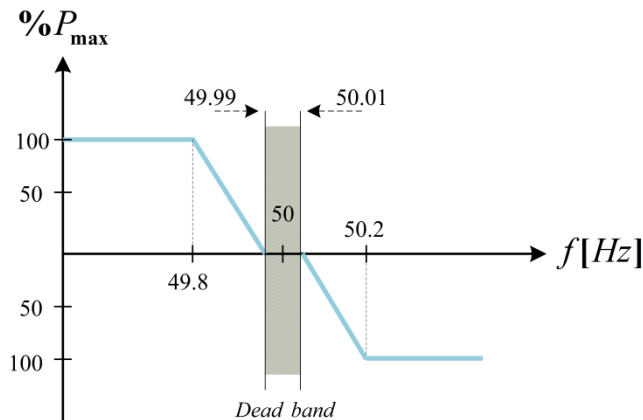


Figure 2-19. Curve P vs. f for primary power/frequency control.

Secondary power/frequency control: It is also called aFRR (automatic Frequency Restoration Reserve). After a disturbance occurs within a control area or control block, for example, lack of active power generation by a certain source, the instantaneous reserve and then the primary power/frequency control are activated in all control areas or control blocks (included the affected control area). Then, the secondary power/frequency control of the control area or control block, where the power unbalance occurred, is initiated to accomplish the following goals (Schäfer K. F., 2020):

- To restore the power balance within the unbalanced control area
- To bring the frequency to its nominal value
- To keep the power interchanges within the control areas to their programmed scheduled values

The block diagram of the secondary power/frequency control is illustrated in Figure 2-20.

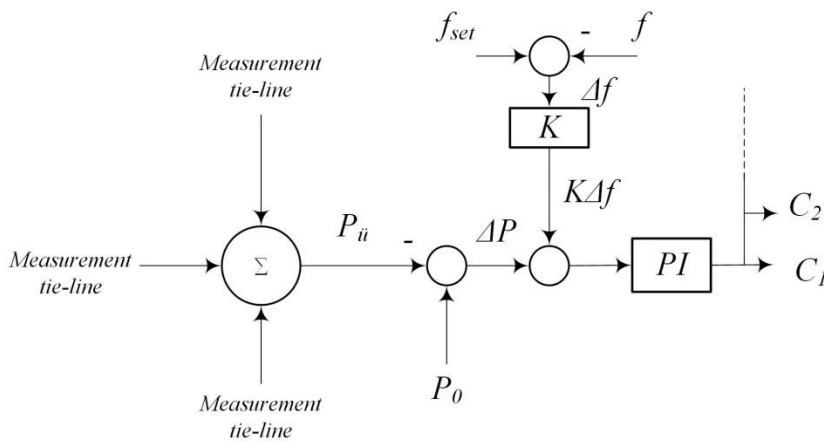


Figure 2-20. Block diagram of the secondary power/frequency control (Fussi, 2011).

At the tie-lines of each control block or control area, power measurements are performed. Then, the addition of all the measurements $P_{\ddot{u}}$ is compared with the programmed schedule values at these tie-lines P_0 :

$$\Delta P = P_{\ddot{u}} - P_0 \quad (2-6)$$

Next, the power variation ΔP is added to $K\Delta f$. K is a factor similar to the network power frequency characteristic. The result of this addition is the ACE (Area Control Error):

$$ACE = P_{\ddot{u}} - P_0 + K(f_{set} - f) = \Delta P + K\Delta f \quad (2-7)$$

In Figure 2-20, the block PI is the proportional integral controller whose output goes to the corresponding power plants part of the secondary power/frequency control. It is necessary to point out that each of these power plants has a corresponding participation factor C .

For a better understanding of this controller, the following example is presented (Fussi, 2011). Suppose that there are two control areas within a control block with the following parameters (assumption $K = \lambda$):

- Control area 1 $\rightarrow K_1 = \lambda_1 = 1,000 \text{ MW/Hz}$
- Control area 2 $\rightarrow K_2 = \lambda_2 = 600 \text{ MW/Hz}$

Suddenly, the control area 2 loses one power plant with a rated power of 800 MW. This means a frequency variation of -0.5 Hz:

$$\begin{aligned} \lambda_{total} = -\frac{\Delta P}{\Delta f}; \Delta f &= -\frac{\Delta P}{\lambda_{total}} = -\frac{800 \text{ MW}}{\frac{1,600 \text{ MW}}{\text{Hz}}} \\ &= -0.5 \text{ Hz} \end{aligned} \quad (2-8)$$

Subsequently, the primary power/frequency control set in each control area is

$$P_1 = -\lambda_1 \Delta f = -1,000 * (-0.5) = 500 \text{ MW} \quad (2-9)$$

$$P_2 = -\lambda_2 \Delta f = -600 * (-0.5) = 300 \text{ MW} \quad (2-10)$$

These results show that there is a load flow of 500 MW from control area 1 to control area 2. The ACE for each control area is given by

$$ACE_1 = 500 + 1,000 * (-0.5) = 0 \text{ MW} \quad (2-11)$$

$$ACE_2 = -500 + 600 * (-0.5) = -800 \text{ MW} \quad (2-12)$$

The ACE value is not zero in the control area, where the power plant is missing.

Additionally, the characteristics of the secondary power/frequency control are:

- According to (ENTSO-E. 2009, Policy1, 2009), this control can be centralized, pluralistic (decentralized) and hierarchical.
- It is fully implemented within a maximum of 5 minutes after its activation and should be completed after 15 minutes.
- In Germany, the parameters of the PI control can vary between 0 and 0.5 for the proportional part as well as between 60 s and 300 s for the integral time constant (Zeitler, 2022).
- Generators participating in the secondary power/frequency control must be connected to the controller with a secured communication link (Brauner, 2016).

Tertiary power/frequency control: It is also called minute reserve or mFRR (manual Frequency Restoration Reserve). This type of control is activated manually or automatically by performing re-scheduling/change in the dispatch of the participant generation units. It must be fully activated within the first 15 min (Fussi, 2011). For this type of control, conventional power plants as well as controllable loads can be used (Schäfer K., 2022). Moreover, it has the purpose to relieve or replace the secondary power/frequency control, since power plants providing secondary power/frequency control cannot operate for infinite time. The tertiary power/frequency control is applied for restoring the secondary power/frequency control, to manage eventual congestions, to bring the frequency to its nominal value as well as the tie-line powers to the specified values if the secondary power/frequency control is not enough (Bevrani, 2014).

The TSO's responsibility for the frequency control ends after one hour (Schäfer K., 2022).

Reserve Replacement Process: If the frequency deviation cannot be restored after 60 min by the primary, secondary and tertiary power/frequency controllers, then the balancing group manager (BGM) is responsible for bringing the balance in the transmission system (Schäfer K., 2022).

2.3 Voltage-Sourced Inverters

Commonly, the following RES can be distinguished (Tran-Quoc, et al., 2007):

- RES based on power electronics (e.g., PV systems, batteries)
- RES in combination with asynchronous machines/doubly-fed asynchronous machines/synchronous machines and power electronics, which is the case of wind turbines.
- RES coupled with synchronous generators (e.g., hydropower plants)

Most of the RES are based on DC/AC converters (hereunder: inverter), which make the conversion from DC to AC power possible. Importantly, these inverters could be based on the following technologies (Yazdani & Iravani, 2010):

- MOSFET (Metal-Oxide-Semiconductor Field-Effect Transistor)
- IGBT (Insulated-Gate Bipolar Transistor)
- Gate-Turn-Off Thyristor (GTO)
- Integrated Gate-Commutated Thyristor (IGCT)

Furthermore, inverters can be categorized as current-sourced inverters (CSI) and voltage-sourced inverters (VSI) with the following characteristics (Kharjule, 2015), (Yazdani & Iravani, 2010):

- CSI: The DC-side current is not changed, but the DC-side voltage. Thus, at the DC-side of the converter, a large inductor is applied.
- VSI: The DC-side voltage is not changed, but the DC-side current. Thus, at the DC-side of the converter, a large capacitor is used.

For active and reactive power provision of RES with VSI inverters, the dq -Frame is widely applied in the modelling of these inverters in order to guarantee not only a decoupled control of active/reactive power, but also its transfer to the external grid (Yazdani & Dash, 2009), (Beg, Rahmoun, Armstorfer, Rosin, & Biechl, 2016), (Rodríguez Amenedo, Alnartés Gómez, Alonso-Martínez, & González de Armas, 2021), (Bisht, Subramaniam, Bhattarai, & Kamalasadán, 2018), (Khan & Memon, 2023).

For frequency and voltage support, RES with VSI inverters use also measurements (voltage, frequency as well as active power) at its PCC in order to generate new set points of active and reactive power for the internal controllers of the VSI (see Figure 2-21). These characteristic curves can be classified as (VDE, VDE-AR-N 4105, 2011), (VDE, VDE-AR-N 4110, 2018), (VDE, VDE-AR-N 4120, 2018), (Juamperez, Yang, & Kjær, 2014):

- $P(f)$: Active power as a function of the grid frequency
- $Q(V)$: Reactive power as a function of the voltage at PCC
- $Q(P)$: Reactive power as a function of the active power at PCC
- $\cos\phi(P)$: Power factor as a function of the active power at PCC

These strategies are even being implemented in countries with high penetration of RES. One example here is Germany. In the HV, MV, and LV levels, these curves are part of the grid codes of the country.

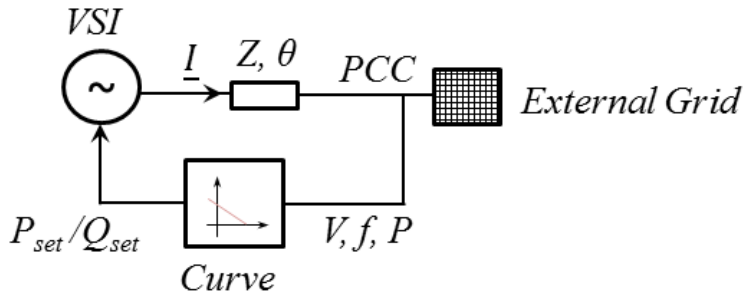


Figure 2-21. VSI with a characteristic curve.

2.4 Clustering Generation and Load

This section presents how nowadays load and generation are being clustered. The literature classifies this into nanogrids, microgrids, virtual power plants, and topological power plants.

2.4.1 Nanogrid

Up to now there is no a clear definition of a nanogrid, but according to (Dafalla, et al., 2020), a nanogrid can be defined as a small (typically less than 20 kW (Roasto, Jalakas, & Rosin, 2018)) electricity prosumer (consumption and generation) in the LV level, such as one-family house, which is capable, for example, in grid mode, of injecting or consuming active/reactive power to or from the grid. Power generation then is usually carried out by RES in nanogrids. Importantly, a nanogrid can be operated in grid as well as island mode. In addition to this, depending on the bus system, one can differentiate between AC, DC, and hybrid (combination of AC and DC) nanogrids (Roasto, Jalakas, & Rosin, 2018). Hereunder the focus is on AC bus systems. Nanogrids work generally in combination with distributed generators and distributed storages. Usually, an example of a distributed generator is a PV system. In addition to this, a nanogrid includes a control centre with a communication network (wired or wireless). This means that a nanogrid must include at least one load or a source of power and a gateway to the outside (Nordman, Christensen, & Meier, 2012) in order to be defined as a nanogrid. The basic components of a nanogrid in Figure 2-22 are:

- Local load
- Distributed generation
- Distributed storages
- Measurement devices
- Control centre
- Communication network

The application of a control centre as well as a communication network is only possible if all the components work with protocols that allow the communication between them. A very good example is Modbus TCP (Transmission Control Protocol), which runs on Ethernet. The aim of the control centre is, for example, to interface the nanogrid to other nanogrids or microgrids for power exchange. Furthermore, the control centre distributes power to the local load in an effective way and prioritizes the

distribution if the nanogrid includes more than one load (Nordman, Christensen, & Meier, 2012). The control centre can also manage the power within the nanogrid from an economical perspective.

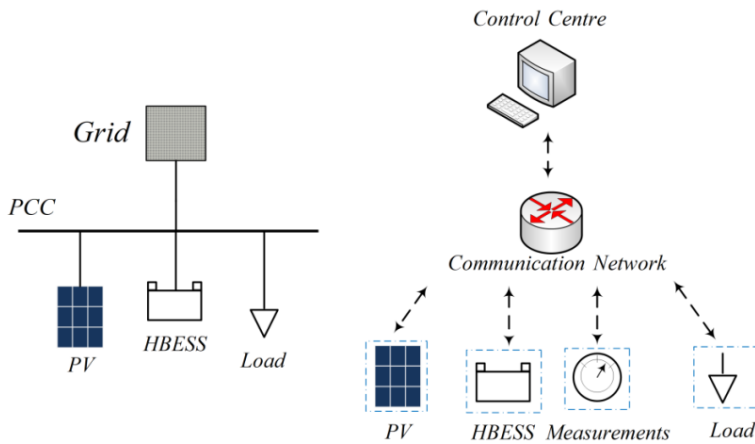


Figure 2-22. Nanogrid with communication network.

Definitely, the implementation of control algorithms in the control centre depends on how the nanogrid will be operated (Labella, Filipovic, Petronijevic, Bonfiglio, & Procopio, 2020).

- Grid-feeding: The nanogrid is required to supply a specific value of active and reactive power at its PCC.
- Grid-forming: The nanogrid defines its frequency and voltage. This operation is required in island mode.
- Grid-supporting: This is based on the droop control and can be applied in grid and island mode. In simple terms, the active and reactive power of the nanogrid is adjusted depending on the frequency and voltage at the PCC. A very good example is the primary power/frequency control. In this case, the nanogrid works in grid mode and supports the grid by consuming/injecting active power depending on the grid frequency.

The operation of the nanogrid requires also that the distributed generators as well as distributed storages have interfaces that allow the operation mentioned above. Figure 2-23 shows the different interfaces. It can be seen that the interface (in other words inverter) behaves as a voltage or current source, depending on the type of operation.

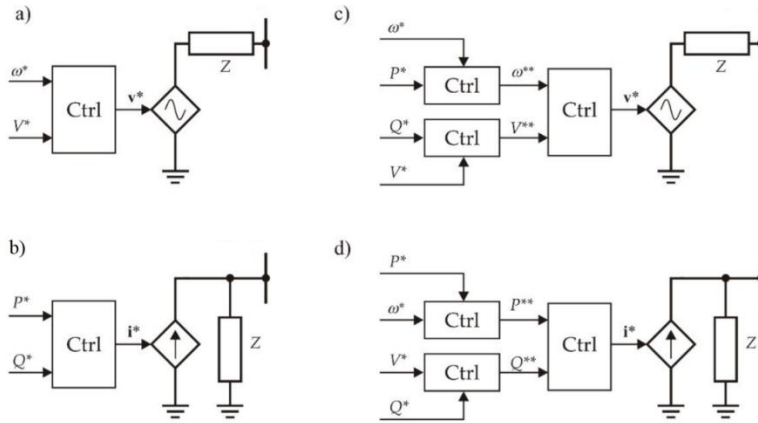


Figure 2-23. Different interfaces for distributed generators and storages: a) Grid-forming; b) Grid-feeding; c) Grid-supporting as voltage source; d) Grid-supporting as current source (Labella, Filipovic, Petronijevic, Bonfiglio, & Procopio, 2020).

2.4.2 Microgrid

As in the case of nanogrids, the definition of a microgrid is not clear. In (Mohammed, Refaat, Bayhan, & Abu-Rub, 2019), for example, a microgrid is considered as a distribution network that consists, like a nanogrid, of distributed generation, distributed storages, loads, and controllers. In (Schwab, 2020), microgrids are defined as minigrids that have at least one connection to the neighbouring distribution grid. In this definition, minigrids are electrical networks that have no connection with the main grid and are formed exclusively by diesel generators as well as by consumers. Nowadays these minigrids are experimenting changes in the power generation due to the integration of PV systems, wind power systems, and energy storages.

Microgrids can also work in grid-connected or island mode and have the capacity of transfer and thus selling/buying power to/from the external grid or other microgrids. Microgrids are more complex systems than nanogrids since they could include a combination of more distributed generators, the number of loads could be high and the distances between the distributed generators and loads could be in the range of kilometres. These factors make the control strategies for microgrids more sophisticated.

Importantly, microgrids work also with communication infrastructures, which present communication time delays. The literature presents many studies regarding the impact of these delays on the stability of the microgrid (Alfergani & Khalil, 2017), (Yao, Wang, Xu, & Naayagi, 2020), (Liu, Wang, & Xiaoping Liu, 2015), (Khalil, Elkawafi, Elgaiyar, & Wang, 2016).

2.4.3 Virtual and Topological Power Plant

A single RES can provide active/reactive power exchange with the external grid. Definitely, a single RES can also interact with other RESs as wells loads so that a specific task is accomplished by the whole group. In the literature, such a concept is called a virtual power plant (VPP). A VPP aggregates many types of RESs, such as hydropower plants, wind power systems, PV power plants, electrical energy storages, loads etc.

Indeed, the application of communication technologies is extremely important for the aggregation and interoperability of a variety of RESs within the VPP nowadays (Etherden, Vyatkin, & Bollen, 2015), (Hernandez, et al., 2013). Consequently, a VPP can be also defined as a system which clusters generation, storages, (controllable) loads as well as a communication infrastructure in order to make them turn out as a single power plant (Etherden, Vyatkin, & Bollen, 2015), (Zhang, et al., 2022), (Venegas-Zarama, Muñoz-Hernandez, Baringo, Diaz-Cachinero, & De Domingo-Mondejar, 2022). Furthermore, VPPs are usually implemented in the MV and LV levels.

Apart from this, VPPs can provide ancillary services (Ali, Massucco, & Silvestro, 2018). For example, (Hu, et al., 2022) proposed a framework for provision of the ancillary service inertia support (or instantaneous reserve) by coordinating the parameters of the inverters within the VPP. In (Zwaenepoel, Vandoorn, Van Eetvelde, & Vandeveld, 2014), VPPs participate in the ancillary services congestion management and frequency stability.

The high presence of RES in distribution networks includes new questions regarding the potential of providing ancillary services from distribution grids. For such investigations, iterative processes as well as optimization algorithms are applied (Sowa, Goergens, Schnettler, Koeberle, & Metzger, 2016), (Greve, Schwippe, Noll, & Rehtanz, 2014), (Barth, et al., 2013), (Kaempf, Abele, Stepanescu, & Braun, 2014). For providing an ancillary service, it is essential that the requirements of the distribution as well as the transmission system are recognized, such as reactive power (Weber, Zdrallek, Abele, Brenneisen, & Mogel, 2021). Furthermore, grid codes or guidelines of the country influence the potential of provision of ancillary services. This is studied in (Goergens, Potratz, Götde, & Schnettler, 2015), where the reactive power provision of a distribution grid with only PV systems and, in parallel, taking into account the German national grid code for low voltage level VDE-AR-N 4105 is small compared to the case without considering the mentioned guideline.

Furthermore, the integration of RES and the decommissioning of conventional power plants bring new challenges in the transmission systems. Besides, TSOs have not direct access to the RES connected in distribution systems. This leads to think that nowadays a proper coordination between the distribution and the transmission system is required. The literature presents approaches for a proper coordination between TSO and DSO (Rodio, Giannoccaro, Bruno, Bronzini, & La Scala, 2020), (Bachouris, Kaskouras, Papaioannou, & Sousounis, 2021), (Marten, et al., 2013). For instance, in the latter, it is mentioned that in Switzerland, some TSOs send reactive power schedules (for voltage control) to DSOs to be accomplished (for the next day) at the coupling point of the two systems. This action is remunerated by the TSO. On the other hand, as in the case of VPP, communication technologies and automation are important in the coordination between TSO and DSO due to the increased number of RES to be monitored and controlled in the distribution systems (Migliavacca, 2020).

On the other hand, the definition of a topological power plant or TPP comes from the research project (IREN2, 2018). Importantly, contrary to a VPP, a TPP is an electrical coupled network section of generation and load that, together, can provide ancillary services as conventional power plants do for the overlaid or the neighbouring grid (Vasconcellos, et al., 2018). The provision of ancillary services takes into account the restrictions of the local grid. In a VPP, sources and load units can be geographically installed in different network sections and, thus, with several PCCs. However, a TPP is a

specific case of a VPP, since a TPP is a defined network section and has one PCC (as seen from the overlaid or neighbouring grid).

The operational strategy (from the system-oriented point of view) of a TPP can be summarized as the transfer of active or reactive power at the PCC of the TPP (Vasconcelos, Thie, & Bertram, 2018).

The transfer of active power can be applied in:

- Redispatch, adjustment of active power or also called power curtailment. In this case, a TSO requires an adjustment of active power in the grid, so that congestion within the network can be avoided. Furthermore, redispatch is common in Germany due to the high presence of RES. A TPP can support the grid by varying the active power at the PCC and, thus, participate in the redispatch process.
- Offering of power/frequency control

The transfer of reactive power is focused on alternatives to provide locally the required reactive power when conventional power plants are decommissioned. A local unbalance of reactive power is caused by the shutdown of these power plants. Thus, a TSO/DSO needs to find alternatives to provide the lack of reactive power. If this is not performed locally, the reactive power needs to be transported over long distances. As a result, overvoltage, undervoltage as well as an increase of losses are imminent (Goergens, Potratz, Gödde, & Schnettler, 2015).

2.5 Conclusions

The power generation in Europe is being transformed to a more inverter-based-power-supply. This factor can influence the power system stability if new approaches for the provision of ancillary services are not considered.

In Germany, the high presence of RES and the decommissioning of conventional power plants has led to the implementation of new approaches in the transmission systems for the provision of ancillary services for voltage and frequency stability. Examples are the installation of STATCOM and the implementation of redispatch. While all the RESs installed in different voltage levels in Germany must participate in the power system stability by providing specific ancillary services, there is no information regarding how the clustering of households or nanogrids in LV networks can contribute to the provision of ancillary services and, thus, to the power system stability. For that reason, this research work extends knowledge by considering nano- and microgrids as well as their aggregation for a topological power plant with respect to control purposes. Figure 2-24 shows the TPP developed in this scientific work, which is in a LV network. This TPP is composed by a microgrid and some other loads and PV generation. The microgrid is a set of nanogrids which have distributed storages, distributed generators, a control centre, and loads. The TPP receives set points of active and reactive power from a DSO, which must be accomplished at the point of common coupling of the TPP (PCC_{TPP}). In order to make this possible, the TPP requires a superordinate controller so that the set points can be sent and optimally distributed to each nanogrid. For that reason, the superordinate controller must also take over optimization tasks, which consider network restrictions such as overloading of cables and transformers as well as voltage bands.

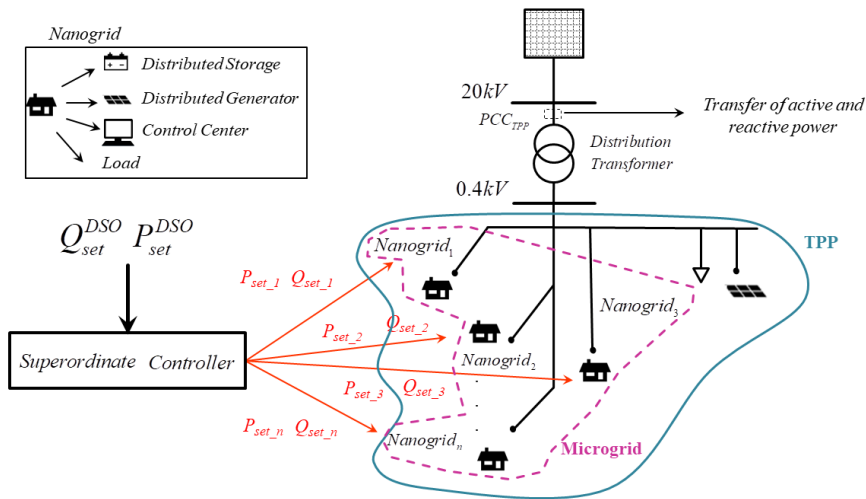


Figure 2-24. TPP in a LV network receiving set points of active and reactive power from a DSO.

Furthermore, in this scientific work, based on the state of the art analysis, the contribution of nano- and microgrids to topological power plants (TPP) regarding voltage and frequency control is explored from the dynamic and steady state point of view. The dynamic and steady state behaviour are analyzed at the nanogrid and TPP level, respectively.

From the dynamic point of view, detailed mathematical models of DG and DS part of a nanogrid are developed and presented in Chapter 3. Since the simplification of these detailed models parts of a nanogrid are not covered in the literature, Chapter 3 focuses on this topic. To investigate the behaviour of these simplified models in combination with a power distribution control, the simplified DG and DS are incorporated in a control centre for the provision of active and reactive power of a nanogrid in grid-connected mode. Moreover, the state of the art shows high presence of communication technologies in modern power systems. Importantly, the application of these technologies implies the presence of communication time delays. No information was found in the literature of how to analyze nanogrids in grid-connected mode with communication time delays in a systematic way. A method for such an analysis is shown in section 3.3.3.

From the steady state point of view, a method for minimizing active power losses when providing reactive power from a TPP mainly formed by nanogrids is developed in Chapter 4. As the literature does not cover relevant issues, the method will be presented in the mentioned chapter.

3 Development and Validation of Mathematical Models of the Nanogrid for Frequency and Voltage Control

This chapter refers to the dynamic behaviour of nanogrid in grid-connected mode, as related to the first and second hypotheses presented in section 1.2.

The first hypothesis states that for the control and stability analysis, the switching of the IGBT of the inverters in DS and DG can be neglected. To test this hypothesis, three steps are performed. Firstly, detailed models based on the components of a real demonstrator are developed. Then, a simplification of each detailed model is carried out. Next, each simplified model is validated by comparing simulation results with measurements at the demonstrator. Finally, to increase the complexity, the simplified models are combined with power distribution control (PDC) in a simulation environment and validated by comparing with measurements.

The second hypothesis states that the stability of a nanogrid can be influenced by time delays present in communication infrastructures. To test this hypothesis, an ordinary differential equation of the system to be analyzed and its small-signal representation are developed. The small-signal models are validated by comparing simulation results with measurements at the demonstrator. Afterwards, the pole-zero plot of the transfer function representing the system (including communication delays) is presented.

3.1 Demonstrator

The demonstrator was set up to show not only theoretical work but also to enable an exemplary demonstration. As seen in Figure 3-1, the demonstrator consists mainly of four containers, where the components are installed.



Figure 3-1. Overview of the demonstrator in Wildpoldsried (copyright: Fotodesign Suchy).

Figure 3-2 depicts a single-line diagram of the demonstrator. There is an on-load tap changer (OLTC) that connects the Wildpoldsried Community and the demonstrator (microgrid and nanogrid) with the MV level. The main protections are represented by the circuit breakers CB1 and CB2. As seen in Figure 3-2, the microgrid consists of a static synchronous compensator (STATCOM), two gensets or a combination of diesel engines and electric generators, two battery energy storage systems (BESS), a back-to-back

station voltage source converter (B2B-VSC), and a nanogrid. The components of the nanogrid are two home battery energy storage systems (HBESSs), a controllable load, a charging station, an air-to-air heat pump, and a PV system. All the components of the nanogrid are connected to the microgrid through a switch cabinet.

The microgrid also includes a switch board, which allows electrical connection between the components with the local grid. Additionally, this switch board enables extension of the distance between the microgrid components and thus, an increase in the cable impedance. This option is useful for analyzing the effect of cable lengths on the stability in islanded microgrids (Beg, Biechl, & Rosin, 2020).

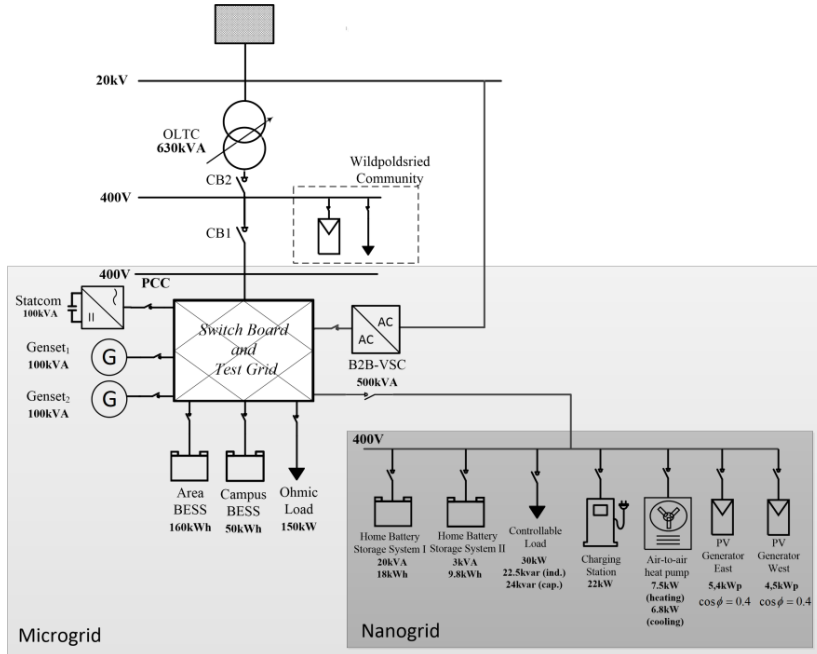


Figure 3-2. Single-line diagram of the demonstrator (IEES).

3.1.1 Nanogrid

This section describes the components of the nanogrid, including the design and setup of the control centre. The charging station is not considered.

3.1.1.1 Integration of Distributed Generators

The nanogrid includes two PV systems with east and west orientation, each of them with a PV inverter. The PV modules installed on the roof of the containers shown in Figure 3-1 have the following characteristics:

- Monocrystalline
- Electrical characteristics under standard conditions:
 - $P_{MPP} = 300 \text{ kWp}$
 - $V_{MPP} = 32.51 \text{ V}$
 - $I_{MPP} = 9.23 \text{ A}$

The east and west orientation have a peak power of 5.4 kWp (18 modules connected in series) and 4.5 kWp (15 modules connected in series), respectively. The inverters (see Figure 3-3) installed in the nanogrid have the following specifications:

- 6 kVA three-phase inverter
- 1 MPPT per inverter
- Maximum DC voltage 1000 V
- Power Factor = 0.4 (inductive and capacitive)
- Communication interface Solarbus (based on RS-485 and Modus ASCII)



Figure 3-3. PV inverters and the switch cabinet of the nanogrid.

The active and reactive power diagram shows the capability of the PV inverters, which is depicted in Figure 3-4 (generation convention). The PV inverters work only in two quadrants. The power factor of 0.4 (66.42°) inductive and capacitive is defined in the figure by PF_{max} . At an angle of 66.42° , the maximum reactive power is reached (Q_{max}). Moreover, if the actual active power is less than P_{BP} (active power break point), then the maximum reactive power that the inverter can provide in the blue zone is given by (3-1), where $P_{PV_{act}}$ is the actual active power.

$$Q_{PV_{max_blue}} = 2.29 \cdot P_{PV_{act}} \quad (3-1)$$

If the actual active power is in the green zone, then the maximum reactive power that the PV inverter can provide is calculated by (3-2).

$$Q_{PV_{max_green}} = \sqrt{S_{PV_{rated}}^2 - P_{PB}^2} \quad (3-2)$$

Furthermore, a reduction of the active power will be carried out, so that the rated apparent power of the PV inverter $S_{PV_{rated}}$ is not exceeded.

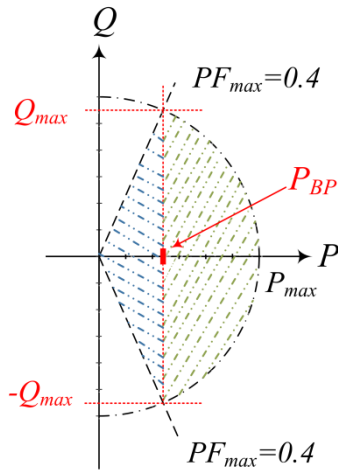


Figure 3-4. PQ diagram of one PV inverter.

3.1.1.2 Integration of Distributed Storage Systems

Two HBESSs were integrated in the nanogrid: HBESS I and HBESS II.

In the case of HBESS I, the following electrical characteristics are listed:

- 20 kVA three-phase inverter
- Maximal discharge power 18 kW
- Battery cells with Lithium-NMC (Nickel-Mangan-Cobalt-Oxide) technology
- Battery capacity of 18.6 kWh
- DC-Side has three modules, each module with 2p16s configuration (group of two cells in parallel, each group stacked 16 times and connected in series)
- Four quadrant operation: positive and negative active and reactive power set points possible
- Communication interface Modbus TCP/IP



Figure 3-5. HBESS I.

Electrical characteristics of HBESS II are:

- Three-phase system
- Battery capacity of 9.8 kWh
- Maximal active power by charging: 3.4 kW
- Maximal active power by discharging: 3.0 kW
- No reactive power control possible
- Communication interface Modbus TCP/IP



Figure 3-6. HBESS II.

3.1.1.3 Integration of Controllable Loads

These components consist of two controllable loads. The first load is a 3-phase symmetrical/unsymmetrical ohmic/inductive load. The maximum active power that this load bank can consume is 30 kW; in the case of the reactive power 22.5 kvar (steps of 500 W resp. 500 var). The second load is a 3-phase symmetrical/unsymmetrical capacitive load. The maximum reactive power feed-in is 24 kvar (steps of 500 var).

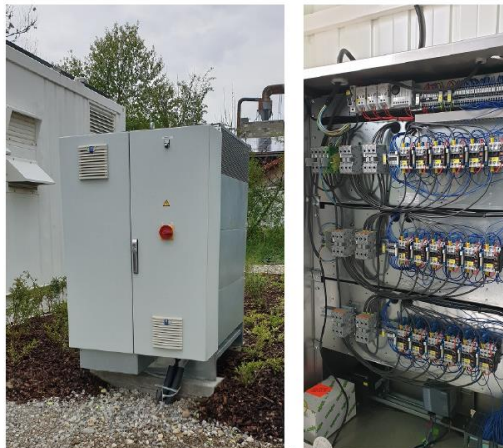


Figure 3-7. Controllable loads: Ohmic/inductive load (left) and capacitive load (right).

3.1.1.4 Air-to-Air Heat Pump

The air-to-air heat pump consists of an internal and external device with the following technical data:

- Three-phase system
- Air cooling/air heating
- SCOP: 4.54
- SEER: 7.0
- Heating capacity 7.5 kW
- Cooling capacity: 6.8 kW
- Communication interface Modbus RTU

The modelling of this device is not part of this scientific work.

3.1.1.5 Design and Setup of the Control Centre

The communication infrastructure is illustrated in Figure 3-8. The tests performed in this scientific work were carried out on a personal computer with the software LabVIEW. This is represented by the block “LabVIEW Nanogrid” in Figure 3-8. The block SP5 means Spectrum Power 5 from the company Siemens and allows data archiving, visualization, and SCADA (Supervisory Control and Data Acquisition). The block SP5 is not part of this scientific work. On the other hand, the controller S7-1200 is the interface between the SP5, the PC with LabVIEW and the components of the nanogrid. In addition, the S7-1200 was set up as part of the research project (pebbles, 2021) and makes the communication between different protocols and standards possible; in this case:

- Modbus TCP
- RS-485
- Profinet
- IO-Link

The control centre for this thesis is based on LabVIEW. The reason for applying this software is the visual programming language. The setup of the control centre was performed in LabVIEW’s Block Diagram window. The main feature of the setup was to read and write Modbus TCP registers in order to be able to establish communication between the PC with LabVIEW and the single components of the nanogrid. Undoubtedly, without this feature, the demonstration is not possible. Particularly, the following performances were implemented in the control centre by applying LabVIEW’s functions:

- Visualization of parameters:
 - Active and reactive power
 - SOC, SOH (in the case of batteries)
 - Error status
 - Frequency and voltages
- Setting up of protections
- Sending of set points for active and reactive power to the individual components of the nanogrid
- Data archiving
- Control of active and reactive power at the PCC of the nanogrid

Figure 3-9 and 3-10 show examples of LabVIEW’s Front Panel for sending set points to HBESS I as well as for the active power control at the PCC, respectively. Unquestionably, the LabVIEW programming (especially data archiving and control) allows performing several tests required for the validation of the single components of the nanogrid (section 3.2) as well as for the complete system including control centre (section 3.3).

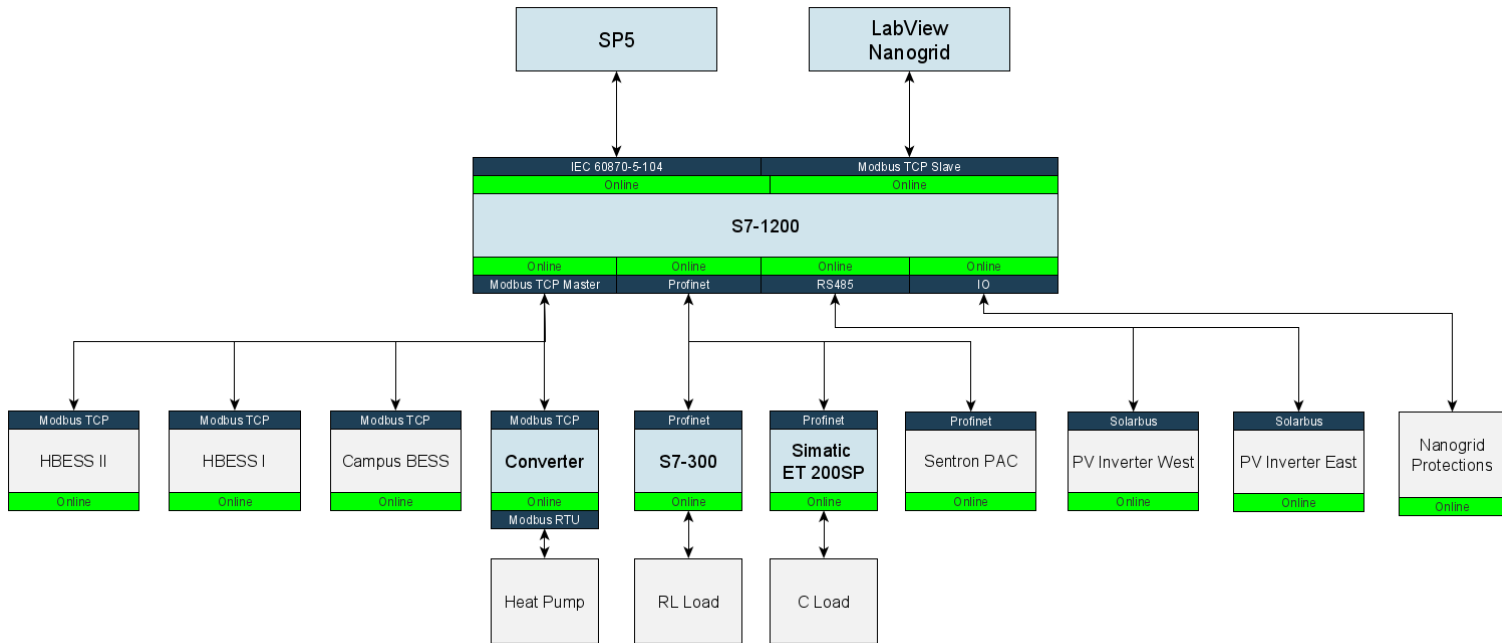


Figure 3-8. Block diagram of the control centre.

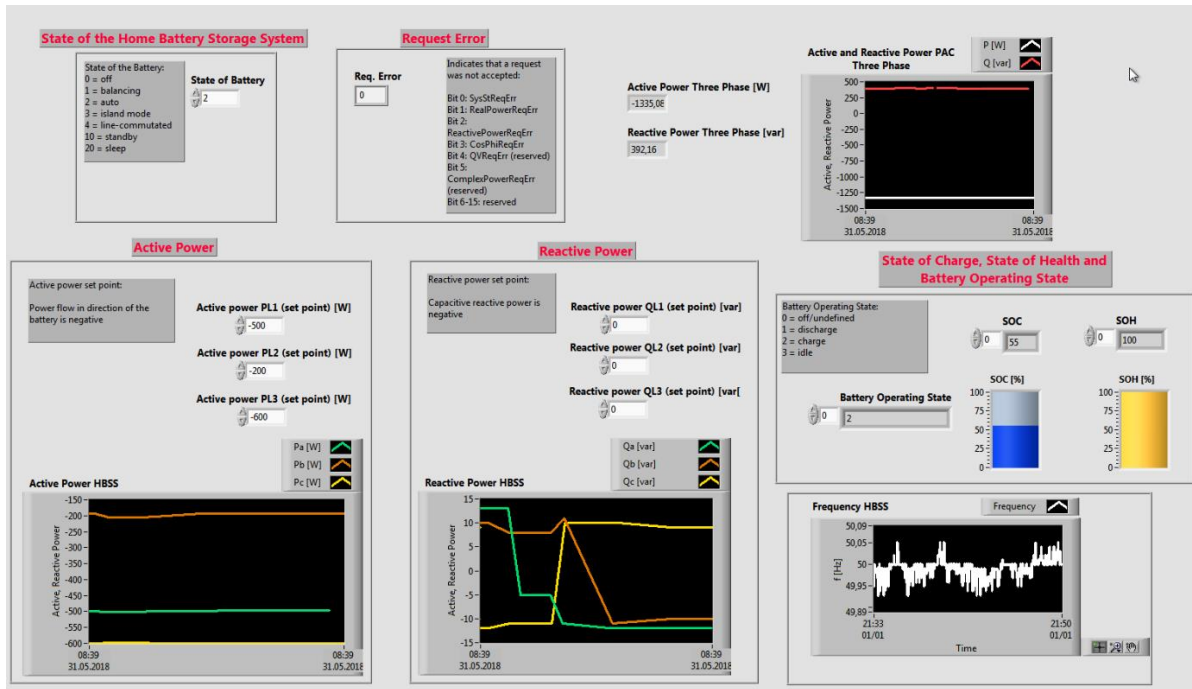


Figure 3-9. Example of visualization in LabVIEW's Front Panel. SOC, SOH, error status, power as well as frequency are visualized. In this case, unsymmetrical set points were sent to HBESS I.

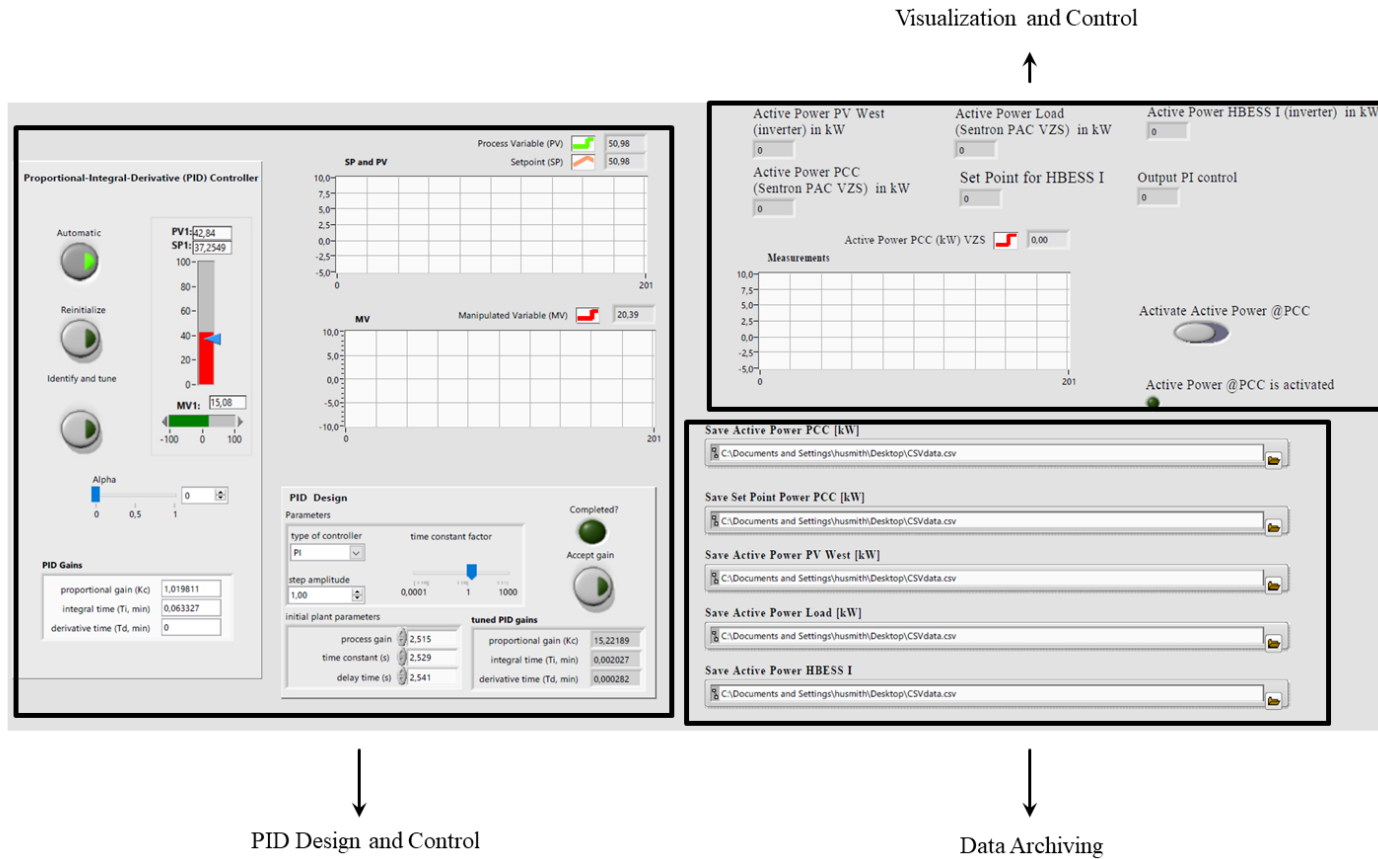


Figure 3-10. LabVIEW's Front Panel for active power control at the PCC considering HBESS I, the load controllable load as well as one PV inverter.

3.1.2 Microgrid

Previously, the nanogrid, which is part of the microgrid, was presented. In this section, the rest of the components of the microgrid are shown. These are not part of sections 3.2 and 3.3. For this reason, a brief explanation of each of them is given.

As seen in Figure 3-2, the main element of the microgrid is the block called “Switch Board and Test Grid”. This is a large switchgear (see Figure 3-11) that allows the connection between the LV grid and the microgrid components. Also, this part has the functionality of network extension through the laid cables seen in Figure 3-12. This permits replication of large distances by increasing the cable length between the microgrid units.



Figure 3-11. Switchgear.



Figure 3-12. Network extension.

Furthermore, the microgrid has two battery energy storage systems (Area BESS and Campus BESS) with different capacities: in this case, 160 and 50 kWh. The Campus BESS has a grid-feeding interface. On the other hand, the four operation modes shown in Figure 2-23 can be set up in the Area BESS. Also, the unit B2B-VSC has a rated apparent power of 500 kVA. This is an inverter-based coupling between MV and LV. This unit is useful for the emulation of battery storage systems with infinite capacity as well as for controllable PV systems. In addition to this, the B2B-VSC permits the generation of

disturbances in island mode (e.g., load steps or variable PV power due to lack of solar radiation). In addition, there are two gensets; one of them is operated with vegetable oil. These gensets have no power electronics and are synchronous machines connected with diesel engines. Next, the STATCOM or static var generator has the functionality of exchanging reactive power with the external grid, and, thus, allowing voltage control. This component has a rated apparent power of 100 kVA; the reactive power (inductive/capacitive) can be provided by sending voltage as well as reactive power set points to the STATCOM controller.

3.2 Subsystems

In this section, detailed and simplified models of each of the subsystems of the nanogrid are presented. The simplified models play an important role in this scientific work, whereby a detailed explanation of the development of these simplified models is required and shown in this section. Figure 3-13 illustrates the control structure of a VSI by applying the dq -Frame. This structure is applied for the subsystems of the nanogrid, which usually have a DC source, a DC/AC converter, and impedance (due to filters and transformers). The signals m_a , m_b and m_c (in short form m_{abc}) are required for modulation, e.g., Pulse Width Modulation (PWM). The dq -Frame is employed as part of the controller, since it provides DC quantities due to synchronization, via the PLL block, between the grid and the DC/AC converter. Thus, the implementation of PI controllers is suitable for this application (VSI Control block).

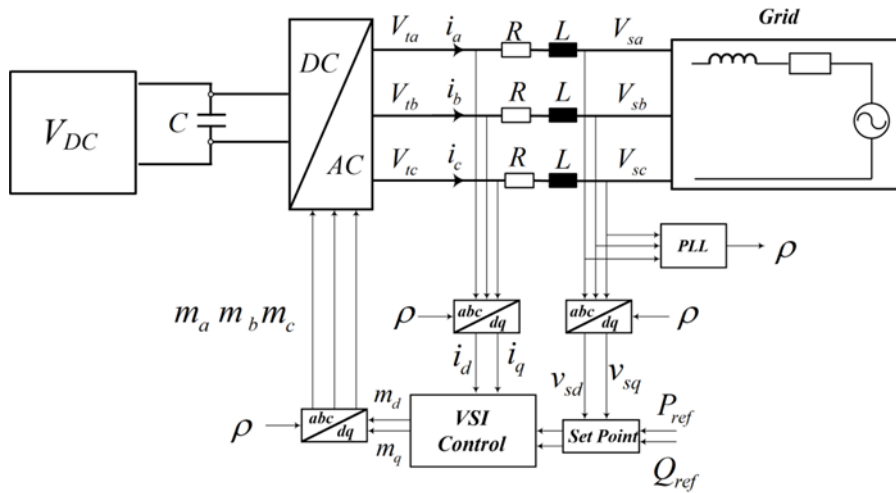


Figure 3-13. VSI and control structure in the dq -Frame (Yazdani & Iravani, 2010).

The $\alpha\beta$ -Frame as well as the dq -Frame representation of a space phasor are the basis of the control structure shown in Figure 3-13. The equations below are developed according to (Yazdani & Iravani, 2010), which means that the rest of this section is based on this reference. First, a three-phase system is defined as

$$\begin{aligned} f_a(t) &= \hat{f} \cos(\omega t + \theta_0) \\ f_b(t) &= \hat{f} \cos\left(\omega t + \theta_0 - \frac{2\pi}{3}\right) \end{aligned} \quad (3-3)$$

$$f_c(t) = \hat{f} \cos\left(\omega t + \theta_0 - \frac{4\pi}{3}\right)$$

where \hat{f} , θ_0 and ω are the amplitude, the initial phase angle and the angular frequency of the sinusoidal functions. A space phasor is defined as

$$\vec{f}(t) = \frac{2}{3} \left[e^{j0} f_a(t) + e^{j\frac{2\pi}{3}} f_b(t) + e^{j\frac{4\pi}{3}} f_c(t) \right] \quad (3-4)$$

If equation (3-3) is inserted in (3-4) and then decomposed into its real and imaginary components, one obtains

$$\vec{f}(t) = f_\alpha + jf_\beta \quad (3-5)$$

which is the $\alpha\beta$ -Frame representation of the three-phase system of equation (3-3). The dq -Frame representation is given by a phase shift by an angle ε of the $\alpha\beta$ -Frame representation.

$$f_d + jf_q = (f_\alpha + jf_\beta) e^{-j\varepsilon(t)} \quad (3-6)$$

DC quantities can be obtained from the dq -Frame representation if $\frac{d\theta(t)}{dt} = \frac{d\varepsilon(t)}{dt}$ can be guaranteed. Next, the dynamic model of the converter shown in Figure 3-13 in the dq -Frame is described. The AC voltages at the output of the impedance are

$$\begin{aligned} V_{sa}(t) &= \hat{V}_s \cos(\omega_0 t + \theta_0) \\ V_{sb}(t) &= \hat{V}_s \cos\left(\omega_0 t + \theta_0 - \frac{2\pi}{3}\right) \\ V_{sc}(t) &= \hat{V}_s \cos\left(\omega_0 t + \theta_0 - \frac{4\pi}{3}\right) \end{aligned} \quad (3-7)$$

The dynamics of the AC side of the converter can be represented as

$$\begin{aligned} L \frac{di_a}{dt} &= -Ri_a + V_{ta} - V_{sa} \\ L \frac{di_b}{dt} &= -Ri_b + V_{tb} - V_{sb} \\ L \frac{di_c}{dt} &= -Ri_c + V_{tc} - V_{sc} \end{aligned} \quad (3-8)$$

The space-phasor equivalents of equations (3-7) und (3-8) are given by

$$\vec{V}_s(t) = \hat{V}_s e^{j(\omega_0 t + \theta_0)} \quad (3-9)$$

$$L \frac{d\vec{i}}{dt} = -R\vec{i} + \vec{V}_t - \vec{V}_s \quad (3-10)$$

If equation (3-9) is inserted in (3-10), one obtains

$$L \frac{d\vec{i}}{dt} = -R\vec{i} + \vec{V}_t - \hat{V}_s e^{j(\omega_0 t + \theta_0)} \quad (3-11)$$

Next, the dq -Frame representation is defined as

$$\begin{aligned} \vec{f}(t) &= f_\alpha + jf_\beta = (f_d + jf_q) e^{j\rho(t)} = f_{dq} e^{j\rho(t)} \\ \vec{i}(t) &= i_{dq} e^{j\rho(t)} \\ \vec{V}_{tdq} &= V_{tdq} e^{j\rho(t)} \end{aligned} \quad (3-12)$$

where ρ is the phase shift required for the dq -Frame representation, as shown previously. Equation (3-12) can be used to rewrite equation (3-11) as follows:

$$L \frac{d}{dt} (i_{dq} e^{j\rho(t)}) = -R i_{dq} e^{j\rho(t)} + V_{tdq} e^{j\rho(t)} - \hat{V}_s e^{j(\omega_0 t + \theta_0)} \quad (3-13)$$

Equation (3-13) can be rearranged as

$$L \frac{d}{dt} (i_{dq}) = -jL \frac{d\rho}{dt} i_{dq} - R i_{dq} + V_{tdq} - \hat{V}_s e^{j(\omega_0 t + \theta_0 - \rho)} \quad (3-14)$$

The PLL block of Figure 3-13 plays an important role in the synchronization of the grid and the converter since it controls ρ at $\omega_0 t + \theta_0$. Under steady state, the PLL and the derivatives of equation (3-14) can be expressed as follows:

$$\rho = \omega_0 t + \theta_0 \quad (3-15)$$

$$\frac{d\rho}{dt} = \omega_0 \quad (3-16)$$

$$\frac{di_{dq}}{dt} = 0 \quad (3-17)$$

Then, equation (3-14) can be written as

$$V_{tdq} - \hat{V}_s = [j\omega_0 L + R] i_{dq} \quad (3-18)$$

which represents an equivalent single-phase circuit with its phasor representation. Figure 3-14 depicts the simplified model in the abc-Frame according to Figure 3-13 and equation (3-18). Additionally, this equation is the basis of the simplified models applied in this scientific work and can be used for control design if a quasi-steady-state condition is assumed. Moreover, it is important to highlight that in the simplified model $m_{abc} = V_{tabc}$.

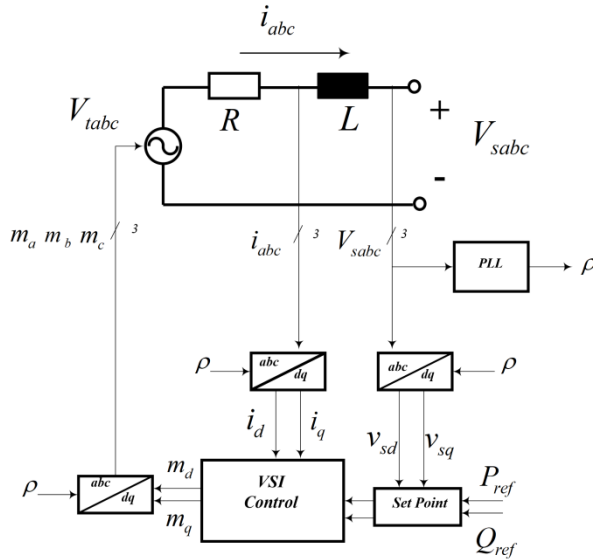


Figure 3-14. Simplified model.

3.2.1 Home Battery Energy Storage System I

3.2.1.1 Detailed Model

A detailed model for HBESS I and its topology is shown in Figure 3-15. This topology can be divided into three subsystems: the battery model, the bidirectional DC/DC converter, and the AC inverter with its corresponding filter. The battery model block of Figure 3-15 has the following characteristics:

- Nominal voltage of each cell: 3.7 V
- 32 cells pro module (2 p16s)
- Lithium-NMC (Nickel-Mangan-Cobalt-Oxide)
- Three Modules in series
- Nominal voltage pro module: 59.2 V

The bidirectional DC/DC converter consists of voltage and current control. The first controller regulates the voltage at the DC link ($V_{DClink}^{HBESS_I}$) and gives the reference value to the current control, which regulates the current at the output of the battery model ($i_{bat}^{HBESS_I}$). The output of this controller provides the duty cycle for the switches S_1 (boost converter) and S_2 (buck converter) (Arancibia, Strunz, & Mancilla-David, 2013), (Bae & Kang, 2013), (Camara, Gualous, Gustin, & Berthon, 2008), (De Castro, et al., 2011). In order to be able to generate enough voltage for the LV three-phase network, the DC-link voltage control is required (Mertens, 2015).

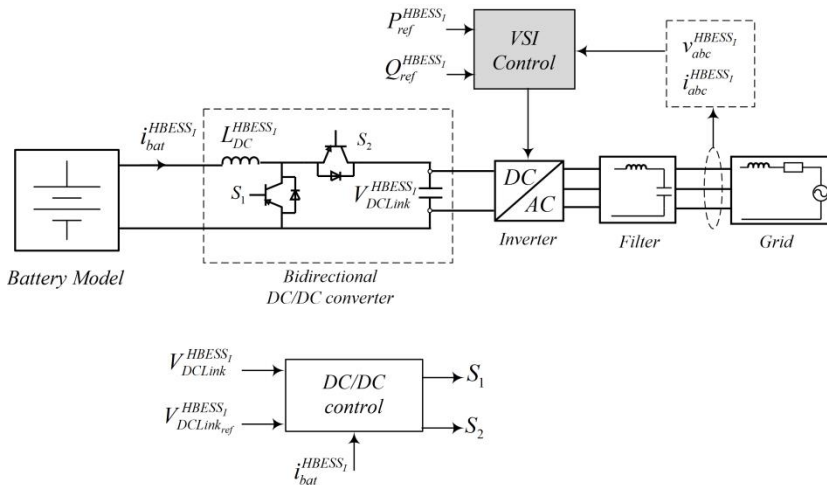


Figure 3-15. Topology of HBESS I.

In the case of the AC inverter, it is based on a VSI control in order to regulate the active and reactive power at the PCC of HBESS I. The VSI control consists of an inner (current control) and outer loop (power control). Figure 3-16 shows the block diagram of it. The delay due to the switching frequency of the inverter (converter block in Figure 3-16) as well as the parameters of the inverter filter are part of the inner loop. On the other hand, the outer loop receives set points of active or reactive power and then provides the current set point for the inner loop. The control strategy presented in this work is described in (Yazdani & Iravani, 2010). Additionally, the pole placement method is applied for tuning the controllers as the first step.

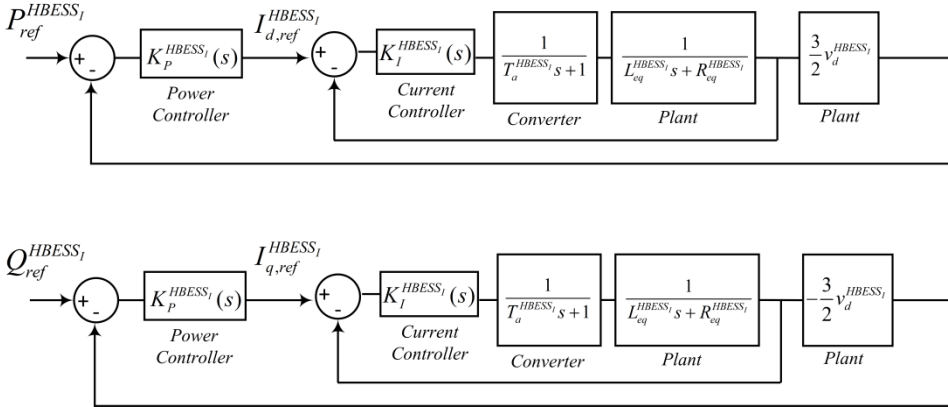


Figure 3-16. Block diagram of the power and current control of HBESS I.

In Figure 3-17a, the active power set point is varied from 0 kW to -17 kW (charging of HBESS I), while the reactive power is set to 0 kvar. It can be seen that the voltage at the output of the battery model depicted in Figure 3-15 increases (Figure 3-17b), while the current $i_{bat}^{HBESS I}$ decreases due to the charging process, as seen in Figure 3-17c. This confirms the correct functionality of the controllers of the DC/DC converter as well as of the AC inverter.

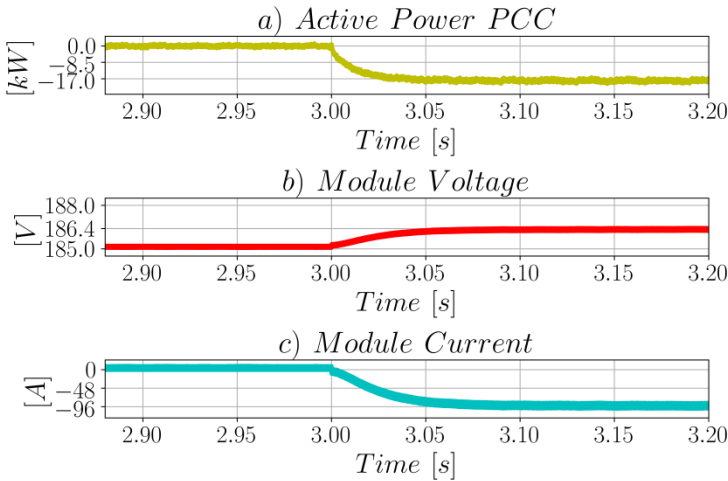


Figure 3-17. Charging of HBESS I with a set point of -17kW: a) Active power at the PCC of HBESS I; b) Voltage at the terminals of the battery model; c) Battery current.

3.2.1.2 Simplified Model

The simplification of the detailed model is carried out once its functionality is verified. This reduction of the complexity consists of an equivalent resistance and inductance (due to inverter filter) and a controlled voltage source (Armstorfer, Beg, Rahmoun, Rosin, & Biechl, 2017), see also section 3.2. The simplified model of HBESS I and its control are depicted in Figure 3-18.

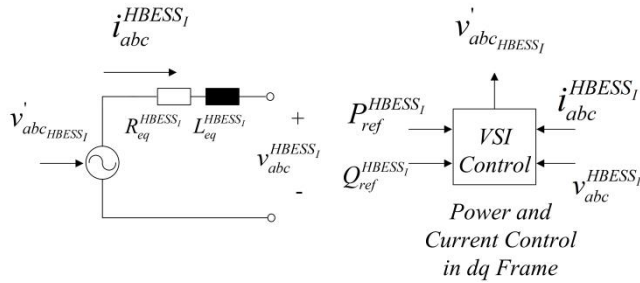


Figure 3-18. Simplified model of HBESS I.

3.2.1.3 Validation

The simplified model of HBESS I is compared, firstly, with the detailed model and then with transient measurements. For the two cases, the validation is performed by measuring the active and reactive power at the PCC of HBESS I.

The comparison of the detailed and simplified model is depicted in Figure 3-19 when an active and reactive power set points of +18 kW and +20 kvar are applied, respectively. Results show a very good correlation between the two models.

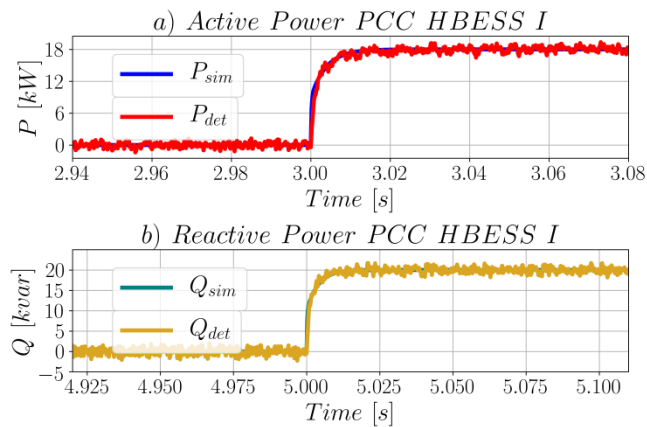


Figure 3-19. Comparison between the detailed and the simplified model: a) Active power set point equals 18 kW and reactive power 0 kvar; b) Reactive power set point equals 20 kvar and active power 0 kW.

The simplified model is then validated. This step is performed by comparing simulation results with transient measurements. Figure 3-20 shows an example of the validation of the simplified models for two different set points for the active and reactive power at the PCC of HBESS I.

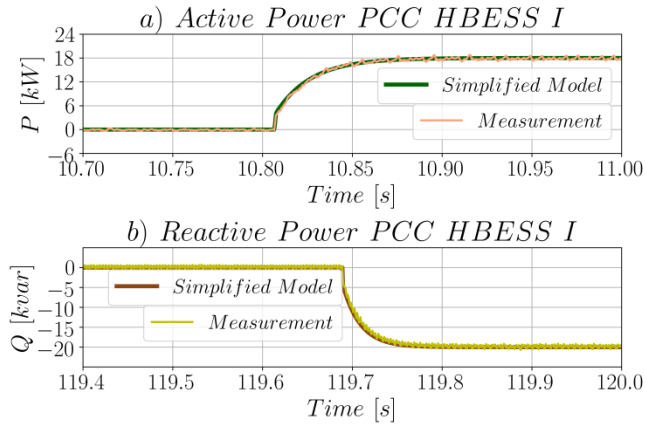


Figure 3-20. Comparison between the simplified model and transient measurements: a) Active power set point equals 18 kW and reactive power 0 kvar; b) Reactive power set point equals -20 kvar and active power 0 kW.

3.2.2 Home Battery Energy Storage System II

3.2.2.1 Detailed Model

The detailed model of this subsystem of the nanogrid is depicted in Figure 3-21. It consists of two DC/DC converters and an AC inverter.

In the DC side, two battery modules with a capacity of 3 kWh and 6 kWh are part of HBESS II. The number of cells connected in series and in parallel of the battery modules were adjusted according to the data sheet of HBESS II:

- 3 kWh module: 14s1p
- 6 kWh module: 14s2p

The battery modules are connected to the two bidirectional DC/DC converters whose controllers require active power set points $P_{batset1}$ and $P_{batset2}$ for generating the pulses for the switches S_1 , S_2 , S_3 , and S_4 .

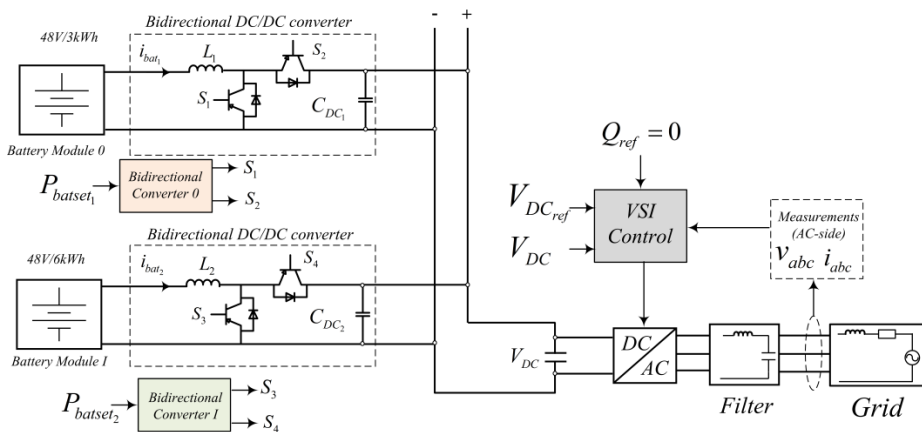


Figure 3-21. Topology of HBESS II.

The AC side is based on an VSI control. Figure 3-22 shows the control structure of the AC inverter of HBESS II according to (Yazdani & Iravani, 2010). This consists of two outer loops. The first outer loop regulates the DC link voltage, which, in turn, gives the set point for the inner current loop related to the direct component of the three-phase current at the PCC of HBESS II. Additionally, the first outer loop considers the dynamics of the DC link capacitor. On the other hand, the second outer loop allows an independent control of the reactive power. The pole placement method is applied for the tuning of the controllers of the AC inverter.

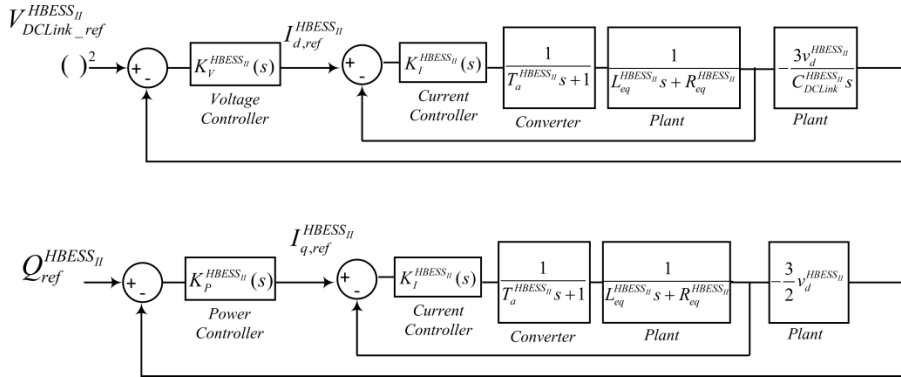


Figure 3-22. Block diagram of the voltage, reactive power and current controllers.

Figure 3-23 shows an example of a discharging process of HBESS II. An active power step of 2 kW is required at the AC side of HBESS II (Figure 3-23a). The voltages at the output of the battery modules (Figure 3-23b) are slightly reduced, while the currents (Figure 3-23c) are increased due the discharging process. In this example, the reactive power set point is set to zero.

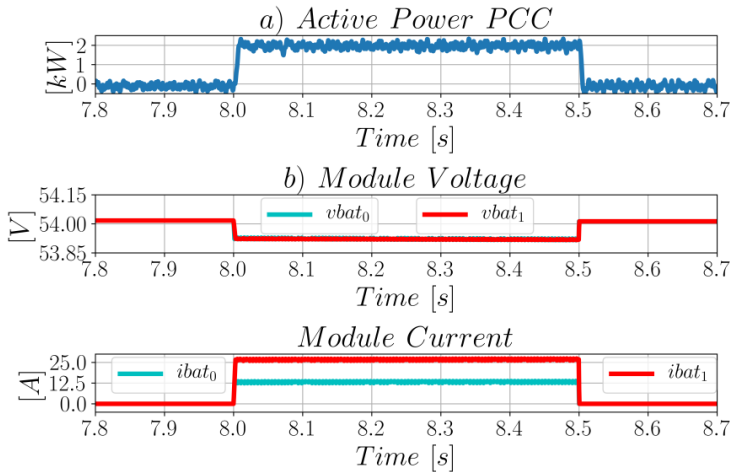


Figure 3-23. Discharging process by applying a set point of 2 kW: a) Active power at the PCC of HBESS II; b) Voltages at the output of the two battery modules; c) Currents at the output of the two battery modules.

3.2.2.2 Simplified Model

The topology shown in Figure 3-21 is simplified according to Figure 3-24. The simplified model of HBESS II regulates the active and reactive power at its PCC. This means that the DC voltage control of Figure 3-22 is replaced by an active power control and the reactive power control remains as presented. Furthermore, an equivalent resistance and inductance due to the AC filter are part of the model.

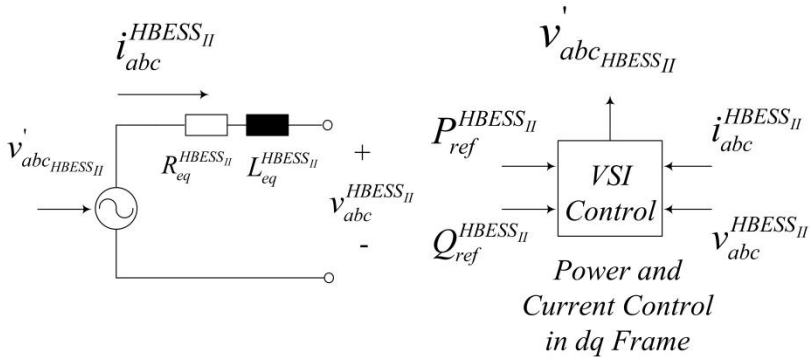


Figure 3-24. Simplified model of HBESS II.

3.2.2.3 Validation Model

Firstly, the simplified model is validated by comparing it with the corresponding detailed model (Figure 3-25). Secondly, the verified simplified model is compared with transient measurements and adjusted by setting a ramp to the simplified model (Figure 3-26). For both scenarios, the active power is only analyzed.

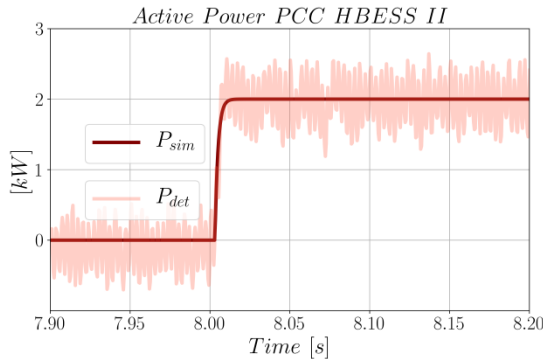


Figure 3-25. Comparison between the detailed and simplified models of HBESS II when applying a set point of 2 kW.

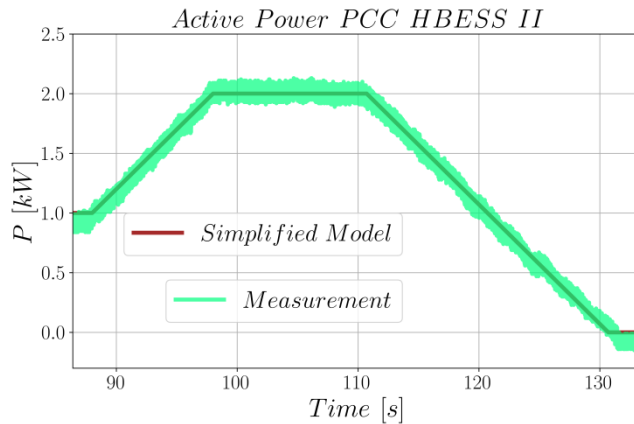


Figure 3-26. Comparison between the simplified model of HBESS II and transient measurements.

3.2.3 Photovoltaic System

The PV system of the nanogrid consists of two inverters with east-west oriented modules. The models described in this section are the same for both inverters and are called PV system I and PV system II. The only difference between them is the number of modules of the PV strings connected to the inverters.

3.2.3.1 Detailed Model

The inverters of PV system I and II can perform reduction of active power as well as absorption/generation of reactive power.

For the reduction of the active power, the topology in Figure 3-27 is applied according to (Yang, Blaabjerg, & Wang, 2014), (Sangwongwanich, Yang, & Blaabjerg, 2017) and (Wandhare & Agarwal, 2014). Furthermore, for the analysis of this topology, the reactive power set point is set to zero. If a reduction of the active power for PV systems 1 or 2 ($P_{red_{1,2}}$) is required, the control of the DC/DC converter verifies the criteria $P_{red_{1,2}} > P_{MPP_{1,2}}$ and $P_{red_{1,2}} \leq P_{MPP_{1,2}}$, where $P_{MPP_{1,2}}$ is the maximum power available at the moment of the verification (see Figure 3-27 and Figure 3-28). The maximum power tracker algorithm called incremental conductance is selected in PSCAD. Then, if the first inequality is true, the maximum power point power is chosen. On the other hand, if the second inequality is valid, a reduction of the active power is set. Both criteria apply a PI controller whose output value goes to the SPWM block, where the switching frequency for the DC/DC converter is generated. Finally, the VSI control block regulates, similar to HBESS II, the DC-link voltage as well as the reactive power at the PCC of PV system I and II.

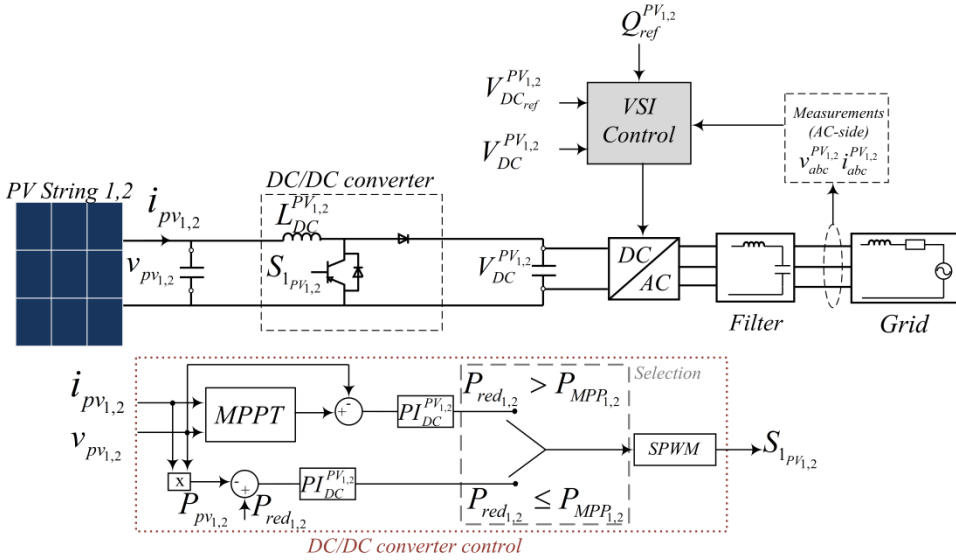


Figure 3-27. Topology used for PV system I and II in the case of the reduction of the active power.

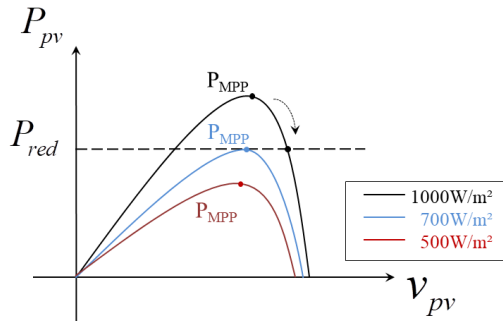


Figure 3-28. Reduction of the active power considering different solar radiations.

For the provision of the reactive power, the topology in Figure 3-29 is set up. A reactive power set point is sent to the controller. Depending on the PQ curve block, the reactive power at the PCC is generated (see section 3.1.1.1). Additionally, if the active power generated by PV system I or II is reduced due to a reactive power set point, then the control strategy for the DC/DC converter shown in Figure 3-27 is also applied to the strategy of Figure 3-29.

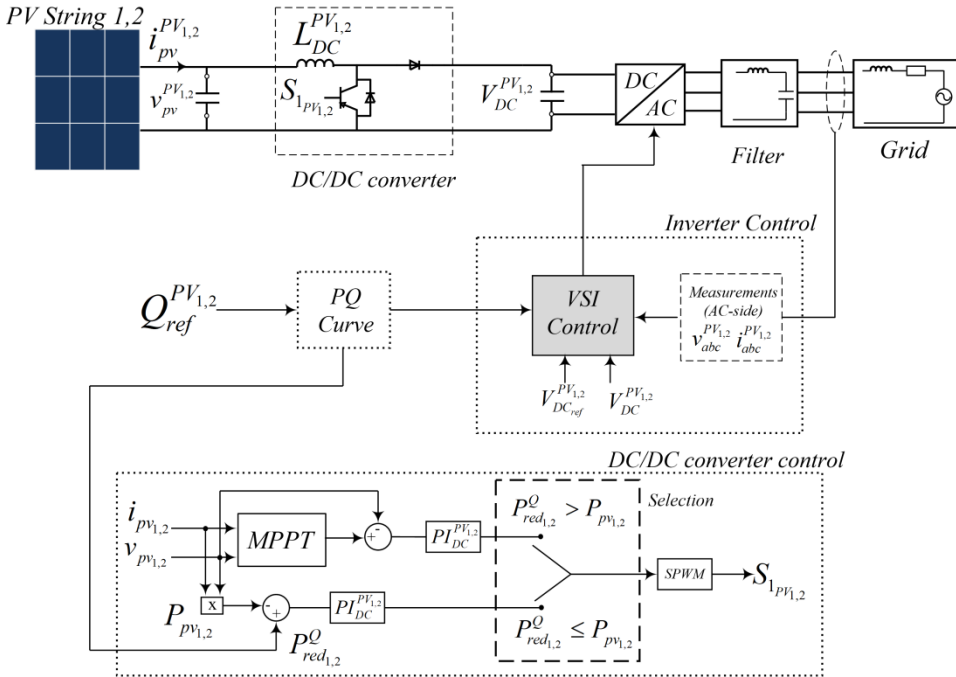


Figure 3-29. Topology used for PV system I and II in the case of reactive power provision.

The VSI control block regulates, similar to HBESS II, the DC link voltage and the reactive power at the PCC of each PV system. The block diagram of these controllers and transfer functions is shown in Figure 3-30.

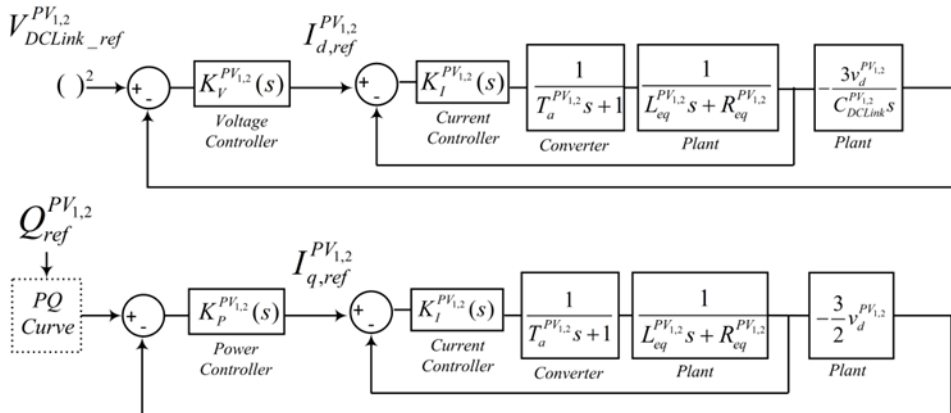


Figure 3-30. Block diagram of the voltage and reactive power control for PV system I and II.

3.2.3.2 Simplified Model

The same structure presented for HBESS I and HBESS II is applied for PV system I and II. This structure is illustrated in Figure 3-31.

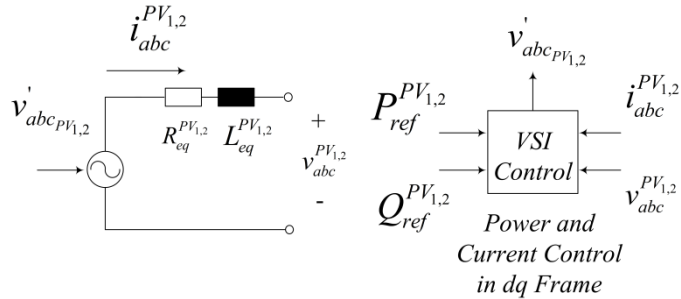


Figure 3-31. Simplified model of PV system I and II.

The set point $P_{ref}^{PV_{1,2}}$ refers to the active power generated by PV system I or II at the PCC of each one. To calculate $P_{ref}^{PV_{1,2}}$, the procedure of Figure 3-32 is followed. The Python tool, pvlib, is used to generate a lookup table that contains the global radiation, the cell temperature and the active power generated by the PV string (set of PV modules). The tool pvlib provides functions and classes for simulating the performance of PV energy systems (Python). The required inputs for pvlib are:

- **Input 1:** The parameters related to the PV cell at standard conditions according to PSCAD (ideality factor, photocurrent, saturation current, series resistance, and shunt resistance) and information from the data sheet of the PV module (cell arrangement, short circuit current, open circuit voltage, maximum current and voltage, and temperature coefficients).
- **Input 2:** Measurements of the global radiation and cell temperature.

The outputs of the block pvlib in Figure 3-32 are related to one PV module. These are the short circuit current (I_{sc}), the open circuit voltage (V_{oc}), the current (I_{mpp}), as well as the voltage (V_{mpp}) at maximum power point. The last two outputs are used for calculating the active power of a PV string.

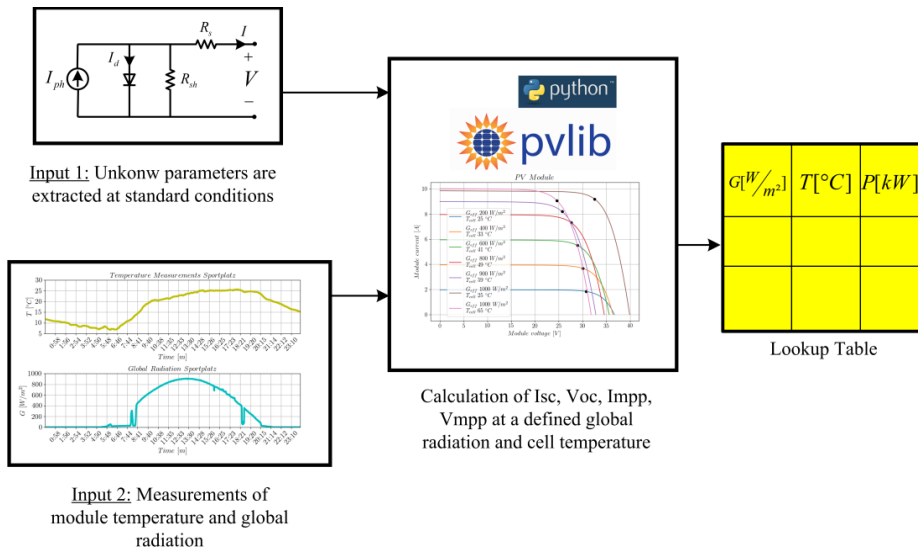


Figure 3-32. Procedure for obtaining the active power generated of PV system I and II.

3.2.3.3 Validation Model

First, the simplified model of section 3.2.3.2 is compared with the detailed model of section 3.2.3.1. Then, the simplified model is verified by comparing it with transient measurements.

Figure 3-33 depicts the comparison between the simplified and detailed model for PV system I in case an active power reduction set point of 2 kW is required at the PCC of the system. The comparison is done for standard conditions, which means, for a global radiation of 1,000 W/m² and cell temperature of 25 °C. In this example, the pvlb tool is not applied since the active power set point of the simplified model applied before the active power reduction is calculated according to the data sheet of the PV module.

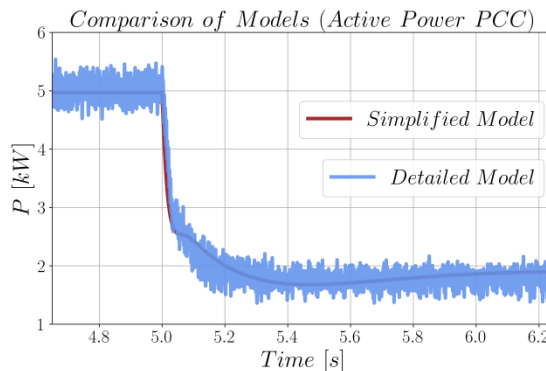


Figure 3-33. Comparison between the simplified and the detailed model for PV system I when a set point of the active power reduction of 2 kW is required.

For the validation of the active power reduction, PV system 1 is used. Figure 3-34a illustrates the temperature of one PV module of PV system 1 in a typical summer day. Additionally, Figure 3-34b shows the global radiation from a weather station called “Sportplatz”, which is located 100 meters away from the demonstrator. The information from Figure 3-34 is used as input for the pvlib tool. Additionally, the unknown parameters of the PV cell are entered.

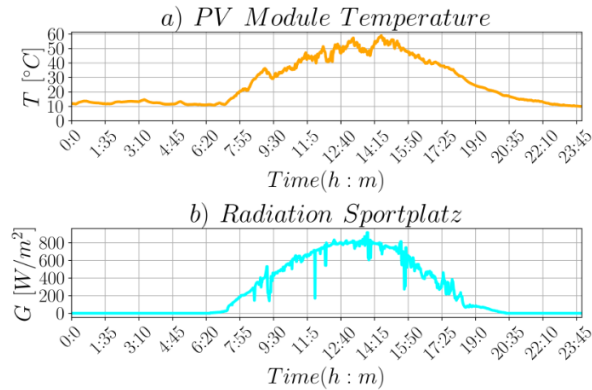


Figure 3-34. Inputs for the pvlib tool: a) Temperature of one PV module of PV system I; b) Global radiation of the weather station “Sportplatz”.

Results of the pvlib tool are shown in Figure 3-35. The y-axis represents the current and the x-axis the voltage of the PV module of PV system I for different global radiations and fixed cell temperature, which in this case is 40 °C. The black points show the maximum power point. These points are used for the lookup table that provides the set points of active power for PV system I.

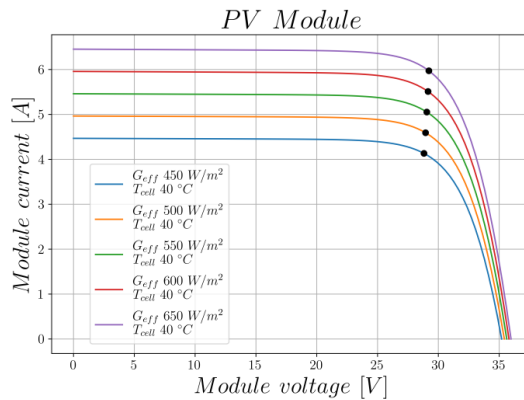


Figure 3-35. I vs. V curves of a PV module for different global radiations and a cell temperature of 40 °C.

Figure 3-36 shows the verification of the simplified model in the case of an active power reduction. The example is related to PV system 1. The active power generated before the reduction is around 2.45 kW. Then, a set point of 2 kW is sent to the PV inverter. In this case, the inequality $P_{red} \leq P_{MPP}$ is valid and the active power reduction is possible.

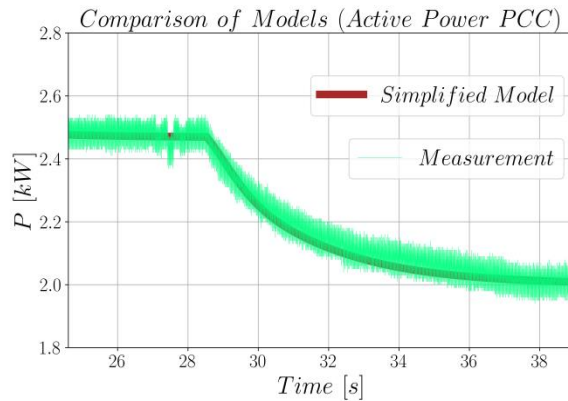


Figure 3-36. Comparison between the simplified model and transient measurements in the case of an active power reduction set point of 2 kW.

The simplified and detailed models are compared in the case of reactive power provision, too. Simulations results are shown in Figure 3-37 in the case of a reactive power set point of 5 kvar at $t = 5$ s (Figure 3-37b). An active power reduction occurs, as defined in the PQ curve (Figure 3-37a), so that the rated apparent power of the inverter is not exceeded.

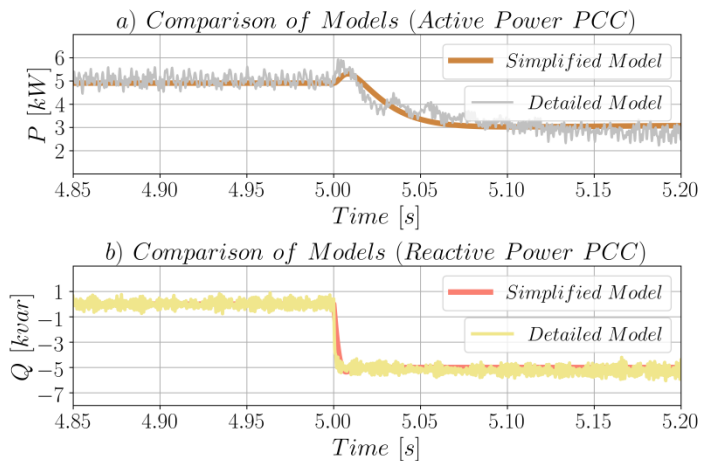


Figure 3-37. Comparison between the detailed and simplified models for PV system I in the case of reactive power provision: a) Active power reduction due to reactive power provision; b) Reactive power at the PCC at $t = 5$ s.

Finally, the simplified model is verified by the comparison with transient measurements, as seen in Figure 3-38. The increase of the reactive power from 2 kvar to 4 kvar does not reduce the active power, since the rated apparent power of the inverter is not exceeded in this case.

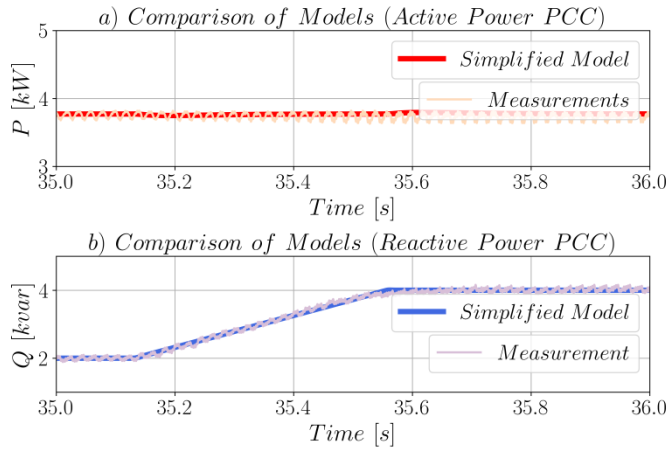


Figure 3-38. Comparison between the simplified model and transient measurements for PV system I: a) Active power at the PCC; b) Reactive power at the PCC.

3.3 Complete System Including Control Centre

In section 3.2, detailed and simplified models of the active components of the nanogrids were developed. This section investigates the behaviour of these simplified models in combination with power distribution control (PDC). Before the PDC is combined with the simplified models, the dynamic model of the grid-connected nanogrid is analyzed.

3.3.1 Dynamic Model of the Grid-Connected Nanogrid

The high number of elements of the nanogrid leads immediately to an idea that the nanogrid can be seen as a MIMO system. Additionally, this kind of a system is characterized by the coupling between the inputs and outputs, as illustrated in Figure 3-39. The aim of this section is to develop a dynamic model of the nanogrid and then to investigate if the active and the reactive power control at the PCC of the nanogrid can be controlled independently (decentralized control). The assumption is that this is possible. For this purpose, the RGA matrix is obtained based on the dynamic model of the grid-connected nanogrid. Due to the complexity of the nanogrid, different cases of use are analyzed.

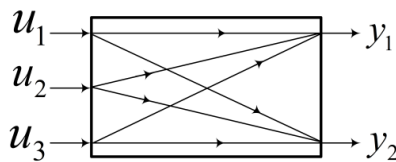


Figure 3-39: Coupling of a MIMO system with 3 inputs and 2 outputs (Lunze, 2016).

The process of developing the dynamic model of the nanogrid and analyzing the interaction between inputs and outputs of the MIMO system is depicted in Figure 3-40. The first step is called the dynamic model of the nanogrid. Here the following dynamics for each active component of the nanogrid are obtained based on the simplified models described in section 3.2:

- Power circuit: Dynamics associated with the filter
- PLL: Dynamics of the model of the Phase-Locked Loop
- Controller: Dynamics of the outer and inner loops

Furthermore, the dynamics related to the power network is considered in this step. This means that cable impedances and loads are connected to the nanogrid. Then, the small-signal model of the respective use case is obtained. In this step, the equations found in the previous step are linearized around an operating point and then expressed in state equation form. The first two steps, which means the dynamic model as well as the small-signal model, are based on (Kazempour, 2016) and (Katiraei, 2005).

Once the state equation of the system is acquired, the transfer function matrix $G(s)$ of the system model is found. Next, a decoupling analysis is carried out based on the RGA matrix, which requires $G(s)$. Information regarding the quantification of the interactions between the inputs and outputs of the MIMO system is given by the RGA matrix (Lunze, 2016), (Skogestad & Postlethwaite, 2001). This information enables investigation of the input-output pairing of the controller and if a decentralized control for the active and reactive power at the PCC can be applied (It is plausible to regulate the active and reactive power in this way, but it must be mathematically provable). The RGA matrix is defined mathematically as

$$RGA = G \times (G^{-1})^T \quad (3-19)$$

where the symbol \times denotes the Schur product. Moreover, this matrix is a function of the frequency.

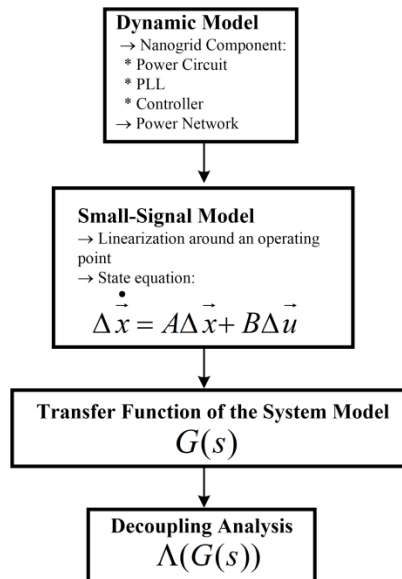


Figure 3-40. Flow chart for the analysis of the dynamics of the nanogrid.

Use Case I: This use case considers HBESS I and the load as seen in the single line diagram of Figure 3-41. The system of Use Case I has two inputs (active and reactive power set points of HBESS I) and two outputs (active and reactive power at the PCC of

the nanogrid). Additionally, the equations of the power network are related to Figure 3-41. These equations consider resistances and inductances of cables as well as the load. The linearized equations of the dynamic model (power circuit, PLL and controller) of HBESS I as well as for the power network are written in Matlab according to the parameters of the simplified model presented in 3.2.1.2 and rearranged in state equation form. In this use case, 14 states are obtained.

The small-signal model of Use Case I is verified by the comparison with transient measurements when a small disturbance occurs. The power system, in this case, the nanogrid of Use Case I, is operating in a steady state condition and suddenly the set point at the PCC is changed. If this change can be properly investigated by the linearized model, a small disturbance will occur (Grainger & Stevenson, 1994). In Figure 3-42, HBESS I is discharged with a set point of 5 kW while a load of 4.5 kW is connected to the nanogrid. On the other hand, in Figure 3-43, a capacitive set point is applied to HBESS I while an inductive load of 4.5 kvar is present. Results shows very good match between the small-signal models and the transient measurements.

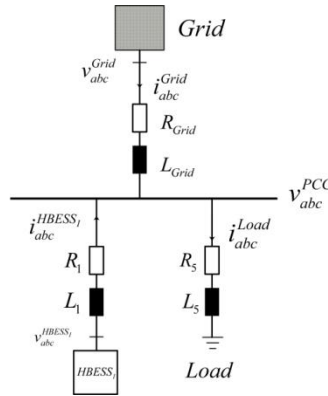


Figure 3-41. Single-line diagram of Use Case I.

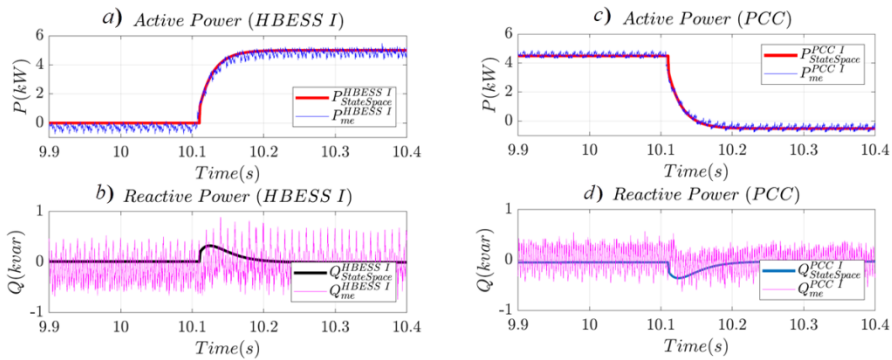


Figure 3-42. Comparison between the small-signal model and transient measurements for Use Case I if a discharge set point of 5 kW is applied to HBESS I and a load of 4.5 kW is present: a) Active power HBESS I; b) Reactive power HBESS I; c) Active power at the PCC; d) Reactive power at the PCC.

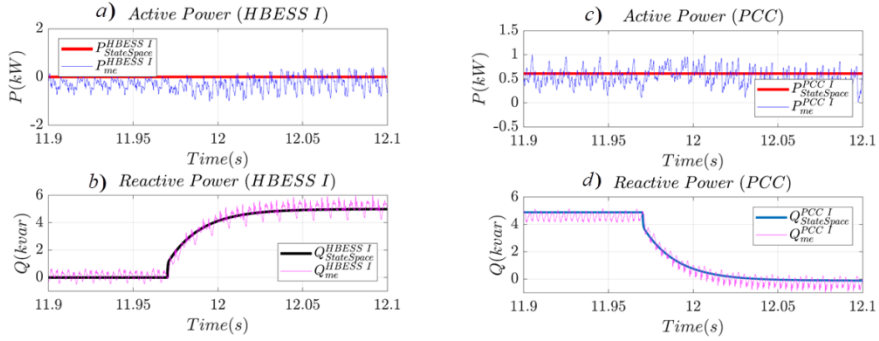


Figure 3-43. Comparison between the small-signal model and transient measurements for Use Case I if a capacitive set point of 5 kvar is applied to HBESS I and an inductive load of 4.5 kvar is present: a) Active power HBESS I; b) Reactive power HBESS I; c) Active power at PCC; d) Reactive power at PCC.

The system mathematically described in the current use case can be also represented by a transfer function whose dimension is 2x2. The transfer function is used as input for the calculation of the RGA matrix. The elements of this matrix, which are depicted in Figure 3-44 at $s = 0$, show a diagonal dominance. This means that a decentralized control can be applied, and the active and reactive power can be regulated independently for Use Case I. If the value of an element of the matrix is close to 1, then the pairing should be selected (Skogestad & Postlethwaite, 2001). In Figure 3-44, this means $u_1 - y_1$ and $u_2 - y_2$.

$$RGA = \begin{array}{cc|cc} P_{HBESS_I} & Q_{HBESS_I} & & \\ u_1 & u_2 & & \\ \hline 1 & 0 & P_{PCC} & y_1 \\ \hline 0 & 1 & Q_{PCC} & y_2 \end{array}$$

Figure 3-44. Elements of the RGA matrix for Use Case I.

Use Case II: This use case considers HBESS I, PV II, and the load. With such of configuration (see Figure 3-45), the linearized dynamic model in state-space form has 4 inputs (active and reactive power set points of HBESS I and PV II), 2 outputs (active power and reactive power at PCC), and 24 states. The validation of the linearized dynamic model is shown in Figure 3-46 and 3-47 for an active and reactive power set point applied to HBESS I and PV II, respectively. The resistance of the load bank affects the results of Figure 3-47 e).

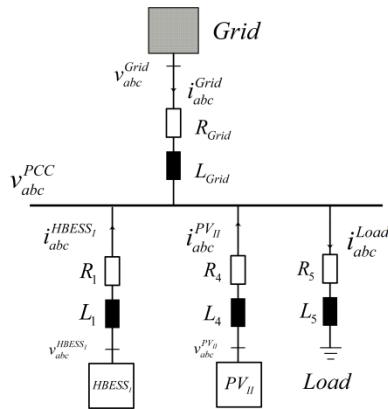


Figure 3-45. Single-line diagram of Use Case II.

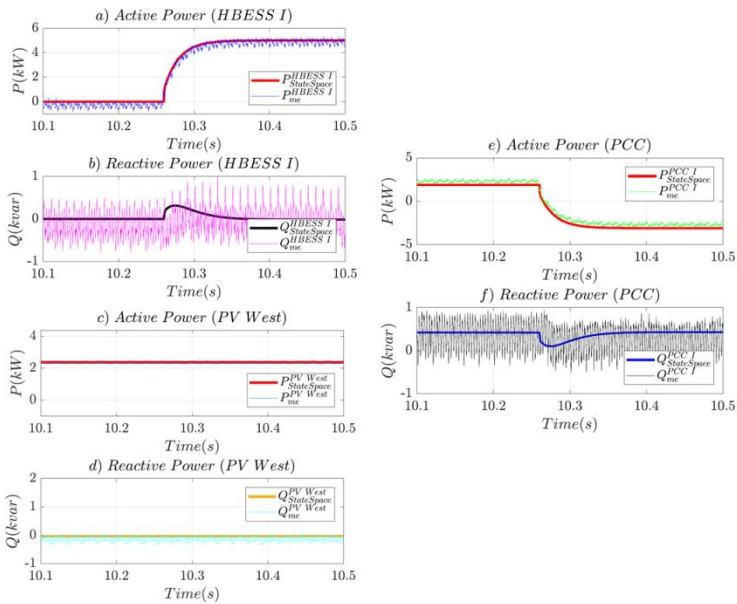


Figure 3-46. Dynamics of the nanogrid for Use Case II in case an active power step is applied to HBESS I and a load of 4.5 kW: a) Active power HBESS I; b) Reactive power HBESS I; c) Active power PV West; d) Reactive power PV West; e) Active power PCC; f) Reactive power PCC.

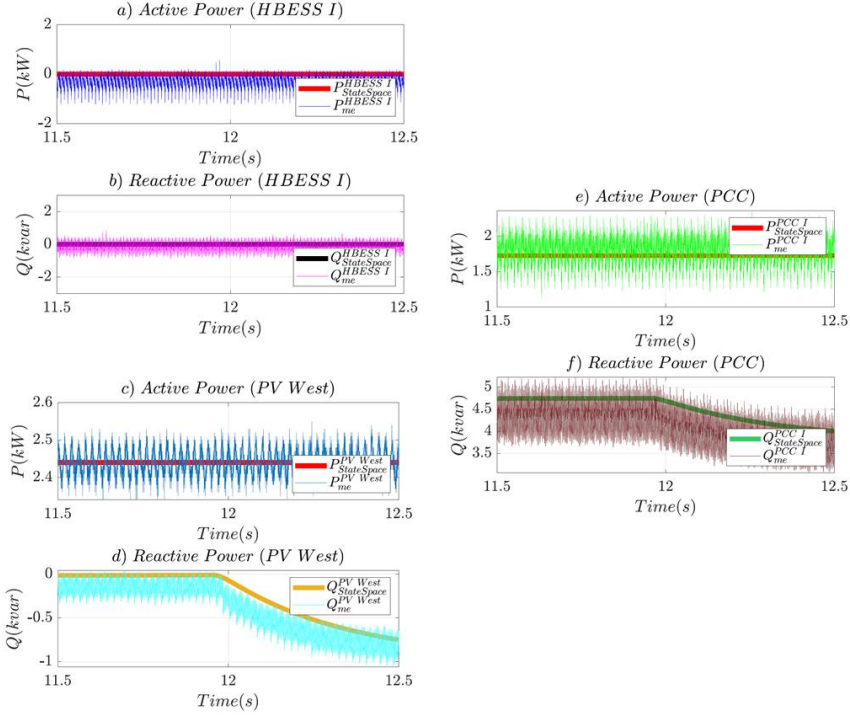


Figure 3-47. Dynamics of the nanogrid for Use Case II in case a reactive power step is applied to PV West and a load of 4.5 kvar: a) Active power HBESS I; b) Reactive power HBESS I; c) Active power PV West; d) Reactive power PV West; e) Active power PCC; f) Reactive power PCC.

The transfer function matrix of the system shown in Figure 3-45 has a dimension of 2x4. The elements of the RGA matrix are illustrated in Figure 3-48. At $s = 0$, if the value of an element of the matrix is close to 1, then the pairing should be selected (Skogestad & Postlethwaite, 2001); in this case, $u_1 - y_1$ and $u_3 - y_1$ as well as $u_2 - y_2$ and $u_4 - y_2$.

$$RGA = \begin{bmatrix} P_{HBESS_I} & Q_{HBESS_I} & P_{PV_{II}} & Q_{PV_{II}} \\ u_1 & u_2 & u_3 & u_4 \\ \hline 0.5 & 0 & 0.5 & 0 \\ 0 & 0.5 & 0 & 0.5 \end{bmatrix} \begin{matrix} P_{PCC} & y_1 \\ \hline Q_{PCC} & y_2 \end{matrix}$$

Figure 3-48. Elements of the RGA matrix for Use Case II.

Use Case III: This use case considers HBESS I and II as well as the load, as seen in Figure 3-49. The validation of the linearized dynamic model is shown in Figure 3-50.

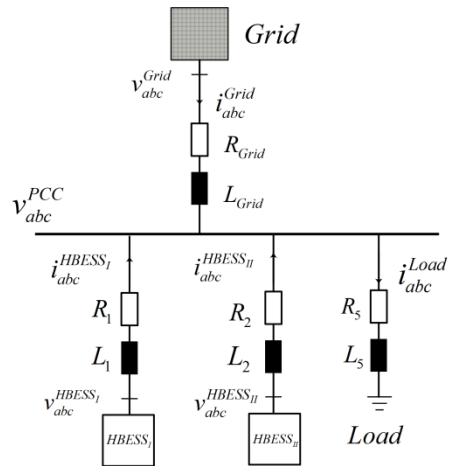


Figure 3-49. Single-line diagram of Use Case III.

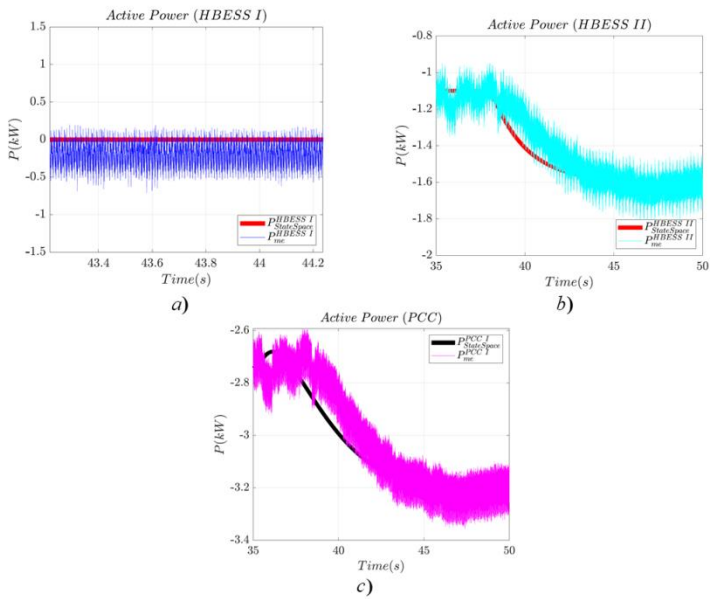


Figure 3-50. Dynamics of the nanogrid for Use Case III in case an active power step is applied to HBESS II and a load of 1.5 kW: a) Active power HBESS I; b) Active power HBESS II; c) Active power PCC.

The elements of the RGA matrix are illustrated in Figure 3-51.

$$RGA = \begin{array}{c} \begin{array}{cc} P_{HBESS_I} & Q_{HBESS_I} \\ u_1 & u_2 \end{array} \quad \begin{array}{cc} P_{HBESS_{II}} & Q_{HBESS_{II}} \\ u_3 & u_4 \end{array} \\ \left[\begin{array}{cc|cc} 0.5 & 0 & 0.5 & 0 \\ \hline 0 & 0.5 & 0 & 0.5 \end{array} \right] \begin{array}{l} P_{PCC} \quad y_1 \\ Q_{PCC} \quad y_2 \end{array} \end{array}$$

Figure 3-51. Elements of the RGA matrix for Use Case III.

3.3.2 Power Distribution Control (PDC)

In this section, the developed simplified models are combined with a control centre for the provision of the active and reactive power of the nanogrid in grid-connected mode. This is carried out in a simulation environment, whereas the results are validated by comparing the results with the measurements at the demonstrator. An optimization of the control is not performed in this thesis and can be seen as part of future work. Moreover, the PI controllers are set up by trial-and-error.

The block diagram of the PDC is depicted in Figure 3-52. The PDC can distribute active and reactive power set points among the RES and storages present in the system. The block network represents cables and loads.

In this section, Use Cases I and II shown in 3.3.1 are analyzed.

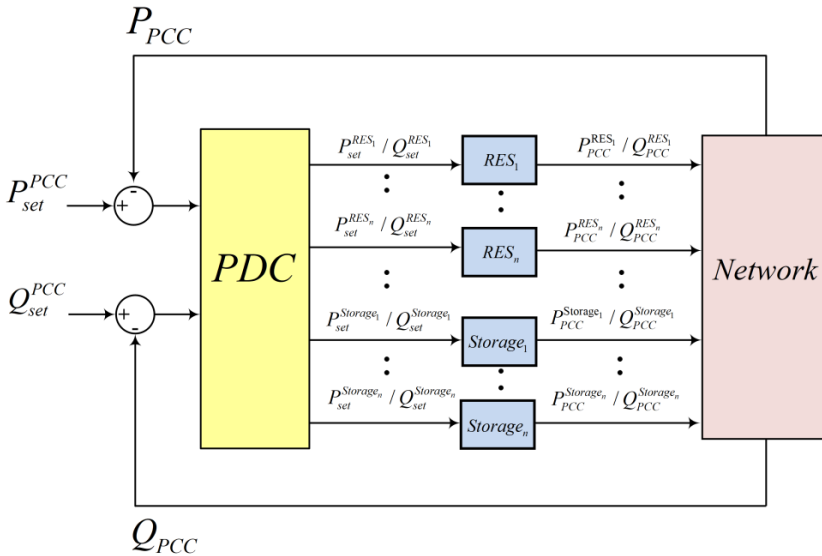


Figure 3-52. Block diagram of the PDC with several RES and storages.

Use Case I: This use case considers just HBESS I and a load, as presented in section 3.3.1. In this section, it was determined that for this use case, decentralized control is possible, which means that the active and reactive power at the PCC can be controlled separately. The network shown in Figure 3-41 and the corresponding control structure according to Figure 3-52 are implemented in the demonstrator as well as in the simulation environment PSCAD (applying simplified models). Figure 3-53 and 3.54 show the comparison between the measurements from the control centre and the simulation. The PDC in this use case was tuned by applying the trial-and-error method. In the case of the provision of the active power (Figure 3-53), the load was set to 4.5 kW and for every variation in the set points, the active power is compensated by HBESS I. Figure 3-54 illustrates the provision of the reactive power at the PCC of the nanogrid when an inductive load of 4.5 kvar is connected during the test. For every set point, HBESS I compensates the reactive power required at the PCC. It is necessary to point out the presence of a variable communication delay due to communication between HBESS I and the control centre.

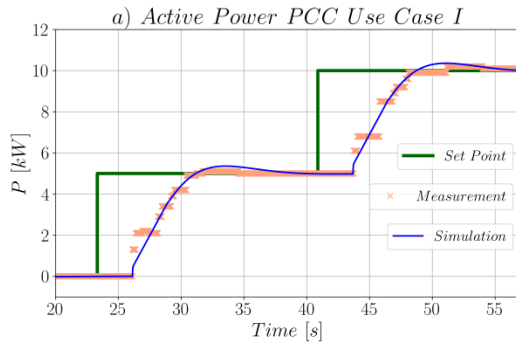


Figure 3-53. Results of simulation and measurements at the PCC of the nanogrid for Use Case I in the case of active power provision.

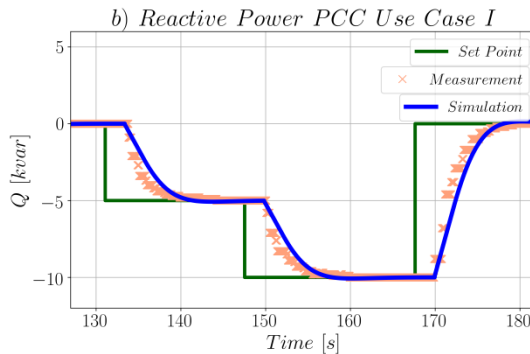


Figure 3-54. Results of simulation and measurements at PCC of the nanogrid for Use Case I in the case of reactive power provision.

Use Case II: The network shown in Figure 3-45 and the corresponding control structure according to Figure 3-52 are implemented in the demonstrator as well as in the simulation environment PSCAD (simplified models). The PDC is tuned according to the trial-and-error method. Figure 3-55 depicts the results of the simulation and the measurement from the control centre when several set points of the active power are applied to the PCC of the nanogrid and a constant load of around 4.5 kW is connected. Figure 3-55 also indicates how HBESS I supports the nanogrid in order to accomplish the active power set point at the PCC of it. Furthermore, the active power generation of the connected PV system is lower than the active power consumed by the load during the experiment. In Figure 3-55a, the simplified models developed in PSCAD (see sections 3.2.1.2 and 3.2.3.2) are compared with the measurements from the control centre. In Figure 3-55b, the measurements of the PV system with east orientation are used as active power profiles for the simplified model of the PV system in the PSCAD simulation. Figure 3-55c illustrates the comparison between the simplified model in PSCAD of HBESS I (see section 3.2.1.2) and the measurements from the control centre. It is necessary to point out the application of the load and generation conventions that influence the signs of the active power measurements. Communication delays are also present in the experiment.

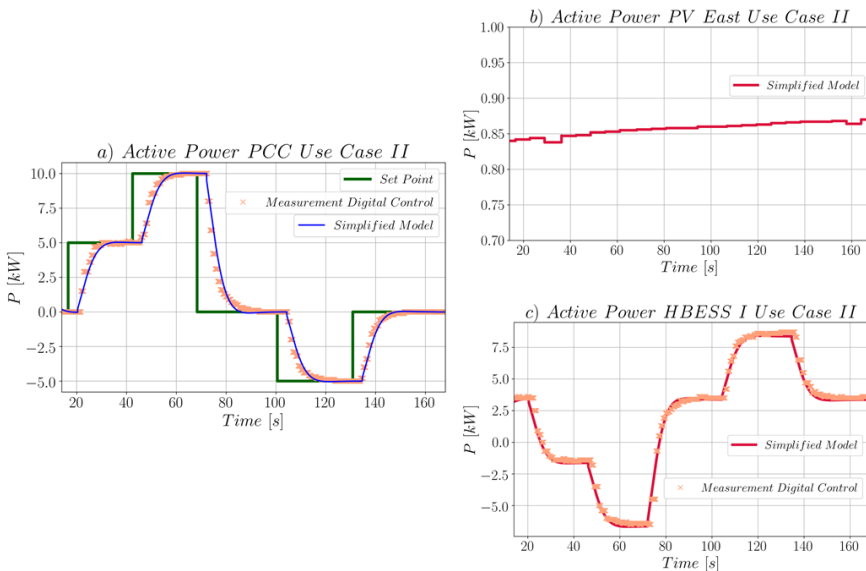


Figure 3-55. Results of simulation and measurements for active power provision in Use Case II: a) Active power at PCC of the nanogrid in load convention; b) Active power PV East in generation convention; c) Active power HBESS I in generation convention.

In the case of the reactive power provision, an inductive load of around 1.5 kvar is connected. Figure 3-56 shows the comparison between the simulation and the measurements from the control centre. In this case, the PDC includes participation factors for the distribution of the reactive power between the PV inverter and HBESS I:

- HBESS I: $\frac{\text{Rated Power HBESS I}}{\text{Total rated Power}} = \frac{20\text{kVA}}{20\text{kVA}+6\text{kVA}} = 10/13$
- PV East: $\frac{\text{Rated Power PV East}}{\text{Total rated Power}} = \frac{6\text{kVA}}{20\text{kVA}+6\text{kVA}} = 3/13$

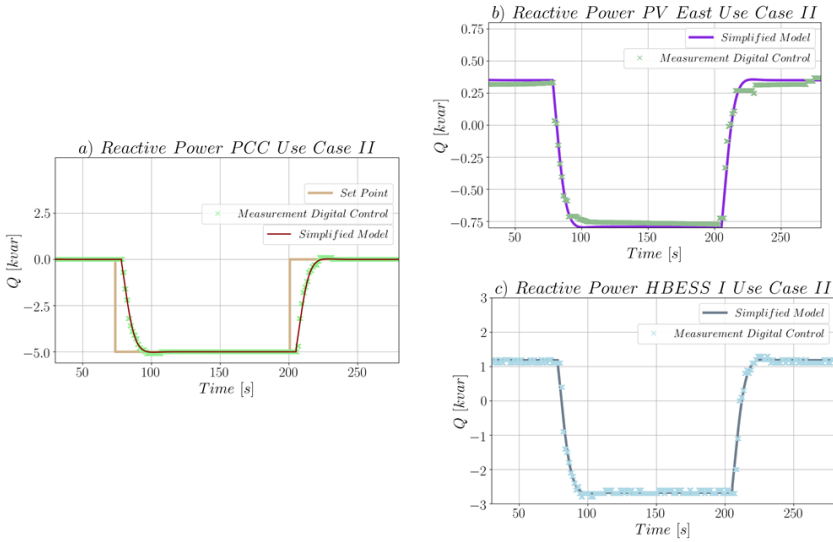


Figure 3-56. Results of simulation and measurements for reactive power provision in Use Case II: a) Reactive power at PCC of the nanogrid in generation convention; b) Reactive power PV East in generation convention; c) Reactive power HBESS I in generation convention.

3.3.3 Stability Analysis Considering Communication Delays

The performance of the whole control loops might be affected by the communication delays present in the communication infrastructure, which could show a random behaviour. For this reason, it is necessary to analyze the stability of the system considering communication delays at the nanogrid level. Due to simplicity reasons, this scientific work presents the stability analysis of Use Case I. Firstly, the ordinary differential equations are presented. Then, a small-signal model of the system and its validation are shown. Since the nanogrid is a multiple-input multiple-out system, a decoupling analysis is performed first. At the end, the stability analysis is made.

The single-line diagram of the system including active and reactive power control is depicted in Figure 3-57. The cable that connects HBESS I to the grid is represented by R_1 and L_1 . R_5 and L_5 stand for the load as well as its cable connection of the grid. Additionally, the cable connecting the nanogrid with the grid is defined by R_{Grid} and L_{Grid} . In order to obtain the small-signal model of the nanogrid, first, it is necessary to develop the ordinary differential equations (ODE) of the whole system. In the case of HBESS_i, the power circuit, controllers as well as the phase-locked loop (PLL) are taken into account (Katiraei, 2005), (Kazempour, 2016).

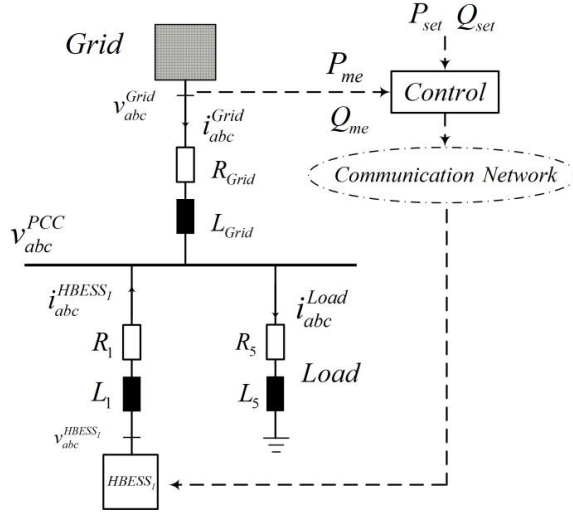


Figure 3-57. Use Case I with active and reactive power control as well as communication network.

ODE of the power circuit of HBESS_I

This part of the modelling is based on the simplified models, which means that the IGBT and the DC side (in this case, the battery modules and DC/DC converter) of HBESS I can be ignored. Especially, for control and stability analysis, the switching of the IGBT in the voltage source inverter can be neglected due to the low content of the harmonics in the current. Figure 3-58 shows the simplified model of HBESS I in the dq-Frame. The variables $i_d^{HBESS_I}$ and $i_q^{HBESS_I}$ are the output currents of the battery system. On the other hand, v'_{dHBESS_I} and v'_{qHBESS_I} represent the input voltages of the voltage source. The variables $v_d^{HBESS_I}$ and $v_q^{HBESS_I}$ donate the voltage at the terminals of HBESS I.

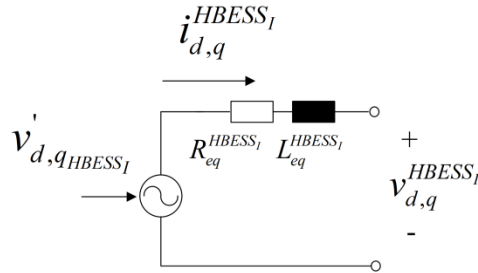


Figure 3-58. Power circuit of HBESS I.

Based on Figure 3-58 and applying Kirchhoff's voltage law, the ODE of the power circuit of HBESS I is given by

$$\frac{d}{dt} i_d^{HBESS_I} = -\frac{R_{eq}^{HBESS_I}}{L_{eq}^{HBESS_I}} i_d^{HBESS_I} + \omega_r^{HBESS_I} i_q^{HBESS_I} + \frac{1}{L_{eq}^{HBESS_I}} [v'_{dHBESS_I} - v_d^{HBESS_I}] \quad (3-20)$$

$$\frac{d}{dt} i_q^{HBESS_I} = -\frac{R_{eq}^{HBESS_I}}{L_{eq}^{HBESS_I}} i_q^{HBESS_I} - \omega_{rHBESS_I} i_d^{HBESS_I} + \frac{1}{L_{eq}^{HBESS_I}} [v_{qHBESS_I}' - v_q^{HBESS_I}] \quad (3-21)$$

ODE of the PLL

The PLL is required for the synchronization of the battery system with the grid. The ODE of the PLL is based on the control block diagram shown in Figure 3-59 (Yazdani & Iravani, 2010), where k_{sPLL} , k_{pPLL} and k_{iPLL} are the smoothing, proportional and integral gains of the controller, respectively. Furthermore, θ_{HBESS_I} and $\omega_{ref,HBESS_I}$ are defined as the phase angle and the angular frequency of HBESS I.

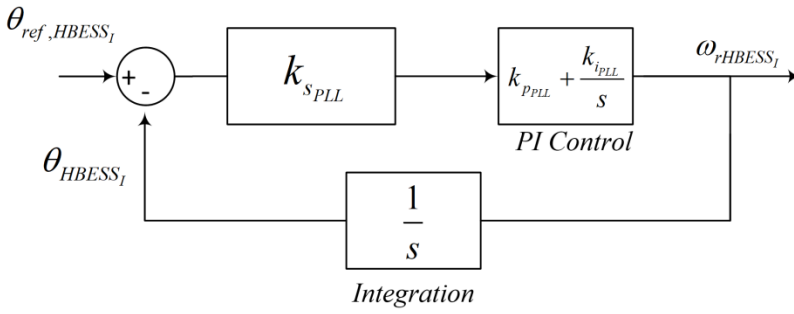


Figure 3-59. Block diagram of the PLL.

$$\begin{aligned} \frac{d}{dt} \omega_{rHBESS_I} &= k_{sPLL,HBESS_I} k_{pPLL,HBESS_I} \frac{d}{dt} \theta_{ref,HBESS_I} \\ &\quad - k_{sPLL,HBESS_I} k_{pPLL,HBESS_I} \frac{d}{dt} \theta_{HBESS_I} \\ &\quad + (k_{sPLL,HBESS_I} k_{iPLL,HBESS_I}) (\theta_{ref,HBESS_I} \\ &\quad - \theta_{HBESS_I}) \end{aligned} \quad (3-22)$$

ODE of the controller

The outer (power) as well as the inner (current) controllers are considered in the modelling of the ODE. The control loops for the active and reactive power regulation of HBESS I are depicted in Figure 3-60. The parameters $k_{pp}^{HBESS_I}$ and $k_{pi}^{HBESS_I}$ are the proportional and integral gains of the power controllers. $k_{pi}^{HBESS_I}$ and $k_{ii}^{HBESS_I}$ are the proportional and integral gains related to the current controllers. The following mathematical expressions represent the ODE of the active and reactive power controllers according to Figure 3-60.

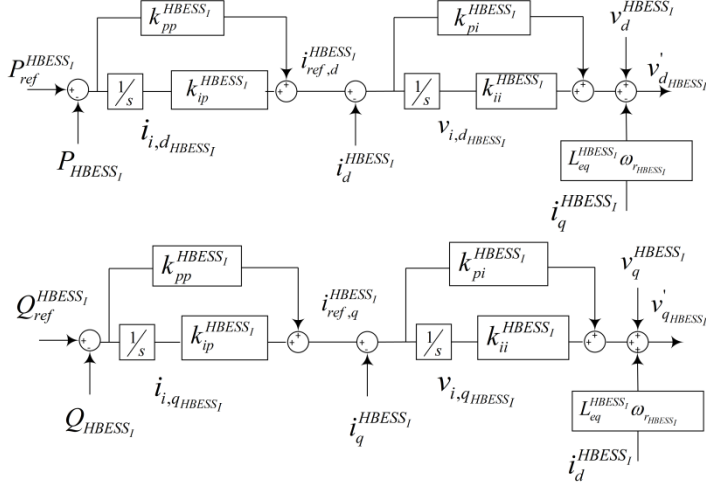


Figure 3-60. Active and reactive power control.

$$P_{HBESS1} = 1.5v_d^{HBESS1}i_d^{HBESS1} + 1.5v_q^{HBESS1}i_q^{HBESS1} \quad (3-23)$$

$$Q_{HBESS1} = -1.5v_d^{HBESS1}i_q^{HBESS1} + 1.5v_q^{HBESS1}i_d^{HBESS1} \quad (3-24)$$

$$\begin{aligned} \frac{d}{dt}v_{i,d}^{HBESS1} &= P_{ref}^{HBESS1}k_{pp}^{HBESS1} - P_{HBESS1}k_{pp}^{HBESS1} \\ &\quad + i_{i,dHBESS1}k_{ip}^{HBESS1} - i_d^{HBESS1} \end{aligned} \quad (3-25)$$

$$\begin{aligned} \frac{d}{dt}v_{i,q}^{HBESS1} &= Q_{ref}^{HBESS1}k_{pp}^{HBESS1} - Q_{HBESS1}k_{pp}^{HBESS1} \\ &\quad + i_{i,qHBESS1}k_{ip}^{HBESS1} - i_q^{HBESS1} \end{aligned} \quad (3-26)$$

$$\begin{aligned} v_{dHBESS1}' &= v_d^{HBESS1} - \omega_r^{HBESS1}L_{eq}^{HBESS1}i_q^{HBESS1} \\ &\quad + v_{i,dHBESS1}k_{ii}^{HBESS1} + k_{pi}^{HBESS1} \frac{d}{dt}v_{i,d}^{HBESS1} \end{aligned} \quad (3-27)$$

$$\begin{aligned} v_{qHBESS1}' &= v_q^{HBESS1} - \omega_r^{HBESS1}L_{eq}^{HBESS1}i_d^{HBESS1} \\ &\quad + v_{i,qHBESS1}k_{ii}^{HBESS1} + k_{pi}^{HBESS1} \frac{d}{dt}v_{i,q}^{HBESS1} \end{aligned} \quad (3-28)$$

$$\frac{d}{dt}i_{i,dHBESS1} = P_{ref}^{HBESS1} - P_{HBESS1} \quad (3-29)$$

$$\frac{d}{dt}i_{i,qHBESS1} = Q_{ref}^{HBESS1} - Q_{HBESS1} \quad (3-30)$$

ODE considering the external grid

The ODEs of the system shown in Figure 3-57 in dq-Frame are given by

$$\frac{d}{dt} i_d^{Grid} = \frac{1}{L_{Grid}} (v_d^{g,Grid} - v_d^{PCC}) - \frac{R_{Grid}}{L_{Grid}} i_d^{Grid} + \omega_s i_q^{Grid} \quad (3-31)$$

$$\frac{d}{dt} i_q^{Grid} = \frac{1}{L_{Grid}} (v_q^{g,Grid} - v_q^{PCC}) - \frac{R_{Grid}}{L_{Grid}} i_q^{Grid} + \omega_s i_d^{Grid} \quad (3-32)$$

$$\frac{d}{dt} i_{HBESS1,d}^g = \frac{1}{L_1} (v_d^{g,HBESS1} - v_d^{PCC}) - \frac{R_1}{L_1} i_{HBESS1,d}^g + \omega_s i_{HBESS1,q}^g \quad (3-33)$$

$$\frac{d}{dt} i_{HBESS1,q}^g = \frac{1}{L_1} (v_q^{g,HBESS1} - v_q^{PCC}) - \frac{R_1}{L_1} i_{HBESS1,q}^g - \omega_s i_{HBESS1,d}^g \quad (3-34)$$

$$\frac{d}{dt} i_d^{Load} = \frac{1}{L_5} (v_d^{PCC}) - \frac{R_5}{L_5} i_d^{Load} + \omega_s i_q^{Load} \quad (3-35)$$

$$\frac{d}{dt} i_q^{Load} = \frac{1}{L_5} (v_q^{PCC}) - \frac{R_5}{L_5} i_q^{Load} + \omega_s i_d^{Load} \quad (3-36)$$

The global dq-frame reference is denoted by the superscript g . Furthermore, the angular frequency of the global frame is defined by ω_s .

Small-signal model of the system and validation

The ODEs presented are rearranged in state-space form and then linearized around an operating point. The matrixes \tilde{A} , \tilde{B}_1 , \tilde{B}_2 , \tilde{B}_3 , and \tilde{B}_4 are a function of the system parameters and are calculated according to (Kazempour, 2016):

$$\frac{d}{dt} \Delta \vec{x} = \tilde{A} \Delta \vec{x} + \tilde{B}_1 \Delta \vec{u}_{HBESS1} + \tilde{B}_2 \Delta \vec{v}^{g,Grid} + \tilde{B}_3 \Delta \omega_s + \tilde{B}_4 \Delta \vec{u}_{pl} \quad (3-37)$$

$$\Delta \vec{y} = \tilde{C} \Delta \vec{x} \quad (3-38)$$

where the vectors are defined as

$$\Delta \vec{x} = \begin{bmatrix} \Delta \vec{x}_{HBESS1}^g \\ \Delta \vec{x}_{cc} \\ \Delta \vec{x}_{Network} \end{bmatrix} \quad (3-39)$$

$$\Delta \vec{x}_{HBESS_I}^g = \begin{bmatrix} \Delta \vec{\theta}_{HBESS_I}^g \\ \Delta \theta_{HBESS_I} \\ \Delta \omega_{HBESS_I} \end{bmatrix} \quad (3-40)$$

$$\Delta \vec{i}_{HBESS_I}^g = \begin{bmatrix} \Delta i_{HBESS_I,d}^g \\ \Delta i_{HBESS_I,q}^g \end{bmatrix} \quad (3-41)$$

$$\Delta \vec{x}_{cc} = \begin{bmatrix} \Delta v_{i,dHBESS_I} \\ \Delta v_{i,qHBESS_I} \\ \Delta i_{i,dHBESS_I} \\ \Delta i_{i,qHBESS_I} \end{bmatrix} \quad (3-42)$$

$$\Delta \vec{x}_{Network} = \begin{bmatrix} \Delta i_d^{Grid} \\ \Delta i_q^{Grid} \\ \Delta i_{HBESS_I,d}^g \\ \Delta i_{HBESS_I,q}^g \\ \Delta i_d^{Load} \\ \Delta i_q^{Load} \end{bmatrix} \quad (3-43)$$

$$\Delta \vec{u}_{HBESS_I} = \begin{bmatrix} \Delta P_{ref}^{HBESS_I} \\ \Delta Q_{ref}^{HBESS_I} \end{bmatrix} \quad (3-44)$$

$$\Delta \vec{v}^{g,Grid} = \begin{bmatrix} \Delta v_d^{g,Grid} \\ \Delta v_q^{g,Grid} \end{bmatrix} \quad (3-45)$$

$$\Delta \vec{u}_{pll} = \begin{bmatrix} \Delta \theta_{ref,HBESS_I} \\ \Delta \omega_{ref,HBESS_I} \end{bmatrix} \quad (3-46)$$

$$\begin{aligned} \Delta \vec{y} &= \begin{bmatrix} \Delta i_d^{Grid} \\ \Delta i_q^{Grid} \end{bmatrix}; \tilde{C} = [\tilde{Y}_1 \quad \tilde{0} \quad \tilde{0} \quad \tilde{0} \quad \tilde{Y}_2]; \tilde{Y}_1 = \begin{bmatrix} -1 & 0 \\ 0 & -1 \end{bmatrix}; \tilde{Y}_2 \\ &= \begin{bmatrix} 0 & 0 & 0 & 0 & 1 & 0 \\ 0 & 0 & 0 & 0 & 0 & 1 \end{bmatrix} \end{aligned} \quad (3-47)$$

The small-signal model presented previously is validated by varying the active power of the battery system. Figure 3-61 and 3-62 show the comparison between the measurements and the small-signal model. In this case, a constant load of 4.5 kW is

used for the experiment and HBESS I is discharged with a set point of 5 kW. On the other hand, the reactive power set point of HBESS I is set to 0 kvar. Results show a very good match between the small-signal model of the system and the measurements.

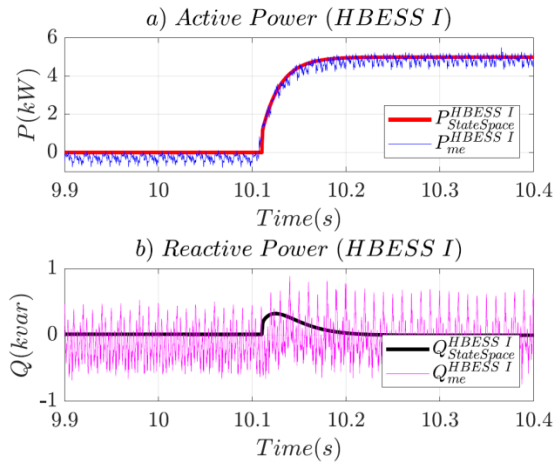


Figure 3-61. Comparison between simulation and measurements for HBESS I in the generation convention system: a) Active power at the output terminals of HBESS I; b) Reactive power at the output terminals of HBESS I.

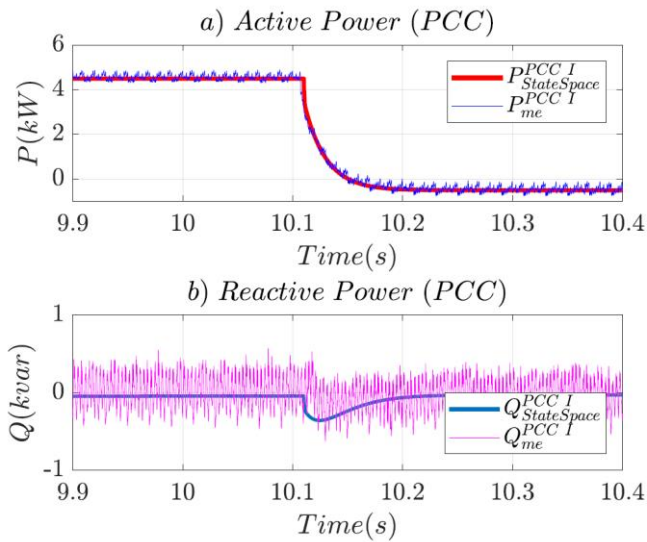


Figure 3-62. Comparison between simulation and measurements for the PCC in the load convention system: a) Active power at the PCC; b) Reactive power at the PCC.

Decoupling and stability analysis

The small-signal model can be represented in the frequency domain by its transfer function. In this case, the small-signal model is a multiple-input multiple output (MIMO) system with a transfer function matrix whose dimension is 2x2 according to

$$\tilde{G}(s) = \begin{bmatrix} G_{11}(s) & G_{12}(s) \\ G_{21}(s) & G_{22}(s) \end{bmatrix} \quad (3-48)$$

Assuming a constant voltage at the PCC, the inputs of the MIMO system are the active and reactive power set points of HBESS I. On the other hand, the outputs are the active and reactive power at the PCC. The transfer functions of the main diagonal of the transfer function matrix represent the relationship between output 1 and input 1 (G_{11}) as well as between output 2 and input 2 (G_{22}). The coupling elements are given by the relationship between output 1 and input 2 (G_{12}) as well as by the relationship between output 2 and input 1 (G_{21}). If this coupling is weak, then the transfer functions G_{12} and G_{21} can be neglected. In addition, G_{11} as well as G_{22} can be considered as single-input single-output (SISO) systems, which can be analyzed separately, as depicted in Figure 3-63.

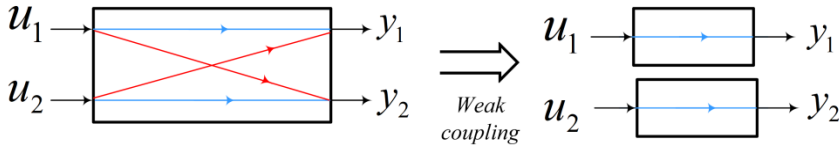


Figure 3-63. Coupling in a MIMO system (Lunze, 2016).

The quantification of the interactions between the inputs and outputs of a MIMO system is given by the RGA (Relative Gain Array) matrix, which is defined as

$$RGA = \tilde{G} \times (\tilde{G}^{-1})^T \quad (3-49)$$

where the symbol \times denotes the Schur product. It is important to point out that the RGA matrix is a function of the frequency and if the value of an element of the matrix is close to 1, then the pairing should be selected. Figure 3-64 illustrates the RGA matrix of the small-signal model. It can be seen that the coupling is weak, since the elements λ_{12} and λ_{21} are zero, whereas, the elements of the main diagonal are 1, which means that $u_1 - y_1$ and $u_2 - y_2$ can be paired and considered as SISO systems.

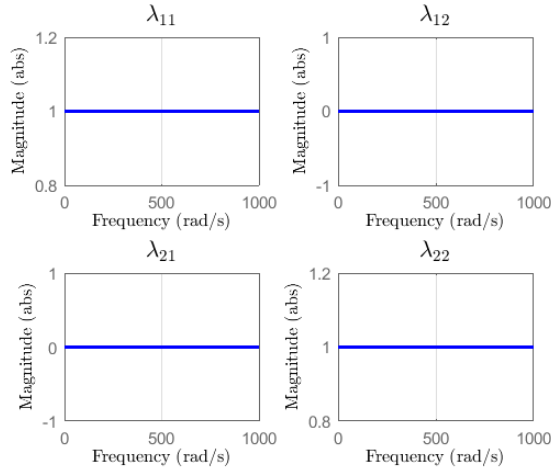


Figure 3-64. RGA matrix of the small-signal model.

Next, the matrices G_{11} and G_{22} are analyzed as SISO systems. Furthermore, an approximation of a time delay is multiplied to each of the transfer functions (Figure 3-65) mentioned earlier in order to perform the stability analysis.

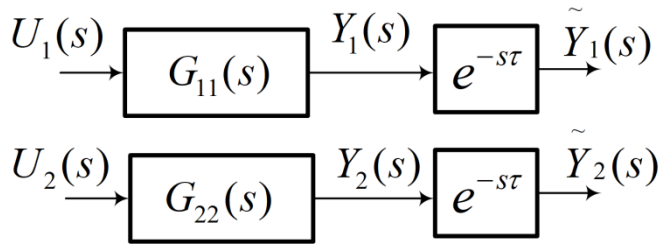


Figure 3-65. Matrices G_{11} and G_{22} with time delay.

The time delay is represented by a Padé approximation (Dutton, Thompson, & Barraclough, 1997). In this case, a second order ($n = 2$) is applied, which ensures good accuracy of the modelling of the time delay (Franklin, Powell, & Emami-Naeini, 2010):

$$e^{-s\tau} \approx \frac{2 + \sum_{i=1}^n \frac{(-s\tau)^i}{i!}}{2 + \sum_{i=1}^n \frac{(s\tau)^i}{i!}} \quad (3-50)$$

The pole-zero plots of the open-loop systems of Figure 3-65 are depicted, and in this case, the transfer function G_{11} is analyzed without (Figure 3-66a) and with (Figure 3-66b) communication delay time for poles and zeros near the real and imaginary axis. Without communication delay time, there are two poles: on the real axis and located on the left side of the s-plane. On the other hand, when adding the communication delay time, zeros are introduced and located on the right side of the s-plane. This is due to the numerator of the approximation of the communication delay time. In addition to

this, systems with such characteristics have usually an inverse response, which means that if the positive step function is applied to the open-loop transfer function, the system responds initially in a negative direction and not from the initial steady state value (Dutton, Thompson, & Barraclough, 1997), (Maciejowski, 2018). Furthermore, it can be noticed in Figure 3-66b that the higher the communication delay in this system, the higher is the approximation of the poles to the origin. In (Dutton, Thompson, & Barraclough, 1997), it is highlighted that the impulse response of a system with one pole in the origin is marginally stable. In addition, it is also mentioned that if two poles are in the origin, the impulse response of the system is unstable. As a consequence, a high value of the communication delay time influences the stability of the analyzed system.

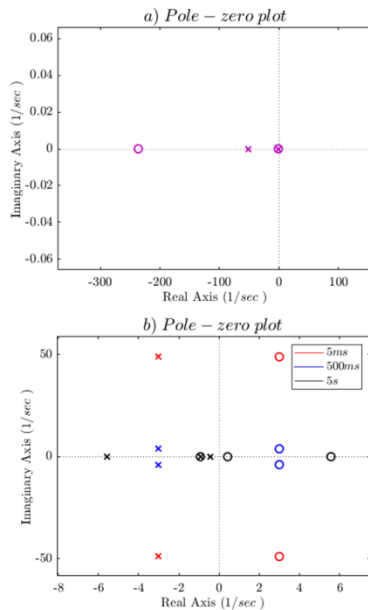


Figure 3-66. Pole-zero plots for G_{11} : a) Without communication delay; b) With communication delay (5 ms, 500 ms and 5 s).

3.4 Conclusions

According to the first hypothesis in section 1.2, for the control and stability analysis, the switching of the IGBT of the inverters can be neglected. This is due to the low content of the harmonics in the current. The validity of the hypothesis was achieved by developing simplified models of the DG and DS part of a nanogrid and then comparing them with measurements. Afterwards, the simplified models were combined with the control centre. In both cases, the results showed a very good match between the simulation and the measurement results.

The dynamics of the nanogrid depends on the control parameter of the components of the nanogrids (in this case, HBESS and PV) as well as on the control centre. Undoubtedly, a grid code in a specific country can have specific requirements regarding the transient response at the PCC of the nanogrid. These specifications could be not only related to the rise time, settling time or overshoot, but also to the behaviour of

the response, which could be a PT_1 element or even a ramp. The fulfilment of the requirements of a grid code depends on how the control centre as well as DG and DS are parametrized.

Finally, the second hypothesis in section 1.2 was verified. In this case, communication delays influence the stability of a nanogrid. The proof is - the higher the delay time, the closer are the poles to the origin.

4 Development of a Method for the Optimal Provision of Ancillary Services by a TPP

As opposed to the previous chapter, which focused on the dynamics of a nanogrid including a control centre in a real demonstrator, this section aims to present a method for the minimization of active power losses when providing reactive power by a TPP formed mainly by nanogrids and other DG in a LV network. Since the main point is the operation including optimization, this chapter centres on the steady state of the TPP, which in turn means that load flow calculation as well as optimization methodologies are required. This chapter is related to the third and fourth hypothesis of this scientific work.

4.1 Modelling and Simulation of Active and Reactive Power Flow and Node Voltages

In the following, load flow calculation and optimization methodologies are presented. Next, simulation results that combine the load calculations and optimization are shown.

4.1.1 Load Flow Calculation Methodology

Load flow calculations are performed in the operation and planning of power systems. In these stages, the following conditions are analyzed (Glover, Sarma, & Overbye, 2012):

- Supplying of the demand
- Bus voltage magnitudes
- Power limits of generators
- Loading of branches (transmission lines and transformers)

At the end of the calculations, the voltage magnitudes and the angles at each node are computed. Furthermore, the active and reactive power flow, losses as well as loading are calculated.

Formulating the power-flow problem is primordial for this chapter. This consists in determining the voltage magnitude and phase angle at each node (hereunder: bus) of the power system to be analyzed by assuming a balanced three-phase steady state condition. Importantly, four variables are always associated with the buses. These are: voltage magnitude, phase angle, active and reactive power. In addition, buses are classified as (Grainger & Stevenson, 1994):

- Slack bus: This is the reference bus whose angle serves as reference for the angles of all other buses.
- Load buses (P-Q buses): These are the buses at which the active and reactive powers are defined.
- Regulated buses (P-V buses): These are the generator buses. Here the active power and the voltage magnitude are specified; the voltage magnitude is kept constant.

After introducing the variables associated with the buses and the corresponding classification, the power flow equation is presented (Saadat, 1999). This equation is based on Figure 4-1, which is a typical bus of a power system. Here the transmission lines are presented by the per unit admittances.

$$I_i = y_{i0}V_i + y_{i1}(V_i - V_1) + y_{i2}(V_i - V_2) + \dots + y_{in}(V_i - V_n) \quad (4-1)$$

rearranging,

$$I_i = V_i \sum_{j=0}^n y_{ij} - \sum_{j=1}^n y_{ij} V_j \quad j \neq i \quad (4-2)$$

At the bus, the real and reactive power is given by

$$P_i + jQ_i = V_i I_i^* \quad (4-3)$$

also expressed as

$$I_i = \frac{P_i - jQ_i}{V_i^*} \quad (4-4)$$

Combining equations (4-2) and (4-4) we obtain

$$V_i \sum_{j=0}^n y_{ij} - \sum_{j=1}^n y_{ij} V_j = \frac{P_i - jQ_i}{V_i^*} \quad j \neq i \quad (4-5)$$

Equation (4-5) is the mathematical formulation of the power flow problem, which is an algebraic nonlinear equation. This equation can be solved by iterative methods, such as Gauss-Seidel as well as Newton-Raphson. The latter is more efficient and practical and it is less susceptible to divergence (Saadat, 1999). This method was selected in this scientific work. For this reason, the solution of the mathematical formulation of the power flow problem based on Newton-Raphson Method is also described in this section.

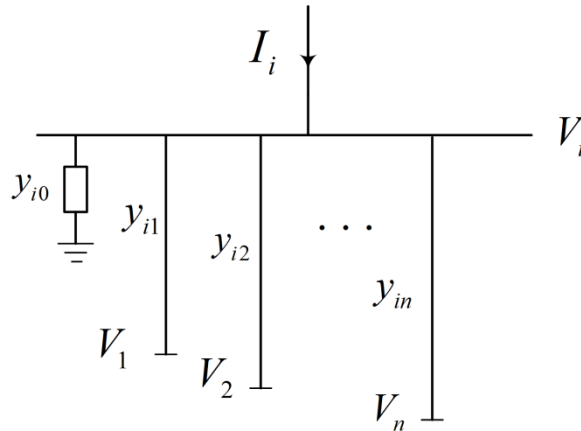


Figure 4-1. Typical bus in a power system (Saadat, 1999).

Newton-Raphson Method: For a better understanding of the method and for simplicity reasons, a one-dimensional equation is considered:

$$f(x) = c \quad (4-6)$$

Additionally, $x^{(0)}$ and $\Delta x^{(0)}$ are defined as the initial estimation of the solution and as the small deviation from the final solution, respectively:

$$f(x^{(0)} + \Delta x^{(0)}) = c \quad (4-7)$$

Applying the Taylor' series to the left side about $x^{(0)}$

$$f(x^{(0)}) + \left(\frac{df}{dx}\right)^{(0)} \Delta x^{(0)} + \frac{1}{2!} \left(\frac{d^2f}{dx^2}\right)^{(0)} (\Delta x^{(0)})^2 + \dots = c \quad (4-8)$$

Assuming that the small deviation from the final solution is very small, this and thus also the higher order terms can be neglected:

$$f(x^{(0)}) + \left(\frac{df}{dx}\right)^{(0)} \Delta x^{(0)} = c \quad (4-9)$$

rearranging,

$$c - f(x^{(0)}) = \left(\frac{df}{dx}\right)^{(0)} \Delta x^{(0)} \quad (4-10)$$

$$\Delta c^{(0)} = \left(\frac{df}{dx}\right)^{(0)} \Delta x^{(0)}$$

$$c = \Delta c^{(0)} + f(x^{(0)})$$

When adding the small deviation and the initial estimation, the second approximation is given by

$$x^{(0)} + \Delta x^{(0)} = x^{(1)} \quad (4-11)$$

$$x^{(0)} + \frac{\Delta c^{(0)}}{\left(\frac{df}{dx}\right)^{(0)}} = x^{(1)} \quad (4-12)$$

Generally, the previous equations can be represented as

$$\Delta c^{(k)} = c + f(x^{(k)}) \quad (4-13)$$

$$\Delta x^{(k)} = \frac{\Delta c^{(k)}}{\left(\frac{df}{dx}\right)^{(k)}} \quad (4-14)$$

$$x^{(k)} + \Delta x^{(k)} = x^{(k+1)} \quad (4-15)$$

$$\Delta c^{(k)} = j^{(k)} \Delta x^{(k)} \quad (4-16)$$

$$j^{(k)} = \left(\frac{df}{dx}\right)^{(k)} \quad (4-17)$$

The method described above is valid also for multivariable functions. In this case, the equation (4-17) is called the Jacobian matrix.

Solution of the power flow problem by applying the Newton-Raphson Method:
When applying this method, the polar form is applied. Figure 4-1 is again taken into account. For each bus (in terms of the admittance matrix), we have

$$I_i = \sum_{j=1}^n Y_{ij} V_j \quad (4-18)$$

In polar form, equation (4-18) can be written as

$$I_i = \sum_{j=1}^n |Y_{ij}| |V_j| e^{\theta_{ij} + \delta_j} \quad (4-19)$$

The complex power at bus i can also be expressed as

$$P_i - jQ_i = V_i^* I_i \quad (4-20)$$

Combining the equations (4-19) and (4-20), we obtain

$$P_i - jQ_i = |V_i|e^{-\delta_i} \sum_{j=1}^n |Y_{ij}| |V_j| e^{\theta_{ij} + \delta_j} \quad (4-21)$$

Equation (4-21) can be separated into real and imaginary parts

$$P_i = \sum_{j=1}^n |V_i| |V_j| |Y_{ij}| \cos(\theta_{ij} - \delta_i + \delta_j) \quad (4-22)$$

$$Q_i = - \sum_{j=1}^n |V_i| |V_j| |Y_{ij}| \sin(\theta_{ij} - \delta_i + \delta_j)$$

which can be seen as multivariable nonlinear functions with the voltage magnitude and phase angle as the independent variables

$$P_i = f(|V_i|, |V_j|, \delta_i, \delta_j) = c_i \quad (4-23)$$

$$Q_i = f(|V_i|, |V_j|, \delta_i, \delta_j) = d_i \quad (4-24)$$

Applying the Taylor's series about the initial estimation of the solution, we have

$$\begin{bmatrix} \Delta P_2^{(k)} \\ \vdots \\ \Delta P_n^{(k)} \\ \Delta Q_2^{(k)} \\ \vdots \\ \Delta Q_n^{(k)} \end{bmatrix} = \begin{bmatrix} \left[\frac{\partial P_2^{(k)}}{\partial \delta_2} \right] & \dots & \left[\frac{\partial P_2^{(k)}}{\partial \delta_n} \right] \\ \vdots & \ddots & \vdots \\ \left[\frac{\partial P_n^{(k)}}{\partial \delta_2} \right] & \dots & \left[\frac{\partial P_n^{(k)}}{\partial \delta_n} \right] \\ \left[\frac{\partial Q_2^{(k)}}{\partial \delta_2} \right] & \dots & \left[\frac{\partial Q_2^{(k)}}{\partial \delta_n} \right] \\ \vdots & \ddots & \vdots \\ \left[\frac{\partial Q_n^{(k)}}{\partial \delta_2} \right] & \dots & \left[\frac{\partial Q_n^{(k)}}{\partial \delta_n} \right] \end{bmatrix} \begin{bmatrix} \left[\frac{\partial P_2^{(k)}}{\partial |V_2|} \right] & \dots & \left[\frac{\partial P_2^{(k)}}{\partial |V_n|} \right] \\ \vdots & \ddots & \vdots \\ \left[\frac{\partial P_n^{(k)}}{\partial |V_2|} \right] & \dots & \left[\frac{\partial P_n^{(k)}}{\partial |V_n|} \right] \\ \left[\frac{\partial Q_2^{(k)}}{\partial |V_2|} \right] & \dots & \left[\frac{\partial Q_2^{(k)}}{\partial |V_n|} \right] \\ \vdots & \ddots & \vdots \\ \left[\frac{\partial Q_n^{(k)}}{\partial |V_2|} \right] & \dots & \left[\frac{\partial Q_n^{(k)}}{\partial |V_n|} \right] \end{bmatrix} \begin{bmatrix} \Delta \delta_2^{(k)} \\ \vdots \\ \Delta P \delta_n^{(k)} \\ \Delta |V_2^{(k)}| \\ \vdots \\ \Delta |V_n^{(k)}| \end{bmatrix} \quad (4-25)$$

Bus 1 is the slack in equation (4-25). Furthermore, the matrix with the partial derivatives in (4-25) is the so-called Jacobian matrix.

The algorithm works as follows:

1. Setting of initial values for the P-Q buses and P-V buses:
 - a. As stated previously, the active and the reactive power are defined in P-Q buses. In this case, these values are defined and named as schedule values (P_i^{sch} and Q_i^{sch}). The initial values of the voltage magnitudes and phase angles are set equal to the slack bus. This means $|V_i^{(0)}| = 1.0$ and $\delta_i^{(0)} = 0.0$.
 - b. In P-V buses, the voltage and active power are defined (V_i and P_i^{sch}). The phase angles are set equal to the slack bus angle ($\delta_i^{(0)} = 0$).
2. The next approximation and the deviation from the initial solution are calculated:
 - a. For P-Q buses, in the next solution, the active ($P_i^{(k)}$) and reactive ($Q_i^{(k)}$) power are calculated using (4-22). The deviations are given by
$$\Delta P_i^{(k)} = P_i^{sch} - P_i^{(k)} \quad (4-26)$$

$$\Delta Q_i^{(k)} = Q_i^{sch} - Q_i^{(k)} \quad (4-27)$$
 - b. For P-V buses, the next solution for the active power $P_i^{(k)}$ is computed using (4-22). In the case of the deviation of the active power, equation (4-23) is applied.

3. The elements of the Jacobian matrix are computed.
4. The next solutions for voltages and phase angles are calculated by applying

$$\delta_i^{(k+1)} = \delta_i^k - \Delta\delta_i^{(k)} \quad (4-28)$$

$$|V_i^{(k+1)}| = |V_i^{(k)}| - \Delta|V_i^{(0)}| \quad (4-29)$$

5. The method ends when the deviations are less than the specified limits.

The Newton-Raphson method is very robust, but one disadvantage is that the Jacobian matrix should be solved in each iteration. It could also happen that the transmission or distribution system operator requires a fast solution of the power flow problem, for example, for contingency analysis. For this purpose, there are techniques that speed up the power flow calculations. These are:

- Decouple power flow: In (Saadat, 1999) and (Crow M. , 2010), it is mentioned that the Jacobian matrix can be simplified if it is assumed that the power system has transmission lines whose X/R ratios are very high. This means that changes in the active power are less sensitive to changes in voltages, but more to changes in the phase angle. In the same way, reactive power is less sensitive to changes in the phase angle, but more to changes in the voltage magnitude. As a result, the partial derivatives $\frac{\partial P}{\partial V}$ and $\frac{\partial Q}{\partial \delta}$ of the Jacobian matrix can be set to zero. Under those assumptions, the computation time of the load flow can be significantly reduced, but the Jacobian matrix should still be recalculated in each iteration.
- Fast decoupled power flow: The computation time in the decouple power flow method can be even more improved if the Jacobian matrix is constant (Crow M. , 2010), (Grainger & Stevenson, 1994). This can be done assuming the following:
 - The angular differences between the buses if the system is usually so small. Keeping this in mind, the cosine function of the angular differences is equal to 1 and the sine function is approximately equal to the difference of the angles.
 - The ration X/R of the lines is very high.
 - All voltage magnitudes are equal to 1.0 p.u.

With this assumption, the partial derivatives $\frac{\partial Q}{\partial V}$ and $\frac{\partial P}{\partial \delta}$ of the Jacobian matrix are constant.

- DC power flow: This approach is applicable to power systems that operate in high voltage levels, since in these systems there is a strong coupling between the active power and the voltage angle. On the other hand, this method cannot be applied to power systems in the low voltage level, since here the active power flow depends on the voltage drops. In the DC power flow method, it is assumed (Milano, 2010), (Seifi & Sepasian, 2011) that
 - Reactive power flow is discarded
 - The ration X/R is very high
 - All node voltages are the same and equal to 1.0 p.u.

When taking into account these assumptions, the power flow becomes completely linear. It is called DC due to the linearity of the equations, which are similar to the DC resistive circuits.

4.1.2 Optimization Methodologies

Optimization means finding optimum solutions for a given problem. Any optimization needs three steps, which are the problem description, modelling, and application of an algorithm for finding the optimum solution. The latter can be categorized in local and global optima.

When describing the problem, the variables, the constraints as well as the object function are defined. Modelling means writing properly down the mathematical equations whose representation is given by (4-30).

$$\begin{cases} \text{Minimize or Maximize } O(x) \\ \text{Subject to } c(x) \leq b \end{cases} \quad (4-30)$$

where in this case, x is the independent variable, $O(x)$ is the object function and $c(x)$ is the constraint. In the case of the algorithms, these are classified basically as deterministic and stochastic, as seen in Figure 4-3 (Kreutziger, Schegner, Wende-von-Berg, Braun, & Bornhorst, 2018) and (Hanif Halim & Ismail, 2019).

The deterministic algorithms are based on mathematical equations and are sometimes slow when the number of equations is high and complex. Even when the objective function is complex, the constraints are too complicated or the problem is too large, an optimum solution is impossible to be found (Graham, Grötschel, & Lovász, 1995). These kinds of algorithms provide the same output by a given input. Furthermore, they can be classified as linear programming and gradient based. In linear programming, the objective function as well as the constraints are linear function of x . In addition to this, the gradient-based algorithms solve the optimization by searching in the direction of the gradient of the objective function at a given point (Chong & Zak, 2013).

The stochastic algorithms are based on combinatorial problem solution and are applied when optimum solutions are difficult to find through deterministic algorithms (Graham, Grötschel, & Lovász, 1995). Stochastic algorithms are usually faster than the deterministic approach and behave randomly. The stochastic algorithms are mainly classified as heuristic and meta-heuristic. The heuristic algorithms find solutions by “trial and error”, which does not guarantee that the global optimum is achieved, but the results are promising (Yang X.-S., 2010). On the other hand, meta-heuristic algorithms are an advanced development of the heuristic algorithms based on the combination of local search and randomness (de Smith, Longley, & Goodchild, 2007).

The solutions given by an algorithm are classified in local and global optima, which in turn could be maxima and minima. Figure 4-2 shows an objective function (one-dimensional) $O(x)$ as well as the local and global maximum.

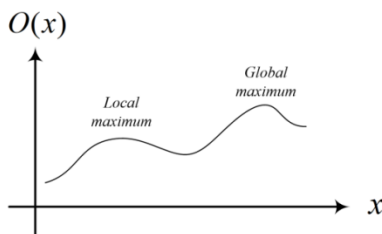


Figure 4-2. Objective function.

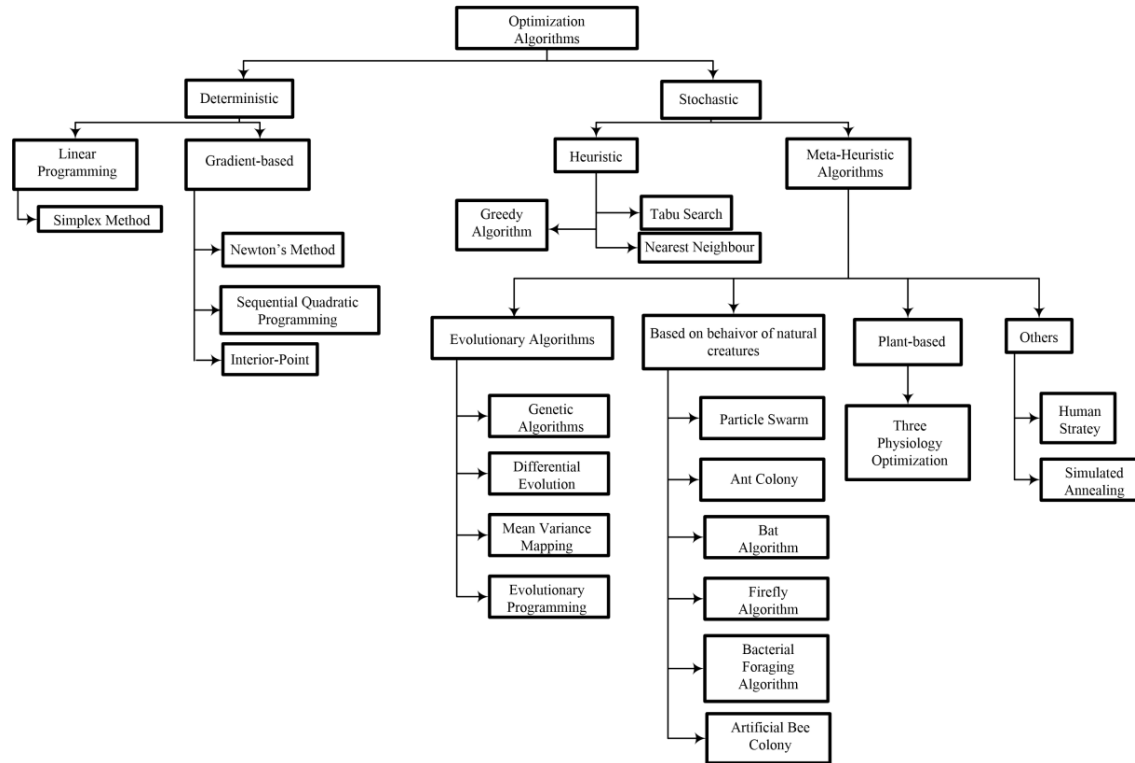


Figure 4-3. Classification of optimization algorithms.

In order to understand the fundamentals and the complexity of deterministic optimization in power systems, this section also presents the mathematical description of the economic dispatch and the optimal power flow. The description of these two topics in this section reflects theories from the book “Power Generation, Operation, and Control” (Wood, Wollenberg, & Sheblé, 2014).

First, it is necessary to understand the economic dispatch. Imagine a power system with N_{gen} generation units connected to a bus bar. The N_{gen} generation units supply power to an electrical load P_{load} also connected to this bus bar. Additionally, each generation unit outputs electrical power represented by P_i . Furthermore, cost rates F_i (e.g., fuel consumption) are associated with each generation unit and are the function of P_i . The total cost rate of the system (F_T) is the sum of the cost of each generation unit. Moreover, the sum of the output power of each unit must be equal to the load consumption, neglecting losses. The optimization problem can be easily stated. It means that to minimize F_t (objective function) subject to the constraint, the sum of the output power of each unit must be equal to the load consumption and each generator must be within the minimum and maximum limits:

$$F_T = F_1 + F_2 + \dots + F_{N_{gen}} \quad (4-31)$$

$$F_T = \sum_{i=1}^{N_{gen}} F_i(P_i) \quad (4-32)$$

$$\emptyset = 0 = P_{load} - \sum_{i=1}^{N_{gen}} P_i \quad (4-33)$$

$$P_i^{min} \leq P_i \leq P_i^{max}, \text{ for } i = 1 \dots N_{gen} \quad (4-34)$$

The economic operating point for the problem mentioned above can be solved by applying the Lagrange function for finding the optimum solution. This means that the operating points of each generation unit P_i can be found such that the total cost F_T is minimized.

As mentioned earlier, the economic dispatch neglects losses. Otherwise stated, the economic dispatch omits the effect that the dispatch of the generation units has on the network. Hence, the loading of the lines as well as the bus voltages are ignored. The optimal power flow combines the economic dispatch with the power flow, so that at the end, both are solved. The objective function is slightly modified in the optimal power flow, since P_i is related to the bus i :

$$\min \sum_{i=1}^{N_{bus}} F_i(P_i) \quad (4-35)$$

Each generator must be within the minimum and maximum limits (active and reactive power):

$$P_i^{min} \leq P_i \leq P_i^{max}, \text{ for } i = 1 \dots N_{bus} \quad (4-36)$$

$$Q_i^{min} \leq Q_i \leq Q_i^{max}, \text{ for } i = 1 \dots N_{bus} \quad (4-37)$$

Taking into account the network and recalling equation (4-18), the net power flow at each bus is

$$P_{net_i} + jQ_{net_i} = V_i I_i^* = V_i \left(\sum_{j=1}^{N_{bus}} Y_{ij} V_j \right)^* \quad (4-38)$$

Considering the network as the generation minus the load and then separate into the active and reactive power, the two new constraints are given by

$$P_i - P_{load_i} - Re \left\{ V_i \left(\sum_{j=1}^{N_{bus}} Y_{ij} V_j \right)^* \right\} = 0 \quad (4-39)$$

$$Q_i - Q_{load_i} - Img \left\{ V_i \left(\sum_{j=1}^{N_{bus}} Y_{ij} V_j \right)^* \right\} = 0 \quad (4-40)$$

Furthermore, each bus in the network must be within the limits. The new constraint is

$$V_i^{min} \leq V_i \leq V_i^{max}, \text{ for } i = 1 \dots N_{gen} \quad (4-41)$$

Similarly, for each branch (transmission line, cable or transformer), the current flow must be less than or equal to the branch current limit:

$$I_{ij} \leq I_{ij}^{max} \quad (4-42)$$

The optimal power flow, in other words, the combination of the economic dispatch and the power flow, is a complex task from the deterministic point of view, since the network equations are not linear and the number of variables is relatively high.

The solutions of the combinatorial problem as well as the optimization in this chapter are based on the greedy algorithm, which is a heuristic method. It takes the best local solution, where “best”, as mentioned in (Faigle, 1993), is defined by an objective function, which is evaluated locally. Furthermore, the greedy algorithm, as stated in (Vimali, Srivastava, & Gupta, 2017) and (Azis, Mallongi, Lantara, & Salim, 2018), constructs a solution based on local optima and here it is assumed that at the end, the optimal solution will be achieved (Kostenko, 2017). The solutions reached by greedy algorithms are reasonably good, may not be optimal, but close to it (Kodaganallur & Sen, 2010). Contrary to other approaches, the greedy algorithm was selected due to the easiness of its implementation and the high computational speed (Simmons, Hoeppeke, & Sutherland, 2018), (Mari, 2020).

A very simple example of the functionality of the greedy algorithm is shown in Figure 4-4, which represents the travel salesman’s problem (TSP) (Johnson & McGeoch, 1997). The TSP is a classical optimization problem in which a salesperson needs to travel to a given number of cities in such a way that the salesman achieves the minimum distance while traveling between the cities. For this problem, the greedy algorithm immediately takes the shortest distance (orange lines). Next, the global solution is updated every step until all the cities are visited. In this example, the global solution equals the addition of the following distances 3 km, 1 km, 1 km, and 4 km. This example shows that the greedy algorithm seems the most natural or intuitive approach for solving optimization problems (Haouari & Chaouachi, 2002).

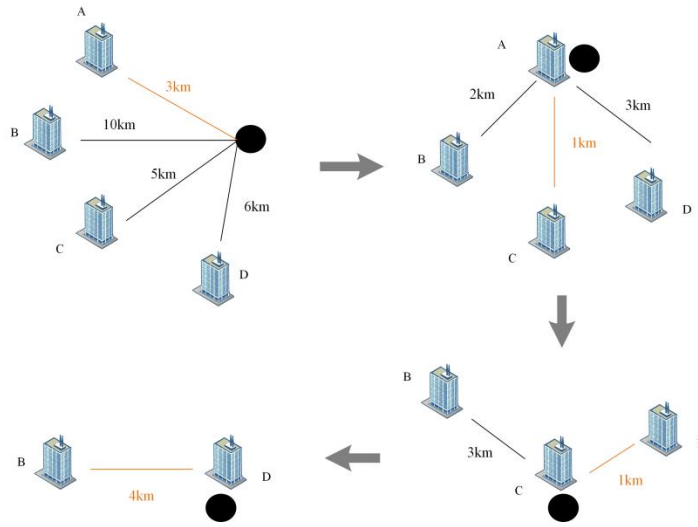


Figure 4-4. Traveling salesman.

4.1.3 Simulation Results with Respect to Distribution Grid Restrictions

4.1.3.1 Study Network

Previously, the fundamentals of optimization in power systems were presented. This section presents the simulation results of an optimization problem focused on reactive power provision as well as on minimization of active power losses by a topological power plant (TPP). In order to solve the optimization problem, a stochastic algorithm is applied.

Before giving more details about the optimization problem, the study network where the TPP is operated is specified. The network is in the LV level of a rural area in the south of Germany, as shown in Figure 4-5. This network has the following characteristics:

- The network has a radial structure and is fed by one distribution transformer with a rated apparent power of 250 kVA. It has 81 nodes and 200 branches (cables and distribution transformer).
- The network consists of 24 nanogrids, represented by family houses. Additionally, there are two farms with two photovoltaic (PV) systems each.

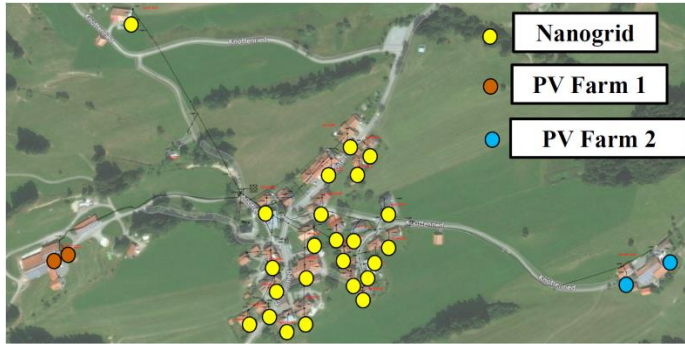


Figure 4-5. Study network.

It is assumed that all 24 nanogrids are equipped by one HBESS, one PV, and a load. Figure 4-6 illustrates information regarding the nanogrids used for the network calculations. There are three types of them in the study network. The type means the number of personas living in each house. Type A is a household of five persons. Types B and C are households of four and three persons, respectively. The load of each household is represented by the behaviour of a standard load profile H0 (bdew, 2017). Figure 4-6 also mentions the number of nanogrids according to the type, the yearly energy consumption of each type of the nanogrid, the rated apparent power and the capacity of the HBESS, the peak power of the PV system, and the corresponding apparent rated power of the PV inverter.

Nanogrids						
Type	Amount	Energy Consumption (kWh/annum)	HBESS (kVA)	HBESS (kWh)	PV (kWp)	PV inverter (kVA)
A	15	6900	32	32	6	7
B	6	5700	26	26	5	6
C	3	4600	21	21	4	5

Figure 4-6. Types of nanogrids.

Furthermore, in each of the PV farms, two PV systems are installed, which follow the German Code of Practice VDE-AR-N 4105 for generating plants connected in the LV network (VDE, VDE-AR-N 4105, 2011). This grid code states that the PV inverter varies its power factor as a function of the active power supply into the network (see Figure 4-7). Figure 4-8 depicts a summary of the PV system installed at the farms. Moreover, these farms follow a standard load profile L2 (for agriculture) (bdew, 2017) and it is assumed that they have a yearly energy consumption of 11.5 MWh.

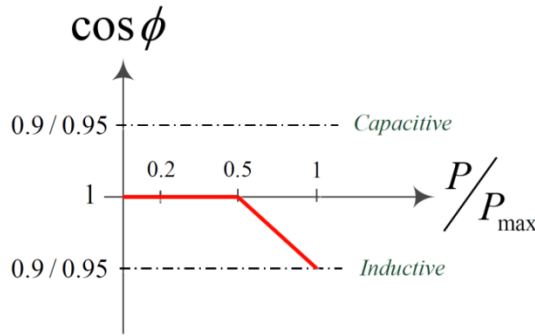


Figure 4-7. German code of practice VDE-AR-N 4105 (VDE, VDE-AR-N 4105, 2011).

Farm	Farm PV Systems	
	PV system	Peak Power (kWp)
Farm 1	PV System 1	89.6
	PV System 2	21.7
Farm 2	PV System 3	5.7
	PV System 4	29.5

Figure 4-8. PV systems installed at the farms.

4.1.3.2 Superordinate Controller

The reactive power provision and the active power losses are analyzed with a time step of 15 minutes for a time span of 24 hours. A power profile of the load (H0 for the nanogrids and L2 for the PV farms) and the PV generation in a summer day for each generator is used in this case. This information allows determining the reactive power capability for the next 15 min considering the self-consumption of each nanogrid. Once the capability is computed, the optimization process subject to constraints is performed. This process is based on a co-simulation between the programming language Python 3.7.6 and PSS® Sincal, as seen in Figure 4-9. The co-simulation provides the corresponding set points to each nanogrid so that the scheduled reactive power profile of the TPP is achieved. The profiles of load and generation, the calculation of the reactive power capability as well as the co-simulation can be seen as part of superordinate controller.

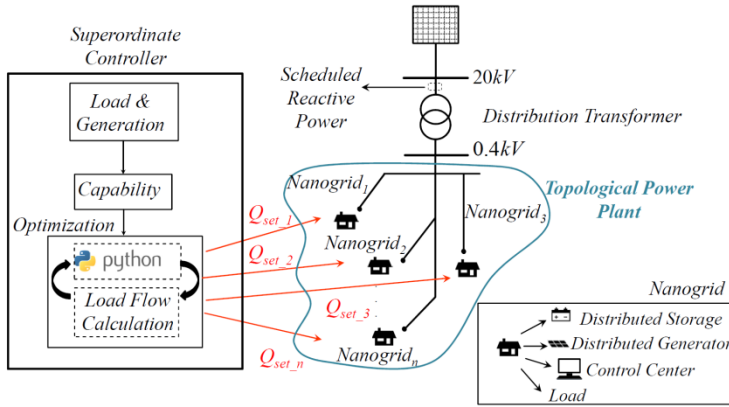


Figure 4-9. Overview of the optimization process for provision of reactive power by a TPP.

Importantly, the reactive power capability of each generator is computed before the optimization is initialized. Firstly, the functionality (identical to all the nanogrids) of the inverters of the HBESS and PV is mentioned and then the reactive power generation of each nanogrid is described.

Each PV inverter allows a two-quadrant operation with a power factor between 0.4 capacitive and 0.4 inductive. The functionality of PV inverters is the same as described in section 3.1.1.1. On the other hand, each HBESS allows a four-quadrant operation. The maximum reactive power a HBESS can provide can be calculated according to (4-43), where $S_{HBESS_{rated}}$ and $P_{HBESS_{act}}$ are the rated apparent power and the actual active power of the battery, respectively:

$$Q_{HBESS_{max}} = \sqrt{S_{HBESS_{rated}}^2 - P_{HBESS_{act}}^2} \quad (4-43)$$

The self-consumption is a priority in each nanogrid. In other words, supplying the local load of each nanogrid is of the highest preference. Due to this reason, the combination of the PV system and the HBESS is used to supply active power to the load. The permissible state of charge (SOC) limits of each HBESS are set according to (Helguero, 2019), considering the optimum lifetime and the availability of the storage system. First, if the surplus defined in (4-44) is positive, the HBESS is charged as long as the SOC is lower than 80%. On the other hand, if the surplus is negative and the SOC is between 20% and 80%, the HBESS is discharged.

$$P_{surplus} = P_{PV} - P_{load} \quad (4-44)$$

After calculating the active power HBESS produces or consumes, the maximum reactive power that the elements of the nanogrid can provide is calculated every 15 minutes. The expression given by (4-44) is used for the HBESS; one PV inverter provides reactive power only if the HBESS is fully charged and the surplus is positive.

To clarify the operation of a nanogrid, Figure 4-10 shows an example of the active power production by the PV and the active power consumed by the load for a nanogrid type A. Furthermore, it can be seen that the reduction of the active power of the PV system occurs between 09:45 and 17:15 when the SOC is 80%; the surplus is positive and the active power of the PV system is greater than the break point (see section 3.1.1.1). In this period, the maximum reactive power of the PV system is given by

equation (3-2). Between 17:15 and 18:15, the SOC is 80%, the surplus is positive, but the PV generation is lower than the break point. In this period, the maximum reactive power that the PV system can provide is computed by applying (3-1). The SOC of the HBESS for the nanogrid type A is illustrated in Figure 4-10a). When a positive surplus occurs (e.g., at 07:30), the HBESS is charged. On the other hand, during the afternoon, the HBESS is used to supply the load, when the PV generation is not enough to cover the load (from 18:30 until 23:00). Since the charging and discharging of the HBESS is limited by the SOC, during the early morning, the load is supplied by the external grid (from 00:00 until 07:30).

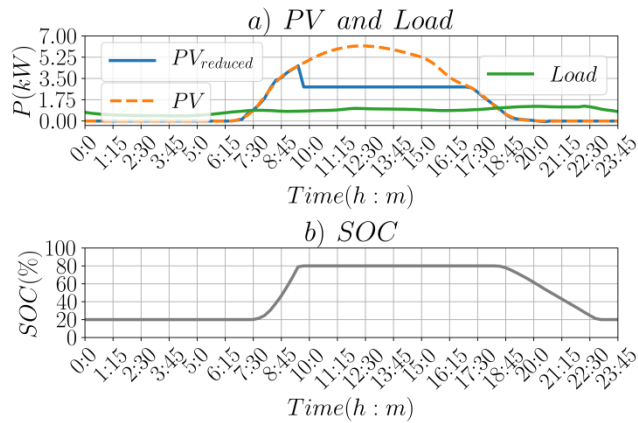


Figure 4-10. Nanogrid type A: a) PV production and load; b) SOC.

The active and reactive power at the PCC of the nanogrid type A are illustrated in Figure 4-11. Three types of cases are shown. The first one is the import of the active power from the external grid, for example, from 0:00 until 07:30. In the second case, there is no exchange of the active power with the external grid (from 07:30 until 09:45, since the load is supplied by the PV system). Finally, the third case is an export of the active power to the grid (from 09:45 until 18:30, since the battery is charged, and the PV system supplies the load). Figure 4-11 also depicts the maximum absolute value of the reactive power that the nanogrid can provide at every time step. From 00:00 until 09:45, the reactive power provision can only be performed by the HBESS. After this period and until 18:15, the reactive power is provided by the PV system and the HBESS. Lastly, only the HBESS is able to generate/consume reactive power.

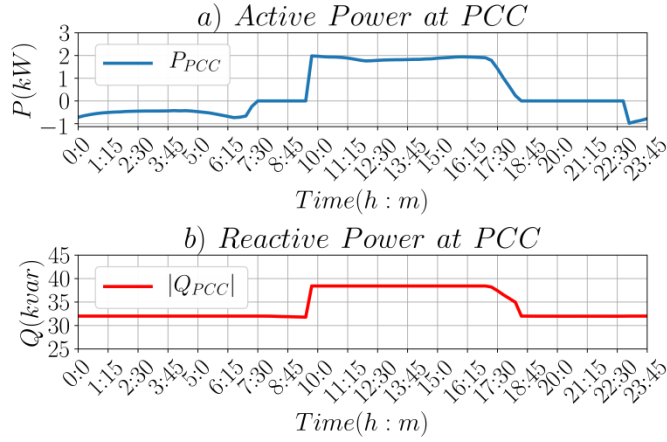


Figure 4-11. Nanogrid type A: a) Active power at the PCC; b) Maximum absolute value of reactive power at the PCC.

4.1.3.3 Optimization

To provide a better understanding of the optimization problem, we divide it into two use cases:

- Use Case I: This is just a combinatorial problem whose objective is to accomplish a reactive power set point at the PCC of the TPP, by varying the reactive power of the nanogrids and by considering the loading of the branches. In other words, the sum of the reactive power of the elements of the TPP is satisfied by (4-45), where $\sum_{x=1}^m Q_{Nanogrid_x}^i$, $\sum_{y=1}^f Q_{Farm_y}^i$, Q_{losses}^i and $Q_{set,TPP}^i$ are the total reactive power of the m nanogrids, the total reactive power of the f PV farms, the reactive power losses and the reactive power set point at the PCC at the time step i . It is necessary to highlight that $\sum_{y=1}^f Q_{Farm_y}^i$ is kept fixed at each time step i .

$$Q_{set,TPP}^i = \sum_{x=1}^m Q_{Nanogrid_x}^i + \sum_{y=1}^f Q_{Farm_y}^i + Q_{losses}^i \quad (4-45)$$

- Use Case II: The focus is on the minimization of the active power losses within the TPP, while accomplishing a reactive power set point at the PCC of the TPP as well as considering the network constraints. The mathematical equations representing this use case are given according to (4-46), where P_{losses} represents the active power losses within the TPP, I_b means the loading of the branch b , I_{max} is the maximum loading (100%), V_d is the voltage of the bus bar d , v_{min} and v_{max} are the permissible voltage band (+/-10% of nominal voltage).

$$\left\{ \begin{array}{l} \text{Minimize: } P_{losses} \\ \text{Subject to: } Q_{set,TPP}^i = \sum_{x=1}^m Q_{Nanogrid_x}^i + \sum_{y=1}^f Q_{Farm_y}^i + Q_{losses}^i \\ \text{Subject to: } I_b \leq I_{max}; v_{min} \leq V_d \leq v_{max} \end{array} \right. \quad (4-46)$$

The basic idea of the algorithm is presented in Figure 4-12. It begins with an initial solution, which is achieved by setting the reactive power of all nanogrids to zero (Solution₀). Next, possible solutions or combinations are generated (e.g., Co_{1₀}, Co_{1₁}, ..., Co_{1_{k×m}}); based on the constraints, one of them is selected (e.g. Co_{1₁}). This selection means that a local optimum was found (orange circles). The algorithm ends when no more possibilities are available.

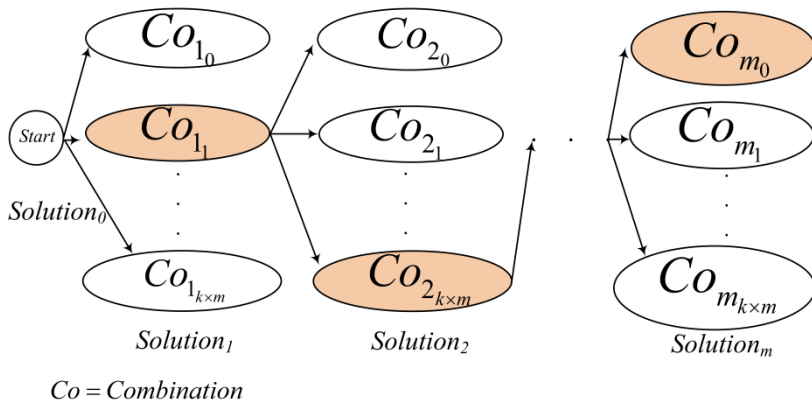


Figure 4-12. General idea of the greedy algorithm.

A detailed description of the implemented algorithm is shown in Figure 4-13. For each time step (15 min), steps 3 to 8 are repeated. The algorithm works as follows:

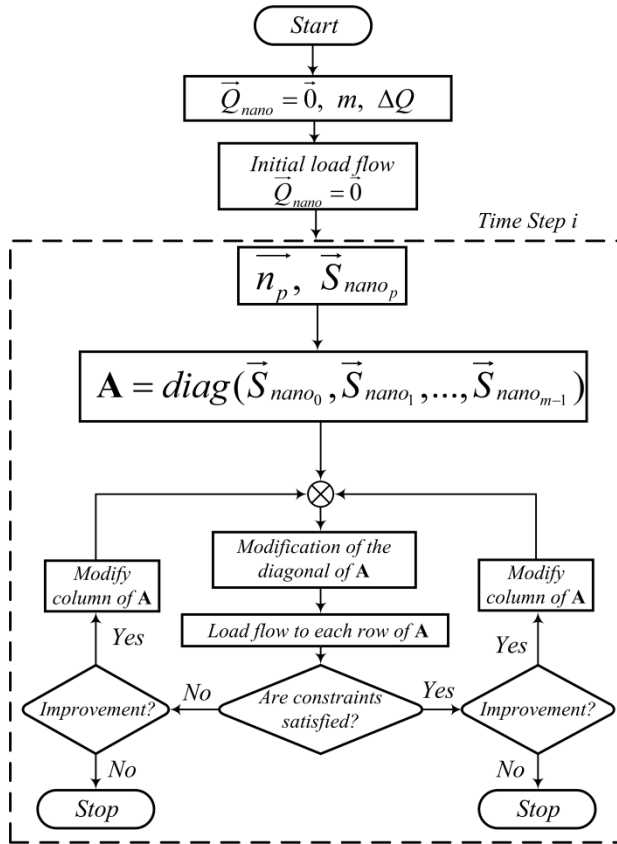


Figure 4-13. Flow chart of the applied algorithm.

- Step 1: The reactive power step ΔQ (variation of the reactive power for each nanogrid) is defined by the user. Furthermore, the Python script extracts the amount of nanogrids m from the data base of PSS® SINCAL.
- Step 2: An initial load flow is performed by setting the reactive power of all nanogrids \bar{Q}_{nano} to zero.
- Step 3: Intervals of reactive power are created for a nanogrid p (vector \vec{S}_{nano_p} in Figure 4-13). These intervals (generated in the capability block of Figure 4-9) define how much reactive power each nanogrid is capable of providing at the time step i . The number of elements of the interval for a nanogrid p is saved in the vector \vec{n}_p .
- Step 4: The matrix \mathbf{A} is created, and its main diagonal is filled with each vector \vec{S}_{nano_p} . The dimension of \mathbf{A} is $k \times m$. The variable k is defined as $k = \sum_{p=0}^{m-1} n_p$, where n_p is the number of elements of the interval of reactive power for the nanogrid p .
- Step 5: The matrix \mathbf{A} is modified by adding the factor $n_p \times \Delta Q$ to each element of the main diagonal. The green area of Figure 4-14 illustrates an example of this step.

- Step 6: The elements of each row of \mathbf{A} (gray arrows of Figure 4-14) are taken and used for load flows calculations.
- Step 7: The constraints are verified for every load flow of step 6, for both use cases, with respect to the loading of cables and distribution transformer, permissible voltage band, and the reactive power at the PCC of the TPP should not differ more than 5% of the set point. For the second use case, the active power losses should be equal or less than the active power losses of Use Case I.
- Step 8: The previous step will generate a list of solutions that satisfy or do not satisfy the constraints. For both use cases, the program selects the best solution and modifies one column of \mathbf{A} . The orange area of Figure 4-14 depicts an example of this modification. In this example, the first row of \mathbf{A}_1 has the best solution. Thus, the first column of \mathbf{A}_2 is modified. Finally, if there is no improvement, the first iteration is ready.

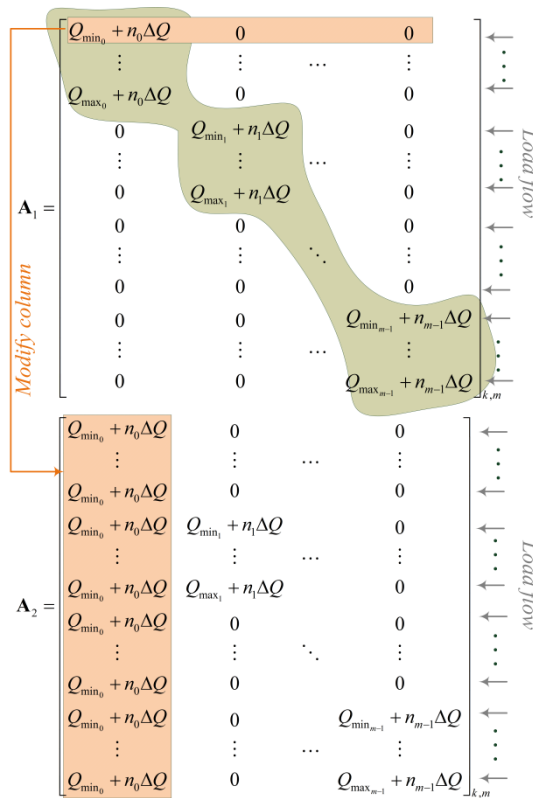


Figure 4-14. Example of the modification of the main diagonal and a column of the matrix \mathbf{A} .

Next, the results of the co-simulation between Python and PSS® SINCAL for the two proposed use cases are presented. Furthermore, the algorithm was run in a Windows 7 Pro 64-bit with an Intel Core i5-2400 CPU @3.10GHz processor and 4 GB of RAM.

Use Case I: The reactive power profile used for this use case and the results of the optimization are presented in Figure 4-15. The sign convention is done from the point of view of the distribution system operator (DSO). This means that it is done according to the consumer perspective:

- $Q > 0$: inductive behaviour of the TPP
- $Q < 0$: capacitive behaviour of the TPP

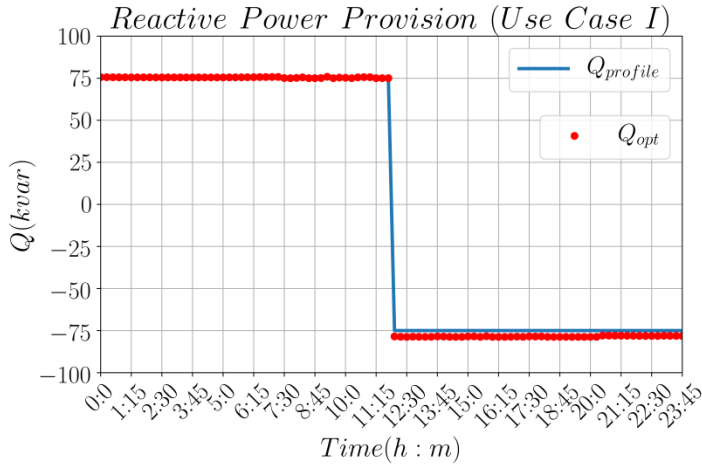


Figure 4-15. Reactive power provision at the PCC of the TPP.

An inductive behaviour of the TPP is required from 00:00 until 12:00 and a capacitive behaviour for the residual time. Figure 4-16a) and b) show the relative error for the inductive and capacitive case, respectively. For both cases, the provided reactive power at the MV side of the distribution transformer is within 5% tolerance.

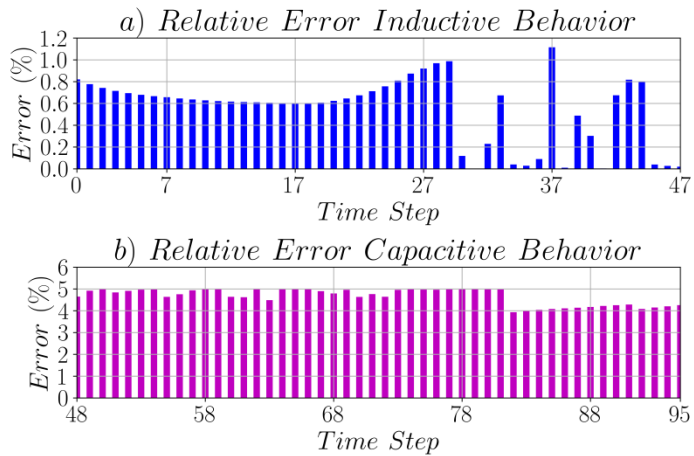


Figure 4-16. Relative error for the reactive power provision: a) For inductive behaviour (positive set point); b) For capacitive behaviour (negative set point).

An example of the node voltages and the loading of the branches (cables and distribution transformer) is depicted in Figure 4-17a) and b), respectively. In this case, iteration 40 (inductive behaviour of the TPP) and iteration 85 (capacitive behaviour of the TPP) are presented. The node voltages are within the permitted voltage band of +/-10% of the nominal value. On the other hand, the load of the branches is less than 100%.

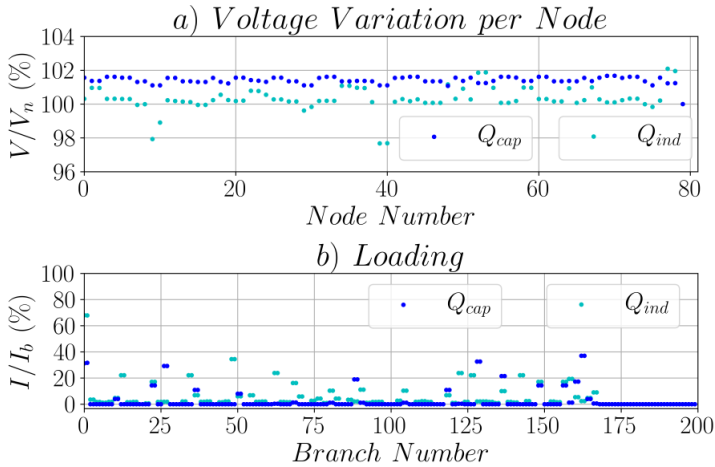


Figure 4-17. Network constraints for iterations 40 and 85: a) Node voltages; b) Loading of the branches.

Use Case II: This use case focuses on the achievement of a reactive power profile (same as the first use case) at the MV side of the transformer while taking into account the minimization of the active power losses within the TPP. The sign convention for the reactive power provision is the same as that of the previous use case. Figure 4-18 shows that the reactive power provision at the MV side follows the required profile.

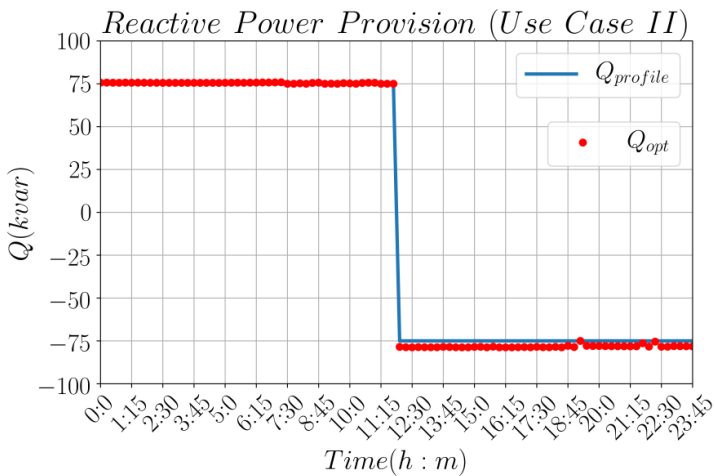


Figure 4-18. Reactive power provision at the PCC of the TPP by taking into account the active power losses.

The active power losses of the study network for both use cases and the percentage decrease are depicted in Figure 4-19a) and b), respectively. This is analyzed in three intervals of time:

- Interval I: This is from 00:00 until 09:45. Here the maximum active power losses reduction achieved is 61%. At dawn, there is no PV generation and almost no consumption from the nanogrids, which means that the network is idle. The reactive power exchange with the grid is compensated basically by the HBESS.
- Interval II: This occurs from 09:45 until 17:30. The reduction of active power losses is 0%. The reactive power capacity of the nanogrids is strongly reduced since the self-consumption is a priority. Thus, the nanogrid cannot support the reduction of active power losses.
- Interval III: It takes place from 17:30 until end of the day. The active power losses can be reduced by up to 35%. During this interval, all HBESSs are discharging and supplying the loads of the nanogrids. Keeping this in mind, there is no exchange of the active power between the nanogrids and the external grid. For this reason, the percentage decrease of interval II is lower than interval I.

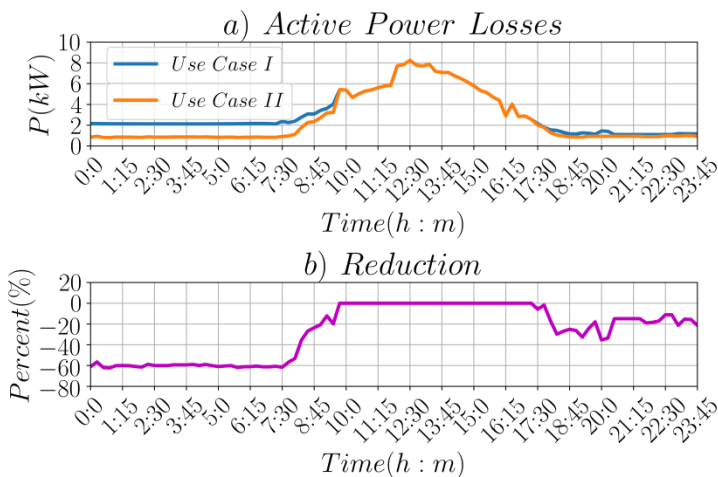


Figure 4-19. Comparison of active power losses: a) Active power losses for use case I and II; b) Decrease in percentage.

4.2 Cost-Benefit Analysis of the Provision of Ancillary Services by Topological Power Plants

The cost-benefit of the provision of ancillary services by a TPP cannot be currently evaluated since the climate change and its consequences are not comparable with the cost-benefits of a TPP.

A very good example of the impact of the climate change occurs in Africa. According to (Clarke, 2016), the continent is suffering from drought and floods. Besides, the economic cost of climate change will be around USD 45-50 billion a year by 2040.

Moreover, according to the same study, this has also political consequences with many conflicts within the continent such as Nigeria or Somalia.

In Europe, the climate change has also its economic impact. According to the official website of the European Union (Eurostat, 2022), heat waves, floods and storms have caused over €145 billion economic losses over the past decade. Figure 4-20 shows the climate-related economic losses by type of event. The highest loss occurred in 2017 (around €27.9 billion) due to the heatwaves registered in that year. This dried the land and caused wildfires on the continent.

The climate change influences not only the economy worldwide, but also impacts the health of human beings. The World Health Organization expects that the climate change causes approximately 250,000 additional deaths per year due to malnutrition, malaria, and heat stress (WHO, 2021).

For the reasons mentioned above, a quantification of the cost-benefit analysis of a TPP is presently not possible.

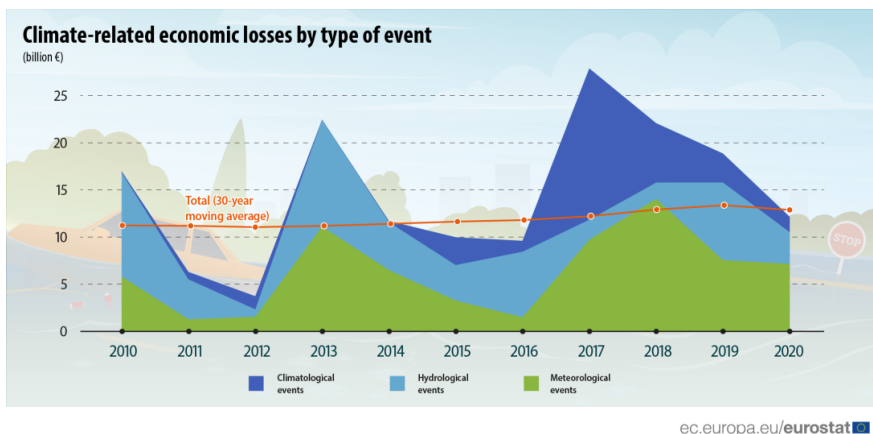


Figure 4-20. Climate-related economic losses by type of event (Eurostat, 2022).

4.3 Planning Criteria for a Distribution Grid with Ancillary Service Capability

Planning in power systems denotes the actions required for the future (Seifi & Sepasian, 2011). Apart from this, traditional planning approaches in distribution networks focus only on the grid reinforcement. Today this not anymore the best choice, since the distribution system operator should also consider the provision of ancillary services when more and more conventional power plants are being decommissioned. As a result, planning should contemplate, for example, the minimization of investments costs and maximization of the provision of ancillary services (Rossi, et al., 2022).

The aim of this section is to conceive criteria for planning purposes that could be applied in distribution grids with high presence of decentralized generation units and ancillary service capability. From the perspective of this scientific work, these criteria could be divided to:

- Controllability
- Communication infrastructure
- Identification of the potential of provision of ancillary services

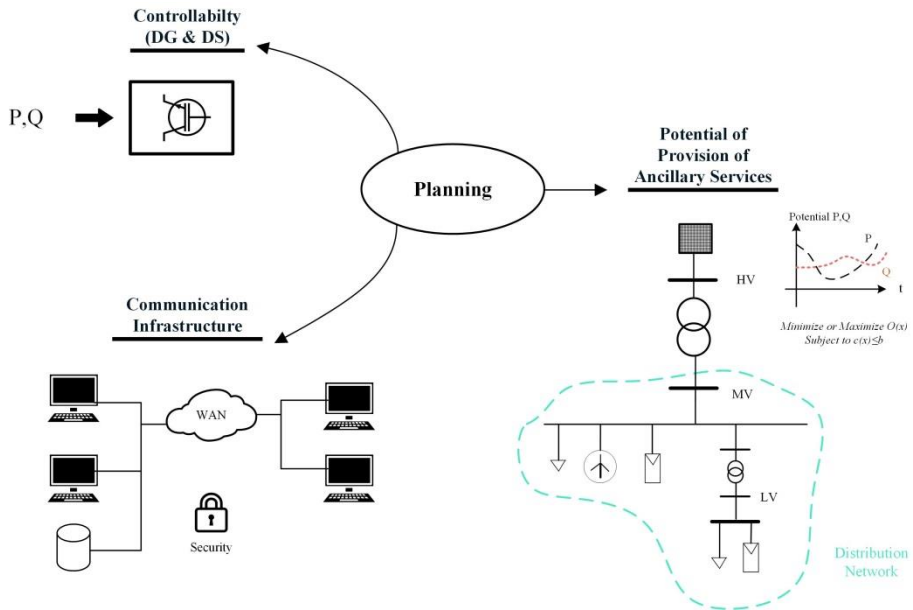


Figure 4-21. Planning criteria for distribution grids with ancillary service capability.

It is very important to recognize if the DG and DS units within the distribution grid are controllable, which means if the regulation of the active and reactive power at the PCC of each unit is available. Nowadays, this should not present any problem since modern DG and DS units provide this functionality (see also section 3.1.1). Undoubtedly, as seen in section 4.1.3, the implementation of a superordinate controller is fundamental for the controllability of the active and the reactive power at the point of common coupling of a topological power plant. In particular, as seen in Figure 4-9, the forecast of solar generation (wind production also possible) is an essential part of algorithms applied in the operation of modern power systems.

Importantly, the communication infrastructure plays a significant role currently in power systems with more presence of digital communication systems. This point takes into account such topics as:

- Communication protocols, for example, Modbus (ASCII, RTU, TCP/IP)
- Computer network: LAN (Local Area Network), MAN (Metropolitan Area Network), WAN (Wide Area Network)
- Transfer of information (wireless/cable)
- Information security

Indeed, a significant part of the planning process is to recognize the potential of provision of ancillary services of a distribution grid, which is performed together with a forecast of the power generation (solar and wind) (Goergens, Potratz, GÖdde, & Schnettler, 2015). Naturally, the potential of providing ancillary services depends also on the grid topology (voltage band and branch loading), the operating range of the inverter (e.g., limitations at night in PV inverters, four-quadrant operation) as well as on the guidelines of the country (also called grid codes). In addition, determining the potential of provision of ancillary services can be seen from the mathematical point of view as an optimization problem. For instance, the objective function could be

represented by the minimization of capacitive reactive power at the point of connection between the distribution and the transmission network. As stated in (Sowa, Goergens, Schnettler, Koeberle, & Metzger, 2016), this contributes to the reduction of reactive power demand of the distribution grid in order to avoid overvoltage in the transmission system. Definitely, the type of required reactive power from distribution systems is important since inductive reactive power is easier to provide than the capacitive variant due to the reactive power losses from the branches. Besides, in order to compute the reactive power potential, it is necessary to investigate the reactive power need (overexcited/underexcited) of the study network. Usually, distribution networks behave overexcited at night (the consumption is very low) and underexcited during the day due to high demand of loads and inductive parts of the distribution grid (Weber, Zdrallek, Abele, Brenneisen, & Mogel, 2021). As opposed to the reactive power, the maximization of the active power import/export from the distribution network to the transmission system also plays a role during the planning process (Rossi, et al., 2022).

When providing power/frequency control ancillary service, a specific capacity is required. For instance, in Germany, the following values are currently valid (minimum capacity):

- Primary power/frequency control: 1 MW
- Secondary power/frequency control: 5 MW
- Tertiary power/frequency control: 5 MW

Power plants that do not fulfil these minimum values must join a virtual power plant, so that the required values can be provided (Lotz, et al., 2022).

4.4 Conclusions

For the purposes of operation and planning of a TPP, power flow and optimization methods are required. The combination of both methods is called an optimal power flow.

Different techniques for speeding up the power flow calculations were presented, which are useful in networks with a high X/R ratio. In the case of a TPP in a LV network, these techniques cannot be applied due to the interactions between the active power and voltage drops in the LV level.

Solving an optimization problem has always two methods, which are categorized in deterministic and stochastic algorithms. A drawback of applying deterministic algorithms is that the computational speed is reduced when the number of equations is high and complex, which is the case in power systems. In some cases, if the complexity of the objective function and the constraints is high, then it is impossible to find an optimum solution. Unlike the deterministic algorithms, stochastic algorithms are based on combinatorial problem solutions and are faster than the deterministic approach.

It was verified that the method based on local optima enables provision of the reactive power to the overlaid voltage grid with a relative error less than or equal to 5%. Furthermore, it was confirmed that the new method makes it possible to reduce power losses significantly when providing reactive power to the MV level by a TPP. This can be seen in Figure 4-19, where a reduction of up to 60% was possible.

The operation strategy to provide reactive power to the overlaid voltage level by a TPP is possible due to the controllability of the DG and DS within the nanogrids. This characteristic was also mentioned in Chapter 3. Importantly, when providing ancillary services by a TPP with interlinked nanogrids, the prioritization of the self-consumption

should be considered. If this is prioritized, the reactive power capability of each nanogrid is reduced, and so is the reactive power capability of the TPP. Another important point is that the reduction of the reactive power capability of each nanogrid also influences the reduction of the active power losses within the TPP.

Given that forecasts are required for the calculation of the reactive power capability of each nanogrid in the presented operation strategy, the accuracy of the forecasts plays a significant role in this approach.

The cost-benefit of the provision of ancillary services by a TPP cannot be currently evaluated since the climate change and its consequences are not comparable with the cost-benefits of implementing a TPP.

Traditional planning approaches in distribution networks focus only on the grid reinforcement. With high presence of RES, today this is not anymore the best choice. From the perspective of this work, these criteria could be categorized in controllability of the DG/DS, communication infrastructure, and identification of the potential of provision of ancillary services of a distribution grid.

5 Conclusions and Future Work

5.1 Conclusions

This thesis shows a new concept for providing ancillary services such as active and reactive power by nano- and microgrids to compensate the decommissioning of conventional power plants. The investigation was conducted in the transient and steady state time range. The following conclusions can be drawn:

- For control and stability analysis, the switching of the IGBT of the inverters in DS and DG can be neglected. The reason is the low content of the harmonics in the current. This is supported by developing and validating detailed and simplified mathematical models of the DG and DS as part of a nanogrid in a simulation environment.
- The inclusion of a control centre and communication technologies in a nanogrid in grid-connected mode influences its stability. This scientific work presents a systematic approach for analyzing nanogrids in grid-connected mode with communication time delays. The results related to this approach show that the higher the delay time, the closer are the poles to the origin in the frequency domain. That means that a very high communication delay time can cause an instability of the system.
- A topological power plant can contribute to voltage and frequency control as well as to the stability of power systems taking into account the dynamic behaviour of the single nanogrids regarding variation of load and generation. With respect to frequency control, the contribution can be done by participating in ancillary services such as congestion management and frequency stability (secondary and tertiary power/frequency control as well as reserve replacement process). Simply put, the TPP just receives an active power set point from the TSO or DSO. Importantly, the application of storage units within the TPP contributes tremendously to negative active power set points at the PCC. Regarding voltage control, a TPP can be considered as a source of reactive power located in other voltage levels. It can contribute to the voltage control of the overlaid transmission grid.
- By the proposed optimization method to minimize active power losses in the grid a relative error less than 5% of the given reactive power set point can be achieved.
- The results of the presented optimization algorithm show that the power losses within the topological power plant can be reduced up to 60%.
- The controllability of inverters in single DG and DS as part of nanogrids is necessary for the provision of ancillary services. Definitely, without this feature the provision of ancillary services from RES could be difficult.

5.2 Future Work

The following topics can be investigated as part of future work:

- Research on the design of a robust controller taking into account random variations of the delay time of the communication system.

- Research on the characteristic curves (e.g., $P(f)$, $Q(V)$) at the nanogrid as well as at the TPP level. The presented research work just considers active and reactive power set points at the PCC.
- Research on the optimization algorithm to find the absolute minimum of power losses should be considered. The current algorithm just finds a local optimum in a multidimensional function.
- The results of the presented method based on local optima consider just nanogrids with DG and DS as well as PV systems of farms. The investigation should be extended by including additional components such as gensets and STATCOM. Additionally, the method should be investigated and tested on other voltage levels, where the constraints (e.g., grid codes) might be different compared to LV networks.

List of Figures

Figure 2-1. Overview of the current situation of a power system: Decommissioning of conventional power plants, integration of RES as well as change in the direction of the power flow (Henninger, 2019).	18
Figure 2-2. Example of a hard coal power plant in Georgia (USA) (Survey, 2021).	19
Figure 2-3. Typical configuration of a mechanical subsystem in a wind power plant (Novakovic, Duan, Solveson, Nasiri, & Ionel, 2016).	20
Figure 2-4. New installations of wind power plants in European countries in 2020 (WindEurope, 2021).	21
Figure 2-5. Installed capacity of wind power plants in Europe from 2011 until 2020 (WindEurope, 2021).	21
Figure 2-6. EU27 Annual solar PV installed capacity 2000-2020 (Schmela, 2020).	22
Figure 2-7. Classification of electrical energy storage systems (Commission I. E., 2021). ..	22
Figure 2-8. Cumulative battery capacity and battery inverter power of home storage systems in Germany (Figgenger, et al., 2020).	23
Figure 2-9. HVDC power link (Heuck, Dettmann, & Schulz, 2013).	24
Figure 2-10. German 380 kV and 220 kV EHV level including HVDC networks (Schäfer K. , 2022).	25
Figure 2-11. Power-voltage curve and equivalent circuit of a transmission system.	26
Figure 2-12. Connection of a RES unit to an external grid.	29
Figure 2-13. Ancillary services (Schäfer K. , 2022).	30
Figure 2-14. Overview of the primary, secondary and tertiary voltage controller in a specific region (Al-Majed, 2008), (Taranto, Martins, Falcao, Martins, & dos Santos, 2000).	32
Figure 2-15. Example of an electrical network with pilot busses and three different regions (Biechl, 1992).	33
Figure 2-16. Synchronous areas in Europe (Bompard, Fulli, Ardelean, & Masera, 2014). ..	34
Figure 2-17. Structure of the UCTE (Fussi, 2011).	34
Figure 2-18. Overview of frequency control as a function of time.	35
Figure 2-19. Curve P vs. f for primary power/frequency control.	36
Figure 2-20. Block diagram of the secondary power/frequency control (Fussi, 2011)...	37
Figure 2-21. VSI with a characteristic curve.	40
Figure 2-22. Nanogrid with communication network.	41
Figure 2-23. Different interfaces for distributed generators and storages: a) Grid-forming; b) Grid-feeding; c) Grid-supporting as voltage source; d) Grid-supporting as current source (Labella, Filipovic, Petronijevic, Bonfiglio, & Procopio, 2020).	42
Figure 2-24. TPP in a LV network receiving set points of active and reactive power from a DSO.	45
Figure 3-1. Overview of the demonstrator in Wildpoldsried (copyright: Fotodesign Suchy).	46
Figure 3-2. Single-line diagram of the demonstrator (IEES).	47
Figure 3-3. PV inverters and the switch cabinet of the nanogrid.	48
Figure 3-4. PQ diagram of one PV inverter.	49
Figure 3-5. HBESS I.	49
Figure 3-6. HBESS II.	50
Figure 3-7. Controllable loads: Ohmic/inductive load (left) and capacitive load (right). ..	50
Figure 3-8. Block diagram of the control centre.	52

Figure 3-9. Example of visualization in LabVIEW's Front Panel. SOC, SOH, error status, power as well as frequency are visualized. In this case, unsymmetrical set points were sent to HBESS I.	53
Figure 3-10. LabVIEW's Front Panel for active power control at the PCC considering HBESS I, the load controllable load as well as one PV inverter.	54
Figure 3-11. Switchgear.	55
Figure 3-12. Network extension.	55
Figure 3-13. VSI and control structure in the dq-Frame (Yazdani & Iravani, 2010).	56
Figure 3-14. Simplified model.	58
Figure 3-15. Topology of HBESS I.	59
Figure 3-16. Block diagram of the power and current control of HBESS I.	60
Figure 3-17. Charging of HBESS I with a set point of -17kW: a) Active power at the PCC of HBESS I; b) Voltage at the terminals of the battery model; c) Battery current.	60
Figure 3-18. Simplified model of HBESS I.	61
Figure 3-19. Comparison between the detailed and the simplified model: a) Active power set point equals 18 kW and reactive power 0 kvar; b) Reactive power set point equals 20 kvar and active power 0 kW.	61
Figure 3-20. Comparison between the simplified model and transient measurements: a) Active power set point equals 18 kW and reactive power 0 kvar; b) Reactive power set point equals -20 kvar and active power 0 kW.	62
Figure 3-21. Topology of HBESS II.	62
Figure 3-22. Block diagram of the voltage, reactive power and current controllers.	63
Figure 3-23. Discharging process by applying a set point of 2 kW: a) Active power at the PCC of HBESS II; b) Voltages at the output of the two battery modules; c) Currents at the output of the two battery modules.	63
Figure 3-24. Simplified model of HBESS II.	64
Figure 3-25. Comparison between the detailed and simplified models of HBESS II when applying a set point of 2 kW.	64
Figure 3-26. Comparison between the simplified model of HBESS II and transient measurements.	65
Figure 3-27. Topology used for PV system I and II in the case of the reduction of the active power.	66
Figure 3-28. Reduction of the active power considering different solar radiations.	66
Figure 3-29. Topology used for PV system I and II in the case of reactive power provision.	67
Figure 3-30. Block diagram of the voltage and reactive power control for PV system I and II.	67
Figure 3-31. Simplified model of PV system I and II.	68
Figure 3-32. Procedure for obtaining the active power generated of PV system I and II.	69
Figure 3-33. Comparison between the simplified and the detailed model for PV system I when a set point of the active power reduction of 2 kW is required.	69
Figure 3-34. Inputs for the pvlib tool: a) Temperature of one PV module of PV system I; b) Global radiation of the weather station "Sportplatz".....	70
Figure 3-35. I vs. V curves of a PV module for different global radiations and a cell temperature of 40 °C.	70
Figure 3-36. Comparison between the simplified model and transient measurements in the case of an active power reduction set point of 2 kW.	71

Figure 3-37. Comparison between the detailed and simplified models for PV system I in the case of reactive power provision: a) Active power reduction due to reactive power provision; b) Reactive power at the PCC at $t = 5$ s.	71
Figure 3-38. Comparison between the simplified model and transient measurements for PV system I: a) Active power at the PCC; b) Reactive power at the PCC.	72
Figure 3-39: Coupling of a MIMO system with 3 inputs and 2 outputs (Lunze, 2016)....	72
Figure 3-40. Flow chart for the analysis of the dynamics of the nanogrid.....	73
Figure 3-41. Single-line diagram of Use Case I.	74
Figure 3-42. Comparison between the small-signal model and transient measurements for Use Case I if a discharge set point of 5 kW is applied to HBESS I and a load of 4.5 kW is present: a) Active power HBESS I; b) Reactive power HBESS I; c) Active power at the PCC; d) Reactive power at the PCC.	74
Figure 3-43. Comparison between the small-signal model and transient measurements for Use Case I if a capacitive set point of 5 kvar is applied to HBESS I and an inductive load of 4.5 kvar is present: a) Active power HBESS I; b) Reactive power HBESS I; c) Active power at PCC; d) Reactive power at PCC.	75
Figure 3-44. Elements of the RGA matrix for Use Case I.	75
Figure 3-45. Single-line diagram of Use Case II.	76
Figure 3-46. Dynamics of the nanogrid for Use Case II in case an active power step is applied to HBESS I and a load of 4.5 kW: a) Active power HBESS I; b) Reactive power HBESS I; c) Active power PV West; d) Reactive power PV West; e) Active power PCC; f) Reactive power PCC.	76
Figure 3-47. Dynamics of the nanogrid for Use Case II in case a reactive power step is applied to PV West and a load of 4.5 kvar: a) Active power HBESS I; b) Reactive power HBESS I; c) Active power PV West; d) Reactive power PV West; e) Active power PCC; f) Reactive power PCC.	77
Figure 3-48. Elements of the RGA matrix for Use Case II.	77
Figure 3-49. Single-line diagram of Use Case III.	78
Figure 3-50. Dynamics of the nanogrid for Use Case III in case an active power step is applied to HBESS II and a load of 1.5 kW: a) Active power HBESS I; b) Active power HBESS II; c) Active power PCC.	78
Figure 3-51. Elements of the RGA matrix for Use Case III.	79
Figure 3-52. Block diagram of the PDC with several RES and storages.	79
Figure 3-53. Results of simulation and measurements at the PCC of the nanogrid for Use Case I in the case of active power provision.	80
Figure 3-54. Results of simulation and measurements at PCC of the nanogrid for Use Case I in the case of reactive power provision.....	80
Figure 3-55. Results of simulation and measurements for active power provision in Use Case II: a) Active power at PCC of the nanogrid in load convention; b) Active power PV East in generation convention; c) Active power HBESS I in generation convention.	81
Figure 3-56. Results of simulation and measurements for reactive power provision in Use Case II: a) Reactive power at PCC of the nanogrid in generation convention; b) Reactive power PV East in generation convention; c) Reactive power HBESS I in generation convention.....	82
Figure 3-57. Use Case I with active and reactive power control as well as communication network.....	83
Figure 3-58. Power circuit of HBESS I.	83
Figure 3-59. Block diagram of the PLL.....	84

Figure 3-60. Active and reactive power control.....	85
Figure 3-61. Comparison between simulation and measurements for HBESS I in the generation convention system: a) Active power at the output terminals of HBESS I; b) Reactive power at the output terminals of HBESS I.....	88
Figure 3-62. Comparison between simulation and measurements for the PCC in the load convention system: a) Active power at the PCC; b) Reactive power at the PCC.	88
Figure 3-63. Coupling in a MIMO system (Lunze, 2016).	89
Figure 3-64. RGA matrix of the small-signal model.....	90
Figure 3-65. Matrices G_{11} and G_{22} with time delay.....	90
Figure 3-66. Pole-zero plots for G_{11} : a) Without communication delay; b) With communication delay (5 ms, 500 ms and 5 s).....	91
Figure 4-1. Typical bus in a power system (Saadat, 1999).	94
Figure 4-2. Objective function.....	98
Figure 4-3. Classification of optimization algorithms.....	99
Figure 4-4. Traveling salesman.....	102
Figure 4-5. Study network.....	103
Figure 4-6. Types of nanogrids.....	103
Figure 4-7. German code of practice VDE-AR-N 4105 (VDE, VDE-AR-N 4105, 2011). ...	104
Figure 4-8. PV systems installed at the farms.	104
Figure 4-9. Overview of the optimization process for provision of reactive power by a TPP.	105
Figure 4-10. Nanogrid type A: a) PV production and load; b) SOC.....	106
Figure 4-11. Nanogrid type A: a) Active power at the PCC; b) Maximum absolute value of reactive power at the PCC.	107
Figure 4-12. General idea of the greedy algorithm.....	108
Figure 4-13. Flow chart of the applied algorithm.	109
Figure 4-14. Example of the modification of the main diagonal and a column of the matrix \mathbf{A}	110
Figure 4-15. Reactive power provision at the PCC of the TPP.....	111
Figure 4-16. Relative error for the reactive power provision: a) For inductive behaviour (positive set point); b) For capacitive behaviour (negative set point).	111
Figure 4-17. Network constraints for iterations 40 and 85: a) Node voltages; b) Loading of the branches.	112
Figure 4-18. Reactive power provision at the PCC of the TPP by taking into account the active power losses.	112
Figure 4-19. Comparison of active power losses: a) Active power losses for use case I and II; b) Decrease in percentage.	113
Figure 4-20. Climate-related economic losses by type of event (Eurostat, 2022).	114
Figure 4-21. Planning criteria for distribution grids with ancillary service capability. ..	115

References

- Alfergani, A., & Khalil, A. (2017). Modeling and control of master-slave microgrid with communication delay. *2017 8th International Renewable Energy Congress (IREC)*. Amman, Jordan: IEEE.
- Ali, J., Massucco, S., & Silvestro, F. (2018). Architecture of Virtual Power Plant for Ancillary Services. *CIGRE Workshop*. - Ljubljana: CIGRE.
- Al-Majed, S. (2008). Secondary Voltage Control: Enhancing power system voltage profile. *2008 IEEE 2nd International Power and Energy Conference*. Johor Bahru, Malaysia: IEEE.
- Analytics, C. (2021, October 01). Retrieved from <https://climateanalytics.org/briefings/eu-coal-phase-out/eu-coal-phase-out-detailed-information/>
- Arancibia, A., Strunz, K., & Mancilla-David, F. (2013). A Unified Single- and Three-Phase Control for Grid Connected Electric Vehicles. *IEEE Transactions on Smart Grid* (pp. 1780 - 1790). IEEE.
- Armstorfer, A., Beg, N., Rahmoun, A., Rosin, A., & Biechl, H. (2017). Mathematical modeling and evaluation of a microgrid demonstrator. Hamburg: VDE.
- Association, W. N. (2021, October 01). Retrieved from <https://world-nuclear.org/information-library/country-profiles/others/european-union.aspx>
- Åström, K., & Hägglund, T. (2006). *Advanced PID Control*. Lund: ISA.
- Azis, H., Mallongi, R., Lantara, D., & Salim, Y. (2018). Comparison of Floyd-Warshall Algorithm and Greedy Algorithm in Determining the Shortest Route. *2018 EIConCIT*. Makassar: IEEE.
- Bachoumis, A., Kaskouras, C., Papaioannou, G., & Sousounis, M. (2021). TSO/DSO Coordination for Voltage Regulation on Transmission Level: A Greek Case Study. *2021 IEEE Madrid PowerTech* (pp. 1-7). Madrid, Spain: IEEE.
- Bae, G.-T., & Kang, F.-s. (2013). Bidirectional DC-to-DC converter employing a selective switch and two inductors for optimal operation in buck and boost mode. *2013 International Conference on Electrical Machines and Systems (ICEMS)*. Busan, South Korea: IEEE.
- Barth, H., Hidalgo, D., Pohlemann, A., Martin, B., Hansen, L., & Knudsen, H. (2013). Technical and economical assessment of reactive power provision from distributed generators: Case study area of East Denmark. *2013 IEEE Grenoble Conference* (pp. 1-6). Grenoble, France: IEEE.
- bdew. (2017, 01 01). *Standardlastprofile Strom*. Retrieved from <https://www.bdew.de/energie/standardlastprofile-strom/>
- Beaty, W. (2013). *Standard Handbook for Electrical Engineers*. New York: McGraw-Hill.
- Beg, N., Biechl, H., & Rosin, A. (2020). Stability Issues with Inverter Loads and Their Control in Low Inertia Islanded Microgrids. *2020 2nd Global Power, Energy and Communication Conference (GPECOM)*. Izmir: IEEE.
- Beg, N., Rahmoun, A., Armstorfer, A., Rosin, A., & Biechl, H. (2016). Determination methods for controller parameters of back-to-back converters in electric power grids. *2016 Electric Power Quality and Supply Reliability (PQ)* (pp. 157-164). Tallinn, Estonia: IEEE.
- Bequette, B. (2003). *Process Control: Modeling, Design and Simulation*. New York: Pearson.
- Bevrani, H. (2014). *Robust Power System Frequency Control*. Switzerland: Springer.

- Biechl, H. (1992). *Unterstützung bei der Durchführung der Vereinbarung zwischen CENTREL und UCPTÉ*.
- Birkelbach, J., Woiton, H., Thiele, M., & Westermann, D. (2018). Methodology for the Evaluation of Existing Black Start Units and Optimization for Future Locations. *NEIS 2018; Conference on Sustainable Energy Supply and Energy Storage Systems*. Hamburg: VDE.
- Bisht, R., Subramaniam, S., Bhattarai, R., & Kamalasadán, S. (2018). Active and reactive power control of single phase inverter with seamless transfer between grid-connected and islanded mode. *2018 IEEE Power and Energy Conference at Illinois (PECI)* (pp. 1-8). Champaign, IL, USA: IEEE.
- Bompard, E., Fulli, G., Ardelean, M., & Masera, M. (2014). It's a Bird, It's a Plane, It's a...Supergrid!: Evolution, Opportunities, and Critical Issues for Pan-European Transmission. *IEEE Power and Energy Magazine* (pp. 40-50). IEEE.
- Braun, M. (2008). *Provision of Ancillary Services by Distributed Generators*. Kassel: kassel university press GmbH.
- Brauner, G. (2016). *Energiesysteme: regenerativ und dezentral*. Wiesbaden: Springer Vieweg.
- Bundesministerium für Wirtschaft und Energie. (n.d.). *Moderne Verteilernetze für Deutschland*. Retrieved from <https://www.bmwk.de/Redaktion/DE/Publikationen/Studien/verteilernetzstudie.html>
- Bundesnetzagentur. (2021, 01 21). *Control area*. Retrieved from <https://www.smard.de/page/en/wiki-article/6138/205642>
- Bundesnetzagentur. (17. September 2021). *Krafwerkliste*. Von https://www.bundesnetzagentur.de/DE/Sachgebiete/ElektrizitaetundGas/Unternehmen_Institutionen/Versorgungssicherheit/Erzeugungskapazitaeten/Kraftwerkliste/start.html abgerufen
- Bundesnetzagentur. (2023, April 29). *Stromnetz*. Retrieved from <https://www.bundesnetzagentur.de/DE/Fachthemen/ElektrizitaetundGas/Versorgungssicherheit/Stromnetz/start.html>
- Bundesnetzagentur. (n.d.). *Netzentwicklungsplan 2030 (2019)*. Retrieved from <https://www.netzentwicklungsplan.de/archiv/netzentwicklungsplan-2030-2019>
- Camara, M. B., Gualous, H., Gustin, F., & Berthon, A. (2008). Design and New Control of DC/DC Converters to Share Energy Between Supercapacitors and Batteries in Hybrid Vehicles. *IEEE Transactions on Vehicular Technology* (pp. 2721-2735). IEEE.
- Chong, E., & Zak, S. (2013). *An Introduction to Optimization*. New Jersey: John Wiley & Sons, Inc.
- Clarke, H. (2016, December). The cruelty of climate change. *Engineering & Technology*, pp. 32-36.
- Commission, E. (2021, December 4). *CHP data*. Retrieved from <https://ec.europa.eu/eurostat/documents/38154/4956229/CHPdata2005-2017.xlsx/871cc151-5733-423f-ae38-de9b733aa81e>
- Commission, I. E. (2021, October 29). *Electrical Energy Storage*. Retrieved from <https://www.iec.ch/basecamp/electrical-energy-storage>
- Crow, M. (2010). *Computational Methods for Electric Power Systems*. CRC Press, Taylor & Francis.

- Crow, M., & Lesieutre, B. (1994, April). Voltage collapse. *IEEE Potentials*, pp. 18-21.
- Dafalla, Y., Liu, B., Hahn, D., Wu, H., Ahmadi, R., & Bardas, A. (2020). Prosumer Nanogrids: A Cybersecurity Assessment. *IEEE Access*. IEEE.
- De Castro, R., Trovão, J., Pacheco, P., Melo, P., Pereirinha, P., & Araújo, R. (2011). DC link control for multiple energy sources in electric vehicles. *2011 IEEE Vehicle Power and Propulsion Conference*. Chicago, IL, USA: IEEE.
- de Smith, M., Longley, P., & Goodchild, M. (2007). *Geospatial Analysis: a comprehensive guide to principles, techniques and software tools*. The Winchelsea Press.
- dena. (2014, April). *Deutsche Energie-Agentur (dena)*. Retrieved from https://www.dena.de/fileadmin/dena/Dokumente/Themen_und_Projekte/Energiesysteme/dena-Studie_Systemdienstleistungen_2030/dena_Ancillary_Services_Study_2030.pdf
- DIN. (n.d.). DIN EN 50160: Merkmale der Spannung in öffentlichen Elektrizitätsversorgungsnetzen.
- Dobson, I., Glavitsch, H., Liu, C.-C., Tamura, Y., & Vu, K. (1992, May). Voltage collapse in power systems. *IEEE Circuits and Devices Magazine*, pp. 40-45.
- Dutton, K., Thompson, S., & Barraclough, B. (1997). *The Art of Control Engineering*. Dorchester: Addison-Wesley.
- ENTSO-E. (2020, September 29). *Market Committee*. Retrieved from <https://www.entsoe.eu/about/market/#balancing-and-ancillary-services-markets>
- ENTSO-E. (n.d.). *Vision on Market Design and System Operation towards 2030*. ENTSO-E. Retrieved from <https://vision2030.entsoe.eu/>
- ENTSO-E. 2009, Policy1. (2009, March 19). *ENTSO-E*. Retrieved from https://eepublicdownloads.entsoe.eu/clean-documents/pre2015/publications/ce/oh/Policy1_final.pdf.
- Etherde, N., Vyatkin, V., & Bollen, M. (2016). Virtual Power Plant for Grid Services Using IEC 61850. *IEEE Transactions on Industrial Informatics* (pp. 437-447). IEEE.
- Etherden, N., Vyatkin, V., & Bollen, M. (2015). Virtual Power Plant for Grid Services Using IEC 61850. *IEEE Transactions on Industrial Informatics* (pp. 437-447). IEEE.
- Europe, C. A. (2021, October 01). Retrieved from <https://caneurope.org/europe-halfway-to-closing-all-its-coal-plants-by-2030/>
- Eurostat. (2022, 10 24). *Eurostat*. Retrieved from Losses from climate change: €145 billion in a decade: <https://ec.europa.eu/eurostat/de/web/products-eurostat-news/-/ddn-20221024-1>
- Faigle, U. (1993). Greedy Algorithms in Combinatorial Optimization. *Operations Research Proceedings 1993*. Springer, Berlin, Heidelberg.
- Figgenger, J., Stenzel, P., Kairies, K.-P., Linßen, J., Haberschusz, D., Wessels, O., . . . Uwe Sauer, D. (2020). The development of stationary battery storage systems in Germany – status 2020. *Journal of Energy Storage*.
- Franklin, G., Powell, J., & Emami-Naeini, A. (2010). *Feedback Control of Dynamic System*. Pearson.
- Fussi, A. (2011, February). *Technische Universität Graz*. Retrieved from <https://diglib.tugraz.at/download.php?id=576a8cf4dbb4d&location=browse>
- Gerasimov, K., Gerasimov, K., & Nikolaev, N. (2014). Advanced Tools for Stability Improvement of Interconnected Electric Power Systems. *International Scientific Symposium "Electrical Power Engineering 2014"*, (pp. 5-9). Varna.

- Glover, J., Sarma, M., & Overbye, T. (2012). *Power System Analysis and Design*. Stamford: CENGAGE Learning.
- Goergens, P., Potratz, F., Gödde, M., & Schnettler, A. (2015). Determination of the potential to provide reactive power from distribution grids to the transmission grid using optimal power flow. *2015 50th International Universities Power Engineering Conference (UPEC)*. Stoke on Trent: IEEE.
- Graham, R., Grötschel, M., & Lovász, L. (1995). *Handbook of Combinatorics Volume 1*. Cambridge, MA U.S.A.: Elsevier.
- Grainger, J., & Stevenson, W. (1994). *Power System Analysis*. Singapore: McGraw-Hill, Inc.
- Greve, M., Schwippe, J., Noll, T., & Rehtanz, C. (2014). Vertical Provision of Reactive Power for Voltage Stability. *IEEE PES Innovative Smart Grid Technologies, Europe* (pp. 1-6). Istanbul, Turkey: IEEE.
- Grumm, F., Plenz, M., Meyer, M., Jordan, M., Kaatz, G., & Schulz, D. (2018). Influence of PV-Systems on Short-Circuit Currents in Low-Voltage Distribution Grids in Structurally Weak Areas. *018 IEEE International Conference on Environment and Electrical Engineering and 2018 IEEE Industrial and Commercial Power Systems Europe (EEEIC / I&CPS Europe)* (pp. 1-6). Palermo, Italy: IEEE.
- Hanif Halim, A., & Ismail, I. (2019). Combinatorial Optimization: Comparison of Heuristic Algorithms in Travelling Salesman Problem. *Archives of Computational Methods in Engineering* 26 (pp. 367–380). SpringerLink.
- Haouari, M., & Chaouachi, J. (2002). A Probabilistic Greedy Search Algorithm for Combinatorial Optimisation with Application to the Set Covering Problem. *The Journal of the Operational Research Society* (pp. 792-799). JSTOR.
- Helguero, J. (2019). *DECAS – Demonstration of coordinated ancillary services covering different voltage levels and the integration in future markets*. Hochschule Kempten.
- Henninger, S. (2019). *Netzdienliche Integration regenerativer Energiequellen über stromrichtergekoppelte Einspeisernetze mit integrierten Energiespeichern*. Erlangen: FAU University Press.
- Hernandez, L., Baladron, C., Aguiar, J., Carro, B., Sanchez-Esguevillas, A., Lloret, J., . . . Cook, D. (2013). A multi-agent system architecture for smart grid management and forecasting of energy demand in virtual power plants. *IEEE Communications Magazine* (pp. 106 - 113). IEEE.
- Heuck, K., Dettmann, K.-D., & Schulz, D. (2013). *Elektrische Energieversorgung Erzeugung, Übertragung und Verteilung elektrischer Energie für Studium und Praxis*. Hamburg: Springer Vieweg.
- Hu, Q., Han, R., Quan, X., Wu, Z., Tang, C., Li, W., & Wang, W. (2022). Grid-Forming Inverter Enabled Virtual Power Plants With Inertia Support Capability. *IEEE Transactions on Smart Grid* (pp. 4134-4143). IEEE.
- IEES. (n.d.). *Single-Line Diagram of the Microgrid Campus Wildpoldsried (internal document): technical report*. Kempten: Hochschule Kempten.
- Ippolito, M., Musca, R., & Zizzo, G. (2021). Analysis and Simulations of the Primary Frequency Control during a System Split in Continental Europe Power System. *Energies* 2021. MDPI.
- IREN2. (2018). *zukunftsfähige Netze für die Integration regenerativer Energiesysteme*. Retrieved from <http://www.iren2.de/en/>

- Johnson, D., & McGeoch, L. (1997). *The traveling salesman problem: a case study in local optimization*. John Wiley and Sons.
- Juamperez, M., Yang, G., & Kjær, S. (2014). Voltage regulation in LV grids by coordinated volt-var control strategies. *Journal of Modern Power Systems and Clean Energy* (pp. 319-328). SGPRI.
- Kaempf, E., Abele, H., Stepanescu, S., & Braun, M. (2014). Reactive power provision by distribution system operators — Optimizing use of available flexibility. *IEEE PES Innovative Smart Grid Technologies, Europe* (pp. 1-5). Istanbul, Turkey: IEEE.
- Katiraei, F. (2005). *Dynamic Analysis and Control of Distributed Energy Resources in a Micro-Grid*. Toronto, Canada.
- Kaushal, A., & Van Hertem, D. (2019). An overview of Ancillary Services and HVDC systems in European Context. *Energies 2019*. MDPI.
- Kazempour, F. (2016). *A Robust Hierarchical Control Structure for Virtual Power Plants*. Toronto, Canada.
- Keller, J., Kroposki, B., Bravo, R., & Robles, S. (2011). Fault current contribution from single-phase PV inverters. *2011 37th IEEE Photovoltaic Specialists Conference* (pp. 001822-001826,). Seattle: IEEE.
- Khalil, A., Elkawafi, S., Elgaiyar, A., & Wang, J. (2016). Delay-dependent stability of DC Microgrid with time-varying delay. *2016 22nd International Conference on Automation and Computing (ICAC)*. Colchester, UK: IEEE.
- Khan, H., & Memon, A. (2023). Active and Reactive Power Control of the Voltage Source Inverter in an AC Microgrid. *Sustainability 2023*. MDPI.
- Kharjule, S. (2015). Voltage source inverter. *2015 International Conference on Energy Systems and Applications* (pp. 537-542). Pune, India: IEEE.
- Kodaganallur, V., & Sen, A. (2010). Greedy by Chance - Stochastic Greedy Algorithms. *2010 Sixth International Conference on Autonomic and Autonomous Systems*. Cancun: IEEE.
- Kostenko, V. (2017). Combinatorial Optimization Algorithms Combining Greedy Strategies with a Limited Search Procedure. *Journal of Computer and Systems Sciences International* (pp. 218–226). Pleiades Publishing.
- Kreutziger, M., Schegner, P., Wende-von-Berg, S., Braun, M., & Bornhorst, N. (2018). Reactive Power Management of Distributed Generators for Selective Voltage Optimization in 110-kV-Subtransmission Grids. *NEIS 2018; Conference on Sustainable Energy Supply and Energy Storage Systems*. Hamburg, Germany: VDE.
- Kundur, P. (1993). *Power System Stability and Control*. McGraw-Hill.
- Labella, A., Filipovic, F., Petronijevic, M., Bonfiglio, A., & Procopio, R. (2020). An MPC Approach for Grid-Forming Inverters: Theory and Experiment. *Energies 2020*. MDPI.
- LabVIEW. (2020, 10 28). Retrieved from LabVIEW: <https://www.ni.com/de-de.html>
- LEAG. (2021, August 06). *LEAG*. Retrieved from <https://www.leag.de/en/business-fields/power-plants/>
- Li, Q., Ren, B., Tang, W., Wang, D., Wang, C., & Lv, Z. (2022). Analyzing the inertia of power grid systems comprising diverse conventional and renewable energy sources. *Energy Reports*. Elsevier.
- Liang, X., Chai, H., & Ravishankar, J. (2022). Analytical Methods of Voltage Stability in Renewable Dominated Power Systems: A Review. *Electricity 2022* (pp. 75-107). MDPI.

- Liu, S., Wang, X., & Xiaoping Liu, P. (2015). Impact of Communication Delays on Secondary Frequency Control in an Islanded Microgrid. *IEEE Transactions on Industrial Electronics* (Volume: 62, Issue: 4, April 2015). IEEE.
- Lopera-Mazo, E., & Espinosa, J. (2018). Secondary voltage regulation based on average voltage control . *Tecnológicas* (pp. 63-78). Instituto Tecnológico Metropolitano Colombia.
- Lotz, M., Majumdar, N., Beutel, V., Gerlach, J., Wegkamp, C., Hoffmann, M., . . . von Maydell, K. (2022). Potentials and Technical Requirements for the Provision of Ancillary Services in Future Power Systems with Distributed Energy Resources. *NEIS 2021; Conference on Sustainable Energy Supply and Energy Storage Systems*. Hamburg: VDE.
- Ltd., D. C. (2021, October 01). Retrieved from <https://www.datacenterdynamics.com/en/opinions/what-fuel-is-used-by-power-stations-in-europe-and-the-us-today/>
- Lunze, J. (2016). *Regelungstechnik 2*. Heidelberg: Springer.
- Maciejowski, J. (2018). Right-half plane zeros are not necessary for inverse response. *2018 European Control Conference (ECC)*. Limassol, Cyprus: IEEE.
- Mari, M. (2020). *Greedy approaches to approximation of some NP-hard combinatorial optimization problems*. PSL Université Paris.
- Marten, F., Diwold, K., Löwer, L., Faiella, L., Hochloff, P., Hansen, L., & Braun, M. (2013). Analysis of a reactive power exchange between distribution and transmission grids. *2013 IEEE International Workshop on Intelligent Energy Systems (IWIES)* (pp. 52-57). Vienna, Austria: IEEE.
- Mathworks. (2020, 10 02). *balred*. Retrieved from <https://de.mathworks.com/help/control/ref/balred.html>
- Mehigan, L., Al Kez, D., Collins, S., Foley, A., O'Gallachoir, & Deane, P. (2020). Renewables in the European power system and the impact on system rotational inertia. *Energy*. Elsevier.
- Melo, S., Yahyaoui, I., Farias, J., Frizzera, L., & Tadeo, F. (2018). A review of fuel cell and energy cogeneration technologies. *2018 9th International Renewable Energy Congress (IREC)*. Hammamet: IEEE.
- Mertens, K. (2015). *Photovoltaik Lehrbuch zu Grundlagen, Technologie und Praxis*. Carl Hanser Verlag GmbH & Co. KG.
- Migliavacca, G. (2020). *TSO-DSO Interactions and Ancillary Services in Electricity Transmission and Distribution Networks*. Springer Nature Switzerland AG.
- Milano, F. (2010). *Power System Modelling and Scripting*. Springer Berlin, Heidelberg.
- Mohammed, A., Refaat, S., Bayhan, S., & Abu-Rub, H. (2019, June). AC Microgrid Control and Management Strategies. *IEEE Power Electronics Magazine*, pp. 18-31.
- Nature, W. W. (2021, October 8). *Hydropower pressure on European rivers: The story in numbers*. Retrieved from <https://www.wwf.eu/?356638/Hydropower-pressure-on-European-rivers-The-story-in-numbers>
- Nayak, R., Sehgal, Y., & Sen, S. (2006). EHV transmission line capacity enhancement through increase in surge impedance loading level. *2006 IEEE Power India Conference*. New Delhi, India: IEEE.
- Nordman, B., Christensen, K., & Meier, A. (2012, September 09). Think Globally, Distributed Power Locally: The Promise of Nanogrids. *Computer*, pp. 89-91.

- Novakovic, B., Duan, Y., Solveson, M., Nasiri, A., & Ionel, D. (2016). From Wind to the Electric Grid: Comprehensive Modeling of Wind Turbine Systems. *IEEE Industry Applications Magazine (Volume:22, Issue: 5)*, 73-84.
- Parliament, E. (2021, August 20). *Fact Sheets on the European Union*. Retrieved from <https://www.europarl.europa.eu/factsheets/en/sheet/68/energiepolitik-allgemeine-grundsatz>
- pebbles. (2021). Retrieved from Peer-to-Peer-Energiehandel auf Basis von Blockchains: <https://pebbles-projekt.de/>
- Pisani, C., Bruno, G., Saad, H., Rault, P., & Clerc, B. (2019). Functional validation of a real VSC HVDC control system in black start operation. *2019 AEIT HVDC International Conference (AEIT HVDC)*. Florence: IEEE.
- Plenz, M., Grumm, F., Meyer, M., Boden, S., Schulz, D., & Lehmann, K. (2021). Szenariobasierte Analyse der Kurzschlussströme im deutschen Niederspannungsnetz unter Verwendung der CIGRE-Referenznetze. *e & i Elektrotechnik und Informationstechnik* (S. 289–299). Springer.
- Python. (n.d.). Retrieved from pvlb python: <https://pvlb-python.readthedocs.io/en/stable/>
- Quaschnig, V. (2021, 08 20). *volker-quaschnig*. Retrieved from https://www.volker-quaschnig.de/datserv/CO2-spez/index_e.php
- Rebours, Y., Kirschen, D., Trotignon, M., & Rossignol, S. (2007). A Survey of Frequency and Voltage Control Ancillary Services—Part I: Technical Features. *IEEE Transactions on Power Systems (Volume: 22, Issue: 1)* (pp. 350 - 357). IEEE.
- Roasto, I., Jalakas, T., & Rosin, A. (2018). Bidirectional Operation of the Power Electronic Interface for Nearly-Zero Energy Buildings. *2018 20th European Conference on Power Electronics and Applications (EPE'18 ECCE Europe)*. Riga: IEEE.
- Rodio, C., Giannoccaro, G., Bruno, S., Bronzini, M., & La Scala, M. (2020). Optimal Dispatch of Distributed Resources in a TSO-DSO Coordination Framework. *2020 AEIT International Annual Conference (AEIT)* (pp. 1-6). Catania, Italy: IEEE.
- Rodríguez Amenedo, J., Alnartés Gómez, S., Alonso-Martínez, J., & González de Armas, M. (2021). Grid-Forming Converters Control Based on the Reactive Power Synchronization Method for Renewable Power Plants. *IEEE Access*. IEEE.
- Rossi, M., Rossini, M., Vigano, G., Migliavacca, G., Siface, D., Faifer, I., . . . Sperstad, I. (2022). Planning of distribution networks considering flexibility of local resources: how to deal with transmission system services. *CIGRE 2021 - The 26th International Conference and Exhibition on Electricity Distribution*. Online Conference: IET.
- Saadat, H. (1999). *Power System Analysis*. WCB McGraw-Hill.
- Sangwongwanich, A., Yang, Y., & Blaabjerg, F. (2017). Development of Flexible Active Power Control Strategies for Grid-Connected Photovoltaic Inverters by Modifying MPPT Algorithms. *2017 IEEE 3rd International Future Energy Electronics Conference and ECCE Asia (IFEEC 2017 - ECCE Asia)*. Kaohsiung, Taiwan: IEEE.
- Sanner, B. (2019). Summary of EGC 2019 Country Update Reports on Geothermal Energy in Europe. *European Geothermal Congress 2019*. Den Haag.
- Schäfer, K. (2022). *Systemführung Betrieb elektrischer Energieübertragungsnetze*. Wuppertal: Springer Vieweg.

- Schäfer, K. F. (2020). *Netzberechnung Verfahren zur Berechnung elektrischer Energieversorgungsnetze*. Wuppertal: Springer Vieweg.
- Schittekatte, T., Reif, V., & Meeus, L. (2019, March 05). *European University Institute*. Retrieved from THE EU ELECTRICITY NETWORK CODES (2019 ED.): <https://fsr.eui.eu/publications/?handle=1814/61644>
- Schmela, M. (2020). *SolarPower Europe (2020): EU Market Outlook for Solar Power 2020-2024*. Brussels: SolarPower Europe.
- Schwab, A. (2020). *Elektroenergiesysteme*. Karlsruhe: Springer-Verlag GmbH.
- Seifi, H., & Sepasian, M. (2011). *Electric Power System Planning: Issues, Algorithms and Solutions*. Springer Berlin, Heidelberg.
- Simmons, B., Hoeppeke, C., & Sutherland, W. (2018). Beware greedy algorithms. *Journal of Animal Ecology*. Wiley Online Library.
- Skogestad, S., & Postlethwaite, I. (2001). *Multivariable Feedback Control: Analysis and design*. Wiley.
- Sowa, T., Goergens, P., Schnettler, A., Koeberle, R., & Metzger, M. (2016). Potential of the AUEW Network Area to Provide Reactive Power to Transmission Network Level. *International ETG Congress 2015; Die Energiewende - Blueprints for the new energy age*. Bonn: VDE.
- Survey, U. G. (2021, October 1). Retrieved from https://www.usgs.gov/special-topic/water-science-school/science/a-coal-fired-thermoelectric-power-plant?qt-science_center_objects=0#qt-science_center_objects
- Taranto, G., Martins, N., Falcao, D., Martins, A., & dos Santos, M. (2000). Benefits of applying secondary voltage control schemes to the Brazilian system. *2000 Power Engineering Society Summer Meeting (Cat. No.00CH37134)*. Seattle, WA, USA: IEEE.
- Tran-Quoc, T., Braun, M., Marti, J., Kieny, C., Hadjsaid, N., & Bacha, S. (2007). Using Control Capabilities of DER to Participate in Distribution System Operation. *2007 IEEE Lausanne Power Tech* (pp. 561-566). Lausanne, Switzerland: IEEE.
- TransnetBW. (2023, June). *Technologie und Umwelt*. Retrieved from <https://www.transnetbw.de/de/netzentwicklung/projekte/umspannwerk-wendlingen/technologie-und-umwelt>
- Turiman, M., Sarmin, M., Saadun, N., Chong, L., Ali, H., & Mohammad, Q. (2022). Analysis of High Penetration Level of Distributed Generation at Medium Voltage Levels of Distribution Networks. *2022 IEEE International Conference on Power Systems Technology (POWERCON)* (pp. 1-6). Kuala Lumpur, Malaysia: IEEE.
- Ulbig, A., Borsche, T., & Andersson, G. (2015). Analyzing Rotational Inertia, Grid Topology and their Role for Power System Stability. *IFAC (International Federation of Automatic Control)*. Elsevier.
- Valov, B. (2020). *Handbuch Netzintegration Erneuerbarer Energien*. Kassel: Springer Vieweg.
- Vasconcellos, M., Thie, N., Schnettler, A., Metzger, M., Hammer, A., Reischböck, M., & Koeberle, R. (2018). Topological Power Plants as Embedded Microgrids for the Market and Grid Integration of Distributed Energy Resources. *CIREN 2018 Workshop*. Ljubljana: CIREN.
- Vasconcelos, M., Thie, N., & Bertram, R. (2018). *Abschlussbericht zum Verbundvorhaben IREN2*. Aachen: RWTH Aachen, IFHT.
- VDE. (2011). *VDE-AR-N 4105*. VDE.

- VDE. (2016). *DIN EN 60909-0*. VDE.
- VDE. (2018). *VDE-AR-N 4110*. VDE.
- VDE. (2018). *VDE-AR-N 4120*. VDE.
- Venegas-Zarama, J., Muñoz-Hernandez, J., Baringo, L., Diaz-Cachinero, P., & De Domingo-Mondejar, I. (2022). A Review of the Evolution and Main Roles of Virtual Power Plants as Key Stakeholders in Power Systems. *IEEE Access* (pp. 47937-47964). IEEE.
- Vimali, M., Srivastava, P., & Gupta, S. (2017). A Novel Approach for Mining Temporal Pattern Database Using Greedy Algorithm. *International Conference on Innovations in Information, Embedded and Communication Systems (ICIIECS)*. Coimbatore: IEEE.
- Wandhare, R., & Agarwal, V. (2014). Precise Active and Reactive Power Control of the PV-DGS Integrated with Weak Grid to Increase PV Penetration. *2014 IEEE 40th Photovoltaic Specialist Conference (PVSC)*. Denver, CO, USA: IEEE.
- Weber, J., Zdrallek, M., Abele, H., Brenneisen, O., & Mogel, M. (2021). Potential of distribution networks to provide reactive power for the transmission network level. *ETG Congress 2021*. Online: VDE.
- WHO. (2021, October 30). *World Health Organization*. Retrieved from Climate change and health: <https://www.who.int/news-room/fact-sheets/detail/climate-change-and-health#:~:text=Climate%20change%20affects%20the%20social,malaria%2C%20diarrhoea%20and%20heat%20stress>.
- WindEurope. (2021, October 15). *Wind energy in Europe 2020 Statistics and the outlook for 2021-2025*. Retrieved from <https://windeurope.org/intelligence-platform/product/wind-energy-in-europe-in-2020-trends-and-statistics/>
- Wood, A., Wollenberg, B., & Sheblé, G. (2014). *Power Generation, Operation and Control*. John Wiley & Sons, Inc.
- Xu, T., & Taylor, P. (2008). Voltage Control Techniques for Electrical Distribution Networks Including Distributed Generation. *17th IFAC World Congress* (p. 5). Seoul, Korea: IFAC.
- Yang, X.-S. (2010). *Nature-inspired metaheuristic algorithms*. Luniver Press.
- Yang, Y., Blaabjerg, F., & Wang, H. (2014). Constant Power Generation of Photovoltaic Systems Considering the Distribution Grid Capacity. *2014 IEEE Applied Power Electronics Conference and Exposition - APEC 2014*. Fort Worth, TX, USA: IEEE.
- Yao, W., Wang, Y., Xu, Y., & Naayagi, R. (2020). Communication Time-Delay Stability Margin Analysis of the Islanded Microgrid under Distributed Secondary Control. *2020 IEEE Power & Energy Society General Meeting (PESGM)*. Montreal, QC, Canada: IEEE.
- Yazdani, A., & Dash, P. (2009). A Control Methodology and Characterization of Dynamics for a Photovoltaic (PV) System Interfaced With a Distribution Network. *IEEE Transactions on Power Delivery* (pp. 1538-1551). IEEE.
- Yazdani, A., & Iravani, R. (2010). *Voltage-Source Converters in Power Systems*. Wiley-IEEE Press.
- Zeitler, G. (2022). Netzregelung, Netzregelverbund, PICASSO – Entwicklungen der Netzregelung im Rahmen der Electricity Balancing Guideline. *Transformation der Stromversorgung – Netzregelung und Systemstabilität - 14. ETG/GMA-Fachtagung*. Leipzig: VDE.

- Zeraati, M., Hamedani Golshan, M., & Guerrero, J. (2018). Distributed Control of Battery Energy Storage Systems for Voltage Regulation in Distribution Networks With High PV Penetration. *IEEE Transactions on Smart Grid* (pp. 3582-359). IEEE.
- Zhang, W., He, C., Qian, H., Lin, Z., Li, Y., Zhao, X., . . . Shu, C. (2022). Virtual power plant integration with smart grids: a Review. *2022 IEEE 5th International Electrical and Energy Conference (CIEEC)* (pp. 4755-4759). Nangjing, China: IEEE.
- Zhang, Y., Gevorgian, V., Wang, C., Lei, X., Chou, E., Yang, R., . . . Jiang, L. (2017). Grid-Level Application of Electrical Energy Storage: Example Use Cases in the United States and China. *IEEE Power and Energy Magazine (Volume: 15, Issue: 5)*, 51-58.
- Zwaenepoel, B., Vandoorn, T., Van Eetvelde, G., & Vandeveldel, L. (2014). Virtual power plant to deliver congestion management and frequency restoration reserve. *2014 IEEE 5th International Symposium on Power Electronics for Distributed Generation Systems (PEDG)* (pp. 1-4). Galway, Ireland: IEEE.

Acknowledgements

Undoubtedly, I would like to thank my supervisors Prof. Dr. Argo Rosin and Prof. Dr.-Ing. Dr. h.c. Helmuth Biechl for their support during all these years. Especially, many thanks to Prof. Dr.-Ing. Dr. h.c. Helmuth Biechl for giving me the opportunity to start my research career in power systems. I have learned a lot from him.

I would also like to thank my colleagues from the Institute of Electrical Power Systems (IEES) for supporting me during my stay at the research centre. I really enjoyed the professional as well as personal talks, which let me grow in every aspect of my life.

Above all, I would like to thank my father Jorge, my mother Laura, my brother Eduardo and my sister María Laura for being always by my side and supporting me.

Last but not least, I would like to thank my wife for her patience, her love and for being there at every moment since I started this journey.

This work was carried out in the frame of the research projects “IREN2” and “DeCAS”, which were funded by the German Federal Ministry for Economic Affairs and Climate Action.

This scientific work was supported by the Estonian Centre of Excellence in Zero Energy and Resource Efficient Smart Buildings and Districts, ZEBE (grant No 2014-2020.4.01.15-0016), and by the European Commission through the H2020 project Finest Twins (grant No 856602).

This research/doctoral thesis was supported by the project “Increasing the knowledge intensity of Ida-Viru entrepreneurship” co-funded by the European Union, by the project Estonian Centre of Excellence in Zero Energy and Resource Efficient Smart Buildings and Districts (ZEBE grant No 2014-2020.4.01.15-0016), and by the European Commission through the H2020 project Finest Twins (grant No 856602).

Thank you!
Jorge Luis Helguero Cruz

Abstract

Contribution of Nano- and Microgrids to Topological Power Plants Regarding Voltage and Frequency Control

Conventional power plants provide such ancillary services to the transmission system as the active and the reactive power for frequency and voltage stability, respectively and thus, contribute to a secure energy supply in a power system. However, today, conventional power plants are being decommissioned and replaced by renewable energy sources (RESs) due to climate change and political decisions. Therefore, new solutions for providing ancillary services by RES need to be investigated in order to maintain the stability of modern power systems.

This research work focuses on the provision of the active and the reactive power by distributed generators (DG) and distributed storages (DS) clustered as a nanogrid or a household. This concept is upscaled by aggregating many nanogrids and other DGs for a topological power plant (TPP) in a low voltage network. Previous research work has not covered issues regarding this topic.

The approach presented in this thesis is analyzed from two different time scales: transient and steady-state.

From the transient point of view, single components of the nanogrids (i.e., DG and DS) are mathematically represented by detailed models. In this thesis, simplified versions of these detailed models were created and validated by performing specific measurements at a real demonstrator located in Wildpoldsried (south of Germany). In addition, the dynamics of the nanogrid (DG, DS and load), including the control centre and the simplified models, were analyzed and validated when transferring active and reactive power in the external grid. Because of the presence of delays in communication systems, the stability analysis was also performed.

After analyzing the transient behaviour, the nanogrids were aggregated for a TPP. An operation mechanism based on load flow calculations and optimization methodologies are presented in this PhD work. The operation mechanism allows the provision of ancillary services by the TPP at its point of common coupling (PCC) as well as the minimization of active power losses within the TPP.

In conclusion, the approaches presented in this work contribute to the system stability of the power systems when conventional power plants are shut down and replaced by RES.

Lühikokkuvõte

Nano- ja mikrovõrkude mõju topoloogilistele elektrijaamadele pinge ja sageduse juhtimise kontekstis

Tänase fossiilkütustel töötavad elektrijaamad pakuvad ülekandevõrgule süsteemiteenuseid, nagu aktiiv- ja reaktiivenergia pakkumine sageduse ja pinge stabiilsuse tagamiseks, ning seeläbi aitavad kaasa elektrisüsteemi varustuskindluse tagamisele. Kuna kliimamuutuste ja poliitiliste otsuste tõttu suletakse fossiilkütustel töötavaid elektrijaamu, asendades neid taastuvenergiaallikatega, siis on vaja leida uusi lahendusi süsteemiteenuste osutamiseks, et säilitada taastuvenergiaallikatega elektrisüsteemides stabiilsus.

Käesolev uurimistöö kirjeldab hajutatud nanovõrkude või kodumajapidamiste generaatorite (DG) ja salvestusseadmete (DS) poolt pakutavat aktiiv- ja reaktiivvõimsuse juhtimise lahendust ning selle agregeerimist topoloogilise elektrijaama (TPP) jaoks madalapingevõrgus, mida senised uurimistööd käsitlevad vähe.

Käesolevas töös käsitletud lähenemist on analüüsitud nii püsi- kui siirdetalitluses.

Siirdetalitluses on nanovõrgu üksikomponente (DG, DS) kirjeldatud üksikasjalike matemaatiliste mudelitenä. Lihtsustatud mudelite koostamiseks ja valideerimiseks kasutatakse Wildpoldsried külas (lõuna Saksamaal) asuvat pilootmikrovõrku, mille peal on läbi viidud hulk katsemõõtmisi. Modelleeritud nanovõrgu komponentide (DG, DS, koormuste, juhtimiskeskuse ning lihtsustatud mudelite) dünaamilist käitumist on analüüsitud ning valideeritud katsetega, kus toimus aktiiv- ja reaktiivenergia vahetus välise võrguga. Juhtimissüsteemis tekkivate ajaliste viivituste tõttu on viidud läbi mudeli stabiilsuskontroll.

Pärast siirdetalitlusanalüüsi on nanovõrgu mudelid agregeeritud TPPks. Käesolevas teadustöö tulemusena on valminud TPP juhtimisalgoritm, milles kombineeritakse püsitalitlusarvutused optimeerimismeetoditega. Juhtimisalgoritm võimaldab TPPI pakkuda võrgule süsteemiteenuseid oma liitumispunktis, vähendades samal ajal võrgukadusid TPP siseselt.

Kokkuvõtteks, käesolevas töös esitatud lähenemisviisid aitavad kaasa elektrisüsteemide stabiilsusele, kui vanad fossiilkütustel elektrijaamad asendatakse taastuvelektrijaamadega.

Appendix

Publication I

J. Helguero, A. Rosin, H. Biechl. Stability Analysis of a Nanogrid Considering Communication Delay Time. 10th International Conference on Electrical and Electronics Engineering (ICEEE 2023).

Stability Analysis of a Nanogrid Considering Communication Delay Time

Jorge Helguero¹

¹*Institute of Electrical Power Systems
University of Applied Sciences Kempten
Kempten, Germany
jorge.helguero@hs-kempten.de*

Argo Rosin^{2,3,*}

²*Smart City Center of Excellence (Finest
Twins), Estonia*
³*Department of Electrical Power
Engineering and Mechatronics
Tallinn University of Technology
(TalTech)
Tallinn, Estonia
argo.rosin@ttu.ee*

Helmuth Biechl¹

¹*Institute of Electrical Power Systems
University of Applied Sciences Kempten
Kempten, Germany
biechl@hs-kempten.de*

Abstract—The decommissioning of conventional power plants, the rise of the installation of inverter-based technology for the supply of electrical energy in the distribution network as well as the application of information and communication technologies (ICT) bring new questions to the system stability in power systems. In addition to this, inverter-based technology should be able to provide ancillary services as conventional power plants do, such as active and reactive power provision for frequency and voltage control, respectively. Moreover, nanogrids or households are not only equipped nowadays with inverter-based technology, but also capable of providing these ancillary services. This research work presents a systematic approach for analyzing the stability of a nanogrid considering communication delay time. As noted in this scientific work, the higher the communication delay, the higher is the approximation of the poles to the origin, which influences the stability of the system.

Keywords—nanogrid, simplified model, active power, reactive power, communication delay time, multiple-input multiple output system, stability analysis

I. INTRODUCTION

Power systems have been changing tremendously in the last 20 years not only technically, but also organizationally as mentioned in [1]. In Europe, for example, the combination of the liberalization of the electricity market as well as the climate change has caused depth changes in the energy supply. The liberalization of the electricity market ended with monopolies and gave final consumers the opportunity to choose electricity suppliers independently of the local connection of the grid. On the other hand, climate change brought, from one side, the decommissioning of conventional power plants such as nuclear as well as hard coal power plants and, from the other side, the installation of renewable energy sources (RES) such as wind and photovoltaic power stations, which modified the power flow from unidirectional to bidirectional (see Fig. 1). Moreover, frequency and voltage stability has been affected due to the reduction of conventional power plants and the

increase of feed-in through inverters. For example, the voltage stability is being influenced by the reduction of the subtransient fault current, since RES are based on inverters, whose subtransient fault current is just 1.1 times higher than its nominal current [2]. As seen before the decommissioning of conventional power plants carries to new challenges regarding frequency and voltage stability in modern power systems. Furthermore, these conventional power plants provide ancillary services, which are necessary for a stable operation of the network.

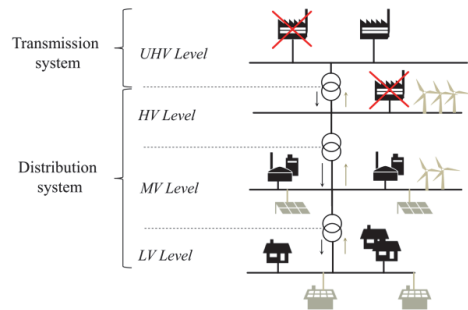


Fig. 1. Overview of the current situation of a power system.

ICT plays also an important role nowadays in the stability of power systems due to the communication delay time. A very good example is a topological power plant or TPP [3]. A TPP is electrical coupled network section of consumers and prosumers [4] that can provide active and reactive power at its PCC, and, thus, provide ancillary services. A TPP can be localized in the LV network as well as made up by households or nanogrids [5]. These are usually equipped with photovoltaics (PV) and home battery storage systems (HBESS) [6], [7], [8]. In this case, set points of active and reactive power are sent to the nanogrids by the superordinate controller of the TPP. The set points are received by the nanogrid controller that allows the regulation of active and reactive power at the PCC of the nanogrid. Due to complexity of the interactions between

*Estonian Partners work was supported by the Estonian Centre of Excellence in Zero Energy and Resource Efficient Smart Buildings and Districts ZEBE, grant 2014- 2020.4.01.15-0016 funded by European Regional Development Fund. Also, it has been supported by the Estonian Ministry of Education and Research and European Regional Fund (grant 2014-2020.4.01.20-0289).

the components of the TPP, the implementation of an ICT infrastructure is essential for the provision of active and reactive power by a TPP in this example. Nevertheless, the performance of the whole control loops might be affected by the communication delays present in the ICT infrastructure, which could show a random behavior. This scientific work presents the stability analysis considering communication delay time at the nanogrid level. Due to simplicity reasons this scientific work presents the stability analysis of a nanogrid in a real demonstrator considering one HBESS and one load. Section 2 describes the ordinary differential equations of the study nanogrid. Section 3 presents the small-signal model of the system and its validation. Since the nanogrid is a multiple-input multiple-output system a decoupling analysis is firstly performed in Section 4 and then the stability analysis is carried out. In the end, the conclusion is shown.

II. ORDINARY DIFFERENTIAL EQUATIONS OF THE STUDY NANOGRID



Fig. 2. Home battery energy storage system I (HBESS₁).

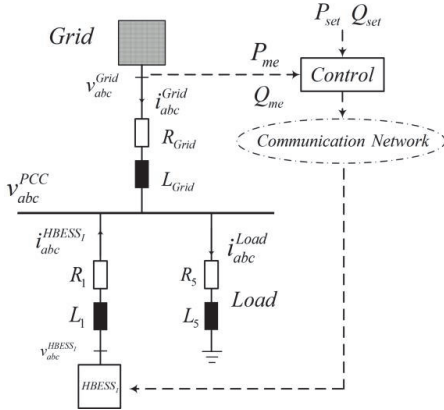


Fig. 3. Single-line diagram of the system and control.

The system to be analyzed is a real nanogrid connected in a LV network in the south of Germany. It is composed by one HBESS (here called HBESS₁), and a resistive/inductive load. HBESS₁ (see Fig. 2) has a rated apparent power of 20kVA and a four-quadrant operation. The single-line diagram of the system with the active and reactive power control is depicted in

Fig. 3. The cable that connects HBESS₁ to the grid is represented by R_1 and L_1 . R_5 and L_5 stands for the load as well as its cable connection to the grid. Additionally, the cable connecting the nanogrid with the grid is defined by R_{Grid} and L_{Grid} . In order to obtain the small-signal model of the nanogrid it is necessary firstly to develop the ordinary differential equations (ODE) of the whole system. In case of HBESS₁ the power circuit, controllers as well as the phase-locked loop (PLL) are taken into account [9], [10].

A. ODE of the Power Circuit of HBESS₁

This part of the modelling is based on simplified models, which means that the insulated-gate bipolar transistors (IGBT) and the DC side (in this case the battery modules and DC/DC converter) of HBESS₁ can be ignored. Especially, for control and stability analysis the switching of the IGBT in voltage source inverters (VSI) can be neglected due to the low content of the harmonics in the current [5] and if a quasi-steady-state condition is assumed [11]. Fig. 4 shows the simplified model of HBESS₁ in the dq-Frame. The variables $i_d^{HBESS_1}$ and $i_q^{HBESS_1}$ are the output currents of HBESS₁. On the other hand, $v_{d,q}^{HBESS_1}$ and $v_{q,d}^{HBESS_1}$ represent the input voltages of the voltage source. The variables $v_d^{HBESS_1}$ and $v_q^{HBESS_1}$ denote the voltage at the terminals of HBESS₁.

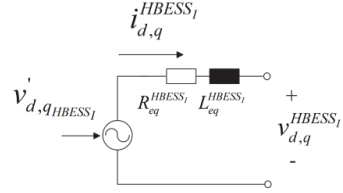


Fig. 4. Power circuit of HBESS₁

Based on Fig. 4 and applying Kirchoff's voltage law the ODE of the power circuit of HBESS₁ is given by:

$$\begin{aligned} \frac{d}{dt} i_d^{HBESS_1} &= -\frac{R_{eq}^{HBESS_1}}{L_{eq}^{HBESS_1}} i_d^{HBESS_1} + \omega_{HBESS_1} i_q^{HBESS_1} + \frac{1}{L_{eq}^{HBESS_1}} [v_{d,q}^{HBESS_1} - v_d^{HBESS_1}] \\ \frac{d}{dt} i_q^{HBESS_1} &= -\frac{R_{eq}^{HBESS_1}}{L_{eq}^{HBESS_1}} i_q^{HBESS_1} - \omega_{HBESS_1} i_d^{HBESS_1} + \frac{1}{L_{eq}^{HBESS_1}} [v_{q,d}^{HBESS_1} - v_q^{HBESS_1}] \end{aligned} \quad (1)$$

B. ODE of the PLL

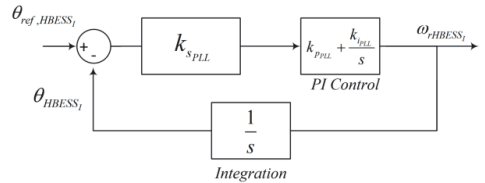


Fig. 5. Block diagram of the PLL.

The PLL is required for the synchronization of HBESS₁ with the grid. The ODE of the PLL are based on the control

block diagram shown in Fig. 5 [11], where k_{sPLL} , k_{pPLL} and k_{iPLL} are the smoothing, proportional and integral gains of the controller, respectively. Furthermore, θ_{HBESS_i} and $\omega_{ref,HBESS_i}$ are defined as the phase angle and the angular frequency of HBESS_i:

$$\begin{aligned} \frac{d}{dt}\omega_{HBESS_i} &= k_{sPLL,HBESS_i} k_{pPLL,HBESS_i} \frac{d}{dt}\theta_{ref,HBESS_i} - \\ &- k_{sPLL,HBESS_i} k_{iPLL,HBESS_i} \frac{d}{dt}\theta_{HBESS_i} + \left(k_{sPLL,HBESS_i} k_{iPLL,HBESS_i} \right) \left(\theta_{ref,HBESS_i} - \theta_{HBESS_i} \right) \end{aligned} \quad (2)$$

C. ODE of the Controller

The outer (power) as well as the inner (current) controllers are considered in the modelling of the ODE. The control loops for active and reactive power regulation of HBESS_i are depicted in Fig. 6. The parameters $k_{pp}^{HBESS_i}$ and $k_{pi}^{HBESS_i}$ are the proportional and integrals gains of the power controllers. $k_{pi}^{HBESS_i}$ and $k_{ii}^{HBESS_i}$ are the proportional and integral gains related to the current controllers, respectively. The mathematical expressions in (3)-(6) represent the ODE of the active and reactive power controllers according to Fig. 6:

$$P_{HBESS_i} = 1.5v_d^{HBESS_i} i_d^{HBESS_i} + 1.5v_q^{HBESS_i} i_q^{HBESS_i} \quad (3)$$

$$Q_{HBESS_i} = -1.5v_d^{HBESS_i} i_q^{HBESS_i} + 1.5v_q^{HBESS_i} i_d^{HBESS_i}$$

$$\frac{d}{dt}v_{1,d}^{HBESS_i} = P_{ref}^{HBESS_i} k_{pp}^{HBESS_i} - P_{HBESS_i} k_{pp}^{HBESS_i} + i_{1,d,HBESS_i} k_{pi}^{HBESS_i} - i_d^{HBESS_i} \quad (4)$$

$$\frac{d}{dt}v_{1,q}^{HBESS_i} = Q_{ref}^{HBESS_i} k_{pp}^{HBESS_i} - Q_{HBESS_i} k_{pp}^{HBESS_i} + i_{1,q,HBESS_i} k_{pi}^{HBESS_i} - i_q^{HBESS_i}$$

$$\dot{v}_{d,HBESS_i} = v_d^{HBESS_i} - \omega_{HBESS_i} L_{eq}^{HBESS_i} i_d^{HBESS_i} + v_{1,d,HBESS_i} k_{pi}^{HBESS_i} + k_{ii}^{HBESS_i} \frac{d}{dt}v_{1,d}^{HBESS_i} \quad (5)$$

$$\dot{v}_{q,HBESS_i} = v_q^{HBESS_i} - \omega_{HBESS_i} L_{eq}^{HBESS_i} i_q^{HBESS_i} + v_{1,q,HBESS_i} k_{pi}^{HBESS_i} + k_{ii}^{HBESS_i} \frac{d}{dt}v_{1,q}^{HBESS_i}$$

$$\frac{d}{dt}i_{1,d}^{HBESS_i} = P_{ref}^{HBESS_i} - P_{HBESS_i} \quad (6)$$

$$\frac{d}{dt}i_{1,q}^{HBESS_i} = Q_{ref}^{HBESS_i} - Q_{HBESS_i}$$

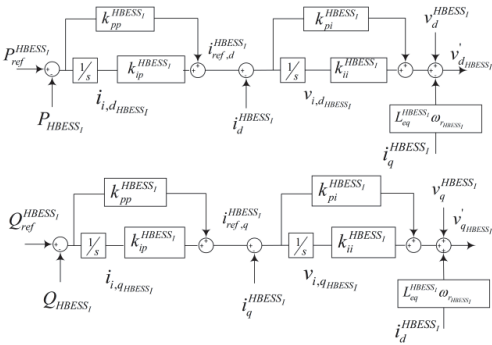


Fig. 6. Active and reactive power control loops.

D. ODE Considering the External Grid

The ODE of the system shown Fig. 1 in dq-Frame are given by:

$$\begin{aligned} \frac{di_d^{Grid}}{dt} &= \frac{1}{L_{Grid}} \left(v_d^{g,Grid} - v_d^{PCC} \right) - \frac{R_{Grid}}{L_{Grid}} i_d^{Grid} + \omega_s i_q^{Grid} \\ \frac{di_q^{Grid}}{dt} &= \frac{1}{L_{Grid}} \left(v_q^{g,Grid} - v_q^{PCC} \right) - \frac{R_{Grid}}{L_{Grid}} i_q^{Grid} - \omega_s i_d^{Grid} \\ \frac{di_{HBESS_i,d}^g}{dt} &= \frac{1}{L_1} \left(v_d^{g,HBESS_i} - v_d^{PCC} \right) - \frac{R_1}{L_1} i_{HBESS_i,d}^g + \omega_s i_{HBESS_i,q}^g \\ \frac{di_{HBESS_i,q}^g}{dt} &= \frac{1}{L_1} \left(v_q^{g,HBESS_i} - v_q^{PCC} \right) - \frac{R_1}{L_1} i_{HBESS_i,q}^g - \omega_s i_{HBESS_i,d}^g \\ \frac{di_d^{Load}}{dt} &= \frac{1}{L_5} \left(v_d^{PCC} \right) - \frac{R_5}{L_5} i_d^{Load} + \omega_s i_q^{Load} \\ \frac{di_q^{Load}}{dt} &= \frac{1}{L_5} \left(v_q^{PCC} \right) - \frac{R_5}{L_5} i_q^{Load} - \omega_s i_d^{Load} \end{aligned} \quad (7)$$

The global dq-frame reference is denoted by the superscript g. Furthermore, the angular frequency of the global frame is defined by ω_s .

III. SMALL-SIGNAL MODEL OF THE SYSTEM AND VALIDATION

The ODE presented in the previous section are rearranged in state-space form and then linearized around an operating point:

$$\begin{aligned} \frac{d}{dt} \vec{\Delta x} &= \underline{A} \vec{\Delta x} + \underline{B}_1 \vec{\Delta u}_{HBESS_i} + \underline{B}_2 \vec{\Delta v}^{s,Grid} + \underline{B}_3 \vec{\Delta \omega}_s + \underline{B}_4 \vec{\Delta u}_{pll} \\ \vec{\Delta y} &= \underline{C} \vec{\Delta x} \end{aligned} \quad (8)$$

where the vectors are defined as:

$$\begin{aligned} \vec{\Delta x} &= \begin{bmatrix} \vec{\Delta x}_{HBESS_i} \\ \vec{\Delta x}_{cc} \\ \vec{\Delta x}_{Network} \end{bmatrix}, \quad \vec{\Delta x}_{HBESS_i} = \begin{bmatrix} \vec{\Delta i}_{HBESS_i} \\ \vec{\Delta \theta}_{HBESS_i} \\ \vec{\Delta \omega}_{HBESS_i} \end{bmatrix}; \quad \vec{\Delta i}_{HBESS_i} = \begin{bmatrix} \vec{\Delta i}_{HBESS_i,d} \\ \vec{\Delta i}_{HBESS_i,q} \end{bmatrix} \\ \vec{\Delta x}_{cc} &= \begin{bmatrix} \vec{\Delta v}_{1,d,HBESS_i} \\ \vec{\Delta v}_{1,q,HBESS_i} \\ \vec{\Delta i}_{1,d,HBESS_i} \\ \vec{\Delta i}_{1,q,HBESS_i} \end{bmatrix}; \quad \vec{\Delta x}_{Network} = \begin{bmatrix} \vec{\Delta i}_d^{Grid} \\ \vec{\Delta i}_q^{Grid} \\ \vec{\Delta i}_{HBESS_i,d}^g \\ \vec{\Delta i}_{HBESS_i,q}^g \\ \vec{\Delta i}_d^{Load} \\ \vec{\Delta i}_q^{Load} \end{bmatrix} \\ \vec{\Delta u}_{HBESS_i} &= \begin{bmatrix} \vec{\Delta P}_{ref}^{HBESS_i} \\ \vec{\Delta Q}_{ref}^{HBESS_i} \end{bmatrix}; \quad \vec{\Delta v}^{s,Grid} = \begin{bmatrix} \vec{\Delta v}_d^{g,Grid} \\ \vec{\Delta v}_q^{g,Grid} \end{bmatrix}; \quad \vec{\Delta u}_{pll} = \begin{bmatrix} \vec{\Delta \theta}_{ref,HBESS_i} \\ \vec{\Delta \omega}_{ref,HBESS_i} \end{bmatrix} \\ \vec{\Delta y} &= \begin{bmatrix} \vec{\Delta i}_d^{Grid} \\ \vec{\Delta i}_q^{Grid} \end{bmatrix}; \quad \underline{C} = \begin{bmatrix} \underline{Y}_1 & \underline{0} & \underline{0} & \underline{0} & \underline{Y}_2 \\ \underline{0} & \underline{0} & \underline{0} & \underline{0} & \underline{0} \end{bmatrix} \\ \underline{Y}_1 &= \begin{bmatrix} -1 & 0 \\ 0 & -1 \end{bmatrix}; \quad \underline{Y}_2 = \begin{bmatrix} 0 & 0 & 0 & 0 & 1 & 0 \\ 0 & 0 & 0 & 0 & 0 & 1 \end{bmatrix}; \end{aligned} \quad (9)$$

In addition to this, the small-signal model of the system described in (8) is validated by varying the active power of

HBESS₁. Fig. 7 and Fig. 8 show the comparison between measurements and small-signal model. In this case a constant load of 4.5kW is used for the experiment and HBESS₁ is discharged with a set point of 5kW. On the other hand, the reactive power set point of HBESS₁ is set to 0kvar. Results show a very good match between small-signal model of the system and measurements.

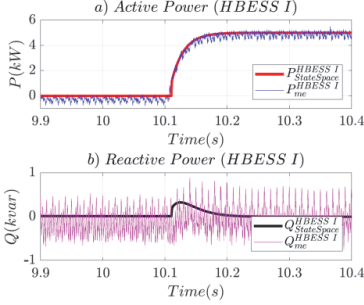


Fig. 7. Comparison between simulation and measurements for HBESS₁ in generation convention system: a) Active power at the output terminals of HBESS₁; b) Reactive power at the output terminals of HBESS₁.

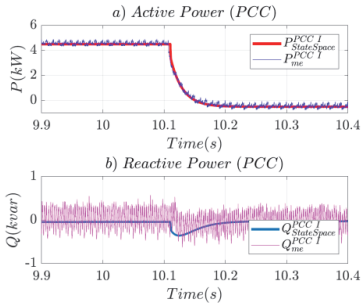


Fig. 8. Comparison between simulation and measurements for PCC in load convention system: a) Active power at PCC; b) Reactive power at PCC.

IV. DECOUPLING AND STABILITY ANALYSIS

The model described by (8) can be represented in the frequency domain by its transfer function. In this case (8) is a multiple-input multiple-output (MIMO) system with a transfer function matrix, whose dimension is 2x2 according to (10). Assuming a constant voltage at PCC, the inputs of the MIMO system are the active and reactive power set points of HBESS₁. On the other hand, the outputs are the active and reactive power at PCC.

$$\tilde{G}(s) = \begin{bmatrix} G_{11}(s) & G_{12}(s) \\ G_{21}(s) & G_{22}(s) \end{bmatrix} \quad (10)$$

The transfer functions of the main diagonal in (10) represent the relationship between output 1 and input 1 (G_{11}) as well as between output 2 and input 2 (G_{22}). The coupling elements are given by the relationship between output 1 and input 2 (G_{12}) as well as by the relationship between output 2

and input 1 (G_{21}). If this coupling is weak, then the transfer functions G_{12} and G_{21} can be neglected. In addition, G_{11} as well as G_{22} can be considered as single-input single-output (SISO) systems, which can be analyzed separately as depicted in Fig. 9.

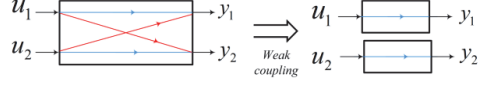


Fig. 9. Coupling in a MIMO system [12].

The quantification of the interactions between the inputs and outputs of a MIMO system is given by the RGA (Relative Gain Array) matrix, which is defined as:

$$RGA = G \times (G^{-1})^T \quad (11)$$

where the symbol \times denotes the Schur product [12]. It is important to point out that the RGA matrix is a function of the frequency and if the value of an element of the matrix closes to 1, then the pairing should be selected. Fig. 10 illustrates the RGA matrix of the system represented in (8) as a function of the frequency. It can be seen that the coupling is weak, since the elements λ_{12} and λ_{21} are zero. Whereas, the elements of the main diagonal are 1, which means that $u_1 - y_1$ and $u_2 - y_2$ can be paired and considered as SISO systems.

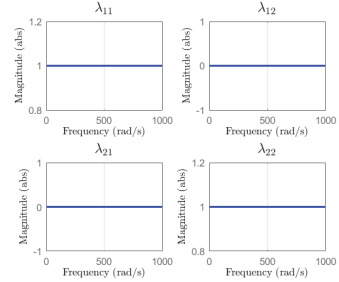


Fig. 10. RGA matrix.

Next, the matrices G_{11} as well as G_{22} are analyzed as SISO systems. Furthermore, an approximation of a time delay is multiplied to each of the transfer functions (see Fig. 11) mentioned before in order to perform the stability analysis.

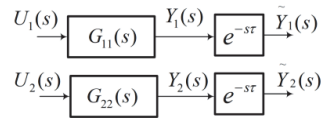


Fig. 11. Matrices G_{11} and G_{22} with time delay.

The time delay is represented by a Padé approximation [13], which is given by (12). In this case, a second order ($n = 2$) is applied, which provides a good accuracy [14] to the modelling of the time delay.

$$e^{-s\tau} \approx \frac{2 + \sum_{i=1}^n \frac{(-s\tau)^i}{i!}}{2 + \sum_{i=1}^n \frac{(s\tau)^i}{i!}} \quad (12)$$

The pole-zero plots of the open-loop systems of Fig. 11 are depicted, and in this case the transfer function G_{11} is analyzed without (Fig. 12a) and with (Fig. 12b) communication delay time for poles and zeros near to the real and imaginary axis. Without communication delay time there are two poles on the real axis and located on the left side of the s-plane. On the other hand, when adding the communication delay time, zeros are introduced and located on the right side of the s-plane. This is due to the numerator of the approximation of the communication delay time given by (12). In addition to this, systems with such characteristics have usually an inverse response, which means that if the positive step function is applied to the open-loop transfer function, the system responds initially in a negative direction and not from the initial steady-state value [13], [15]. Furthermore, it can be noticed in Fig. 12b that the higher the communication delay in this system, the higher is the approximation of the poles to the origin. In [13] it is highlighted that the impulse response of a system with one pole in the origin is marginally stable. Besides, it is also mentioned that if two poles were located in the origin, the impulse response of the system is unstable. All things considered, a high value of the communication delay time influences the stability of the analyzed system.

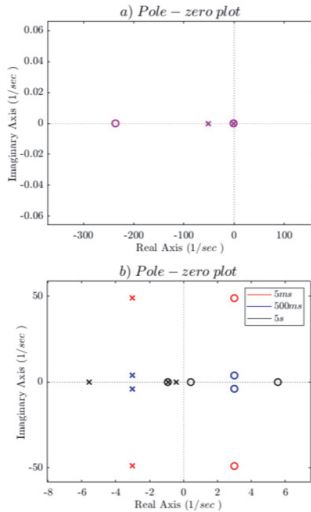


Fig. 12. Pole-zero plots for G_{11} : a) Without communication delay; b) With communication delay (5ms, 500ms and 5s).

V. CONCLUSION

This paper presents a systematic approach for the stability analysis of a real nanogrid demonstrator with one HBESS and one load considering communication time delay. The nanogrid can be seen as a MIMO system. Firstly, in this approach, the

ODE of the study nanogrid are developed, linearized and then validated with transient measurements. In order to investigate if in this case the MIMO system can be reduced, and, thus, simplify the stability analysis, the approach applies the RGA matrix. Results show that under these circumstances the MIMO system can be reduced and be seen as two SISO systems, whose transfer functions are then multiplied by the communication time delay. When taking into account, for example the transfer function G_{11} , and then increasing the communication time delay, the poles i.e. eigenvalues close to the origin of the pole-zero plot. Generally, in case of very a high communication time delay, poles can reach the origin of the pole-zero plot. This makes, according to control theory, the impulse response of the SISO system marginally stable or even unstable. Absolutely, the provision of ancillary services with inverters and controllers including ICT makes the stability analysis considering communication delay time extremely important in modern power systems. As future work, the magnitude of communication time delays as well as the randomness in ICT should be analyzed, so that better approximations can be applied in such stability analysis.

REFERENCES

- [1] A. Schwab, *Elektroenergiesysteme*, Springer Berlin, 2022.
- [2] B. Valov, *Handbuch Netzintegration Erneuerbarer Energien*, Springer Vieweg, 2022.
- [3] J. Helguero, S. Galeano, A. Rosin, H. Biechl, "Provision of Reactive Power by Nanogrids as part of a Topological Power Plant in a Low Voltage Network," *International Conference on Smart Energy Systems and Technologies (SEST)*, Istanbul, 2020.
- [4] T. Korotko, A. Rosin, R. Ahmadihangar, "Development of Prosumer Logical Structure and Object Modeling," *2019 IEEE 13th International Conference on Compatibility, Power Electronics and Power Engineering (CPE-POWERENG)*, Sonderborg, 2019.
- [5] J. Helguero, A. Rosin, H. Biechl, "Provision of Ancillary Services of a Nanogrid in Grid Connected Mode," *PQ & SEEM Conference*, Kärldla, 2019.
- [6] M. B. Sanjareh, M. H. Nazari, G. B. Gharehpetian, R. Ahmadihangar, A. Rosin, "Optimal scheduling of HVACs in islanded residential microgrids to reduce BESS size considering effect of discharge duration on voltage and capacity of battery cells," *Sustainable Energy, Grids and Networks*. Volume 25. 2021. 100424. ISSN 2352-4677.
- [7] F. Plaum, R. Ahmadihangar, A. Rosin, "Aggregated Energy Flexibility Provision Using Residential Heat Pumps," *2022 IEEE 16th International Conference on Compatibility, Power Electronics, and Power Engineering (CPE-POWERENG)*, 2022.
- [8] F. Plaum, R. Ahmadihangar, A. Rosin, J. Kilter, "Aggregated demand-side energy flexibility: A comprehensive review on characterization, forecasting and market prospects," *Energy Reports*. Volume 8. 2022. Pages 9344-9362. ISSN 2352-4847.
- [9] F. Katiraci, "Dynamic Analysis and Control of Distributed Energy Resources in a Micro-Grid," Toronto, 2005.
- [10] F. Kazempour, "A Robust Hierarchical Control Structure for Virtual Power Plants," Toronto, 2016.
- [11] A. Yazdani, R. Iravani, *Voltage-Source Converters in Power Systems*, Wiley-IEEE Press, 2010.
- [12] J. Lunze, *Regelungstechnik 2*, Springer Vieweg, 2016.
- [13] K. Dutton, S. Thompson, B. Barraclough, *The Art of Control Engineering*, Addison-Wesley, 1997.
- [14] G. F. Franklin, J. D. Powell, A. Emami-Naeini, *Feedback Control of Dynamic Systems*, Pearson, 2010.
- [15] J.M. Maciejowski, "Right-half plane zeros are not necessary for inverse response," *2018 European Control Conference (ECC)*, Limassol, 2018.

Publication II

J. Helguero, S. Galeano, A. Rosin, H. Biechl. Provision of Reactive Power by Nanogrids as part of a Topological Power Plant in a Low Voltage Network. 2020 International Conference on Smart Energy Systems and Technologies (SEST).

Provision of Reactive Power by Nanogrids as part of a Topological Power Plant in a Low Voltage Network

Jorge Helguero
Institute of Electrical Power Systems
University of Applied Sciences
Kempten**
Kempten, Germany
jorge.helguero@hs-kempten.de

Santiago Galeano
Electrical Engineering Faculty
Universidad Pontificia Bolivariana
Kempten, Germany
santiago.galeano@upb.edu.co

Argo Rosin
Smart City Center of Excellence (Finest
Twins) & Department of Electrical
Power Engineering and Mechatronics
Tallinn University of Technology*
Tallinn, Estonia
argo.rosin@ttu.ee

Helmuth Biechl
Institute of Electrical Power Systems
University of Applied Sciences
Kempten**
Kempten, Germany
biechl@hs-kempten.de

Abstract—This research work presents an operation mechanism for supplying a scheduled value of reactive power at the medium voltage (MV) side of the distribution transformer by a group of interlinked nanogrids in the low voltage level (LV), which are part of a topological power plant (TPP). The operation mechanism takes into account the self-consumption of the nanogrid and network constraints, such as the permissible voltage band for each node and the loading of the transformer as well as cables. Furthermore, the minimization of active power losses within the TPP is taken into consideration while the scheduled reactive power at the MV side should be accomplished.

Keywords—Nanogrid, Topological Power Plant, Virtual Power Plant, Ancillary Services, Reactive Power Provision, Optimization

I. INTRODUCTION

A. Motivation and Background

Conventional power plants provide ancillary services, which are required for the stable and secure operation of power systems. One of these ancillary services is the provision of reactive power for solving voltage control and stability problems, caused by renewable energy sources [1]. Usually, the provision of reactive power is carried out by the extra high and high voltage grids, but due to the fact that traditional power plants will be decommissioned by cause of climate change policies, new strategies for providing ancillary services by distributed generators (DG) and distributed storages (DS) [2], [3], [4], [5], [6], [7] should be developed. For example, a nanogrid, which is defined in [8] as a small electricity consumer in the LV level, e.g. one family house, equipped with DG, DS and a control center can contribute to the provision of ancillary services, such as primary control power (active power) for frequency control and reactive power for voltage control at its point of common

*This work has been supported by the European Commission through the H2020 project Finest Twins (grant No. 856602); and Estonian Centre of Excellence in Zero Energy and Resource Efficient Smart Buildings and Districts ZEBE, grant 2014-2020.4.15-0016 funded by European Regional Development Fund.

**This research has been conducted in the context of the project “pebbles – Peer-to-peer energy trade based on Blockchain technology”. pebbles is funded by the German Federal Ministry of Economic Affairs and Energy within the funding program “Smart Service Welt II” (Grand ID.: 01MD18003D).

coupling (PCC) [9].

B. Contribution and Organization

The main contribution of this research work is to present an operation mechanism that shows how to provide reactive power to the MV level from households or nanogrids, which are part of a TPP in a LV network. A TPP is an electrical coupled network section of producers and consumers that can provide ancillary services as conventional power plants do [10]. Furthermore, a TPP is a specific case of a virtual power plant (VPP). The difference between the two concepts is that a TPP requires a PCC, whereas a VPP not. Section 2 describes the LV network to be studied. Additionally, in order to reach the reactive power set points for each nanogrid, a superordinate controller is required. This is described in Section 3. In section 4 simulation results are shown. Finally, section 5 summarizes this research article.

II. STUDY NETWORK

The study network is located in the LV level of a rural area in the south of Germany as shown in Fig. 1. This network has the following characteristics and elements:

- The network has a radial structure and is fed by one distribution transformer with a rated apparent power of 250kVA. It has 81 nodes and 200 branches (cables and distribution transformer).
- The network consists of 24 nanogrids, represented by family houses. Additionally, there are two farms with two photovoltaic (PV) systems each.

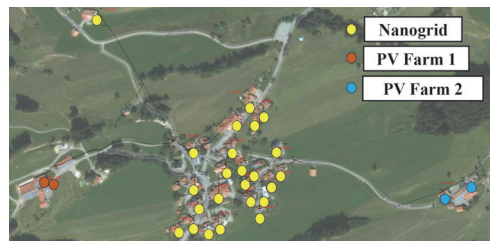


Fig. 1. Study network.

A. Nanogrids

It is assumed that all 24 nanogrids are equipped as mentioned in [9]. This means that each of them has one home battery energy storage system (HBESS), one PV system and a load. Table I illustrates information regarding the nanogrids used for the network calculations. There are three types of them in the study network. The type means the number of persons living in each house. The type A is a household of 5 persons. The type B and C are households of 4 and 3 persons, respectively. The load of each household is represented by the behavior of a standard load profile H0 [11]. Table I also mentions the number of nanogrids according to the type, the yearly energy consumption of each type of nanogrid, the rated apparent power and the capacity of the HBESS, the peak power of the PV system and the corresponding apparent rated power of the PV inverter.

TABLE I. TYPES OF NANOGRIDS

Nanogrids						
Type	Amount	Energy Consumption (kWh/annum)	HBESS (kVA)	HBESS (kWh)	PV (kWp)	PV inverter (kVA)
A	15	6900	32	32	6	7
B	6	5700	26	26	5	6
C	3	4600	21	21	4	5

B. PV Farms

In each of the PV farms two PV systems are installed, following the German Code of Practice VDE-AR-N 4105 for power generating plants connected in the LV network [12]. This code states that the PV inverter varies its power factor as a function of the active power supply into the network (see Fig. 2). Table II shows a summary of the PV system installed at the farms. Moreover, these farms follow a standard load profile L2 (for agriculture) [11] and it is assumed that they have a yearly energy consumption of 11.5MWh.

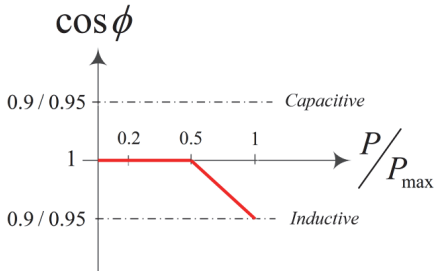


Fig. 2. German code of practice VDE-AR-N 4105 [12].

TABLE II. PV SYSTEMS INSTALLED AT THE FARMS

Farm	Farm PV Systems	
	PV system	Peak Power (kWp)
Farm 1	PV System 1	89.6
	PV System 2	21.7
Farm 2	PV System 3	5.7
	PV System 4	29.5

III. SUPERORDINATE CONTROLLER

An overview of the superordinate controller is shown in Fig. 3. First, it is assumed that a forecast (15 minutes time step for a time span of 24 hours) of the load and the PV generation in a summer day for each nanogrid is available. Next, the previous information will allow determining the reactive power capability of each nanogrid for the next 15 minutes considering the self-consumption. Then, an optimization process subject to constraints will be performed. Here the reactive power set points for each nanogrid are generated, so that the scheduled reactive power profile of the TPP is achieved. Furthermore, the optimization is based on a co-simulation between the programming language Python and PSS® SINCAL.

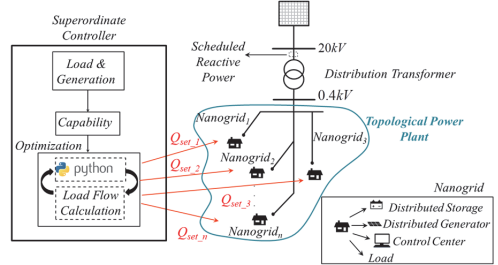


Fig. 3. Superordinate controller.

A. Load and Generation

The load and generation block is the first stage of the superordinate controller. The forecast of the loads for each nanogrid is based on a standard load profile H0 for households and a load profile L2 in the case of the PV farms. On the other hand, the PV profiles for the nanogrids and PV farms are for a summer day.

B. Reactive Power Capability

a) *Operation of the HBESS and PV inverter:* First, the functionality (identical for all the nanogrids) of the HBESS and the PV inverters is mentioned. Each HBESS allows a four-quadrant operation. The maximum reactive power a HBESS can provide can be calculated according to (1), where $S_{HBESSrated}$ and $P_{HBESSact}$ are the rated apparent power and actual active power of the battery, respectively:

$$Q_{HBESSmax} = \sqrt{S_{HBESSrated}^2 - P_{HBESSact}^2} \quad (1)$$

Additionally, each PV inverter allows a two-quadrant operation. Furthermore, the PV inverters work with a power factor between 0.4 capacitive and 0.4 inductive as carried out in [13]. The active and reactive power capability of a PV inverter is shown in Fig. 4. P_{BP} is the active power break point calculated according to (2), where $S_{PVrated}$ is the rated apparent power of the PV inverter and PF_{max} is the maximum power factor:

$$P_{BP} = S_{PVrated} \cdot PF_{max} \quad (2)$$

If the actual active power is less than P_{BP} (blue region in Fig. 4), then the maximum reactive power the PV inverter

can provide in the region is given by (3), where P_{PVact} is the actual active power:

$$Q_{PVmax_blue} = 2.29 \cdot P_{PVact} \quad (3)$$

If the active power is greater than P_{BP} (green region in Fig. 4), then the maximum reactive power that the PV inverter can provide in this region is given by (4) and a reduction of the active power will be carried out by the PV inverter, so that the rated apparent power of the PV inverter is not exceeded:

$$Q_{PVmax_green} = \sqrt{S_{PVrated}^2 - P_{PB}^2} \quad (4)$$

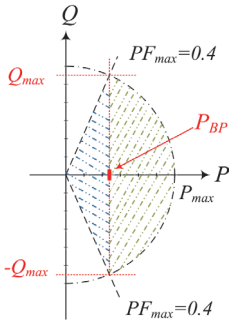


Fig. 4. PQ capability curve of a PV inverter.

b) Reactive power of a nanogrid: Supplying the local load of each nanogrid is a priority. Due to this reason, the combination of the PV system and HBESS is used to supply active power to the load. The permissible state of charge (SOC) limits of the HBESS are set according to [13] considering the optimum lifetime and the availability of storage system. First, if the surplus, which is defined in (5), is positive, the HBESS is charged as long as the SOC is lower than 80%. On the other hand, if the surplus is negative and the SOC is between 20% and 80%, the HBESS is discharged.

$$P_{surplus} = P_{PV} - P_{load} \quad (5)$$

After computing the active power, HBESS produces or consumes and the active power the PV inverter supplies, the maximum reactive power that these elements of the nanogrid can provide is calculated every 15 minutes. Equation (1) is used for the HBESS. On the other hand, the PV inverter provides reactive power only if the HBESS is fully charged and the surplus is positive.

Fig. 5a shows an example of the active power production by the PV and consumed by the load for a nanogrid type A. Furthermore, it can be seen that a reduction of the active power of the PV system occurs between 09:45 and 17:15 when the SOC is 80%, the surplus is positive and the active power of the PV system is greater than P_{BP} . In this period of time the maximum reactive power of the PV system is given by (4). Between 17:15 and 18:15 the SOC is 80%, the surplus is positive, but the active power of the PV system is lower than P_{BP} . In this period the maximum reactive power that the PV system can provide is computed using (3).

The SOC of HBESS for the nanogrid type A is illustrated in Fig. 5b. When a positive surplus occurs (e.g. at 07:30), HBESS is charged. On the other hand, during the afternoon, the HBESS is used to supply the load, when the PV production is not enough to cover the load (from 18:30 until 23:00). Since the charging and discharging of the HBESS is limited by the SOC, during the early morning the load is supplied by the external grid (from 00:00 until 07:30).

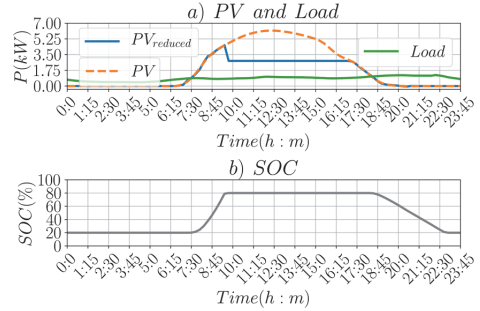


Fig. 5. Nanogrid type A: a) PV production and load; b) SOC of HBESS.

The active and reactive power at the PCC of a nanogrid type A is illustrated in Fig. 6a and Fig. 6b, respectively. Fig. 6a shows three types of cases. The first one is the import of active power from the external grid, for example from 0:00 until 07:30, since the load is supplied by the external grid. The second case is the no exchange of active power with the external grid (from 07:30 until 09:45, since the load is supplied by the PV system). Finally, the third case is an export of active power to the grid (from 09:45 until 18:30, since the battery is charged and the PV system supplies the load). On the other hand, Fig. 6b depicts the maximum absolute value of reactive power that the nanogrid can provide at every time step. From 00:00 until 09:45 the reactive power provision can only be performed by the HBESS. After that and until 18:15 the reactive power is provided by the PV system and the HBESS. Lastly, only the HBESS is able to provide reactive power.

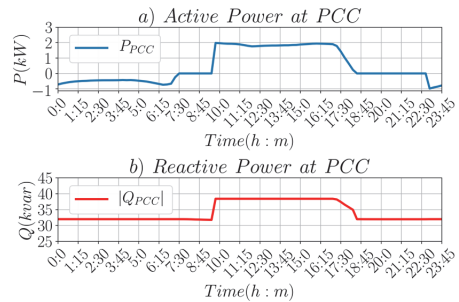


Fig. 6. Nanogrid type A: a) Active power at PCC; b) Maximum absolute value of reactive power at PCC.

C. Optimization

Two use cases are applied in the optimization process. In the first use case the sum of the reactive power of the elements of the TPP is satisfied by equation (6), where $\sum Q_{Nanogrid}^i$, $\sum Q_{Farm}^i$ and $Q_{set,TPP}^i$ are the total reactive power of the nanogrids, PV farms and at the PCC of the TPP at the time step i , respectively. On the other hand, in the second use case the active power losses are minimized within the TPP while (6) is complied. For both use cases and all the time steps, $\sum Q_{Nanogrid}^i$ is optimized and $\sum Q_{Farm}^i$ is kept fixed.

$$\sum Q_{Nanogrid}^i + \sum Q_{Farm}^i = Q_{set,TPP}^i \quad (6)$$

The optimization is based on the greedy algorithm, which is a heuristic optimization method. The greedy algorithm, as mentioned in [14] and [15], constructs a solution based on local optima. Furthermore, in some cases optimal solutions are reached, and in some other cases this algorithm will provide acceptable solutions. This algorithm was selected due to the easiness of its implementation and the high computational speed. The basic idea of the algorithm is presented in Fig. 7. It begins with an initial solution. Next, possible combinations are generated and one is selected based on constraints. This is a local optimum (orange circles on Fig. 7). The algorithm ends when no more possibilities are available.

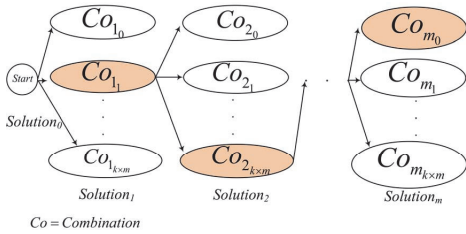


Fig. 7. General idea of the greedy algorithm.

A detailed description of the implemented algorithm is shown in Fig. 8. For each time step (15 minutes) the steps 3 to 8 are repeated. The algorithm works as follows:

- Step 1: The reactive power step ΔQ (variation of reactive power for each nanogrid) is defined by the user. Furthermore, the Python script extracts the amount of nanogrids m from the data base of PSS® SINCAL.
- Step 2: An initial load flow is performed by setting the reactive power of all nanogrids \vec{Q}_{nano} to zero.
- Step 3: Intervals of reactive power are created for a nanogrid p (vector \vec{S}_{nano_p} in Fig. 8). These intervals (generated in the block capability of Fig. 3) define how much reactive power each nanogrid is capable to provide at the time step i . The number of elements of the interval for a nanogrid p is saved in the vector \vec{n}_p .

- Step 4: The matrix \mathbf{A} is created and its main diagonal is filled with each vector \vec{S}_{nano_p} . The dimension of \mathbf{A} is $k \times m$. The variable k is defined in (7), where n_p is the number of elements of the interval of reactive power for the nanogrid p :

$$k = \sum_{p=0}^m n_p \quad (7)$$

- Step 5: The matrix \mathbf{A} is modified by adding the factor $n_p \times \Delta Q$ to each element of the main diagonal. The green area of Fig. 9 illustrates an example of this step.
- Step 6: The elements of each row of \mathbf{A} (gray arrows of Fig. 9) are taken and used for load flows calculations.
- Step 7: The constraints are verified for every load flow of step 6, for both use cases, with respect to the loading of cables and distribution transformer (less than 100%), the permissible voltage band ($\pm 10\%$ of the nominal voltage) and the reactive power at the PCC of the TPP should not differ more than 5% of the set point. For the second use, the active power losses should be equal or less than the active power losses of the use case I.
- Step 8: The previous step will generate a list of solutions that satisfies or not the constraints. For both use cases, the program selects the best solution and modifies one column of \mathbf{A} . The orange area of Fig. 9 depicts an example of this modification. In this example, the first row of \mathbf{A}_1 has the best solution. Thus, the first column of \mathbf{A}_2 is modified. Finally, if there is no improvement, the first iteration is ready.

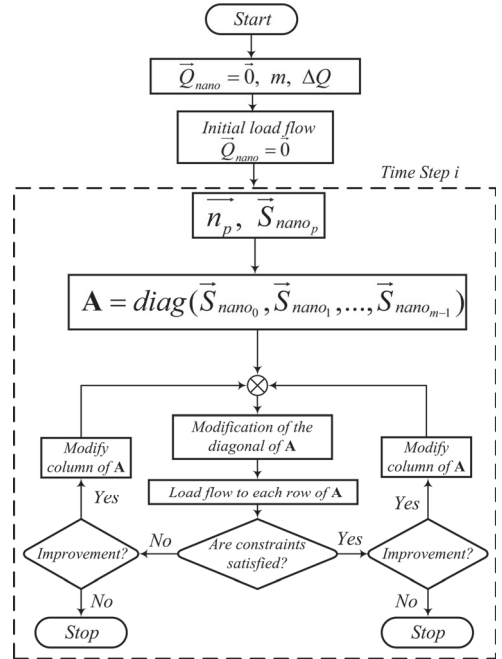


Fig. 8. Flow chart of the applied algorithm.

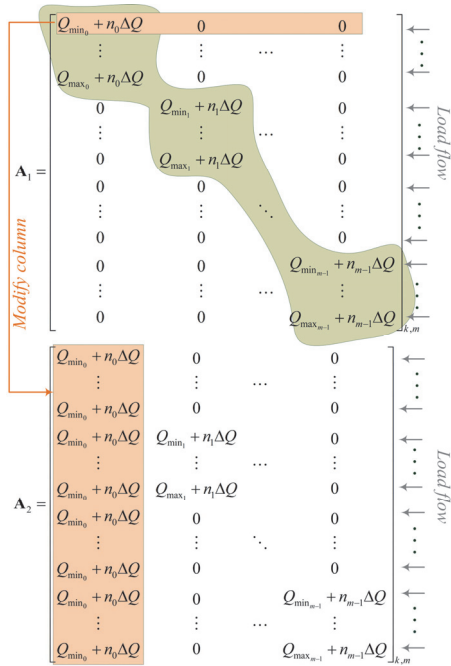


Fig. 9. Example of the modification of the main diagonal and a column of the matrix A .

IV. RESULTS

This section presents the results of the co-simulation between Python and PSS[®] SINCAL for the two proposed use cases.

A. Use Case I: Reactive Power Profile at the PCC of the TPP

The reactive power profile used for this use case and the results of the optimization are presented in Fig. 10. The sign convention is done from the point of view of the distribution system operator (DSO). This means according to the consumer perspective:

- $Q > 0$: inductive behavior of the TPP
- $Q < 0$: capacitive behavior of the TPP

An inductive behavior of the TPP is required from 00:00 to 12:00 and a capacitive behavior for the residual time. Fig. 11a shows the relative error for the inductive behavior and Fig. 11b for the capacitive behavior for each time step (15 minutes). For both cases, the provided reactive power at the MV side of the distribution transformer is within the 5% tolerance.

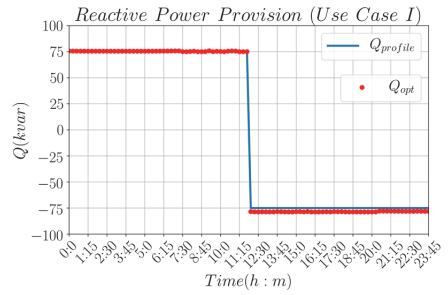


Fig. 10. Reactive power provision at the PCC of the TPP.

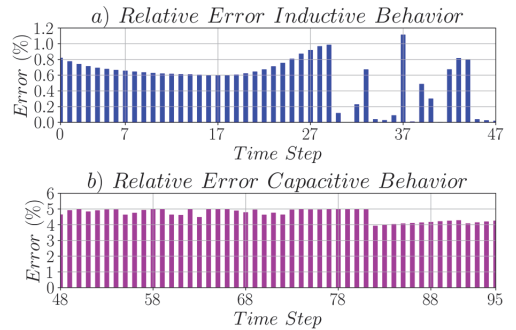


Fig. 11. Relative error for the reactive power provision: a) For inductive behavior (positive set point); b) For capacitive behavior (negative set point).

An example of the node voltages and the loading of the branches (cables and distribution transformer) is depicted in Fig. 12a and Fig. 12b, respectively. In this case the iteration 40 (inductive behavior of the TPP) and for iteration 85 (capacitive behavior of the TPP) are presented. The node voltages are within the permitted voltage band of $\pm 10\%$ of the nominal value. On the other hand, the loading of branches is less than 100%.

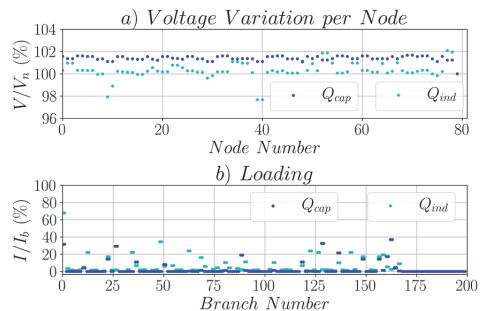


Fig. 12. Network constraints for the iterations 40 and 85: a) Node voltages; b) Loading of the branches.

B. Use Case II: Reactive Power Profile at the PCC of the TPP and Minimization of the Active Power Losses

This use case focuses on the achievement of a reactive power profile (same as the first use case) at the MV side of the transformer while taking into account the minimization of the active power losses within the TPP. The sign convention for the reactive power provision is the same as the previous use case. Fig. 13 shows that the reactive power provision at the MV side follows the required profile.

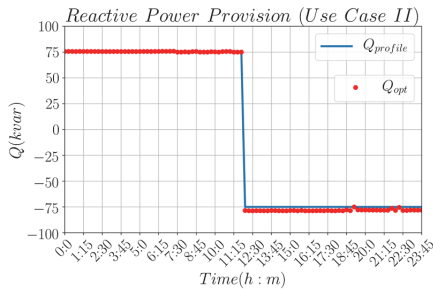


Fig. 13. Reactive power provision at the PCC of the TPP by taking into account the active power losses.

C. Comparison of active power losses

The active power losses of the study network for both use cases and the percentage decrease are depicted in Fig. 14a and Fig. 14b, respectively. This is analyzed in three intervals of time:

- Interval I: This is from 00:00 until 09:45. Here the maximum active power losses reduction achieved is 61%.
- Interval II: This occurs from 09:45 until 17:30. The reduction of the active power losses is 0%.
- Interval III: It takes place from 17:30 until end of the day. The active power losses can be reduced by up to 35%. During this interval all HBESS are discharging and supplying the loads of the nanogrids. Keeping this in mind, there is no exchange of active power between each nanogrid and the external grid. For this reason the percentage decrease of the interval II is lower than the interval I.

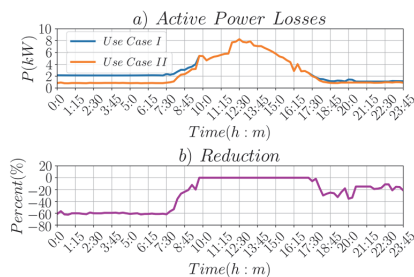


Fig. 14. Comparison of active power losses: a) Active power losses for use case I and II; b) Percentage decrease.

V. CONCLUSION

In this paper it is shown an operation strategy to provide reactive power for voltage control to the overlaid voltage

level by a group of interlinked nanogrids, which are part of a TPP located in a LV network. In this strategy, each nanogrid prioritizes the self-consumption while providing reactive power. Furthermore, the operation strategy applies an optimization method so that a required reactive power profile at the overlaid voltage level can be accomplished when network constraints as well as the reduction of active power losses are taken into account. Finally, it is important to point out the importance of the controllability of the DG and DS together with the availability of PV and load forecast in the operation of a TPP.

REFERENCES

- [1] Y. Liu, W. Qin, X. Han, P. Wang, Y. Wang, L. Wang, F. Li, "Distribution Network Voltage Control by Active Power/Reactive Power Injection from PV Inverters," *2018 13th IEEE Conference on Industrial Electronics and Applications (ICIEA)*, Wuhan, June 2018.
- [2] A. Armstorfer, H. Biechl and A. Rosin, "Analysis of Black Start Strategies for Microgrids with Renewable Distributed Generation," *2019 IECON 2019-45th Annual Conference of the IEEE Industrial Electronics Society*, Lisbon, October 2019.
- [3] A. Rahmoun, N. Beg, A. Rosin and H. Biechl, "Stability and eigenvalue sensitivity analysis of a BESS model in a microgrid," *2018 IEEE International Energy Conference (ENERGYCON)*, Limassol, 2018, pp. 1-6.
- [4] P. Bucko, M. Jaskólski, Z. Lubosny, J. Klucznik and K. Dobrzynski, "Delivery of Ancillary Services in Distribution Power Systems," *2018 15th International Conference on the European Energy Market (EEM)*, Lodz, 2018.
- [5] G. De Zotti, S. Pourmousavi, H. Madsen and N. Poulsen, "Ancillary Services 4.0: A Top-to-Bottom Control-Based Approach for Solving Ancillary Services Problems in Smart Grids," *IEEE Access (Volume:6)*, February 2018.
- [6] J. Rocha, F. Salvadori and C. Gehrke, "Provision of ancillary service in a grid-connected photovoltaic power system," *2018 IEEE Applied Power Electronics Conference and Exposition (APEC)*, San Antonio, TX, March 2018.
- [7] Armstorfer, A., Biechl, H., & Rosin, A. (2017). Energy Scheduling of Battery Storage Systems in Micro Grids, *Electrical, Control and Communication Engineering*, 12(1), 27-33. doi: <https://doi.org/10.1515/ecece-2017-0004>
- [8] M. Sandgani, and S. Sirouspour, "Energy Management in a Network of Grid-Connected Microgrids/Nanogrids Using Compromise Programming", in *IEEE Transactions on Smart Grid*, vol. 9, Issue 3, pp. 2180-2191, May 2018.
- [9] J. Helguero, A. Rosin, and H. Biechl, "Provision of Ancillary Services of a Nanogrid in Grid Connected Model," PQ2019, June 2019.
- [10] M. Vasconcellos, N. Thie, A. Schnetter, M. Metzger, A. Hammer, M. Reischböck and R. Koerberle, "Topological Power Plants as Embedded Microgrids for the Market and Grid Integration of Distributed Energy Resources," in *CIRE2018 Workshop*, 2018.
- [11] Bundesverband der Energie- und Wasserwirtschaft, "Standardlastprofile Strom", 2017. [Online]. Available: <http://www.bdew.de/energie/standardlastprofile-strom/>. [Accessed: 24-Jun-2020].
- [12] Verband der Elektrotechnik Elektronik Informationstechnik e.V., "VDE-AR-N 4105: Erzeugungsanlagen am Niederspannungsnetz – Technische Mindestanforderungen für Anschluss an Parallelbetrieb von Erzeugungsanlagen am Niederspannungsnetz," August 2011.
- [13] J. Helguero, "DECAS – Demonstration of coordinated ancillary services covering different voltage levels and the integration in future markets", 2019. [Online]. Available: <http://www.tib.eu/en/>. [Accessed: 24-Jun-2020].
- [14] M. Vimali, P. Srivastava, S. Gupta, "A Novel Approach for Mining Temporal Pattern Database Using Greedy Algorithm," *2017 International Conference on Innovations in Information, Embedded and Communication Systems (ICIIECS)*, Coimbatore, March 2017.
- [15] H. Azis, R. Mallongi, D. Lantara and Y. Salim, "Comparison of Floyd-Warshall Algorithm and Greedy Algorithm in Determining the Shortest Route," *2018 EICoNCT*, Makassar, November 2018.

Publication III

T. Häring, A. Rosin, T. M. Kull, J. Helguero, H. Biechl. Thermal Modelling of a Control Center for Flexibility Analysis in nZEB Nanogrids. 2020 IEEE 61st International Scientific Conference on Power and Electrical Engineering of Riga Technical University (RTUCON)

Thermal Modelling of a Control Center for Flexibility Analysis in nZEB Nanogrids

Tobias Häring, Argo Rosin
Smart City Center of Excellence
(Finest Twins) & Department of
Electrical Power Engineering and
Mechatronics
Tallinn University of Technology
Tallinn, Estonia
tobias.haring@taltech.ee

Tuule Mall Kull
Department of Civil Engineering and
Architecture
Tallinn University of Technology
Tallinn, Estonia

Jorge Helguero, Helmuth Biechl
Institute of Electrical Power Systems
(IEES)
University of Applied Sciences
Kempten
Kempten, Germany

Abstract— Due to the increasing share of volatile renewable energy sources, like photovoltaics (PV) and wind energy in nearly Zero Energy Buildings (nZEB), there is an increasing need for demand-side management (DSM) or demand response (DR) programs to balance the production and consumption in the grid. The flexibility that can be obtained for smart grids from such DR methods is not limited to appliances like water heaters or dishwashers but can also be achieved with space heating and air-conditioning. In such an interdisciplinary investigation, often one part is simplified, in this case, typically either the thermal models or the implemented DR strategy are very detailed. In this work, a detailed thermal model of a control center is obtained and calibrated in IDA ICE building-modelling software with measurements from a test site in Germany. Afterward, several price-based load matching algorithms are applied to the model to see the possible flexibility exploitation with the thermal capacity of this small building. Not all investigated algorithms show good performance but some of them show promising results. Thus, this model can be used for DR methods and should be extended to work with more DSM strategies and provide ancillary services.

Keywords— Flexibility, Smart City, nZEB, Thermal Storage, Space Heating, Demand Response, Nanogrid

I. INTRODUCTION

As the share of renewable energy production is increasing worldwide, with some countries already having renewable energy shares of 30% and more, the operational complexity for the electrical power grid increases accordingly. This development creates despite its sustainability and environmental friendliness several challenges for grid operators. The volatility and unpredictability of the renewable energy sources, like photovoltaics (PV) or wind power, which are popular to be installed in nearly Zero Energy Buildings (nZEB), can create imbalances between energy production and consumption. This makes the planning of energy production especially complicated to prevent mismatches and therefore unstable energy supply for the customers. One concept to tackle this problem is to use demand response techniques [1], which aim to adapt the load by scheduling certain household devices. Such demand response (DR) or demand-side

This work was supported by the Estonian Centre of Excellence in Zero Energy and Resource Efficient Smart Buildings and Districts ZEBE, grant 2014-2020.4.01.15-0016 funded by European Regional Development Fund; and supported by the European Commission through the H2020 project Finest Twins (grant No. 856602).

management (DSM) methods, which are an important part of smart grids and smart cities, can be applied on many different devices in a household, for example, freezer, water heater [2], or other appliances like dishwashers [3]. These DR and DSM concepts can increase the flexibility [4] of the system, which is an officially recognized concept in power systems [5], [6], which helps to improve the balance between energy production and consumption. Like this, it is possible to react to unexpected changes and more efficiently plan the energy generation and use.

Additionally, it is not just possible to use various appliances in a household for DR. The thermal capacity of the whole building, meaning the space heating, air conditioning [7], and ventilation systems [8] can be used for DSM.

In this context, several publications present a complex DR control approach but use simplified thermal models to estimate the electrical energy demand of the heating systems for example. In [9] the authors propose a price-based control strategy with a minimalistic model of the space heating, assuming it to be a certain percentage of the energy consumption. The authors of [10] show possible DSM strategies with space heating /cooling with a multi-agent system. They are using a simple aggregated model for their research. [11] presents a DSM approach with a simplified thermal model for houses. From that, the flexibility of the system is assessed and the heat pumps are controlled in a DR scheme. Similarly, in [12] different load matching control algorithms are used to optimize the system in a DSM manner. A simplified thermal model based on temperature differences due to different influences is used to estimate the electrical consumption.

On the other hand, there are publications, which consider a very detailed thermal model but use a simple control strategy. The heat pump model presented in [13] is very detailed. The demand response control strategy presented is comparably simple. The thermal models of buildings presented in [14] are quite detailed but the demand response methods are limited somehow and do not show the anticipated results. Several other publications like [15] show very detailed thermal models but do not consider DR or DSM methods at all.

Therefore, this work aims to create a detailed thermal model of a control center, which is part of a nanogrid with PV-installations and home battery energy storage systems. This thermal model should provide good performance based on comparisons with measurements of the real object. It is then being used with different price-based load matching algorithms to achieve an efficient demand response control of the space heating in the control center. The model is additionally already created in a way that it can be used for more detailed future investigations on the nanogrid with more demand-side management methods and providing ancillary services to the grid.

The paper is organized as follows: The methodology, including the measurements, modeling, calibration, and simulation setup, is presented in Section II. Section III shows the results of the simulations. Finally, the results in brief with conclusions are presented in Section IV.

II. METHODOLOGY

The control center is part of the Energy Campus Wildpoldsried in the city of Wildpoldsried in southern Germany. It is part of University of Applied Sciences Kempten, Germany. The work of this paper is a cooperation between Tallinn University of Technology and University of Applied Sciences Kempten.

A. Control Center Measurements

To obtain the necessary data to model the control center and calibrate the model, measurements were needed. Therefore, four temperature sensors were used, three of which were placed inside the control center and one outside. The temperature sensors on the inside were placed on different heights and different positions in the room (c.f. Fig. 1). The sensor outside was placed in a wind and weather protected place. Several days were measured from the 21st Nov. 2019 until 25th Nov. 2019 with a free-floating control center, where all heat sources were turned off, and from 25th Nov. 2019 until 27th Nov. 2019 with an electric heater inside the control center. The power consumption of the electric heater was measured with a portable power meter.

An additional free-floating measurement with three sensors on the outside and 1 sensor on the inside was conducted to see the influence of the outside sensor placement on the measurements. The used temperature sensors were EL-USB-2 EH / Temp Data Loggers.

Additionally, during the measurements, the data of a nearby weather station was stored. It contained measurements for the outside temperature, global irradiation, air pressure, humidity, dew point, wind speed and wind direction.

Thermal imaging of the electric heater was done as well, to see the heat dissipation of the used device. The electric heater from EUROM was operated at 1300 W during the thermal imaging and during the measurement time (c.f. Fig. 2).

B. Control Center Model and Calibration

The container was modeled in IDA ICE 4.8 building simulation software. The floorplan and 3D model pictures of

the container are shown in Fig. 3. The constructions and window parameters were inputs given by the container producer. The small corridor after the external door was not modeled as the corridor door to the room was kept open during the whole experiment. The climate data from the closest weather station were used as boundary conditions.

To calibrate the model, the parameter values for infiltration, power emitted by the computers, and the furniture area were varied. These values were chosen as no information about these was available. As reliable wind direction data was missing, infiltration was set to constant. Although maximum computer power was known, the computers did not work on nominal power the whole time. As the profile of usage was not measured, the computer power was also assumed to be constant. The furniture is modeled in IDA ICE as a capacity with a heat transfer coefficient of 6 W/(m²K). The area of the furniture is the furniture surface facing the room air where the heat is transferred.

The quality of the model was assessed by the average absolute error between the simulated and measured air temperatures in the room. IDA ICE models the room with ideally mixed air so there is one air temperature in the room. The simulated temperature was compared to the average temperature measured by the sensors.

Parametric analysis was carried out first for the free-floating periods to calibrate the envelope and then for the period with an electrical heater to check the heat-up performance. The results were adapted in the simulation of the whole experiment period. The found values for the varied parameters are 0.05 l/s·m² of infiltration rate per external surfaces, 80 W power of the computers, and 26 m² of furniture area.



Fig. 1. EL-USB-2 EH / Temp Data Logger placed on top of a shelf



Fig. 2. EUROM electric heater placed in the middle of the control center for calibration measurement

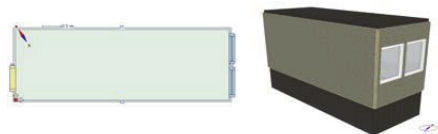


Fig. 3. The container model in IDA ICE with floorplan on the left and 3D view on the right. The compass is shown for orientation in both pictures

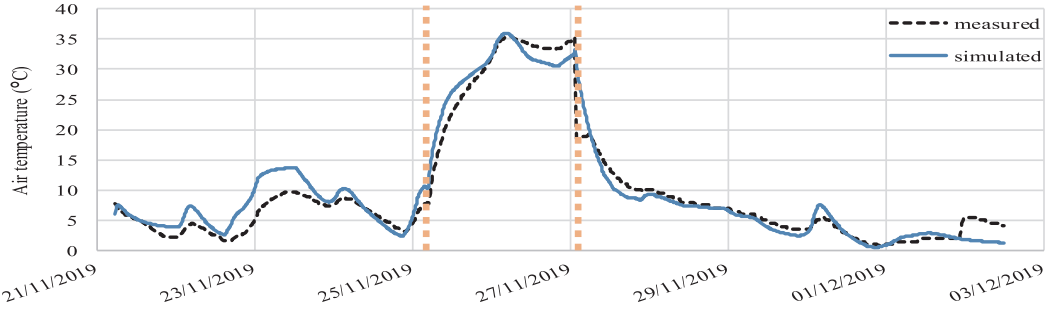


Fig. 4. The behavior of the air temperature in the simulation compared to the average of measurements. The vertical orange lines separate the three different periods – 1st free-floating, electric heating, and 2nd free-floating period

Ideal heater and cooler were set to achieve the initial state of the container. The setpoint value of the cooler was set to 0.1 degrees higher than the heater’s and the latter was estimated by minimizing the average absolute error during the first free-heating period. The lowest error was achieved while aiming for a temperature between 3.75 °C and 3.85 °C, although the initial measured temperature was 8.2 °C. This was probably because the pre-simulation conditioning of the model is constant but the actual behavior is dynamic.

The resulting temperature behavior is compared to the average measured temperature in Fig. 4. The average absolute error for the whole period was 1.61 °C, for the three periods the errors were 1.92 °C, 2.08 °C and 1.00 °C. The error in the heating period is mostly caused by a small shift in time and the moment around the time when heating was turned off. The air temperature in the room drops drastically in a very short time. It is not clear whether the door was opened for a longer time or is this an error in the measurement.

The error during the first period shows that either the initial state was not estimated ideally or the heat capacity or heat loss of the container is modeled too low. The calibration during the last period is almost ideal as in reality the temperatures are not ideally mixed and the energetically effective temperature of the measured period is not known. As the general behavior of the container is close to the average measurements, the achieved result is suitable for the following work.

C. Price-based Load Matching Algorithm Control

Different price-based load matching algorithms were implemented in this model to see the responsiveness of the control center to set point based control strategies. Therefore, the electric heaters were controlled with a thermostatic two-step controller. In the first step, a fixed setpoint value of 22°C was selected with a 1°C deadband. This will be the basic benchmark for comparison with the other control strategies.

To have prices with smaller fluctuations than the spot market prices, the hourly day-ahead prices of the Nordpool database [16] for Estonia were obtained for the setpoint control algorithms. The prices without additional fees and taxes from November 22nd until December 2nd, 2019 were used for the setpoint calculation (c.f. Fig. 5). The seven different price-based setpoint calculation algorithms (A-F) were based on [2],

[17] and [18]. The algorithms are shown in TABLE I. Their performance has been positively evaluated under different occupancy- and other considerations for simple models of a freezer, water heater and space heating for a household in an apartment [19] and [20]. The pre-calculated setpoints for each algorithm were created as an input look-up table for the set point of the thermostatic controller in the IDA-ICE simulations. The parameters for the setpoint calculation algorithms and the two-step thermostatic control are shown in TABLE II. The minimum (Pr_{min}), maximum (Pr_{max}) and average (Pr_{avg}) price, and the price deviation (Pr_{dev}) are calculated from the Nordpool prices for each day. Each simulation was done in the timeframe of Nov. 22nd until Dec. 2nd, 2019.

TABLE I. DESCRIPTION OF PRICE-BASED SET POINT CALCULATION ALGORITHMS [2],[17],[18]

Algorithm	Description of set point calculation algorithm
A	$T_{set} = T_{set,max} - (Pr - Pr_{min}) * \frac{T_{set,max} - T_{set,min}}{Pr_{max} - Pr_{min}}$
B	$T_{set} = T_{goal} - (Pr - Pr_{avg}) * \frac{ T_{set,min} - T_{goal} }{Pr_{dev}}$
C	$T_{set} = T_{goal} - (Pr - Pr_{avg}) * \frac{T_{set,min} - T_{goal}}{Pr_{min} - Pr_{avg}}$
D	$T_{set} = T_{goal} - (Pr - Pr_{min}) * \frac{T_{set,min} - T_{goal}}{Pr_{min} - Pr_{avg}}$
E	$T_{set} = T_{goal} - (Pr - Pr_{avg}) * \frac{T_{set,max} - T_{set,min}}{Pr_{max} - Pr_{min}}$
F	$T_{set} = T_{goal} - (Pr - Pr_{min}) * \frac{T_{set,max} - T_{set,min}}{Pr_{max} - Pr_{min}}$
G	$Pr \geq Pr_{avg} \rightarrow T_{set} = T_{set,min}$; $Otherwise \rightarrow T_{set} = T_{set,max}$;

TABLE II. PARAMETERS FOR SETPOINT CALCULATION ALGORITHMS

Parameter	Symbol	Value
Maximum Set Point	$T_{set,max}$	24 [°C]
Minimum Set Point	$T_{set,min}$	20 [°C]
Goal Set Point	T_{goal}	22 [°C]
Two-step Controller Deadband	-	1 [°C]

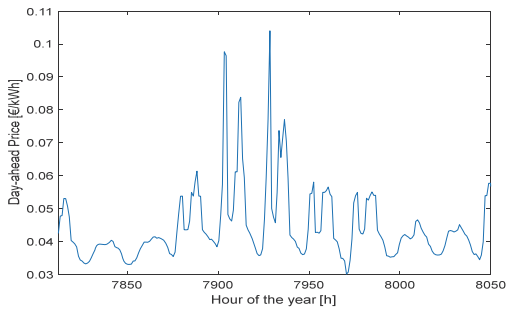


Fig. 5. Nordpool hourly day-ahead prices without additional fees and taxes for November 22nd until December 2nd, 2019

III. RESULTS

The setpoint calculation algorithms show slightly different behavior for the selected price pattern. The results for the indoor air temperature can be seen in Fig. 6. The $\pm 0.5^\circ\text{C}$ deadband is not reached in the shown curves because the data was plotted with a smoothing filter to better compare the behavior of the different algorithms.

Algorithm A, B and C show similar behavior with only slightly different setpoint selection. They vary between the maximum and minimum setpoint. This behavior considers both, user comfort and price orientation.

Algorithm D and F vary between the minimum and goal set point. This means that the setpoint is selected more price-oriented than user comfort-oriented. This was also found in [19].

Algorithm E selected set points between the minimum and the maximum. But it tends to select less extreme set points, which tend to be closer to the goal set point than the ones selected by algorithms A, B and C. This provides both, user comfort and price orientation.

Algorithm G switches between the maximum and minimum setpoint as expected. For the selected set point boundaries this might not be a comfortable temperature behavior for the user as the temperature differences are quite high.

To see which algorithm shows the best price-oriented results, the hourly price multiplied with the consumption due to heating for each hour were cumulated to see the price development over time, which is shown in Fig. 7. The final values for the cumulative costs are additionally shown in TABLE III.

At the end of the simulation time algorithms A, B and C show higher energy consumption costs than the fixed setpoint control. This is an unexpected result. Closer examination shows, that the cumulative costs show strong increases during the price peaks at around hours 7910 and 7920 and this difference only slightly decreases until the end of the simulation. The behavior is similar for algorithm G, which shows final cumulative costs around the costs of the fixed setpoint control. Even though day-ahead prices with typically

smaller fluctuations than spot prices were used for the simulations, the selected algorithms seem to show undesirable behavior for price peaks with this more detailed space heating model.

Algorithm D and F show the best price-oriented performance as expected. The cumulative energy consumption costs are the lowest. The two price peaks do not seem to have a big impact on these algorithms either.

The cumulative costs for algorithm E are lower than for a fixed set point control but higher than with algorithm D or F. The price peaks do not affect this algorithm much. Thus, this algorithm shows the best performance in total, considering user comfort and price orientation.

The user comfort and cost reductions for each algorithm are shown in TABLE III. As can be seen, the algorithms show different results with the simple space heating model from [19] compared to this model. Algorithms A, B and C provide cost reductions with the simple model, whereas the cumulative costs are higher with the IDA-ICE-model. As mentioned before, this is caused by the price peaks of the used price pattern, which are for a different time period than the ones of the simple model. Nevertheless, such an algorithm should work with all different possible price-patterns similarly good and always provide cost reductions or at least price parity with a fixed setpoint control.

IV. CONCLUSIONS

The modeled control center in IDA ICE software was suitable for the use with nanogrid simulations after the initial calibrations. The model showed the expected behavior in comparison to the measurements and could therefore be used for the setpoint algorithm control simulations.

Different load matching control algorithms were implemented to investigate the behavior of space heating as a thermal storage with such a model. To generate set points for the two-step thermostatic control, prices from the Nordpool database could be used.

Not all algorithms showed preferable behavior. Algorithms A; B and C even increased the consumption costs than a fixed set point control while providing average user comfort. Algorithm G provided a lower user comfort while achieving about the same cumulative costs like a fixed set point control. Thus, these implementations provide no benefits while adding

TABLE III. USER COMFORT COMPARED TO A FIXED SETPOINT (FSP) CONTROL AND COST REDUCTION COMPARISON BETWEEN THIS MODEL AND THE SIMPLE MODEL FROM [19]

Algorithm	User Comfort	Cumulative Costs [€]	Cost Reduction	Cost Reduction in [19]
A	0	8.65	--	+
B	0	8.56	-	+
C	0	8.59	-	+
D	--	7.76	++	++
E	0	8.27	+	+
F	--	7.80	++	++
G	-	8.53	0	0
FSP	0	8.54	0	0

++ highest; + high; 0 none; - lower; -- lowest;

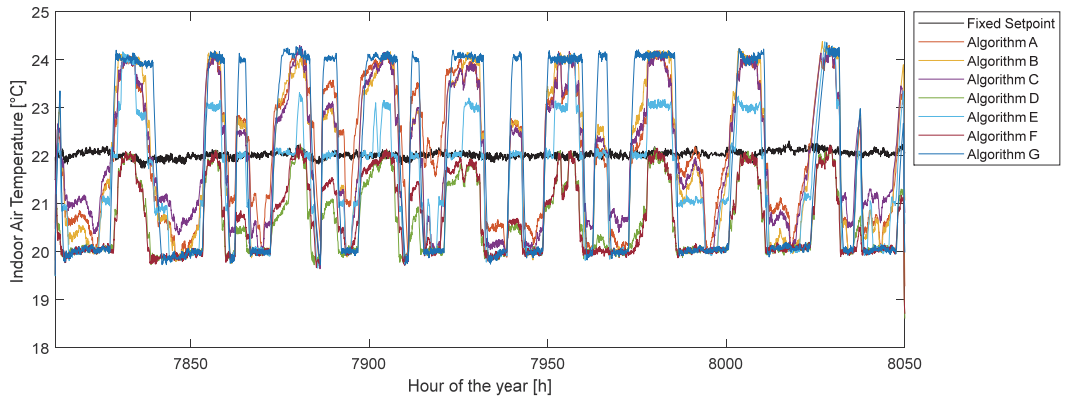


Fig. 6. Indoor air temperature results for set point calculation algorithms A-G and a fixed set point

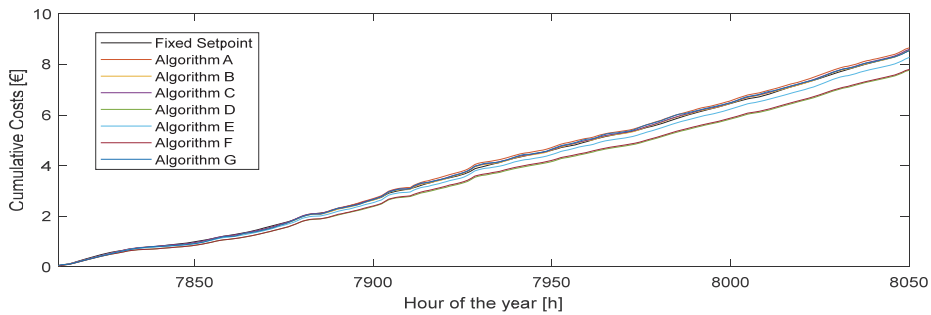


Fig. 7. Cumulative costs for setpoint calculation algorithms A-G and a fixed set point

complexity in this application case. Algorithms D and F reduce consumption costs at the cost of lower user comfort. For some users, this might be the preferred control method to achieve maximum cost reductions. Overall, algorithm E shows the best compromise of the two considerations. The consumption costs can be reduced while maintaining user comfort. Therefore, this is the preferred control strategy to control space heating based on market prices.

The results of the simulations show that such a thermal model can be used for research and development of flexibility-oriented control strategies, as the models show similar results like simple thermal models that have been used before. However, the more complex models also reveal problems of some of these algorithms to work efficiently with space heating, which were not noticed with the simple model before. Therefore, more complex models need to be taken into account for further research.

In future work, this model needs to be extended to more common heating devices such as heat pumps, and control strategies for islanded nanogrids or ancillary services should be taken into account. Using a thermal model of a complete apartment block could be useful for aggregated simulations as well.

REFERENCES

- [1] I. Palu, O. S. Grande, H. Saele, A. Rosin, A. Z. Morch, and L. Aleixo, "Ecogrid EU project - real time price based load control and economic benefits in a wind production based system," in 22nd International Conference and Exhibition on Electricity Distribution (CIRED 2013), 2013, pp. 1474–1474, doi: 10.1049/cp.2013.1253.
- [2] A. Rosin, S. Link, M. Lehtla, J. Martins, I. Drovtnar, and I. Roasto, "Performance and feasibility analysis of electricity price based control models for thermal storages in households," *Sustain. Cities Soc.*, vol. 32, pp. 366–374, Jul. 2017, doi: 10.1016/j.scs.2017.04.008.
- [3] S. Mishra, H. Koduvere, I. Palu, R. Kuhi-Thalfeldt, and A. Rosin, "Assessing demand side flexibility with renewable energy resources," in *EEEIC 2016 - International Conference on Environment and Electrical Engineering*, 2016, doi: 10.1109/EEEIC.2016.7555546.
- [4] R. Ahmadihangar, T. Häring, A. Rosin, T. Korötko, and J. Martins, "Residential Load Forecasting for Flexibility Prediction Using Machine Learning-Based Regression Model," in *Proceedings - 2019 IEEE International Conference on Environment and Electrical Engineering and 2019 IEEE Industrial and Commercial Power Systems Europe, EEEIC/I and CPS Europe 2019*, 2019, pp. 1–4, doi: 10.1109/EEEIC.2019.8783634.
- [5] International Energy Agency, *Harnessing Variable Renewables - A Guide to the Balancing Challenge*. OECD/IEA, 2011.
- [6] North American Electric Reliability Corporation, "Accommodating High Levels of Variable Generation," *North Am. Electr. Reliab. Corp.*, no. April, p. 104, 2009.

- [7] T. Häring, A. Rosin, and H. Biechl, "Using common household thermal storages to support the PV- and battery system in nearly zero energy buildings in off-grid mode," *Sustain. Energy Technol. Assessments*, vol. 35, no. May, pp. 12–24, Oct. 2019, doi: 10.1016/j.seta.2019.05.014.
- [8] V. Maask, T. Haring, R. Ahmadiyahangar, A. Rosin, and T. Korotko, "Analysis of Ventilation Load Flexibility Depending on Indoor Climate Conditions," in 2020 IEEE International Conference on Industrial Technology (ICIT), 2020, pp. 607–612, doi: 10.1109/ICIT45562.2020.9067153.
- [9] O. Kilkki, A. Alahäivälä, and I. Seilonen, "Optimized control of price-based demand response with electric storage space heating," *IEEE Trans. Ind. Informatics*, vol. 11, no. 1, pp. 281–288, Feb. 2015, doi: 10.1109/TII.2014.2342032.
- [10] B. Feron and A. Monti, "Integration of space heating demand flexibility in a home energy management system using a market-based multi agent system," in IEEE Power and Energy Society General Meeting, 2018, vol. 2018-Janua, pp. 1–5, doi: 10.1109/PESGM.2017.8273810.
- [11] M. Pau, J. L. Cremer, F. Ponci, and A. Monti, "Impact of customers flexibility in heat pumps scheduling for demand side management," in Conference Proceedings - 2017 17th IEEE International Conference on Environment and Electrical Engineering and 2017 1st IEEE Industrial and Commercial Power Systems Europe, EEEIC / I and CPS Europe 2017, 2017, doi: 10.1109/EEEIC.2017.7977681.
- [12] T. Haring, R. Ahmadiyahangar, A. Rosin, and H. Biechl, "Impact of Load Matching Algorithms on the Battery Capacity with different Household Occupancies," in IECON 2019 - 45th Annual Conference of the IEEE Industrial Electronics Society, 2019, pp. 2541–2547, doi: 10.1109/IECON.2019.8927495.
- [13] J. Clauß and L. Georges, "Model complexity of heat pump systems to investigate the building energy flexibility and guidelines for model implementation," *Appl. Energy*, vol. 255, p. 113847, Dec. 2019, doi: 10.1016/j.apenergy.2019.113847.
- [14] R. E. Hedegaard, M. H. Kristensen, T. H. Pedersen, A. Brun, and S. Petersen, "Bottom-up modelling methodology for urban-scale analysis of residential space heating demand response," *Appl. Energy*, vol. 242, pp. 181–204, May 2019, doi: 10.1016/j.apenergy.2019.03.063.
- [15] L. Georges, M. Thalfeldt, Ø. Skreiberg, and W. Fornari, "Validation of a transient zonal model to predict the detailed indoor thermal environment: Case of electric radiators and wood stoves," *Build. Environ.*, vol. 149, pp. 169–181, Feb. 2019, doi: 10.1016/j.buildenv.2018.12.020.
- [16] "Market data | Nord Pool." [Online]. Available: <https://www.nordpoolgroup.com/Market-data/Dayahead/Area-Prices/EE/Hourly/?view=table>. [Accessed: 20-Feb-2020].
- [17] H. D.J et al., "Pacific Northwest GridWise™ Testbed Demonstration Projects, Volume I: The Olympic Peninsula Project." 2007.
- [18] C. H. K. Goh and J. Apt, "Consumer Strategies for Controlling Electric Water Heaters under Dynamic Pricing," *Carnegie Mellon Electr. Ind. Cent. Work. Pap.*, pp. 1–8, 2005.
- [19] T. Haring, R. Ahmadiyahangar, A. Rosin, H. Biechl, and T. Korotko, "Comparison of the impact of different household occupancies on load matching algorithms," in 2019 Electric Power Quality and Supply Reliability Conference (PQ) & 2019 Symposium on Electrical Engineering and Mechatronics (SEEM), 2019, pp. 1–6, doi: 10.1109/PQ.2019.8818270.
- [20] T. Häring, "Research And Development Of Thermal Storage Control Models," M.Sc.Eng thesis, Tallinn University of Technology, 2018.

Tobias Häring received the B.Eng. in Industrial Engineering from Kempten University of Applied Sciences, Germany in 2016, M.Eng. in Electrical Engineering from Kempten University of Applied Sciences, Germany in 2018 and M.Sc.Eng. in Electrical Drives and Power Electronics from Tallinn University of Technology, Estonia in 2018. He is currently working as a Doctoral Student / Early Stage Researcher at Tallinn University of Technology, Estonia. His main research interests are microgrids, distributed/renewable generation, demand side management, storage technologies and machine learning.

Publication IV

J. Helguero, A. Rosin, H. Biechl. Provision of Ancillary Services of a Nanogrid in Grid Connected Mode. 2019 Electric Power Quality and Supply Reliability Conference (PQ) & 2019 Symposium on Electrical Engineering and Mechatronics (SEEM).

Provision of Ancillary Services of a Nanogrid in Grid Connected Mode

Jorge Helguero
Institute of Electrical Power Systems
University of Applied Sciences
Kempten
Kempten, Germany
jorge.helguero@hs-kempten.de

Argo Rosin
School of Engineering
Tallinn University of Technology
(TalTech)
Tallinn, Estonia*
argo.rosin@taltech.ee

Helmuth Biechl
Institute of Electrical Power Systems
University of Applied Sciences
Kempten
Kempten, Germany
biechl@hs-kempten.de

Abstract—In the future more and more conventional power plants, which provide ancillary services such as provision of reactive power for voltage control and primary control power (active power) for frequency control to the transmission system and thus secure the energy supply, are going to be replaced by renewable energy sources. Due to this fact new concepts for providing these services by renewable power sources will be necessary in the future to maintain stability of the network operation. This refers to the delivery of active and reactive power by distributed generation (DG) and distributed storage (DS). Beyond that DG and DS can be found nowadays in households or also called nanogrids. This research work presents a concept of a nanogrid that can provide ancillary services to the distribution grid in the low voltage level and transfer reactive power as well as primary control power to higher voltage levels by upscaling, which means the connection of many nanogrids. The implementation of the concept is done in a real system and also in a simulation environment that uses simplified mathematical models.

Keywords—nanogrid, photovoltaic system (PV), home battery energy storage system (HBESS), detailed model, simplified model, ancillary services, active power, reactive power

I. INTRODUCTION

Traditional power systems are changing due to the climate change policies and the increase of renewable energy sources. In other words, this means the decommissioning of conventional power plants, which secure the system stability through the provision of ancillary services [1], [2]. In the research project DeCAS** [3], funded by the German Federal Ministry of Economic Affairs and Energy (BMWi) and ERA-Net Smart Grids Plus, the focus is the provision of ancillary services through the set-up of a nanogrid demonstrator capable of deliver active and reactive power to the distribution grid. The demonstrator incorporates a 20 kVA Li-Ion home battery energy storage system (HBESS), a 7.8 kWp photovoltaic system (PV), a three-phase unsymmetrical resistive-inductive-capacitive load (30 kW/22.5 kvar) and a control center. In order to apply long simulation times the theoretical implementation is using simplified mathematical models of the DG and DS in PSCAD as discussed in [4]. On the other hand, the practical implementation of the control center was carried out in LabVIEW. Section 2 introduces the components of the nanogrid and shows the implementation of the detailed and simplified models in PSCAD for the simulation. Section 3 indicates the set-up of

the control center in LabVIEW. Section 4 presents the comparison between simulation and filed test results. In the end, summary and future work is presented.

II. SPECIFICATIONS AND MATHEMATICAL MODELS OF THE DISTRIBUTED GENERATION AND DISTRIBUTED STORAGE

A. Home Battery Energy Storage System (HBESS)

The HBESS, with a rated apparent power of 20 kVA and a capacity of 18.6 kWh, has a four-quadrant operation, which means that the HBESS is able to work with positive and negative set points of active and reactive power in grid mode. Additionally, in order to communicate with the control center, this storage system utilizes the communication protocol Modbus TCP. Fig. 1 shows the structure of the detailed model of HBESS in grid mode applied for the simulation in PSCAD. It can be seen that a bidirectional DC/DC converter was applied for charge and discharge purposes. Here the current at the output of the battery i_{bat} and the DC link voltage V_{DC} are regulated by using cascade control as mentioned in [5], [6], and [7]. Additionally, a voltage source inverter (VSI) control was implemented in order to regulate the active and reactive power at the point of common coupling (PCC) of the HBESS. This is done by using the dq0-reference frame of the voltages (v_{abc}) and the currents (i_{abc}) at the output of the filter as described in [7] and [8]. In order to reduce the simulation complexity of Fig. 1 and be able to execute long simulation time, a simplified model of the HBESS was developed as seen in Fig. 2. This simplified model consists of an equivalent resistance and inductance (due to the filter in Fig. 1) and a controlled voltage source as mentioned in [4]. For control and stability analysis respectively optimization the switching of the IGBT of the inverters can be neglected due to the low content of the harmonics in the current. This is a consequence of the filters and all the circuit inductances, mainly transformers.

B. Photovoltaic System (PV System)

The PV system of the nanogrid has a rated power of 7.8 kWp and consists of two strings. The first string has 11 panels (connected in series) with west orientation. The second string has 15 panels (connected in series) with east orientation. Each string has a 6 kVA three-phase inverter. The tilt angle of the panels is 10° and each monocrystalline panel has a rated peak power of 300 Wp. The PV inverters are able to work with a power factor between 1 and 0.4 (inductive/ capacitive).

Sending reactive power set points to the PV inverters is possible by using an RS-485/Modbus TCP converter connected to the control center of the nanogrid. In reality, the actual active power generation P_{act} of each PV inverter will be

*The Estonian partner work was supported by Research Grant PUT1680 and the Estonian Centre of Excellence in Zero Energy and Resource Efficient Smart Buildings and Districts ZEBE, grant 2014-2020.4.01.15-0016 funded by European Regional Development Fund.

**This Project has received funding in the framework of the joint programming initiative ERA-Net Smart Grids Plus, with support from the European Union's Horizon 2020 research and innovation programme.

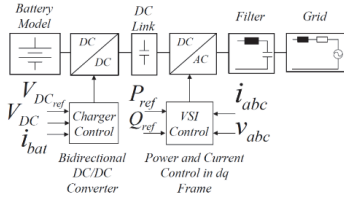


Fig. 1. Detailed model of HBESS in PSCAD.

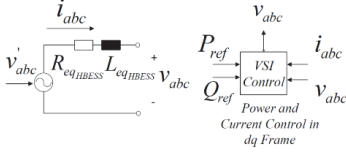


Fig. 2. Simplified model of HBESS in PSCAD.

reduced (Maximum Power Point Tracking will be switched off) so that the reactive power set point can be accomplished and the rated apparent power is not exceeded. On the other hand, it could occur that the generated reactive power by the PV inverters Q_{act} is less than the reactive power set point Q_{set} . This follows if Q_{set} exceeds the relation of (1), which is calculated by using the power factor equals to 0.4.

$$Q_{set} / P_{act} = 2.29 . \quad (1)$$

Fig. 3 shows the control structure of the detailed model of the PV system in PSCAD for one string, since the same structure was implemented for the east and west orientation. The DC/DC converter is used to maintain the voltage (V_{pv}) at the output of the PV Array stable and also to achieve the maximum power point (V_{MPP}) as mentioned in [9]. The VSI control block regulates the DC Link voltage V_{DC} (real power of the PV system) and the reactive power output by using the dq0-reference frame [10]. As mentioned in section A the execution of long simulation time requires simplified models. Fig. 4 shows the simplified model related to the PV system for one string, where the DC Link capacitor, the PV Array, the MPP and the DC Link voltage control were all omitted since it is assumed that the voltage at the DC Link is strongly controlled at a value corresponding to the maximum power point [11]. Keeping this in mind, measurements of active power of the PV system can be used as values for the variable P_{ref} of Fig. 4.

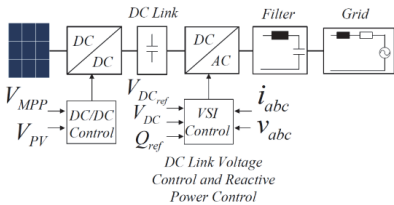


Fig. 3. Detailed model of the PV system for one string in PSCAD.

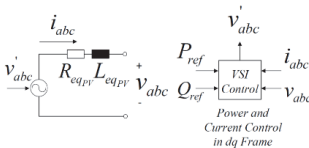


Fig. 4. Simplified model of the PV system for one string in PSCAD.

III. CONTROL CENTER OF THE NANOGRID

The control center was developed in the software LabVIEW in order to visualize measurements and to control active and reactive power at PCC of the nanogrid. As mentioned in II.A and II.B, Modbus TCP is used as communication protocol between the components of the nanogrid and the control center. In Fig. 5 the components of the nanogrid are shown when the provision of active power is applied. The control center receives the set points of active power for the point of common coupling (P_{PCC_set}) and compares the actual value at this point (P_{PCC_me}). The error between these two values is sent to a proportional-integral (PI) controller, which generates the set point for the HBESS (P_{Bat_set}) and thus compensates the active power at the PCC. On the other hand, Fig. 6 shows the components of the nanogrid with provision of reactive power at the PCC through the control center. Here the set points are sent to the LabVIEW program and automatically divided by 2. The result from the division is sent to the PV inverters. For example, if 10 kVA is applied as set point at the PCC, then the PV inverters will receive 5 kvar each. The PI controller compares the set points Q_{PCC_set} with the actual value Q_{PCC_me} and generates the set point Q_{Bat_set} for HBESS and thus compensates the reactive power at the PCC. The optimization of the control parameters of the whole system has been executed in the first step by analytical methods and finally by numerical simulation. Details will be shown in a different scientific paper in the new future.

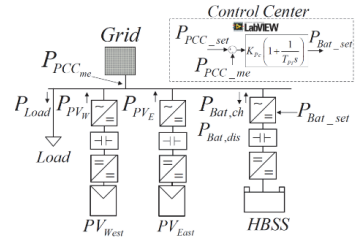


Fig. 5. Overview of the nanogrid and the control center for the provision of active power at the point of common coupling.

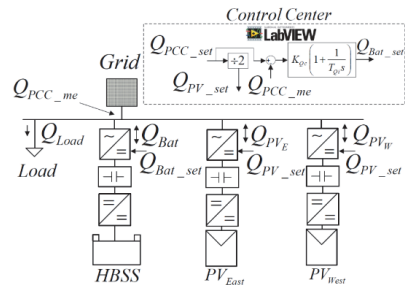


Fig. 6. Overview of the nanogrid and the control center for the provision of reactive power at the point of common coupling.

IV. RESULTS

This section includes the simulation results and the filed tests when applying two scenarios, which were implemented in PSCAD and LabVIEW, respectively:

Scenario I: The first scenario applies a profile of active power at the PCC by using the control center as seen in Fig. 5. Additionally, a constant resistive load is used for this scenario.

Scenario II: The second scenario employs a reactive power profile at PCC of the nanogrid as described in Fig. 6 and just uses a constant inductive load.

A. Scenario I: Active Power Provision at the Point of Common Coupling of the Nanogrid

The active power profile applied at the point of common coupling of the nanogrid and the constant resistive load are shown in Fig. 7a and Fig. 7b, respectively. The profile contains three types of set points. By using the first type there is no exchange of active power with the distribution grid (0 kW set points). The second type means export of active power to the external grid (positive set points). Finally, the third one stands for import of active power by the nanogrid (negative set points).

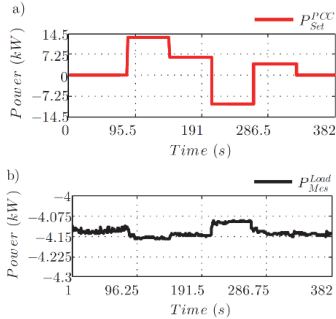


Fig. 7. Inputs for scenario I: a) Active power profile at PCC of the nanogrid; b) Measurement at the resistive load.

In Fig. 8 it is shown the results for simulation and measurements when the active power profile of Fig. 7a is applied at the PCC of the nanogrid. As mentioned in II.B, the measurements of the strings with east and west orientation are used as active power profiles for the simplified models of the PV system in the PSCAD simulation. The active power provision at PCC (simulation and measurement) worked according to the profile used in Fig. 7a. Fig. 8b also shows

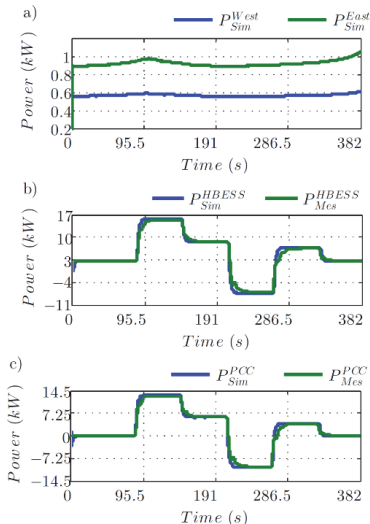


Fig. 8. Simulation and measurement results of scenario I: a) Active power of the PV system; b) Active power of HBESS; c) Active power at PCC of the nanogrid.

how the HBESS supports the nanogrid in order to accomplish the active power profile at PCC. Fig. 8a illustrates that the active power generation from the PV system (east and west orientation) is lower than the active power consumed by the load (Fig. 7b). The difference between these two values (power surplus) is negative during the 382 s of simulation and measurement time. When the active power set point is 0 kW at PCC or in case of exporting power to the distribution grid (positive set point at PCC), active power is supplied by HBESS (discharge) so that the negative power surplus is compensated and thus the requirement at the PCC is accomplished. On the other hand, when it is required that the nanogrid imports active power (negative set point at PCC), a negative value of active power is sent to HBESS (charge process of the battery). Although the steady state results of the home battery energy storage system and the point of common coupling show a very good match, there are some divergences in the transients, since communication delays are not considered in the mathematical modeling of the nanogrid.

B. Scenario II: Reactive Power Provision at the Point of Common Coupling of the Nanogrid

The reactive power profile at the point of common coupling of the nanogrid and the measurement of the applied constant inductive load are shown in Fig. 9a and Fig. 9b, respectively. The profile contains 0 kvar set points, which mean that there is no reactive power exchange with the distribution grid. Also capacitive and inductive set points (positive and negative values respectively) are used.

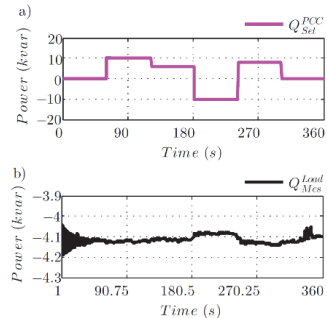


Fig. 9. Inputs for scenario II: a) Reactive power profile at PCC of the nanogrid; b) Measurement at the inductive load.

In Fig. 10 simulation and measurement results are shown when the reactive power profile of Fig. 9a is applied at the PCC of the nanogrid. The active power of the PV system with east and west orientation was around 0.7 kW and 0.5 kW, respectively. When a 0 kvar set point at PCC of the nanogrid is sent, the PV system neither supplies nor consumes reactive power. Due to the inductive load and the 0kvar set point at PCC, capacitive reactive power is provided to the nanogrid by HBESS. On the other hand, if a capacitive reactive power set point is sent to the PCC, like for example 10 kvar, the PV inverters are only able to provide reactive power according to (1) and not 5 kvar for each inverter. The inductive load consumes a part of the capacitive reactive power generated by the PV system, which originates a lack of capacitive reactive power at PCC of the nanogrid. This makes the HBESS respond due to the PI controller at PCC and deliver the necessary capacitive reactive power. In contrast, if an inductive set point of -10 kvar is applied to the PCC, the PV inverters consume reactive power as stated by

(1), since the active power production of the PV panels is low. At this point the PV system and the inductive load are consuming reactive power. This consumption is not enough at the PCC of the nanogrid. As a result, reactive power is also consumed by the HBESS in order to reach the set point at PCC.

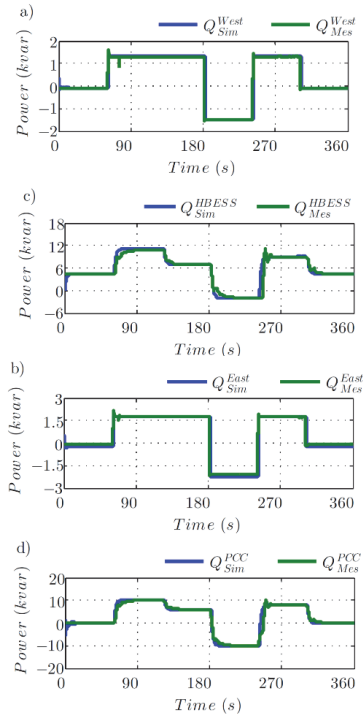


Fig. 10. Simulation and measurement results of scenario II: a) Reactive power of PV string with west orientation; b) Reactive power of PV string with east orientation; c) Reactive power of HBESS; d) Reactive power at the PCC of the nanogrid.

V. SUMMARY

This paper presents the demonstration of the provision of active and reactive power at the point of common coupling of a nanogrid in the low voltage distribution grid, whose implementation was carried out in a time domain simulation tool and verified with tests in a real grid. The comparison between simulation and measurement results of the home

battery energy storage system and the point of common coupling of the nanogrid show a very good match. There are some divergences in the transients, since communication delays are not considered in the mathematical modeling of the nanogrid. Furthermore, measurement results show that the provision of ancillary services to the distribution grid is possible by means of controllable distributed generation units (reactive power control of the PV system) and also by using distributed storages (active and reactive power control of the HBESS). In a continuation of this research work, the communication delays between the components of the nanogrid and their influence on the dynamics are taken into account in detailed.

REFERENCES

- [1] J. Birkelbach, H. Woiton, M. Thiele, and D. Westermann, "Methodology for the evaluation of the existing black start units and optimization for future locations," NEIS Conference, Hamburg, 2018.
- [2] S. Torsten, P. Philipp, A. Schnettler, R. Köberle, and M. Metzger, "Potential of the AÜW network area to provide reactive power to the transmission network level," International ETG Congress, Bonn, 2015.
- [3] "DeCAS," [Online]. Available: <http://www.decas-project.eu/>.
- [4] A. Armstorfer, N. Beg, A. Rahmoun, A. Rosin, and H. Biechl, "Mathematical modeling and evaluation of a microgrid demonstrator in island mode," NEIS Conference, Hamburg, 2017.
- [5] G. Bae and F. Kang, "Bidirectional DC-to-DC converter employing a selective switch and two inductors for optimal operation in buck and boost mode," International Conference on Electrical Machines and Systems, Busan, 2013.
- [6] R. de Castro, J. Trovão, P. Pacheco, P. Melo, P. Pereirinha, and R. Araújo, "DC link control for multiple energy sources in electric vehicles," IEEE Vehicle Power and Propulsion Conference, Chicago, 2011.
- [7] A. Arancibia, K. Strunz, and F. Mancilla-David, "A unified single- and three-phase control for grid connected electric vehicles," IEEE Trans. on Smart Grid, 2013.
- [8] A. Yazdani and R. Iravani, Voltage-Source Converters in Power Systems, Wiley-IEEE Press, 2010.
- [9] J. Li, F. Zhuo, X. Wang, L. Wang, and S. Ni, "A grid-connected PV system with power quality improvement based on boost-dual-level four-leg inverter," IEEE 6th International Power Electronics and Motion Control Conference, Wuhan, 2009.
- [10] A. Yazdani and P. Dash, "A Control methodology and characterization of dynamics for a photovoltaic (PV) system interfaced with a distribution network," in IEEE Trans. on Power Delivery, 2009.
- [11] J. Martínez-Velasco, Transient Analysis of Power Systems, Wiley-IEEE Press, 2015.

Publication V

S. Uebermasser, C. Groiss, A. Einfalt, N. Thie, M. Vasconcelos, J. Helguero, H. Laaksonen, P. Hovila. Requirements for coordinated ancillary services covering different voltage levels. 24th International Conference & Exhibition on Electricity Distribution (CIRED) and IET Journals, Volume 2017, Issue 1, October 2017, p. 1421-1424.

Requirements for coordinated ancillary services covering different voltage levels

Stefan Uebermasser¹ ✉, Christoph Groiss², Alfred Einfalt³,
Nicolas Thie¹, Maria Vasconcelos⁴, Jorge Helguero⁵,
Hannu Laaksonen⁶, Petri Hovila⁶

¹Austrian Institute of Technology (AIT), Vienna, Austria

²Salzburg Netz GmbH, Salzburg, Austria

³SIEMENS, Vienna, Austria

⁴RWTH Aachen, Aachen, Germany

⁵Hochschule-Kempton, Kempton, Germany

⁶ABB Oy, Vaasa, Finland

✉ E-mail: stefan.uebermasser@ait.ac.at

Abstract: The massive development and implementation of small- and medium-scale generation units within the distribution grids result in novel needs and options for ancillary services. The project DeCAS develops solutions for the coordinated activation of ancillary cross-voltage-level services considering the different objective functions of individual voltage levels. This study aims to analyse, define and describe common requirements focusing on a technical, stakeholder and market perspective.

1 Introduction

Power systems have been operated successfully as a combination of large generators, transmission and distribution grid for decades. The European legislation with the related electricity market liberalisation and renewable energy support led to the massive development and implementation of small- and medium-scale generation units (distributed generation, DG), which are usually connected near the consumption mainly in low-voltage (LV) and medium-voltage (MV) networks. Many existing research projects in the field of smart grids focus on the DG integration and on increasing the hosting capacity at one specific voltage level as well as on an individual market and with regard to singular stakeholder aspects. Combining smart grid control and operation algorithms across voltage levels (from LV up to the high-voltage [HV] level), the project DeCAS [1] is the next step, when addressing the challenges of an increasing share of DG from a technical and market perspective. DeCAS is an ERA-Net Smart Grid Plus [2] funded project (launched in February 2016) and aims for mainly two aspects:

- To research and analyse the coordination of ancillary services such as aggregated ‘prosumer’ response control reserve, individual voltage control and reactive power management concepts over traditional boundaries from HV, MV to LV.
- To develop approaches and concepts for a coordinated control approach considering the different objective functions of individual voltage levels. It will include the integration related to monitoring and controls in process control systems as well as to existing and future markets for flexibility.

In order to fulfil these objectives, nine partners from four countries are part of the project DeCAS (see Fig. 1). The DeCAS partners are grouped into three demonstrator sites, so-called innovation cells (ICs), consisting of the respective national partners of the cell (Germany, Austria or Finland). The individual solutions implemented at the three ICs aim for a prototype demonstration of selected ancillary services at different operational environments.

This paper aims to analyse, define and describe common requirements based on the experiences of the individual demonstrator’s (ICs) along to the three research layers:

- Technical requirements** for the HV/MV/LV interaction: Investigation of solutions for the coordinated activation of ancillary cross-voltage-level services considering the different objective functions of individual voltage levels.
- Requirements for **stakeholder integration**: Identification and analysis of benefits and/or barriers regarding the integration of relevant stakeholders (e.g. generators or prosumers).
- Requirements from a **market perspective** for the IC (but also defining requirements for future markets): Focus on market-based solutions as part of network control to involve stakeholders of generation and/or demand side management in future markets.

2 IC Austria

IC Austria is focusing on coordinated voltage control based on existing research infrastructure within the distribution grid area of Salzburg Netz, which includes MV as well as LV networks. Besides Salzburg Netz [3], the IC partners include Siemens [4], AIT [5] and TU-Vienna [6]. This IC enhances concepts and results of the prior projects ZUQDE [7] and LEAFS [8]. As one of the enhancements an intelligent substation (MV/LV interface) will be connected to the supervisory control and data acquisition (SCADA) system to control the reactive power flow over system boundaries.

2.1 Technical requirements

Fig. 2 shows the target schematics of IC Austria mapped to smart grid architecture model (SGAM). The aim of this specific IC is to establish a coordinated Volt-Ampere reactive (VAr) control between HV, MV and LV grids taking augmented concepts for LV grid operation into consideration.

Traditional network operation, still dominant today, is based on three distinct control levels: the HV transmission network with voltage and frequency control, the MV distribution network with

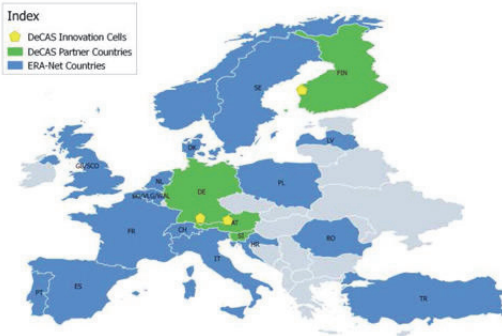


Fig. 1 Location of the DeCAS ICs

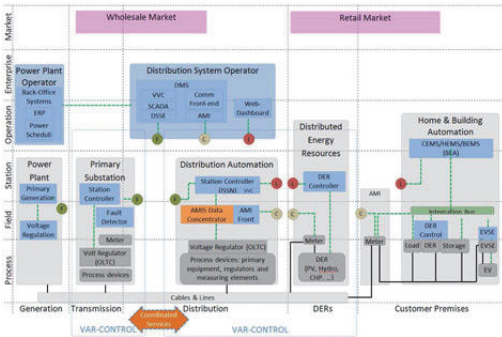


Fig. 2 SGAM mapping of IC Austria

basic voltage control and the LV distribution network, without observability and controllability. This topology is also reflected in most smart grid pilot projects, focusing on the three levels separately. However, with the rising share of DG the influence between the levels will become substantial, and will require addressing the interaction between HV, MV and LV networks. The coordinated network control will form the basis for the definition of new ancillary and market services, and will be tested via simulations and validated on field. A coordinated approach is essential to analyse the interdependencies across voltage levels to guarantee overall system stability with increased hosting capacity at LV and MV level. The northern part of the federal state of Salzburg was chosen as field trial region. This part of the grid is also modelled in an additional, project-specific SCADA system. Also the intelligent substation network (iSSN) Köstendorf is included in the field trial area. Hence, it will be possible to demonstrate the interface and the interaction of the central SCADA system with a decentralised intelligent local grid.

2.2 Stakeholder adoption

The implementation of a smart grid will impact different stakeholders such as customers (prosumers), network operators, aggregators and market actors. In future, the classic consumer will be substituted by prosumers which are operating DG, flexible loads like e-cars and battery storage systems. Through demonstration activities and description of best practices the DeCAS project will reduce the barriers for engaging the prosumers, as well as technicians and other staff at distribution system operators (DSOs) in smart grid topics and describes how to take part in future ancillary service provision. Therefore one part of the planned project will evaluate promising concepts for LV

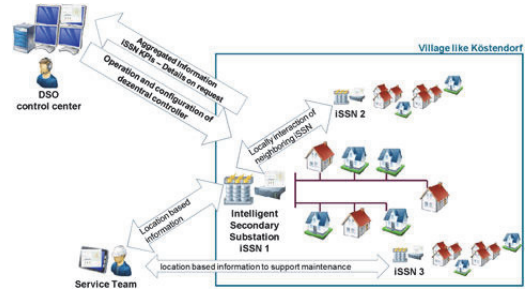


Fig. 3 Exemplary use cases for IoT-based operation of iSSNs

grid operation e.g. transferred from the world of Internet of things (IoT), bringing the stakeholders together. Fig. 3 shows some exemplary use cases for IoT-based operation of iSSNs as well as shows how they could interface with MV/HV SCADA DMS as described above.

In this project, a true interaction between the decentralised controllers (= iSSN) on the LV/MV side and the substation on the MV/HV side will be designed and implemented in a proof-of-concept/field test. To avoid flooding of the control centre, the iSSNs aggregate and process the collected data from prosumer’s technical representatives (e.g. a Customer Energy Management System) and provide key performance indicators. If necessary, more detailed information can be requested by network operators or planners. A further important advantage gained by using IoT for the iSSN is that local information can be provided directly to service teams.

2.3 Market requirements

Future distribution grids will include a range of flexibilities, but these are often not owned by DSOs, but rather by prosumers or independent plant operators. Inter-voltage level ancillary services contracted bilaterally or via flexibility markets could create an incentive for aggregators and prosumers to offer their flexibility also to DSOs or attract DSOs to act as platform operator. However, markets are not in the scope of the developments around the IC Austria.

3 IC Germany

The IC Germany focuses on the provision of reactive power within and across grid levels in the context of a comprehensive operational planning process for local virtual power plants (LVPP) [9]. The IC builds on the IRENE and IREN2 projects [10], in which a LVPP in a local LV grid is set up. In DeCAS, the LVPP will be scaled up by including distributed energy resources (DER) connected to the MV grid. Additionally, the IC Germany will add new DER in the LV grid expanding the demonstrator from the projects IRENE and IREN2. Furthermore, the operational planning process will be extended by an intraday planning process to make better use of short-time generation and load forecasts. In general, virtual power plants (VPPs) are a concept to improve market participation of DER. The IC partners include Allgäu Netz GmbH [11], University of Applied Sciences Kempten and RWTH Aachen.

3.1 Technical requirements

The LVPP set up in the IC Germany includes various DER units e.g. photovoltaic (PV), combined heat and power (CHP) and storage units, which are controlled according to the planned day-ahead schedule via a control system. The operational planning process uses day-ahead generation forecasts as well as real-time grid measurements. Based on this data, a reactive power demand that

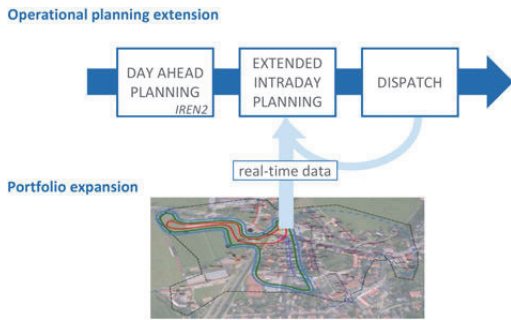


Fig. 4 Scale up of the LVPP infrastructure

represents the demand of the transmission system operator is derived and an optimal aggregated reactive power schedule is calculated. The scale up in DeCAS requires several extensions of the technical infrastructure as well as the operational planning software (cf. Fig. 4).

The extension of the existing microgrid consists of a nanogrid and a controllable biogas CHP (biogas-CHP) plant. The nanogrid is implemented as a smart home including a home battery system, a controllable PV system, and a power-to-heat (P2H) system. The integration of MV units requires a communication interface to the DSO's SCADA system. Due to network security issues, a direct control of DER in the MV grid is not possible. Therefore, an open-loop control via the DSO's control system will be installed, during which the DSO tries to carry out the planned schedule. The expansion of the metering infrastructure to higher grid levels is necessary to analyse the potential of the LVPP's reactive power provision not only from the LV to the MV grid but also to the HV level. Apart from measurements in the MV feeder, the power flow across the HV/MV transformer is an important evaluation criterion to assess the potential. The extensions regarding the operational planning aim at complementing the day-ahead planning process (once every 24 h) by an intraday planning process (hourly). Further automation of the planning process is necessary to realise the short-term planning stage. This relates mainly to the data transfer from and to the control system as well as to the planning algorithm itself. Furthermore, intraday planning requires the update of day-ahead generation forecasts to generate the required input for the planning process. For this purpose, real-time data can be used to correct the day-ahead forecasts' deviations, yielding updated and more accurate intraday forecasts.

3.2 Stakeholder adoption

The realisation of the scale up to the MV-grid level requires additional participants compared to the existing LVPP at LV level. Therefore, the owners of generation units connected to the MV grid i.e. large-scale PV and CHP units, willing to participate in the field test must be recruited. The participation entails allowing the remote control of reactive power feed-in during the field test as well as the installation of additional metering equipment. In addition, further involvement of the DSO is necessary to enable control of units at MV-grid level. The DSO has to dispatch the planned schedules to the respective generation units. Hence, a communication interface in the form of an open-loop control between the operational planning software and the DSO's control system is necessary.

3.3 Market requirements

In addition to the grid-oriented provision of reactive power, the IC Germany aims to investigate the market integration of DER into the energy markets. This investigation is carried out within a simulation environment, independent of the field test. The current

market framework with high requirements regarding minimum volume, block offers and the compliance with the reported schedule obstruct the market participation of VPPs including intermittent generation. Therefore, two approaches to further improve the market participation of VPPs are investigated in this project. The first approach targets the mitigation of market risks caused by intermittent generation. Possible countermeasures include the regional distribution of generation as well as the use of new developed futures products to hedge against risks [12, 9]. The second approach investigates the impact of different market frameworks on the market integration of VPPs. Therefore, frameworks from various European market areas are analysed and included in the simulation environment. The efficiency of the two approaches regarding the market participation of VPPs is analysed and compared using the simulation environment. The investigation requires an adequate data basis for

- local forecasting errors of intermittent generation,
- market data of futures products,
- market data of different European market areas.

4 IC Finland

Sundom Smart Grid (SSG) [13] in Vaasa, Finland (Fig. 5) is a smart grid pilot of ABB Oy, Vaasan Sähkö (local DSO), Elisa (telecommunication company, previously Anvia) and University of Vaasa. SSG serves as Finnish IC in the DeCAS project. IC Finland concentrates on research and development of future active network management (ANM) schemes and related technical flexibility service market structures as well as on development of future-proof islanding detection functionalities.

4.1 Technical requirements

IC Finland, ABB in cooperation with University of Vaasa, utilises accurate measurement data from multiple points and control of available DG units (Wind turbine 3.6 MW, PV unit 33 kW, Fig. 5) on the research and development of different new centralised/ decentralised combined islanding detection schemes [14] and local (DSO) ANM schemes (Fig. 6) which can fulfil multiple targets simultaneously during grid connected operation.

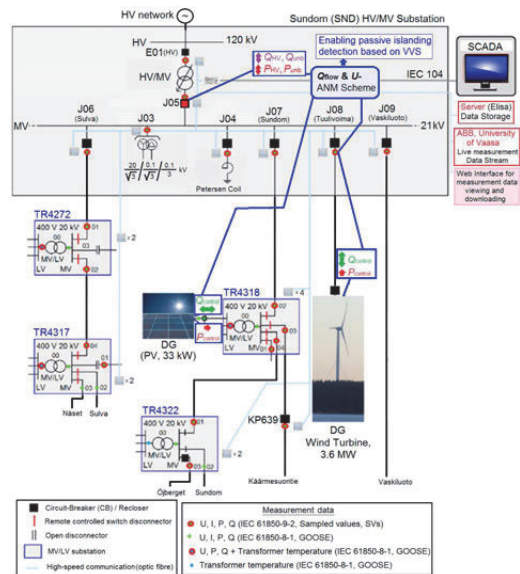


Fig. 5 Schematics and topology of the IC Finland

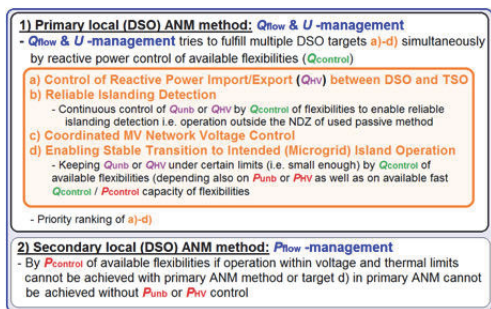


Fig. 6 ANM scheme which can fulfill multiple MV network targets simultaneously

In addition, coupling and potential mutual effects between ANM schemes/targets of different voltage levels (MV/LV) or levels of FlexZones [15] and between local (DSO) and system-wide (TSO) flexibility service schemes will be studied. Studies are expected to show, for example, (a) what is the effect of LV network ANM methods on MV network ANM methods and vice versa, (b) what is the effect of local (DSO) MV network ANM methods (i.e. Q_{flow} and U and P_{flow} management, Fig. 5) on available system-wide (TSO) flexibilities/flexibility forecasts (from that particular DSO network) and (c) how possible system-wide (TSO) flexibility services like P_{ff} control may effect local (DSO) level for example on congestion management (voltage and thermal limits) and on available local (DSO) flexibilities for primary and secondary local ANM schemes. Different scenarios related to above issues will be studied by simulations with larger amount of different available flexibilities connected in MV and LV network than today (Fig. 5).

4.2 Stakeholder adoption

The realisation of Q_{flow} and U -ANM scheme (Fig. 6) in IC Finland (Fig. 5) requires coordinated reactive power control of MV and LV network connected DG units and their owners' willingness to participate. These ANM schemes could be realised alternatively in DSO SCADA or by decentralised, hierarchical and coordinated management solutions at HV/MV, MV/LV substations with management units called FlexZone units (FZUs) [15] including future-proof protection and islanding detection functionalities [14]. In the future, one alternative could be that some of the less critical/high-speed communication-dependent DSO FZU functionalities like ANM schemes would be located in cloud servers.

4.3 Market requirements

IC Finland also studies possible future retail and technical flexibility (ancillary) service market structures in Europe and market models for future ANM schemes (like in Fig. 6) and effects on different

Table 1 Summary based on the three layer approach

Innovation cell	Ancillary service	Stakeholder involvement	Market
Austria	voltage control (HV/MV/LV)	TSO, DSO, generators, consumers	n.a.
Germany	reactive power (MV/LV)	DSO, generators, consumers	day ahead
Finland	ANM and islanding detection (HV/MV/LV)	TSO, DSO, generators, consumers	future markets for ANM

parties considering coupling/potential challenges between local (DSO) and system-wide (TSO) needs.

5 Conclusion and outlook

The previous chapters including the descriptions of the ICs provide insight into the different thematic orientations of the national demonstrators. Overall, a variety of different approaches for ancillary services are being developed, implemented and tested at the ICs. Besides the focus on cross-voltage-level services, the main commonalities and challenges at the ICs based on the three-layer approach are:

- technical perspective: voltage level services,
- stakeholder perspective: participation of owners of DGs,
- market perspective: applicability of (future) flexibility markets.

Table 1 provides a summary from the approaches of different ICs.

The three ICs are following diverse approaches. While IC-Austria focusses on the technical aspect of coordinated network control over all voltage levels, the LVPP of the German IC tries to bridge the gap between centralised energy markets and local network constraints and at IC Finland islanding detection under future conditions is also investigated. Regarding the stakeholder perspective the ICs require a participation of the owners of DGs that take part in ancillary service provision. Project DeCAS aims to ensure replicability and scalability of the developed services. Therefore, the next steps include the development of system models of the individual ICs for simulation and analysis purposes. The exchange of knowledge and experiences will be based on this joint simulation platform. This is expected to lead to project-wide technical recommendations for further developments within DeCAS.

6 Acknowledgments

This project has received funding in the framework of the joint programming initiative ERA-Net Smart Grids Plus, with support from the European Union's Horizon 2020 research and innovation programme.

7 References

- 1 DeCAS –Project: [Online]. Available at www.decas-project.eu, accessed 05 September 2016
- 2 ERA-Net-SG+: [Online]. Available at www.eranet-smartgridsplus.eu, accessed 01 September 2016
- 3 Salzburg Netz: [Online]. Available at www.salzburgnetz.at/content/website_salzburgnetz/de_at.html, accessed 21 December 2016
- 4 Siemens Österreich-Austria: [Online]. Available at www.siemens.com/at/de/home.html, accessed 21 December 2016
- 5 AIT Austrian Institute of Technology: [Online]. Available at www.ait.ac.at, accessed 21 December 2016
- 6 TU Wien: [Online]. Available at www.tuwien.ac.at, accessed 21 December 2016
- 7 ZUQDE: [Online]. Available at <http://ses.jrc.ec.europa.eu/zuqde>, accessed 13 September 2016
- 8 Project -Leafs: [Online]. Available at www.ait.ac.at/departments/energy/smart-grids/smart-grids-projects/leafs, accessed 05 September 2016
- 9 Sowa, T.: 'Modellierung der einsatzplanung lokaler virtueller kraftwerke', RWTH Aachen, Aachen, 2016
- 10 'IREN2' [Online]. Available at www.iren2.de/en, accessed 05 September 2016
- 11 'AllgäuNetz' [Online]. Available at www.allgaeunetz.com, accessed 21 December 2016
- 12 Wind-Power-Futures: 'European Energy Exchange', 2016 [Online]. Available at www.eex.com/de/produkte/energiewendeprodukte/wind-power-futures, accessed 13 January 2017
- 13 Sundom Smart Grid: [Online]. Available at <http://ses.jrc.ec.europa.eu/sundom-smart-grid-ssg>, accessed 05 September 2016
- 14 Laaksonen, H., Hovila, P.: 'Future-proof islanding detection schemes in Sundom smart grid'. Presented at the CIRED, Glasgow, Scotland, 2017
- 15 Laaksonen, H., Hovila, P.: 'Flexzone concept to enable resilient distribution grids -possibilities in Sundom smart grid'. Presented at the CIRED 2016 Workshop, Helsinki, Finland, 2016

Publication VI

A. Rahmoun, A. Armstorfer, J. Helguero, H. Biechl, A. Rosin. Mathematical modeling and dynamic behavior of a Lithium-Ion battery system for microgrid application. 2016 IEEE International Energy Conference (ENERGYCON).

Mathematical Modeling and Dynamic Behavior of a Lithium-Ion Battery System for Microgrid Application

Ahmad Rahmoun^{1,2}, Andreas Armstorfer^{1,2}, Jorge Helguero¹, Helmuth Biechl^{1,2}

¹Institute of Electrical Power Systems (IEES)

¹University of Applied Sciences Kempten

¹Kempten, Germany

ahmad.rahmoun@hs-kempten.de, andreas.armstorfer@hs-kempten.de,

jorge.helguero@hs-kempten.de, biechl@hs-kempten.de

Argo Rosin²

²Faculty of Power Engineering

²Tallinn University of Technology

²Tallinn, Estonia

argo.rosin@ttu.ee

Abstract—This paper deals with the analysis and simulation of a stationary battery system for microgrid application, where the system structure including battery cells, inverters, filters, transformers, control system and a simplified grid model is described and modeled mathematically. For the simulation of the whole system the software PSCAD™ is used. In the first part several equivalent circuit models for Lithium-Ion cells will be compared in order to model the dynamic behavior of the battery system. Particularly the evaluation of the effect of the model's complexity on the dynamics of the entire system will be investigated.

In the second part, the dependency of state of charge (SOC), temperature and aging effects of the Lithium-Ion cells on electrical system quantities will be shown.

It is also investigated the fact that a high frequency battery model has to be taken into account to describe the cells' dynamics if an inverter with Pulse Width Modulation is used.

Index Terms—Microgrid, Batteries Energy Storage, Lithium Batteries and Power System Modeling

I. INTRODUCTION

The research project IREN2 (Future Oriented Electricity Grids for Integration of Renewable Energy Systems) runs from 2014 to 2017 and is executed in a cooperation between the German entities Siemens AG, the electricity supplier Allgäuer Überlandwerk GmbH, ID.KOM, the University RWTH Aachen and the University of Applied Sciences Kempten. The main goals are: the development of mathematical models to analyze the dynamic behavior of microgrids including new control concepts on the one hand, and setting up a real system in the village Wildpoldsried in the south of Germany on the other hand. The microgrid consists of renewable energy sources, a stationary 300kVA/170kWh battery system with Lithium Nickel Cobalt Oxide (NCO) - Titanate cells, an 100kVA Genset with vegetable oil fueling for secondary control, a 500kVA back to back station between the 20kV and the 400 V grid for test purposes and a 3x 50kW unsymmetrical load bank.

The Energy Storage System (ESS) which is analyzed in this paper is a modular system consisting of 6 independent

strings. Each string consist of a Lithium-Ion (li-ion) battery, an inverter and a filter [1]–[3]. Three strings are connected via a transformer to the grid. For this paper only one string is examined. Fig. 1 shows the block diagram of the system.

II. EVALUATION OF THE EQUIVALENT CIRCUIT MODELS' COMPLEXITY

In this section three different Equivalent Circuit Model (ECM) are used in order to simulate the electrical dynamics of the li-ion cells which are utilized in the ESS, the One Time Constant (OTC) model, the Two Time Constants (TTC) model and the Three Time Constants (DTC) model. As shown in Fig. 2 the ECM models consist basically of an ideal voltage source representing the cell's Open Circuit Voltage (V_{oc}) and an impedance composed of parallel RC-elements connected with an ohmic serial resistance. The number of the RC-elements defines the order of the ECM and all the model's parameters are functions of State of Charge (SOC), cell's temperature and State of Health (SOH). The ECM's parameters are identified by applying a sequence of current pulses on the cell then employing the voltage and current measurements in time domain. For optimization using multiple exponential functions, the identification procedure is shown in details in [4], [5]. The identified ECM parameters of one cell are stored in Lookup Tables (LuTs) to be accessed and adapted during the simulation run depending on SOC, cell's temperature and SOH, then they are converted based on the number of cells in parallel and series resulting in a battery model of one string.

In order to choose the right battery's model for the simulation of the ESS, the accuracy of the battery models in estimating the battery's output voltage is evaluated, hence a simulation benchmark is designed, in which the OTC, TTC and DTC models are simulated for an active power pulse of $P_{set}=50kW$ for 5 sec, the initial conditions of the simulation are $SOC=60\%$, $T=20^{\circ}C$ and $SOH=aged/new$ (new: no cycles, aged: after approx. 640 full cycles). The active power pulse (P_{set}), battery current (I_{bat}), battery output voltage (V_{bat}) and

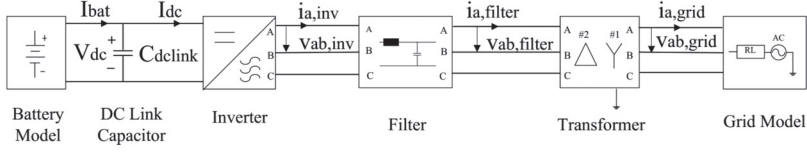


Fig. 1. ESS Structure (for 1 string).

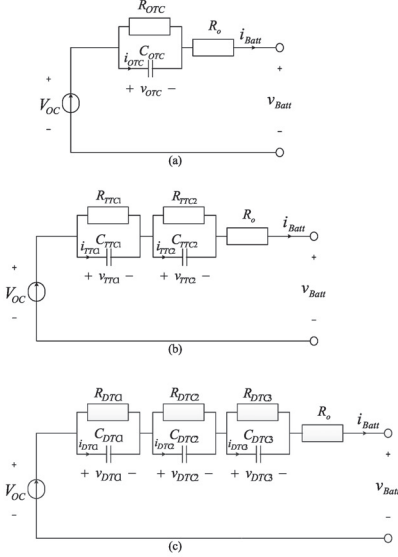


Fig. 2. Battery equivalent circuit diagrams. (a): one time constant model (OTC); (b): two time constant model (TTC); (c): three time constants model (DTC).

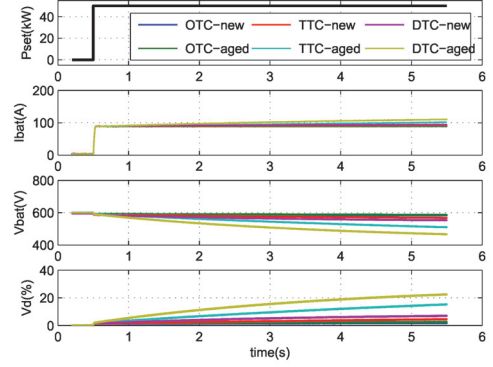


Fig. 3. A comparison between the OTC, TTC and DTC models in estimating the cell output voltage for a new and aged cell.

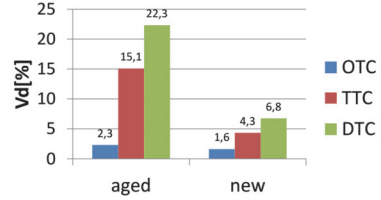


Fig. 4. Voltage difference evaluation of OTC, TTC and DTC models for a new and an aged cell.

the relative voltage difference (V_d) between (V_{bat}) and V_{oc} are plotted in Fig. 3.

The V_d diagram in Fig. 3 shows that the model order plays a bigger roll as the battery ages, so in order to demonstrate the variation between the different models regarding (V_{bat}) calculation, the V_d at the end of the active power pulse is displayed in Fig. 4 for a new and an aged cell. The Fig. 4 manifests that for a new cell, the difference between the three models is about 5 %, but as the cell ages, the difference between the OTC and the TTC models increases faster than the difference between the TTC and DTC models. The reason behind this behavior is that the OTC is very influenced by the long time constants of the cell, thus the TTC and DTC models which include short time constants, lead to bigger voltage drop than the OTC model in the short time range. Based on these evaluation results the DTC model is used for all of the next simulations since it is a capable model to describe the cell behavior for both short and long time ranges.

III. STEADY STATE ANALYSIS

The steady state behavior of the complete system depending on SOC, temperature and aging is analyzed in the following. As described above, the DTC battery model is used for simulation. A reference active power step of 25 kW controlled at the filter output is applied to the system. For variation of SOC, temperature and aging, 9 battery settings are defined and compared (Tab. I). For aging it is distinguished between new cells, aged cells and - to show the effect of dc link voltage drop - an old cell with $SOH \approx 0.87$.

A. Voltage Drop at DC Link

Due to the battery dynamics taken into account by the DTC model, the decrease of the dc link voltage (V_{dc}) depends on: SOC, aging and temperature (Fig. 5). It is illustrated that old cells at the end of their lifetime (setting No. 7) have an early

TABLE I
BATTERY SETTINGS FOR SIMULATION

No.	SOC (%)	Temp. (°C)	Aging
1	30	20	new
2			aged
3	30	35	new
4			aged
5	70	20	new
6			aged
7	70	35	new
8			aged
9	30	20	old

limitation of the maximum power due to the under voltage protection of the system (at $V_{dc} = 450V$). Thus for further analysis it is not taken into account anymore.

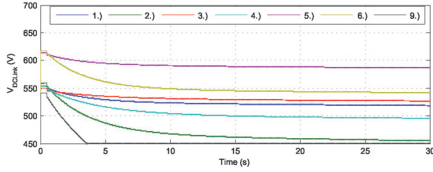


Fig. 5. Battery Voltage Response for a 25kW Active Power Step.

The relative voltage drop at the dc link is investigated as well as the corresponding battery current (rms value).

The relative voltage drop Δv_{dc} is defined as the difference between open circuit voltage V_{OC} and $V_{dc}(30s)$ (1):

$$\Delta v_{dc} = (V_{OC} - V_{dc}(30s))/V_{OC} * 100\% \quad (1)$$

1) *Dependency on SOC:* For SOC dependency simulation, the settings No. 1,2 are compared with the settings No. 5,6. The temperature is kept at 20°C while SOC and aging is varied.

New cells show a relative voltage drop of approx. 6.6% at $SOC = 30\%$ and approx. 4.7% at $SOC = 70\%$ when applying the mentioned active power step. For aged cells, the relative voltage drop is approx. 19.4% at $SOC = 30\%$ respectively 12.8% at $SOC = 70\%$ (Fig. 6).

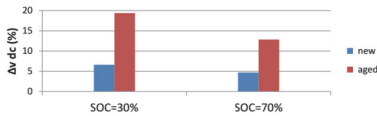


Fig. 6. Relative Voltage Drop at the Battery Terminals after a 30s Power Step.

For the cells used in our ESS it could be shown that the influence of aging has a similar importance than SOC concerning battery voltage dynamics.

Battery currents I_{bat} vary depending on SOC and aging (Fig. 7). As the power at the filter output is controlled to achieve a constant value, a lower dc voltage V_{dc} leads to a higher battery current I_{dc} .

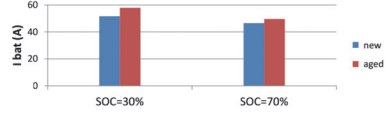


Fig. 7. Battery Current (RMS).

2) *Dependency on Temperature:* The cell temperature as an influence to the system behavior is analyzed in this section. The SOC is set to 30% while temperature (20°C/35°C) and the aging (new/aged) are varied according settings 1-4 (Tab. I). As a result, a higher temperature leads to a voltage drop reduction. Nevertheless, aging effects play a more dominant role than temperature (Fig. 8) in this range.

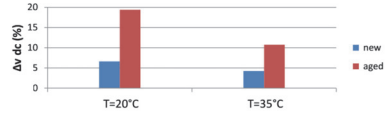


Fig. 8. Relative Voltage Drop after 30s Power Pulse.

B. Harmonics Dependency at the Grid Side

The influence of SOC, temperature and aging of Li-Ion cells on the system's power quality was investigated. Hence the harmonic distortion of the grid current is analyzed. The Fast Fourier Transform (FFT) shows dominant content at order N=1 (50Hz, grid frequency), at order 157 and 161 (7850Hz and 8050Hz, side-bands of switching frequency) as well as at order 317 and 319 (side-bands of the double of switching frequency (15850Hz, 15950Hz)). Hence, for current THD determination only these dominant orders (N=157, N=161, N=317, N=319) are taken into account (2):

$$THD_I = \sqrt{\frac{V_{157}^2 + V_{161}^2 + V_{317}^2 + V_{319}^2}{V_1^2}} \quad (2)$$

In mains parallel operation, current harmonic distortion is low and practically independent from the SOC, temperature (20°C ... 35°C and aging (Tab. II).

C. Steady State Conclusion

It is shown that due to the power control the ac behavior of the battery storage system at the grid side is independent of the SOC and the cell's temperature. This applies as long as the dc voltage does not fall below the under voltage limit. To reach this minimum voltage depends mainly on the parameters SOC, SOH and active power demand.

TABLE II
TOTAL HARMONICS DISTORTION (THD) OF GRID CURRENT

Case	SOC (%)	Temp. (°C)	Aging	THD _I (%)
1	30	20	new	0.80
2	30	20	aged	0.86
3	70	20	new	0.75
4	70	20	aged	0.78
5	30	35	new	0.80
6	30	35	aged	0.82

IV. EVALUATION OF THE ENERGY STORAGE SYSTEM IN THE HIGH FREQUENCY RANGE

The usage of the Pulse Width Modulation (PWM) technique with a switching frequency of $f_s = 7.95kHz$ results, in a high frequency voltage and current harmonics. Therefore, the evaluation of the dc-side signals requires knowledge of the battery dynamics within the High Frequency (HF) range. For this reason the battery's behavior within the HF range is investigated in subsection IV-A, next the necessity of using a HF model is explained in subsection IV-B, and finally the influence of SOC, temperature and SOH on the battery's impact is presented in subsection IV-C.

A. High Frequency Battery Model

The Electrochemical Impedance Spectroscopy (EIS) measurement technique is used to inspect the cell's dynamic characteristics within the $[3kHz, 30kHz]$ frequency range, though several impedance measurements have been done for the operation conditions (1-8) mentioned in Table I describing the dependency of the cell's dynamics on the SOC, the temperature and the SOH. At the first step a 1RL-model is adapted to the complex impedance measurements using the Levenberg-Marquardt Complex Nonlinear Least Squares (CNLS) algorithm, the 1RL-model shown in Fig. 11 (a) forms the equivalent circuit diagram of the cell in the HF range, so it consists of an ideal voltage source representing the cell's Voc wired to an impedance consisting of one RL-element and a serial resistance R_o connected in series. The 1RL-model's impedance together with the cell's measured impedance are plotted in Fig. 12 in bode and nyquist diagrams showing that the 1RL-model fits the measurements well, but the error diagram in Fig. 12 shows that the relative error varies within the $[3kHz, 30kHz]$ range, having a local minimum less than 5% around $7kHz$ then increasing in both directions to about 13% at the range limits. In order to reduce the error over the whole frequency range, one more RL-element is connected in series to the 1RL-model resulting in the 2RL-model shown in Fig. 11 (b). The 2RL-model's impedance in Fig. 13 shows clearly with a relative error less than 3% over the whole frequency range that 2RL-model guarantees a very good accuracy.

The 1RL-model resp. 2RL-model parameters are depicted in Fig. 14 and Fig. 15 for the different operation conditions, it can be seen that both models' parameters are influenced

mainly by aging. Both models are implemented in PSCAD by extending the Low Frequency (LF) part in the battery's model (consisting of RC-elements) with the HF part (consisting of RL-elements) as it is drawn in Fig. 10. The parameters of the HF models are stored in LuTs in order to be accessed and adapted during the simulation run according to the SOC, the cell's temperature and the SOH.

B. Impact of the Battery Behavior on the DC Currents within the HF Range

In order to show the impact of the battery's HF model on the dc currents in the HF range, the ESS is simulated for three different cases:

- 1) Without using HF-model
- 2) Using the 1RL-model
- 3) Using the 2RL-model

In every case an active power pulse of $P = 50kW$ and a reactive power $Q = 0kvar$ are applied for all the operation conditions (1-8) in Table I. The FFT of both I_{bat} and I_{dc} are plotted in Fig. 9 showing the main current harmonics when using the 2RL-model for (SOH: aged, SOC=70 %, T=35 °C), the dominant frequency components are around the switching frequency ($f_s = 7.95kHz$) and at the double of the switching frequency ($2f_s = 15.9kHz$).

The impact of the battery behavior on the dc currents within the HF range is determined by using the harmonic content (H_I) of the I_{dc} and the I_{bat} . The H_I represents the effective value of the ac part of the current in respect to the effective value of the current, and it's given mathematically in (3).

$$H_I = \frac{\text{effective value of } I_{ac}}{\text{effective value of } I} = \frac{I_{ac,eff}}{I_{eff}} \quad (3)$$

In order to eliminate the influence of any noise on the calculation of the harmonic content (H), only frequency components with an amplitude larger than 1% of the dc component are considered. The $H_{I_{dc}}$ and $H_{I_{bat}}$ are shown in Fig. 16 for the three different cases, where it can be seen that the use of HF model in the simulation of the ESS has no influence on Idc, but it influences significantly the harmonic content of Ibat. It can be seen also in Fig. 16 that there is almost no difference in the harmonic content calculation of Idc and Ibat when using 1RL-model or 2RL-model, nevertheless, the 2RL-model has a better accuracy in fitting the battery impedance than the 1RL-model. Based on these results the 1RL-model is always used in the next evaluations for representing the battery dynamics in the HF range.

C. Influence of Operation conditions on the Battery dynamics in the HF Range

The 1RL-model simulation results are used in this section to evaluate the dependency of the harmonic content of I_{bat} and I_{dc} on the SOC, the temperature, and the SOH. The $H_{I_{dc}}$ displayed in Fig. 17 shows a slight dependency on SOC, if one compares between $H_{I_{dc}}$ for $SOC = 30\%$ and $SOC = 70\%$. But it shows almost no dependency neither on the temperature nor on the SOH. The change of the $H_{I_{dc}}$ because of the SOC

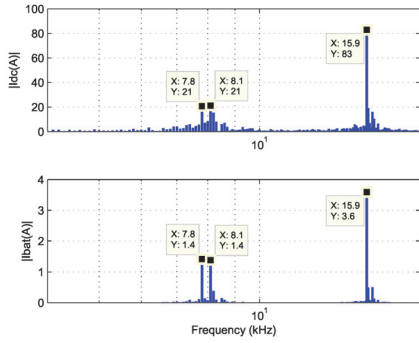


Fig. 9. FFT of I_{dc} and I_{bat} showing the main current harmonic for (SOH: aged, SOC=70 %, T=35 °C) when applying active power pulse of $P = 50kW$ and $Q = 0kvar$ and simulated using the 2RL-model.

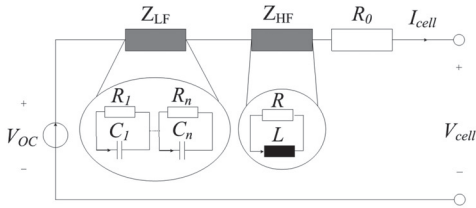


Fig. 10. Li-Ion battery general model structure for high and low frequency application.

is mainly due to the change of the dc component of the Idc as the battery output voltage varies with the SOC.

The H_{Ibat} depicted in Fig. 18 shows almost no dependency neither on temperature nor on SOC. But it shows a slight dependency on SOH, so for an aged battery the H_{Ibat} slightly increases compared to a new battery. This effect is due to the change of HF model parameters when the battery is aged.

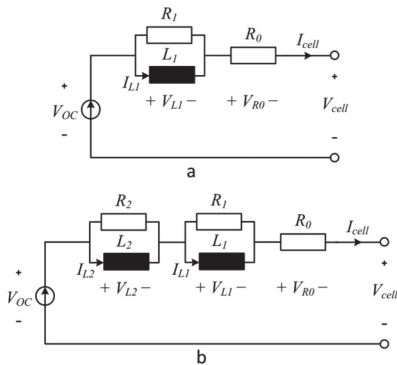


Fig. 11. Battery equivalent circuit models for HF. (a): 1RL-model; (b): 2RL-model.

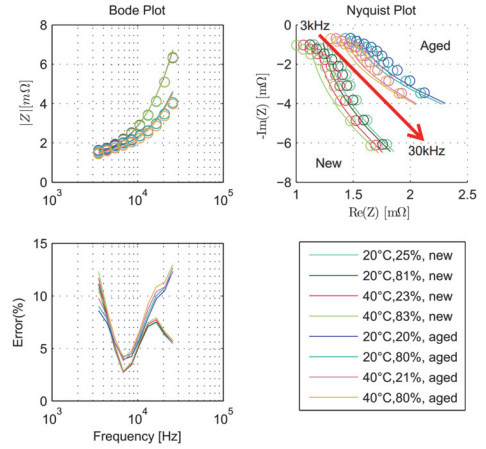


Fig. 12. Bode, Nyquist and error diagrams of cell's measured impedance (circles) and 1RL-model's impedance (line) for various operation conditions.

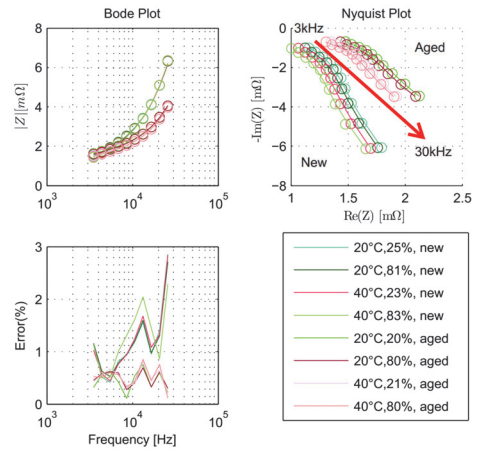


Fig. 13. Bode, Nyquist and error diagrams of cell's measured impedance (circles) and 2RL-model's impedance (line) for various operation conditions.

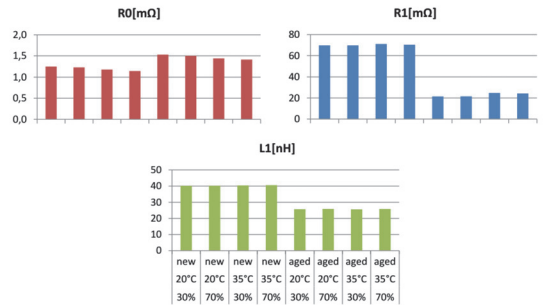


Fig. 14. 1RL-model's parameters dependency on SOC, cell's temperature and SOH.

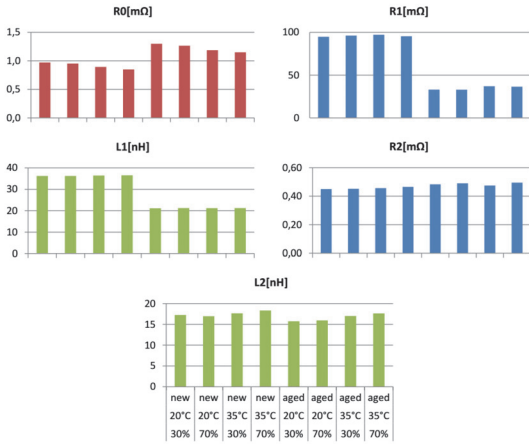


Fig. 15. 2RL-model's parameters dependency on SOC, cell's temperature and SOH.

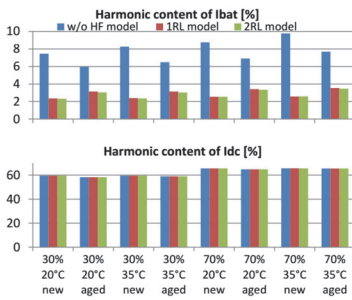


Fig. 16. Harmonic content of I_{dc} and I_{bat} calculated for three different cases and for eight operation conditions.

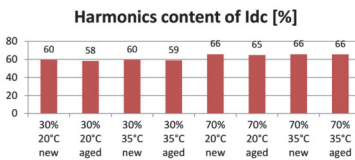


Fig. 17. Harmonic content of I_{dc} calculated based on simulation results when using 1RL-model for the eight operation conditions.

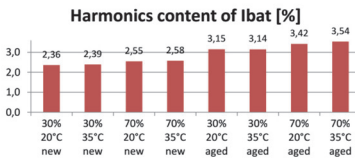


Fig. 18. Harmonic content of I_{bat} calculated based on simulation results when using 1RL-model for the eight operation conditions.

V. CONCLUSION

The paper is analyzing the usage of electrical models of li-ion batteries for the simulation of the ESS. The following 6 results have been found out:

- Battery ECM with one time constant (OTC) does not represent the fast battery's dynamics accurately mainly when the battery is aged. Therefore, at least two time constants (TTC model) are needed in order to represent the slow and fast dynamics of the battery over the whole service life of the cells (Fig. 4).
- Temperature deviation within 20°C to 35°C range as well as aging has a significant effect on the voltage drop at the dc-side and needs to be taken into account (Fig. 6 and Fig. 8).
- The SOC, the aging and the temperature do not have a significant effect on the Total Harmonics Distortion (THD) on the grid side (Tab. II).
- In order to calculate correctly the harmonics of I_{bat} , the usual ECM for low frequencies need to be extended by an HF model with one time constant (1RL-model).
- The harmonic content of I_{dc} and I_{bat} in Fig. 17 and Fig. 18 depicts that the effects of SOC, cells' temperature and aging on the harmonic content can be neglected.

We would underline that our results are only valid for the cells used in this investigation. Other cells might have different behavior.

ACKNOWLEDGMENT

The authors wish to thank the Federal Ministry for Economic Affairs and Energy of Germany for the financial support by the research project IREN2 (Future Oriented Electricity Grids for Integration of Renewable Energy Systems).

Argo Rosin's research work has been supported by Estonian Ministry of Education and Research (Project SF0140016s11).

REFERENCES

- [1] J. L. Helguero, "Modeling and simulation of a big battery storage system of a smart grid including power electronics," master thesis, Hochschule Kempten, March 2013.
- [2] T. Khani, "Modeling and simulation of a big battery storage system of a smart grid including power electronics and control," master thesis, Hochschule Kempten, September 2013.
- [3] L. F. Hoyos, "Simulation of a battery storage system taking into account a thermal-electric model for lithium-ion cells," master thesis, Hochschule Kempten, July 2014.
- [4] A. Rahmoun and H. Biechl, Parameters identification of equivalent circuit diagrams for li-ion batteries, in 11th International Symposium PRNU 2012 TOPICAL PROBLEMS IN THE FIELD OF ELECTRICAL AND POWER ENGINEERING and Doctoral School of Energy and Geotechnology II, 2012, pp. 3537.
- [5] A. Rahmoun, H. Biechl, and A. Rosin, Evaluation of Equivalent Circuit Diagrams and Transfer Functions for Modeling of Lithium-Ion Batteries, Sci. J. Riga Tech. Univ. - Electr. Control Commun. Eng., vol. 2, pp. 3439, 2013.

Curriculum vitae

Personal data

Name: Jorge Luis Helguero Cruz
Date of birth: 20 January 1986
Place of birth: Guayaquil - Ecuador
Citizenship: Ecuadorian / German

Contact data

E-mail: jorge.helguero@web.de

Education

2016–2023 Tallinn University of Technology, PhD
2011–2013 Kempten University of Applied Science, M.Eng.
2004–2009 Escuela Superior Politécnica del Litoral, B.Eng.

Language competence

Spanish native
English fluent
German fluent

Professional employment

2022– Relibell Zertifizierungsgesellschaft mbH, Evaluator
2021–2022 Ingenieurbüro Sing GmbH, Project Engineer
2013–2021 Kempten University of Applied Science, Research Assistant

Honours and awards

2013, VDI award for Master Thesis: “Modelling and simulation of a big battery storage system of a smart grid including power electronics”

Scholarships

2011–2013 Katholischer Akademischer Ausländer-Dienst

Research projects

2016–2019 Project DeCAS (Demonstration of coordinated ancillary services covering different voltage levels and the integration on future markets)
2015–2016 Project IREN2 (Future Oriented Electricity Grids for Integration of Renewable Energy Systems)
2012–2013 Project IRENE (Integration of Renewable Energies and Electromobility)

Elulookirjeldus

Isikuandmed

Nimi: Jorge Luis Helguero Cruz
Sünniaeg: 20. jaanuar 1986
Sünnikoht: Guayaquil - Ecuador
Kodakondsus: Ecuadori / Saksa

Kontaktandmed

E-post: jorge.helguero@web.de

Hariduskäik

2016–2023 Tallinna Tehnikaülikool, PhD
2011–2013 Kempteni Kõrgkool, M.Eng.
2004–2009 Escuela Superior Politécnica del Litoral, B.Eng.

Keelteoskus

Hispaania emakeel
Inglise kõrgtase
Saksa kõrgtase

Teenistuskäik

2022– Relibell Zertifizierungsgesellschaft mbH, evalveerija
2021–2022 Ingenieurbüro Sing GmbH, projekti insener
2013–2021 Kempteni Kõrgkool, uurija-assistent

Preemiad ja tunnustused

2013, VDI award for Master Thesis: “Modelling and simulation of a big battery storage system of a smart grid including power electronics”

Stipendiumid

2011–2013 Katholischer Akademischer Ausländer-Dienst

Projektid

2016–2019 Projekt DeCAS (Demonstration of coordinated ancillary services covering different voltage levels and the integration on future markets)
2015–2016 Projekt IREN2 (Future Oriented Electricity Grids for Integration of Renewable Energy Systems)
2012–2013 Projekt IRENE (Integration of Renewable Energies and Electromobility)

ISSN 2585-6901 (PDF)
ISBN 978-9916-80-064-5 (PDF)